Analysis of Charm Meson Semileptonic Decays and Charm Baryon High Mass States

by

Luca Cinquini

Laurea degree, University of Milan (Italy), 1991

M.S., University of Colorado, 1995

A thesis submitted to the

Faculty of the Graduate School of the

University of Colorado

in partial fulfillment of the requirements for the degree

Doctor of Philosophy

Department of Physics

1996

This thesis for the

Doctor of Philosophy degree

by

Luca Cinquini

has been approved for the

Department of Physics

by

_____

John P. Cumalat

_____

James G. Smith

Date _____

Cinquini, Luca (Ph.D., Physics)
Analysis of Charm Meson Semileptonic Decays
and Charm Baryon High Mass States
Thesis directed by Professor John P. Cumalat

We report on three different analyses performed on the data sample collected by Fermilab high energy charm photoproduction experiment E687.

In the first analysis, we study the semileptonic decays of the neutral charm meson D^0 into pseudoscalar final states: $D^0 \to K^-\mu^+\nu$ (Cabibbo-favored) and $D^0 \to \pi^-\mu^+\nu$ (Cabibbo-suppressed). We measure the ratio of the branching fractions for the two channels to be:

$$\frac{BR\ (D^0 \to \pi^-\mu^+\nu)}{BR\ (D^0 \to K^-\mu^+\nu)} = 0.099 \pm 0.026\ (stat)\ \pm 0.007\ (syst)\ .$$

Assuming a single pole dependence for the hadronic form factors, we measure:

$$\left|\frac{V_{cd}}{V_{cs}}\right|^2 \left|\frac{f_+^\pi(0)}{f_+^K(0)}\right|^2 = \ 0.048 \pm 0.014 \pm 0.003\ .$$

Using unitarity constraints on the CKM matrix, we compute:

$$\left|\frac{f_+^\pi(0)}{f_+^K(0)}\right| = 0.97 \pm 0.14 \pm 0.03\ .$$

In the second analysis, we investigate the semileptonic decays of the charged charm meson D^+ into vector meson final states: $D^+ \to$

$\overline{K}^{*0}\mu^+\nu$ (Cabibbo-favored) and $D^+ \to \varrho^0\mu^+\nu$ (Cabibbo-suppressed). We measure the ratio of the branching fractions of the two decays to be:

$$\frac{BR\ (D^+ \to \varrho^0\mu^+\nu)}{BR\ (D^+ \to K^{*0}\mu^+\nu)} = 0.079 \pm 0.019\ (stat)\ \pm 0.013\ (syst)\ .$$

We further report on weak evidence for the decay $D^+ \to \eta\mu^+\nu,\ \eta \to \pi^+\pi^-\pi^0$. We find the following ratio of branching fractions:

$$\frac{BR\ (D^+ \to \eta\mu^+\nu)}{BR\ (D^+ \to \varrho^0\mu^+\nu)} = 2.8 \pm 1.5\ (stat)\ \pm 0.2\ (syst)\ .$$

In the third analysis, we report on the study of higher mass charm baryons decaying to Λ_c^+: $\Lambda_c^{\star+}(2625) \to \Lambda_c^+\pi^+\pi^-$, $\Lambda_c^{\star+}(2593) \to \Lambda_c^+\pi^+\pi^-$, $\Sigma_c^0 \to \Lambda_c^+\pi^-$ and $\Sigma_c^{++} \to \Lambda_c^+\pi^+$(where the Λ_c^+ is reconstructed through several decay channels). We present confirmation for the state $\Lambda_c^{\star+}(2593)$ and determine its mass difference relative to the Λ_c^+ mass to be:

$$M(\Lambda_c^{\star+}(2593)) - M(\Lambda_c^+) = 309.2 \pm 0.7\ (stat) \pm 0.3\ (syst)\ MeV/c^2\ .$$

The lower limit on the resonant branching fraction of the decay is:

$$\frac{BR(\Lambda_c^{\star+}(2593) \to \Sigma_c\pi^\pm)}{BR(\Lambda_c^{\star+}(2593) \to \Lambda_c^+\pi^+\pi^-)}\ >\ 0.51\ (90\%\ c.l.)\ .$$

We also measure the mass differences for the Σ_c^0, Σ_c^{++} states to be:

$$M(\Sigma_c^0) - M(\Lambda_c^+) = 166.6 \pm 0.5\ (stat) \pm 0.6\ (syst)\ MeV/c^2\ ,$$

$$M(\Sigma_c^{++}) - M(\Lambda_c^+) = 167.6 \pm 0.6\ (stat) \pm 0.6\ (syst)\ MeV/c^2\ .$$

Finally, we report results on the relative photoproduction cross sections for $\Lambda_c^{\star+}$ and Σ_c states with respect to the (inclusive) photoproduction cross section for Λ_c^+.

To my parents, Mauro and Grazia

ACKNOWLEDGMENTS

A High Energy Physics experiment is the result of efforts of hundreds of people. I would therefore like to first thank the entire E687 collaboration for having run one of the most successful fixed target experiments ever.

The person who deserves the highest mention is undoubtedly my advisor, John Cumalat. I can not possibly imagine a better person to work with (with the exception of the owner of a seaside resort at the Carribbean). Every day he forges new ideas like an erupting volcano. But more than a great physicist, he is a great man. I fear the moment when I will have to work for someone else. Thankfully, I am staying, at least for a while.

Among the senior physicists of the collaboration, I would particularly like to thank the "Fantastic Four" (Silvano Sala, Luigi Moroni, Dario Menasce and Daniele Pedrini) for their friendship, their constant advice, for building such an incredible microvertex detector (the true core of the E687 experiment), and in general for being such "out of the ordinary" people. I would also like to single out Joel Butler, for his incessant direction and management, and Jim Wiss, for the theoretical background he gave to the whole collaboration and for his patient review of the $D^0 \to \pi^- l^+ \nu$ analysis presented in this thesis.

Among the younger people in the experiment, I would like to thank the following friends of mine, in the order I came to know them: Carlo Dallapiccola, for our early work on charm baryons and for introducing me to American culture and way of life; Gianluca Alimonti, for being such a fun roommate and for teaching me how to ride a motor bike; Will Johns, for dedicating himself to the experiment and for the guidance he gave all graduate students during these

years; Matt Nehring, for our successful collaboration on the $D^0 \to \pi^- l^+ \nu$ analysis and his great efforts in reducing the Čerenkov misidentification, which made this analysis possible; Harry Cheung, for his work on the baryon sector and his meticulous reviewing of my papers; Brian O'Reilly, for taking care of the muon detector (upon which most of this thesis is based), for introducing me to the pleasures of "beer and pool", and for being a close friend during the bad times; Eric Vaandering, for his work on the new IE and for sharing with me a passion for backpacking and outdoors; and finally, Daniele Brambilla, for his collaboration with Matt and myself on the semileptonic analysis.

I would also like to mention Peter Garbincius, Sergio Ratti, Gianluigi Boca, Phil Yager, Robert Gardner, Paul Sheldon, Ray Culbertson, Arthur Kramer, Peter Kasper, Paul Lebrun, Piero Inzani, John Ginkel, Vittorio Paolone, Vincenzo Arena, Cristina Riccardi, Barbara Caccianiga, Donatella Torretta, Margherita Vittone, Sandra Malvezzi, Franco Leveraro and Gary Grim for their various contributions to the experiment. A special thanks goes to Marco Giammarchi for introducing me to the experiment.

Outside the collaboration, I would like to thank Aldo and Giovanna Paoletti, for their friendship and the good moments we shared together.

I also owe a gratitude to the whole Physics Department at CU for being such a friendly and stimulating environment in which to work: my graduate teachers, the graduate committee of this thesis, and our staff (especially Kathy Oliver and Eric Erdos). I would like to single out Dr. Doug Johnson for taking such good care of the computer crashes and also for his words of advice.

Finally, my deepest gratitude goes to my family, Mauro, Grazia, Al and Carla, for their continuous support and encouragement.

CONTENTS

Chapter

1 CHARM QUARK PHYSICS 1

1.1 Introduction: elementary particles and interactions . . . 1

1.2 Photoproduction of heavy quarks 4

1.3 Weak decays of quarks and leptons 7

1.4 The CKM mixing matrix 8

1.5 Weak decay mechanisms of charm hadrons 10

1.6 Semileptonic decays of charm mesons 14

1.6.1 Pseudoscalar decays 15

1.6.2 Vector meson decays 20

2 THE E687 EXPERIMENTAL APPARATUS 23

2.1 The Fermilab Tevatron 24

2.2 The E687 beamline 26

2.3 The Beam Tagging System 29

2.3.1 The Silicon Microstrip Tagging 29

2.3.2 The Recoil Electron Shower Hodoscope detector . 29

2.3.3 The Beam Gamma Monitor 30

2.4 The interaction target 32

2.5 The silicon microstrip detector 34

2.6 The Analysis Magnets 36

2.7 The Multi-Wire Proportional Chambers 36

2.8 The Čerenkov Counters 37

2.9 The calorimeters 39
2.9.1 The electromagnetic calorimeters 39
2.9.2 The hadron calorimeters 40
2.10 The muon detectors 40
2.10.1 The Inner Muon system 41
2.10.2 The Outer Muon system 42
2.11 The Trigger 43
2.11.1 The First Level Trigger 43
2.11.2 The Second Level Trigger 46
2.12 Data acquisition 47
3 DATA RECONSTRUCTION 49
3.1 Track reconstruction 49
3.1.1 SSD track reconstruction 49
3.1.2 PWC track reconstruction 51
3.1.3 Linking of SSD and PWC tracks 54
3.2 SSD vertices reconstruction 57
3.3 Momentum determination 58
3.4 Čerenkov identification 59
3.5 Vee reconstruction 61
3.5.1 SSD vees 61
3.5.2 M1 vees 64
3.5.3 Recon vees 66
3.5.4 Single-linked SSD vees 67
3.5.5 MIC vees 68
3.5.6 Single-linked PWC vees 68
3.6 Candidate-driven vertexing algorithm 68

3.6.1 Secondary vertex reconstruction 69
3.6.2 Primary vertex reconstruction 71
3.6.3 Isolation 73
3.7 Muon reconstruction 74
3.7.1 The Coulomb scattering radius 77
3.7.2 HC+IE energy 78
3.7.3 Muon identification 80
4 PSEUDOSCALAR D^0 SEMILEPTONIC DECAYS 81
4.1 Analysis algorithm 81
4.2 The data signals 86
4.3 Discussion of backgrounds 86
4.3.1 D^0 tag semileptonic decays 89
4.3.2 Misidentified D^0 tag hadronic decays 95
4.3.3 Non-tag semileptonic decays 97
4.4 The fit 98
4.4.1 Fitting technique 98
4.4.2 The $K^-\mu^+\nu$ fit histogram 100
4.4.3 The $\pi^-\mu^+\nu$ fit histogram 101
4.4.4 Fit results 102
4.5 Branching ratio measurement 106
4.6 Systematic error on branching ratio measurement . . . 107
4.6.1 Split sample systematic error 107
4.6.2 Fit variants 109
4.6.3 Hadron-lepton misidentification background 110
4.6.4 Particle identification 112
4.6.5 $D^0 \to \varrho^-\mu^+\nu$ background 113

4.6.6 Pole mass variation 114
4.6.7 Total systematic error 118
4.7 Form factor ratio measurement 119
4.8 Systematic error on form factor measurement 124
4.9 Summary of results 126
5 VECTOR D^+ SEMILEPTONIC DECAYS 128
5.1 Analysis algorithm 128
5.2 The data signals 131
5.3 Discussion of backgrounds 132
5.3.1 $D^+ \to \overline{K}^{*0}\mu^+\nu$ 133
5.3.2 Non-tag D^+, D_s^+ inclusive semileptonic decays . . . 135
5.3.3 Tag D^0 semileptonic decays 140
5.3.4 Hadron-lepton misidentification background . . . 142
5.4 The fit 144
5.4.1 Fitting technique 144
5.4.2 The $\overline{K}^{*0}\mu^+\nu$ fit 146
5.4.3 The $\phi\mu^+\nu$ fit 146
5.4.4 The $\varrho^0\mu^+\nu$ fit 150
5.5 Branching ratio measurements 154
5.6 Systematic error studies 155
5.6.1 Split sample systematic errors 155
5.6.2 Fit variants 157
5.6.3 Particle identification 160
5.6.4 Total systematic error 161
5.7 Form Factor Measurement 161
5.8 Summary of results 162

6 CHARM BARYONS DECAYING TO Λ_c^+ 164

6.1 Introduction 164

6.2 Reconstruction of Λ_c^+ in several decay modes 166

6.3 $\Lambda_c^{*+}(2593)$ evidence and mass measurement 169

6.4 Analysis of the resonant decay $\Lambda_c^{\star+}(2593) \to \Sigma_c \pi^{\pm}$ . . 175

6.5 Measurement of photoproduction cross sections 180

6.6 Measurement of the Σ_c^0, Σ_c^{++} masses 183

6.7 Summary of results 188

7 SUMMARY AND CONCLUSIONS 190

7.1 Pseudoscalar D^0 semileptonic decays 190

7.2 Vector D^+ semileptonic decays 194

7.3 Charm baryons decaying to Λ_c^+ 196

7.4 Final remarks 198

CHAPTER 1

CHARM QUARK PHYSICS

1.1 Introduction: elementary particles and interactions

The purpose of Particle Physics is to study the ultimate structure of the universe: the fundamental particles which compose the matter the world is made of, and the fundamental interactions between particles, which make matter behave as it does. The best understanding we have today of the laws governing the fundamental particles and interactions is called the *Standard Model*.

In the Standard Model, all matter is composed by 12 pointlike elementary particles, grouped in two families: 6 *leptons* (electron e, muon μ, tau τ, electron neutrino ν_e, muon neutrino ν_μ, tau neutrino ν_τ [1]) and 6 *quarks* (up u, down d, strange s, charm c, beauty or bottom b and top t). For each elementary particle there is a corresponding anti-particle, which has equal and opposite quantum numbers. Both leptons and quarks have spin $\frac{1}{2}$ and are called *fermions*. The three leptons e, μ, τ have unitary (negative) electric charge and are massive, while the three corresponding neutrinos ν_e, ν_μ, ν_τ have zero electric charge and are known to be non-massive (or at least have very small mass). The six quarks are all massive, have fractional electric charge and are further characterized by a *color charge*, which may have three different values - let's say red, green and blue (leptons don't have color charge). Quarks can not be found free in nature, but are compelled to combine into more complex structures called *hadrons*, which must be color neutrals ("quark confinement"). Hadrons can be composed of a quark and an anti-quark (*mesons*: $q\overline{q}$), or by three quarks or three anti-quarks (*baryons*: qqq or $\overline{qqq}$). Mesons have integer

spin (and are called *bosons*), while baryons have half-integer spin (so they are fermions).

Table 1.1.1 Quarks and Leptons Properties

Quarks (spin= $\frac{1}{2}$)			Leptons (spin= $\frac{1}{2}$)		
Flavor	Electric Charge	Mass (GeV/c^2)	Flavor	Electric Charge	Mass (GeV/c^2)
u	+2/3	0.004	e	-1	0.0005
d	-1/3	0.007	ν_e	0	0
c	+2/3	1.3	μ	-1	0.106
s	-1/3	0.3	μ_ν	0	0
t	+2/3	180	τ	-1	1.777
b	-1/3	4.8	ν_τ	0	0

All known interactions between matter particles can be explained in terms of only four fundamental forces, which in order of increasing strength are *the gravitational force*, *the weak force*, *the electromagnetic force*, and the *color force*. The gravitational force acts between particles with mass and is responsible for the binding of matter on a planetary and cosmic scale, but because of its small intensity it has negligible effects on high energy physics phenomena. The weak force acts upon particles with *weak charge* (all leptons and quarks) and accounts for some of the spontaneous transformation of particles into others with lower mass (for example, the β decay of a radioactive nucleus). It is because of the weak force that all the very massive particles created at the birth of the universe, have since decayed to the less massive particles that compose the world we experience today. Quark or lepton flavor is not conserved during weak interactions. Particles with electric charge (all

quarks and the three charged leptons) interact through the electromagnetic force: this force binds atoms and molecules together. Finally, the color force acts between particles with color charge (all quarks but not the leptons) and is responsible for the confinement of the quarks inside a hadron (and on a larger scale, for the binding of the hadrons in a nucleus). Both the electromagnetic and the color force conserve quark and lepton flavor.

When two matter particles interact through a fundamental force, the process is described as the exchange of "force particles" called *gauge bosons* (which have integer spin)[2]. The gauge bosons are the vehicle through which fundamental forces are conveyed between particles. The range of each fundamental force is inversely proportional to the mass of the corresponding gauge boson. For example, the electromagnetic force is mediated by the *photon* γ, which has zero mass: consequently its range is infinite. The weak force instead is mediated by two very massive bosons, the $W^{\pm}$ and the Z^0, and it has very short range. Also the color force has short range: the corresponding gauge bosons are called *gluons* g[3][4].

Table 1.1.2 Gauge Bosons Properties

Gauge Bosons (spin= 1)				
Boson	Electric Charge	Mass (GeV/c^2)	Force Mediated	Exchanged between
γ	0	0	electromagnetic	e, μ, τ and all quarks
$W^{\pm}$	± 1	80.6	weak	all leptons and quarks
Z^0	0	91.2	weak	all leptons and quarks
g	0	0	color	quarks

1.2 Photoproduction of heavy quarks

Hadrons composed of heavy quarks may be generated in high energy interactions between lower mass particles. In *photoproduction*, this is realized by impacting a high energy photon beam on a fixed target of some material. Because of flavor conservation, heavy quark particles must always be produced in pairs - one containing the quark Q and another containing the anti-quark $\overline{Q}$ (mesons with "hidden" flavor, i.e. composed by $Q\overline{Q}$, are singularly produced).

The mechanism primarily responsible for heavy quark photoproduction is known as *Photon-Gluon Fusion* (PGF). When a photon comes in the range of a target nucleus, it may interact with a gluon from the nucleus and produce a $Q\overline{Q}$ pair. The two "leading-order" diagrams for this process (amplitude proportional to $\alpha_{qed}\alpha_s$) are shown in Figures 1.2.1 (a), (b). Higher order diagrams involving external gluon lines and virtual gluon exchange ("next-to-leading-order", amplitude proportional to $\alpha_{qed}\alpha_s^2$) are also possible, and may contribute $20 - 30\%$ to the total amplitude[5] (Figures 1.2.1 (c)-(f)).

After the $Q\overline{Q}$ pair is produced, it has to "dress" itself in the form of the heavy quark hadrons which are observed in the experiments. Since the pair is not color neutral (retaining the color of the exchanged gluon), the *dressing* or *fragmentation* process must involve the quarks composing the nucleus, in addition to the quark pairs materialized from the vacuum (see Figure 1.2.2). As a side product, non-heavy quark hadrons may be produced at the primary interaction point.

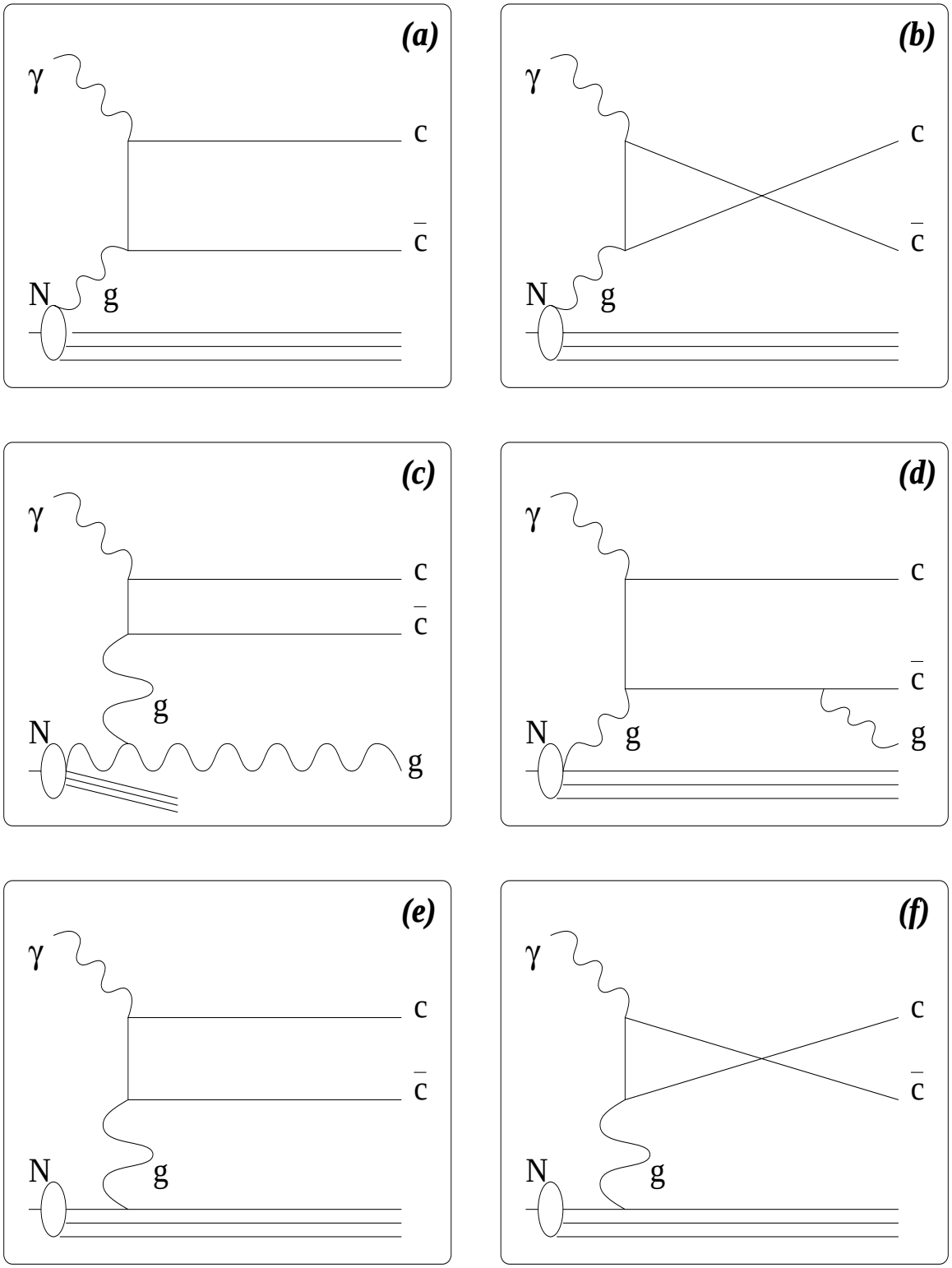

Figure 1.2.1 Leading-order (a)-(b) and next-to-leading-order (c)-(f) diagrams for Photon-Gluon-Fusion leading to charm photoproduction.

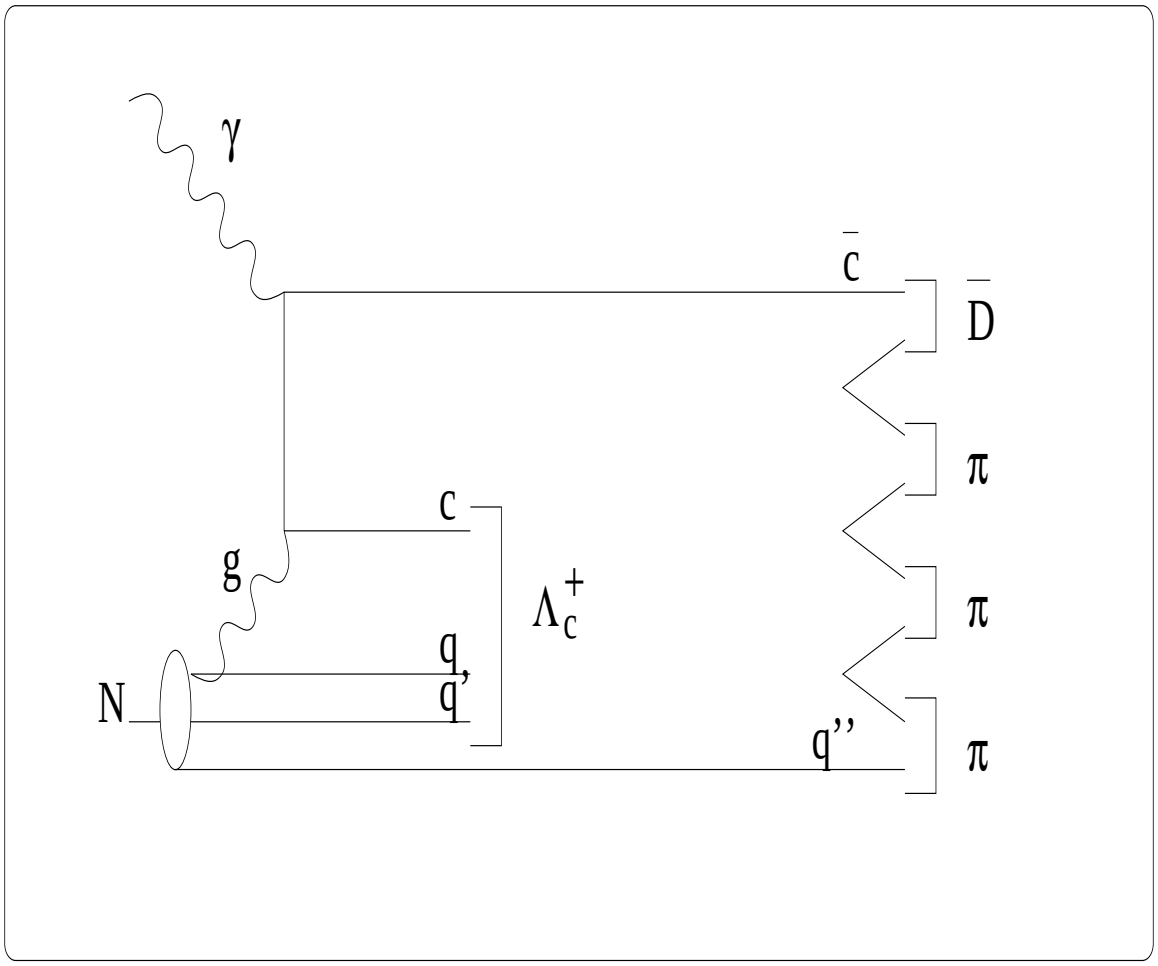

Figure 1.2.2 Schematic picture of a fragmentation process leading to associate production of a charm baryon and a charm anti-meson.

In case heavy flavor baryon production takes place, the fragmentation model anticipates there will be an excess of baryons over anti-baryons produced (and consequently, an excess of anti-mesons over mesons). This is because it is easier for the Q quark to couple to a light di-quark from the target, rather than for the $\overline{Q}$ to couple to a pair of anti-quarks which would have to be produced from the sea. This anticipated baryon-anti-meson *associated*

production is actually observed in experiments at low energy, near the $Q\overline{Q}$ production threshold.

Heavy flavor mesons and baryons are short-lived. After being photo-produced, they travel a short distance (depending on their energy and actual lifetime) and then decay via the weak interaction into lighter-quark hadrons.

1.3 Weak decays of quarks and leptons

In the Standard Model both leptons and quarks are grouped into three generations of electroweak doublets:

$$\begin{pmatrix} \nu_e \\ e \end{pmatrix} \begin{pmatrix} \nu_\mu \\ \mu \end{pmatrix} \begin{pmatrix} \nu_\tau \\ \tau \end{pmatrix} ,$$

$$\begin{pmatrix} u \\ d' \end{pmatrix} \begin{pmatrix} c \\ s' \end{pmatrix} \begin{pmatrix} t \\ b' \end{pmatrix} .$$

In a lepton doublet, the upper component has electric charge 0 and the lower component has electric charge -1 (in unit of the electron charge); in a quark doublet, the upper and lower components have charge $+\frac{2}{3}$ and $-\frac{1}{3}$, respectively.

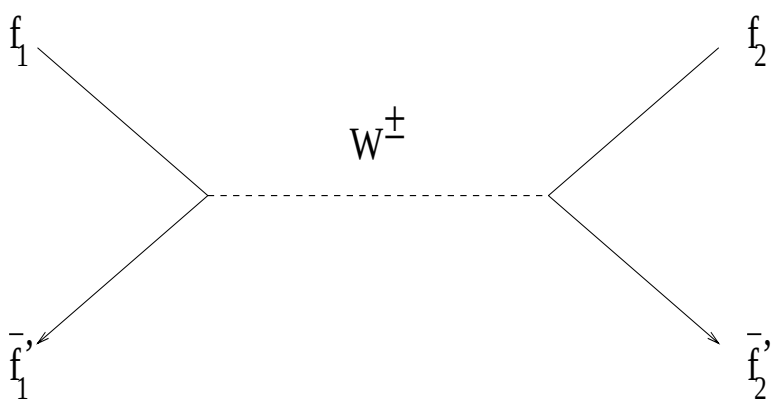

Figure 1.3.1 Schematic representation of a weak decay. Here (f_1, f_1') and (f_2, f_2') are fermions belonging to the same electroweak doublet.

During a weak decay a fermion (lepton or quark) transforms into its doublet partner by emission of a charged weak boson $W^{\pm}$. The $W^{\pm}$ can then either materialize a fermion-anti-fermion pair belonging to the same doublet, or couple to another fermion and transform it in its doublet partner (see Figure 1.3.1). A weak decay can therefore be represented as the interaction of two fermion currents (either leptonic or hadronic), mediated by a charged $W^{\pm}$ bosonic current. Since only transitions between doublet partners are possible, the weak current mediating the decay process is always charged. Obviously, a weak decay can take place only if it is energetically possible, i.e. if the parent fermion has a larger mass than the daughter fermion. For this reason the quark u and the lepton e, being the lowest mass quark and lepton, do not decay.

1.4 The CKM mixing matrix

The lower components of the electroweak quark doublets d', s', b' are not the mass eigenstates entering the QCD lagrangian d, s, b, but rather are linear combinations defined by[7] :

$$\begin{pmatrix} d' \\ s' \\ b' \end{pmatrix} = \begin{pmatrix} V_{ud} & V_{us} & V_{ub} \\ V_{cd} & V_{cs} & V_{cb} \\ V_{td} & V_{ts} & V_{tb} \end{pmatrix} \begin{pmatrix} d \\ s \\ b \end{pmatrix} = \bigvee \begin{pmatrix} d \\ s \\ b \end{pmatrix} .$$

The mixing matrix $\bigvee$, which "rotates" the mass eigenstates d, s, b into the electroweak eigenstates d', s', b' is called the Cabibbo-Kobayashi-Maskawa (CKM) matrix[8]. It is a 3×3 (complex) unitary matrix which depends on four independent parameters (since the phases of five of the six quark fields can be chosen arbitrarily). One possible parameterization consists of choosing the degrees of freedom to be expressed by three real angles of rotation (i.e.

the parameters for a rotation in a three dimensional euclidean space) and a complex phase:

$$V_{ud} = c_1 \quad V_{us} = -s_1 c_3 \quad V_{ub} = -s_1 s_3$$
$$V_{cd} = s_1 c_2 \quad V_{cs} = c_1 c_2 c_3 - s_2 s_3 e^{i\delta} \quad V_{cb} = c_1 c_2 s_3 + s_2 c_3 e^{i\delta}$$
$$V_{td} = -s_1 s_2 \quad V_{ts} = c_1 s_2 c_3 + c_2 s_3 e^{i\delta} \quad V_{tb} = c_1 s_2 s_3 - c_2 c_3 e^{i\delta}$$

where $s_i = \sin\theta_i$ and $c_i = \cos\theta_i$. The complex phase is related to CP violation; values of δ different from 0 or 2π imply a violation of CP invariance by the Electroweak Interaction within the framework of the Standard Model. In the limit where $s_2 = s_3 = 0$, the third generation of quarks decouples from the first two and the 2×2 upper portion of the CKM matrix becomes:

$$\begin{pmatrix} cos\theta_c & -sin\theta_c \\ sin\theta_c & cos\theta_c \end{pmatrix}$$

which is called the Cabibbo matrix and was first introduced by Cabibbo in the framework of a four quark model. The Cabibbo matrix is parameterized by a single real parameter, the Cabibbo angle $\theta_c \sim 13^0$.

The coupling constant associated with a quark electroweak vertex $Q \to qW^{\pm}$ (describing the decay of a heavier quark Q into a lighter quark q) is proportional to the CKM matrix element V_{Qq}. As a consequence, the rate of the decay is proportional to $|V_{Qq}|^2$. Since the diagonal elements V_{ud}, V_{cs}, V_{tb} are (in magnitude) close to 1, the most probable weak decays between quarks are $t \to b$, $c \to s$ and $u \to d$. The off-diagonal elements are much smaller, and therefore the corresponding transitions $t \to s$, $b \to c$, $c \to d$, $s \to u$ are much less likely to happen. As a consequence, particles with b or s content have

longer lifetimes than one would predict from pure phase space considerations. Finally, the remaining 2 elements V_{ub}, V_{td} are close to zero, making the decays $t \rightarrow d$ and $b \rightarrow u$ extremely unlikely. In the context of a four quark model, the decays $c \rightarrow s$ and $u \rightarrow d$ (probability $\propto cos^2\theta_c \sim 0.95$) are said to be *Cabibbo-favored*, while the decays $c \rightarrow d$ and $s \rightarrow u$ (probability $\propto sin^2\theta_c \sim 0.05$) are said to be *Cabibbo-suppressed*. A weak decay which is Cabibbo-suppressed at both vertices is said to be *doubly Cabibbo-suppressed* (see Figure 1.4.1).

The unitarity condition on V implies that the sum of the squared magnitudes of the elements belonging to any row or column must be one. This requirement allows computation of higher generation CKM matrix elements with much better accuracy than current experimental measurements alone would permit.

1.5 Weak decay mechanisms of charm hadrons

In the Standard Model, the charm quark decays via a weak charged current into the strange or down quark. The lowest order diagrams (i.e. neglecting gluon emission) through which the decay can proceed are shown in Figure 1.5.1 (for the case of a charm meson $D = (c\overline{q})$).

In the (external) *spectator decay* (Figure 1.5.1 (a)), the W boson emitted by the charm quark either materializes as a lepton-neutrino pair (semileptonic decay), or as a quark-anti-quark pair (hadronic decay), which then hadronize into a daughter meson (K or π). The light anti-quark $\overline{q}$ is a spectator to the charm decay process and afterwards combines with the daughter s or d quark to form another daughter meson. In the spectator mechanism, the decay rate into any $q'\overline{q}'$ pair is favored by a factor of three over the decay rate into a $l\,\nu_l$ pair, because there are three color degrees of freedom.

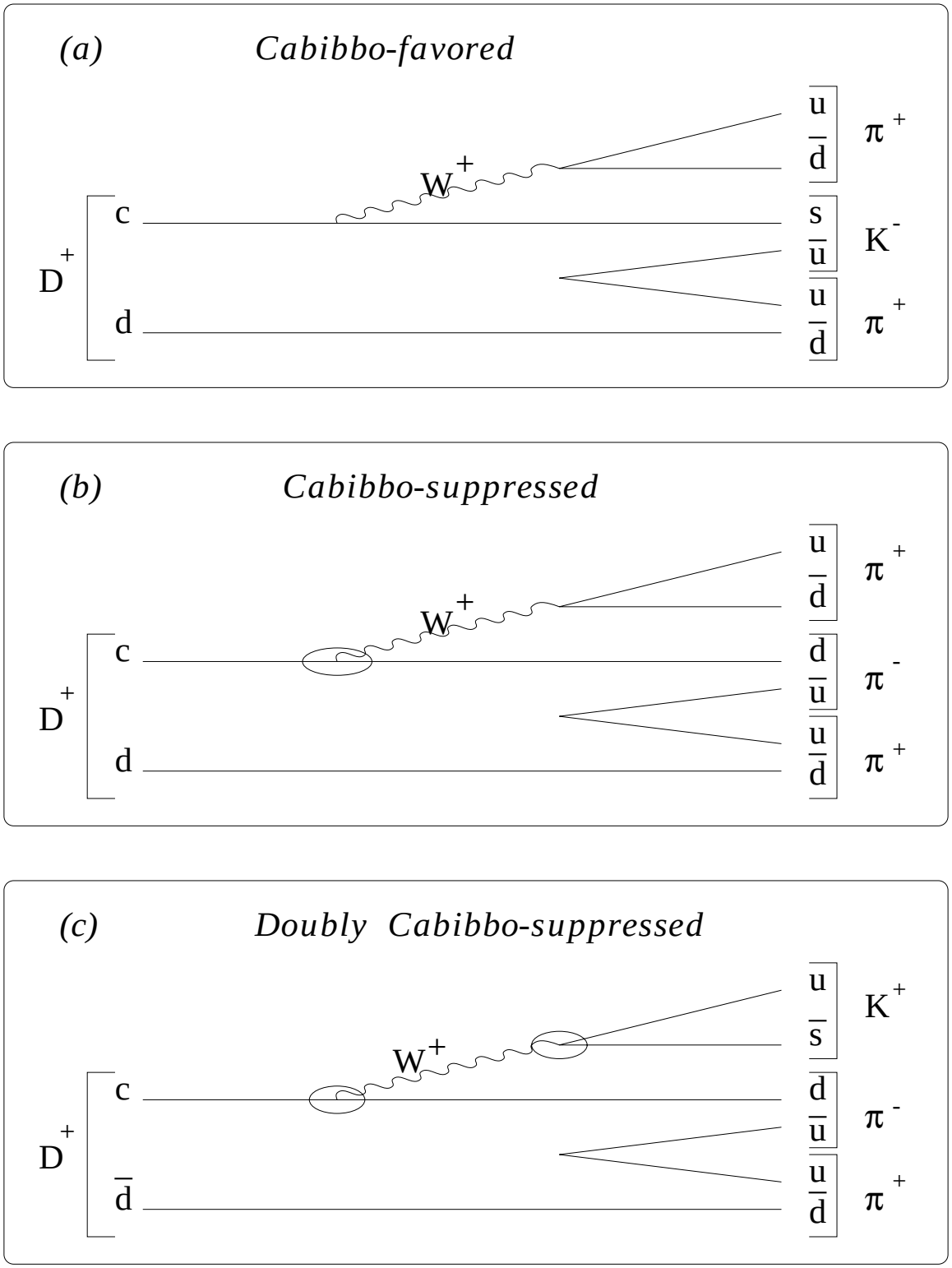

Figure 1.4.1 Decay diagrams for (a) $D^+ \to K^-\pi^+\pi^+$, (b) $D^+ \to \pi^-\pi^+\pi^+$, (c) $D^+ \to K^+\pi^+\pi^-$. Cabibbo-suppressed vertices are indicated by an ellipse.

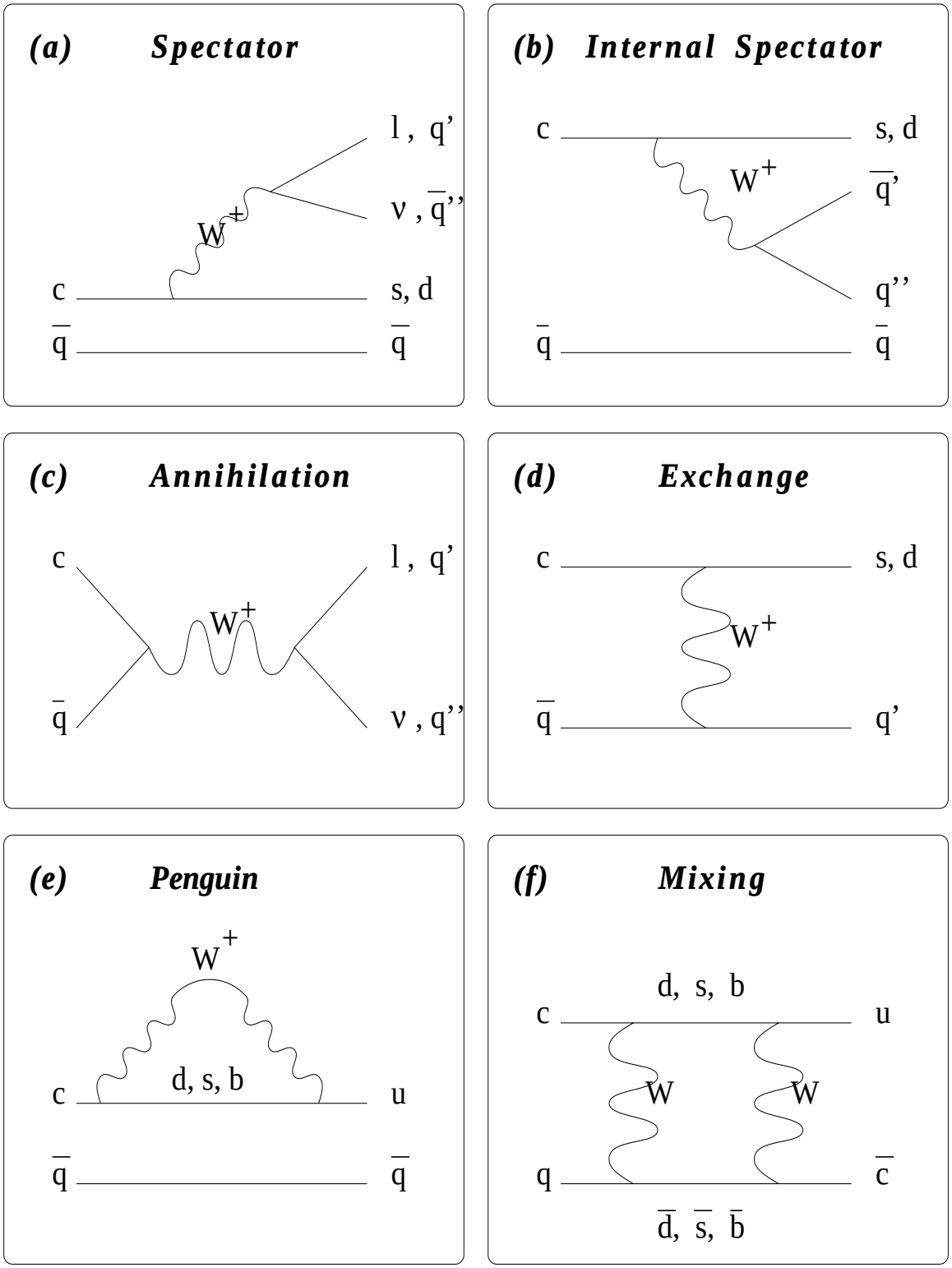

Figure 1.5.1 Possible decay diagrams for charm mesons. In all cases, it is possible to materialize $q\overline{q}$ pairs from the quark sea, resulting in higher multiplicity final states.

In the *internal spectator decay* (Figure 1.5.1 (b)), the $\overline{q}'q''$ pair resulting from the W boson decay couples to the charm daughter quark s or d and the light anti-quark $\overline{q}$ to produce the final state hadrons. Since the color degree of freedom of the coupling quarks must match, the internal spectator decay rate is suppressed by a factor of three with respect to the external spectator (although soft gluon exchange might ameliorate color suppression and enhance the rate[9][10]). The final state for an internal spectator decay is always purely hadronic.

In the *annihilation diagram* (Figure 1.5.1 (c)), the charm quark combines with its light anti-quark partner to produce a virtual W, which then decays into a lepton-neutrino pair (purely leptonic decay) or a quark-anti-quark pair (hadronic decay). The hadronic modes are again favored by the color degrees of freedom with respect to the leptonic modes.

In the *exchange diagram* (Figure 1.5.1 (d)), the charm quark and the light anti-quark composing the meson exchange a virtual W boson and transform into their doublet partners. The final state is always hadronic.

In the case of charm mesons, the decay rate for both the annihilation and the exchange diagrams are *helicity-suppressed*[11][12], and consequently the spectator diagrams are expected to be the dominant mechanisms of decay. In the case of charm baryons, *helicity suppression* is avoided by the presence of the additional light quark, so that both the internal spectator and the exchange diagrams may in principle contribute significantly to the total decay rate (no annihilation diagram is possible for baryons).

Other more exotic possible decay mechanisms are the *penguin diagram* (Figure 1.5.1 (e)) and the *mixing* or *double-exchange diagram* (Figure 1.5.1 (f)).

In loop diagrams though, the heaviest virtual quark produces the largest effects. In a charm decay, the heaviest possible virtual quark produced is the b quark, and the amplitude of the process is proportional to $|V_{cb}| \cdot |V_{bu}|$, which is very small. These exotic diagrams are not expected to be significant for charm quark decays.

1.6 Semileptonic decays of charm mesons

Much knowledge of the weak decays of heavy-quark particles can be gained from the study of charm meson semileptonic decays. The advantage of studying semileptonic decays comes from the fact that the underlying interaction process is relatively simple.

First, semileptonic decays can proceed only through the spectator diagram, so that there is no contribution to the decay rate coming from other diagrams (as it happens for hadronic decays). This means there is no possibility of interference between the final state leptons and quarks. Secondly, the matrix amplitude for the decay may be factorized as the product of a leptonic and a hadronic current; since the leptonic current is well understood, the study of semileptonic decay provides information about the hadronic current.

The decay of a parent pseudoscalar ($J^P = 0^-$) charm meson can produce either a pseudoscalar meson ($D \to h\, l\, \nu$) or a vector ($J^P = 1^-$) meson ($D \to h^*\, l\, \nu$). The first case is simpler from a kinematic point of view and will be discussed in some detail, while the second case will be addressed only briefly.

1.6.1 Pseudoscalar decays

We are interested in the exclusive semileptonic decay of a pseudoscalar charm meson D into a lighter pseudoscalar meson h: $D \to h\, l\, \nu$, where the lepton can be either an electron or a muon and the hadron h is either a kaon or a pion. Specific examples of this type of decay are $D^0 \to K^- l^+ \nu$, $D^0 \to \pi^- l^+ \nu$ and $D^+ \to \overline{K}^0 l^+ \nu$. The Feynman diagram for the decay is sketched in Figure 1.6.1, where the four-momenta of all the particles are indicated in parentheses. Four-momentum conservation requires $P = Q + p + k$.

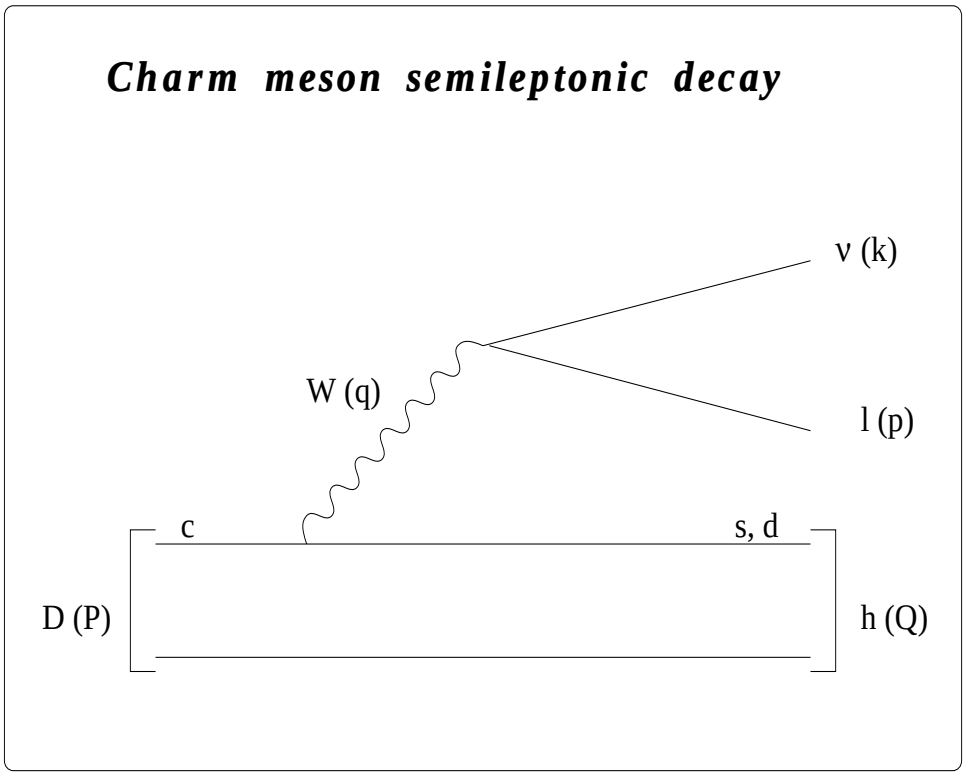

Figure 1.6.1 Feynman diagram for the pseudoscalar semileptonic decay of a D meson.

In the *rest frame of the parent D meson*, where $P = (M_D, 0, 0, 0)$, the decay rate is given by:

$$d,\ (D \to hl\nu) = \frac{|\mathcal{M}(D \to hl\nu)|^2}{2M_D} d\Pi_3 \ ,$$

where the three-body phase space is:

$$d\Pi_3 = (2\pi)^4 \delta^4(P - Q - p - k) \frac{d^3Q}{(2\pi)^3 2E_h} \frac{d^3p}{(2\pi)^3 2E_l} \frac{d^3k}{(2\pi)^3 2E_\nu} \ ,$$

and the matrix element for the decay is computed as (by use of the Feynman rules for the electroweak theory):

$$\mathcal{M}(D \to hl\nu) = (\frac{g}{2\sqrt{2}})^2 V_{cq} L^\alpha \left[-i(\frac{g_{\alpha\beta} - q_\alpha q_\beta}{q^2 - M_W^2}) \right] H^\beta \ .$$

In the above expression q is the four-momentum carried by the virtual boson W^+, i.e. the invariant mass of the lepton-neutrino pair:

$$\begin{aligned} q^2 &\equiv (p+k)^2 = m_l^2 + 2\ p \cdot k = M_{l\nu}^2 \\ &= (P - Q)^2 = P^2 + Q^2 - 2\ P \cdot Q \\ &= M_D^2 + m_h^2 - 2\ (E_D E_h - \vec{P} \cdot \vec{Q}) \\ &\overset{D\ rest\ frame}{=} M_D^2 + m_h^2 - 2M_D E_h \leq (M_D - m_h)^2 . \end{aligned}$$

In the limit where $q^2 \ll M_W^2$ (i.e. of a pointlike interaction), the propagator for the boson line becomes simply $\frac{g_{\alpha\beta}}{M_W^2}$, and the matrix element simplifies to:

$$\mathcal{M}(D \to hl\nu) = \frac{G_F}{\sqrt{2}} V_{cq} L^\alpha H_\alpha$$

(where the identity $\frac{G_F}{\sqrt{2}} = \frac{g^2}{8M_W^2}$ was used). Here L^α and H_α are the leptonic and hadronic currents involved in the decay, respectively, and V_{cq} is the CKM matrix element for the specific weak transition of the charm quark $c \to q$.

The leptonic current is simply obtained by coupling the Dirac bispinors of the massive lepton and the neutrino through the usual $V-A$ prescription for the weak interaction:

$$L^{\alpha} = \overline{u}_{\nu}\gamma^{\alpha}(1-\gamma^{5})v_{l} \ .$$

The hadronic current must be constructed from the four momenta of the problem and Lorentz-invariant dimensionless form factors (representing the unknown details of the hadronic process). *For the case of a pseudoscalar meson in the final state*, the spins of both the parent and the daughter hadrons are zero, so there are only two independent four-momentum vectors P and Q. As a consequence, the decay can proceed only through the vector part of the $V-A$ interaction[13], and the hadronic current is written through the use of *two* form factors:

$$H_{\alpha} =< Q|V_{\alpha}|P >= f_{+}^{h}(q^{2})\ (P+Q)_{\alpha} + f_{-}^{h}(q^{2})\ (P-Q)_{\alpha} \ .$$

The form factors will in general be functions of the four momentum transferred q^2, and may depend on the flavor of the two quarks composing the hadronic current. They are usually[14] parameterized by a *single pole mass* dependence:

$$f_{\pm}^{h}(q^{2}) = \frac{f_{\pm}^{h}(0)}{1-q^{2}/M_{pole}^{h\,2}} \ ,$$

where $f_{\pm}^{h}(0)$ represent the form factor normalization, i.e. the form factor at zero momentum transferred $q=0$. The pole mass M^h is expected to be equal to the mass of the lowest vector meson resonance composed of the two quarks

involved in the weak decay. Therefore it is expected $M^K_{pole} = M(D_s^{*+}) = 2.11\ GeV/c^2$ for a $c \to s$ decay, and $M^\pi_{pole} = M(D^{*+}) = 2.01\ GeV/c^2$ for a $c \to d$ decay.

In the parent rest frame, the decay is completely described by two independent variables[15]. We can choose for example the energies of the daughter hadron E_h and the daughter lepton E_l. Integrating over all the other variables[13], the decay rate becomes:

$$d^2,(D \to hl\nu) = \frac{|\mathcal{M}(D \to hl\nu)|^2}{64\pi^3 M_D} dE_h dE_l \ ,$$

and computing explicitly the semileptonic matrix element[13]:

$$\frac{d^2,(D \to hl\nu)}{dE_h dE_l} = \frac{G_F^2}{16\pi^3}|V_{cq}|^2 \ |f_+^h(q^2)|^2 \left\{ A + B \ Re\xi + C \ |\xi|^2 \right\} \ ,$$

where $\xi(q^2) \equiv \frac{f_-^h(q^2)}{f_+(q^2)}$ is the ratio of the two form factors entering the hadronic current, and A, B, C are kinematic factors given by:

$$\begin{aligned}
A &= M_D \left[2E_l E_\nu - M_D \left(E_{h,max} - E_h \right) \right] + \frac{1}{4} m_l^2 \left(E_{h,max} - E_h \right) - m_l^2 E_\nu \ , \\
B &= m_l^2 \left[E_\nu - \frac{1}{2} \left(E_{h,max} - E_h \right) \right] \ , \\
C &= \frac{1}{4} m_l^2 \left(E_{h,max} - E_h \right) \ ,
\end{aligned}$$

with:

$$\begin{aligned}
E_\nu &= M_D - E_h - E_l \ , \\
E_{h,max} &= \frac{(M_D^2 + M_h^2 - m_l^2)}{2M_D} \ .
\end{aligned}$$

It can be noticed that ξ enters the decay rate only through terms proportional to the lepton mass squared m_l^2. If the lepton mass is neglected (as it is certainly

allowed in a semi-electronic decay, and in first approximation also in a semi-muonic decay), the second form factor $f_-^h(q^2)$ drops out of the calculation and the decay rate expression depends only on one unknown form factor, $f_+^h(q^2)$.

Another possible choice for the two independent variables consists in using the four momentum transferred q and the two-body hadron-lepton invariant mass m_{hl}. The relation between the two sets of variables is given by:

$$E_h = \frac{(M_D^2 + m_h^2 - q^2)}{2M_D} \ ,$$
$$E_l = \frac{(m_{lh}^2 - m_h^2 + q^2)}{2M_D} \ ,$$

or

$$q^2 = M_D^2 + m_h^2 - 2M_D E_h \ ,$$
$$m_{hl}^2 = (Q+p)^2 = -M_D^2 + 2M_D E_h + 2M_D E_l \ .$$

Using q^2 and m_{hl}^2, the decay rate can be rewritten as:

$$\frac{d^2, (D \to hl\nu)}{dq^2 dm_{hl}^2} = \frac{G^2}{64\pi^3 M_D^2} |V_{cq}|^2 \ |f_+^h(q^2)|^2 \left\{ A + B \ Re\xi + C \ |\xi|^2 \right\}$$

where A, B, C must now be expressed through the new set of variables. This equation describes how semileptonic decay events $D \to h\,l\,\nu$ are distributed over the kinematicaly allowed region of the Dalitz plot $q^2 (= m_{l\nu}^2)$ vs. m_{hl}^2. This density depends on the functional form of the hadronic form factors and on their relative strength. Consequently, important information on the structure of the hadronic current can be derived from studying the Dalitz plot density of a sufficiently large sample of $D \to h\,l\,\nu$ decays.

Another important piece of information which can be derived from the above equation is the ratio of the form factor normalizations for two different semileptonic decays, when the two corresponding rates are compared. Let's consider the two decays $D \to K\, l\, \nu$ (quark transitions $c \to s$) and $D \to \pi\, l\, \nu$ (quark transition $c \to d$). By integrating the differential decay rate over the *full region* of the Dalitz plot, and taking the ratio of the two modes, we obtain:

$$\frac{,\,(\pi l \nu)}{,\,(K l \nu)} = \left|\frac{V_{cd}}{V_{cs}}\right|^2 \left|\frac{f_+^{\pi}(0)}{f_+^{K}(0)}\right|^2 \times \frac{\int_{(m_\pi+m_l)^2}^{M_D^2} dm_{\pi l}^2 \int_{q^2_{min}}^{q^2_{max}} dq^2 \left|\frac{f_+^{\pi}(q^2)}{f_+^{\pi}(0)}\right|^2 \left[A + BRe\xi + C|\xi|^2\right]_{\pi l \nu}}{\int_{(m_K+m_l)^2}^{M_D^2} dm_{Kl}^2 \int_{q^2_{min}}^{q^2_{max}} dq^2 \left|\frac{f_+^{K}(q^2)}{f_+^{K}(0)}\right|^2 \left[A + BRe\xi + C|\xi|^2\right]_{K l \nu}} ,$$

where the two limits in the inner integration q^2_{min}, q^2_{max} are functions of m^2_{hl} [16]. In the above expression, we have assumed a single pole mass dependence for the form factors and we have factorized out the normalization constants. Since the integrals on the right hand side can be computed analytically, this equation can be used to calculate the combined quantity

$$FV \equiv \left|\frac{V_{cd}}{V_{cs}}\right|^2 \left|\frac{f_+^{\pi}(0)}{f_+^{K}(0)}\right|^2 ,$$

once the branching ratio of the two decays has been determined. In Table 1.6.1 we report the value of the ratio of integrals for different values of the lepton mass.

Table 1.6.1 Ratio of integrals [$*$]

	$I(\pi\, l\, \nu)/I(K\, l\, \nu)$
$m_l = 0$	1.9712390
$m_l = m_e$	1.9712396
$m_l = m_\mu$	1.9946779

[$*$] The values listed are obtained by considering a single pole mass dependence for the form factors and by further assuming $\xi = -1$, $M^K_{pole} = 2.11\ GeV/c^2$, $M^\pi_{pole} = 2.01\ GeV/c^2$. The numbers are determined by an integration over the whole Dalitz plot.

At present, the uncertainty in the theoretically predicted value for $\left|\frac{f_+^\pi(0)}{f_+^K(0)}\right|^2$ is too large to use this technique to obtain a useful measurement of the $\left|\frac{V_{cd}}{V_{cs}}\right|$ ratio. On the contrary, it is possible to use the value for $\left|\frac{V_{cd}}{V_{cs}}\right|$ which is deduced from other measurements of CKM matrix elements and from CKM unitarity, to obtain an estimate for $\left|\frac{f_+^\pi(0)}{f_+^K(0)}\right|^2$.

1.6.2 Vector meson decays

The decay of a pseudoscalar charm meson into a vector meson $D \to h^*\, l^+\, \nu$ is more complicated than the decay into a pseudoscalar meson. First of all, the process can now be mediated by both the vector and the axial vector parts of the weak current. Also, there is another vector to be taken into account in constructing the hadronic current, namely the polarization vector ϵ of the vector meson. Consequently, the hadronic current is written by use of

four form factors[14] [17] [21]:

$$H_\alpha = < Q, \epsilon | V_\alpha | P > - < Q, \epsilon | A_\alpha | P > ,$$

$$< Q, \epsilon | V_\alpha | P >= \frac{2i\varepsilon_{\alpha\beta\gamma\delta}}{(M_D + m_{h^*})} \epsilon^{*\beta} Q^\gamma P^\delta V(q^2) ,$$

$$< Q, \epsilon | A_\alpha | P > = (M_D + m_{h^*}) \epsilon^*_\alpha A_1(q^2) - \frac{\epsilon^* \cdot q}{(M_D + m_{h^*})} (P + Q)_\alpha A_2(q^2)$$
$$- 2\, m_{h^*} \frac{\epsilon^* \cdot q}{q^2} q_\alpha \left[A_3(q^2) - A_0(q^2) \right] ,$$

where the independent form factors are V, A_0, A_1, A_2 while A_3 is a linear combination defined by:

$$A_3(q^2) = \frac{M_D + m_{h^*}}{2m_{h^*}} A_1(q^2) - \frac{M_D - m_{h^*}}{2m_{h^*}} A_2(q^2)$$

and subject to the constraint $A_0(0) = A_3(0)$.

The final expression for the decay rate is considerably more complicated than in the case of the pseudoscalar meson: it depends on four form factors (V, A_0, A_1, A_2), of which one (A_0) drops out of the calculation if the lepton mass is neglected. If in addition we consider the limit of zero momentum transfer, the decay rate is determined by only one form factor $A_3(0)$[22]:

$$\lim_{q^2 \to 0} \frac{d, (D \to h^* l \nu)}{dq^2} = \frac{G^2}{192\pi^3 M_D^3} |V_{cq}|^2 (M_D^2 - m_{h^*}^2)^3 |A_3^{h^*}(0)|^2 .$$

By comparing the rates for two different vector meson semileptonic decays, and using our knowledge of $\left|\frac{V_{cd}}{V_{cs}}\right|$ from CKM unitarity, it is possible to compute the ratio of the form factor normalizations for the two modes and compare it to theoretical predictions.

CHAPTER 2

THE E687 EXPERIMENTAL APPARATUS

E687 is a fixed target charm photoproduction experiment. The use of a photon beam, instead of a hadronic beam (for example, π or p) as in other fixed target experiments, involves some advantages and some drawbacks. First of all, the ratio of charm interactions to non-charm hadronic interactions is more favorable in photoproduction ($\sim 0.6\%$) than in hadroproduction ($\sim 0.08\%$). This compensate for the fact that the absolute heavy quark production cross section is actually lower for a photon beam ($\sim 1\mu b$) than for a hadron beam ($\sim 20 - 30\mu b$). Also, photoproduced events have a lower average multiplicity than in hadroproduction, where the incident particle has an internal structure and is fragmented in the interaction process. As a consequence, photoproduced events have less combinatoric and charm background. The major source of background in photoproduction is constituted by electromagnetic events (electron pairs produced in the target $\gamma \rightarrow e^+e^-$), which can be greatly suppressed by the trigger apparatus because of the characteristic topology. On the other hand, photon beams (which are typically produced by bremsstrahlung of electrons on some material) have lower intensity than hadron beams, and therefore require the use of thicker production targets, resulting in greater multiple Coulomb scattering and increased secondary interactions. Also, in photoproduction it is more difficult to determine the location of the primary interaction, because of the lower track multiplicity per event and because it is not possible to use the traceless photon trajectory as a seed to guide the search.

In modern high energy fixed target experiments (either photoproduction or hadroproduction), heavy quark events are detected by large acceptance, multi-purpose spectrometers composed of several detectors. Charged particles are detected by several tracing stations which determine their trajectory over a length of several tens of meters. In the region immediately downstream of the interaction target, tracing is provided by silicon microstrip planes, whose high resolution power allow to separate the charm production and decay vertices. Momentum determination is realized by the use of deflecting magnets, which bend charged particle trajectories. Neutral particles are detected by systems of calorimeters, and charged particle identification is accomplished by Čerenkov detectors and muon counters. Finally, a trigger system is used to select the heavy quark events from the elevated background (hadronic and electromagnetic), so that only interesting events may be recorded on tape.

In this chapter we first describe the beamline and the experimental setup used in E687 to produce charm events, then the spectrometer used to detect, select and record these events[23][24].

2.1 The Fermilab Tevatron

The Fermilab Tevatron is currently the highest energy accelerator in the world. Protons are accelerated to a final energy of 800 GeV through a series of successive steps (see Figure 2.1.1):

• First, negative hydrogen ions are produced by injecting electrons into a hydrogen sample. The ions are then accelerated by a Cockroft-Walton accelerator to an energy of 750 KeV.

• Next the negative ions enter a linear accelerator (the LINAC, 500 feet long) where they are boosted to 400 MeV. The LINAC is composed of a series

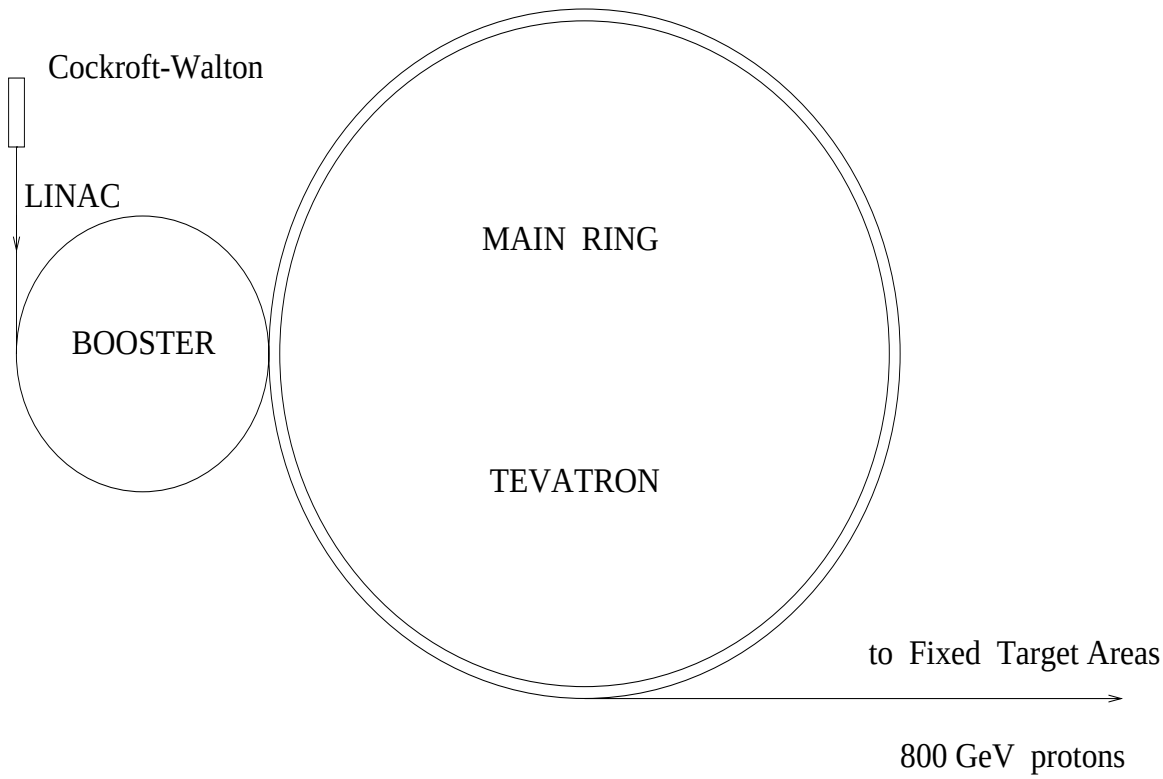

Figure 2.1.1 Schematic drawing of the successive steps through which the Tevatron proton beam is accelerated to its final energy.

of metallic cavities to which a rapidly oscillating potential difference is applied, so that the electric field created between the cavities is repeatedly reversed in direction (while the electric field vanishes within the cavities). The ions are then increasingly accelerated every time they traverse the space between two cavities, while they travel undisturbed within each cavity. Upon exiting the LINAC the ions pass through a carbon foil, which removes the electrons leaving only the protons.

• The protons then enter a rapid cycling synchroton (the Booster, 500 feet in diameter) where they reach an energy of 8 GeV. Inside the Booster, the protons move in a circular path within a continuously increasing magnetic field, while being accelerated by a radiofrequency electric field at each revolution.

• From the Booster the protons pass to the Main Ring, a much larger proton synchroton (four miles in circumference) which uses conventional copper-coiled magnets. Here the beam is raised to an energy of 150 GeV.

• Finally, the protons are injected into the Tevatron, a superconducting magnets proton synchroton which shares the same tunnel as the Main Ring. Superconducting magnets are able to produce much stronger magnetic fields than conventional magnets, so that the proton beam can be accelerated to its final energy of 800 GeV. The proton beam is composed of packets or *bunches* of $\sim 5 \cdot 10^{10} p/bunch$.

When the Tevatron is operated in fixed target mode, the proton beam is extracted by a deflecting magnet and it is used to produce (via collisions on fixed targets of different materials) three different secondary beams of particles: protons, mesons (K,π) and neutrinos. The secondary beams are conveyed through long tunnels to several experimental areas, where they are made to collide on other fixed targets in order to study the interaction products. In particular, the proton beam is on its turn divided into three lines: East, Center and West. The Proton East beam is finally directed towards the Wide Band Photon Laboratory, where experiment E687 is located.

2.2 The E687 beamline

E687 makes use of a high intensity, high energy, wide band photon beam which is produced from the Proton East beam in the following way (see Figure 2.2.1):

Bremsstrahlung Photon Beam

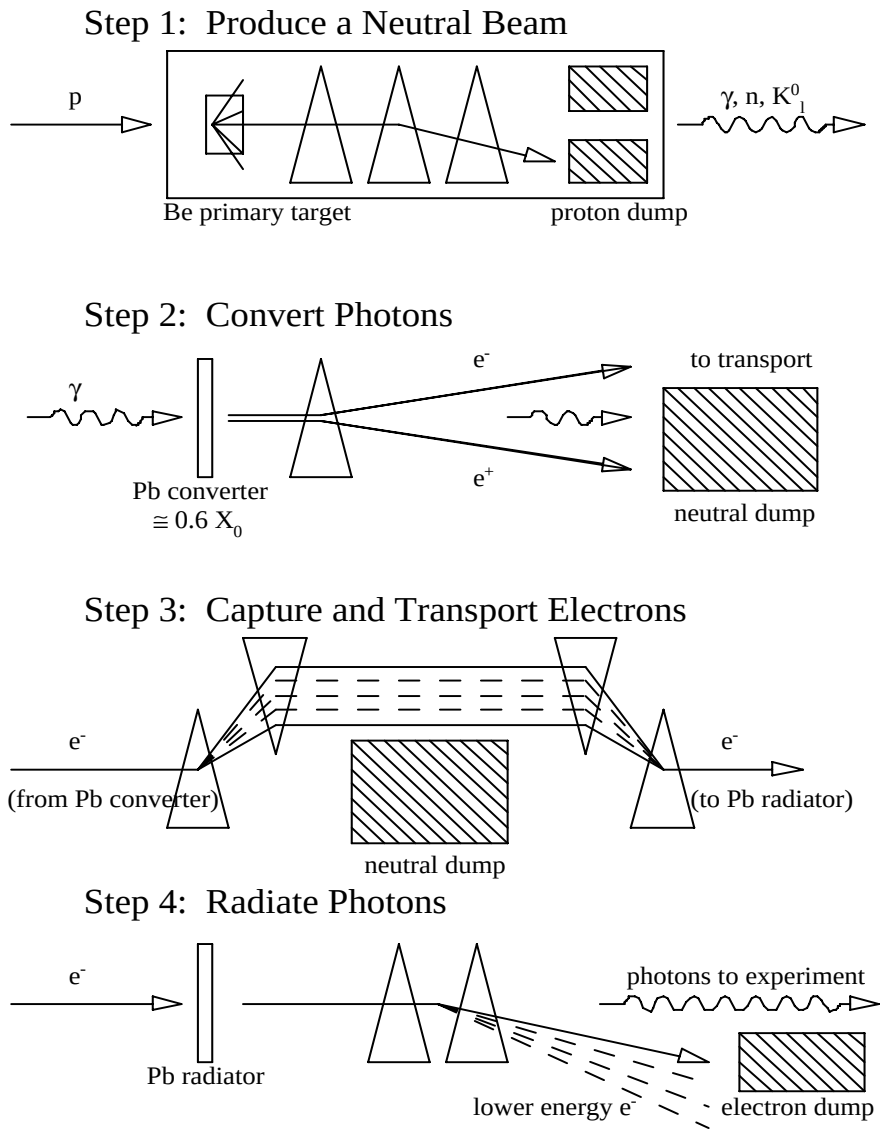

Figure 2.2.1 Schematic drawing of the successive steps through which the E687 photon beam is produced from the Tevatron proton beam.

• The Proton East beam (which has an average intensity of $3 \cdot 10^{22} p$ in 22 seconds -spill time- per minute) is made to impact on a Deuterium target (the primary production target). The hadronic interactions produce (among other particles) neutral pions, which immediately decay to photons ($\pi^0 \rightarrow \gamma\gamma$). The charged particles are deflected by magnets and are lost, while the neutral particles (γ, n, K^0,Λ^0) travel in a straight line.

• The neutral beam impacts on a lead target (the converter, which has a thickness of 0.6 radiation lengths), where the high energy photons materialize into e^+e^- pairs.

• The electron beam is bent from the direction of flight by a system of dipoles, while the neutral portion of the beam (n, K^0,Λ^0 and γ which didn't interact) is absorbed. The positron beam is also dumped and not used in the following steps of the process. After the dump, the electron beam (composed of $\sim 10^8 e/spill$ with an average energy of 350 GeV) is realligned with the original direction.

• The electrons impact on yet another lead target (the radiator, which is 0.27 radiation lengths thick) where they emit photons by bremsstrahlung effect. The photon beam has an intensity of $\sim 5 \cdot 10^6 \gamma/spill$ and a continuous energy spectrum extending to the maximum energy of the radiating electrons, i.e. 400 GeV.

The final photon beam has very little hadronic contamination, about ~ 1 hadron (mostly neutrons) every 10^5 photons. Taking into account the interaction probability, the number of events which are hadroproduced in the interaction target is $\sim 1\%$ of the photoproduced events. The drawback of this many-stage production technique is that, in order to have a sufficiently high intensity photon beam, it is necessary for the dipole system to accept electrons

over a wide momentum range. The momentum spread of the electron beam is $\Delta P/P \sim 13\%$: this means that the energy of the radiating electron is known a priori with a large uncertainty: $\Delta E_e \sim \pm 50\ GeV$ around a central value $\overline{E}_e \sim 350\ GeV$.

2.3 The Beam Tagging System

The purpose of the tagging system is to measure the energy of the photon interacting in the target on an event by event basis. The system is composed of three parts:

2.3.1 The Silicon Microstrip Tagging

The Silicon Microstrip Tagging measures the energy of the primary electron, i.e. before it interacts in the radiator and radiates the photon. This goal is achieved by tracking the electron path through the deflecting dipoles with five planes of silicon microstrip (see Figure 2.3.1). From the measurement of the track deflection inside the magnetic field, the energy of the electron can be computed with high accuracy: $\Delta P/P \sim 2\%$.

2.3.2 The Recoil Electron Shower Hodoscope detector

The Recoil Electron Shower Hodoscope detector (RESH) is used to measure the energy of the secondary electron E_e'. It is composed of a system of magnets which deflect the electron beam after it passes through the radiator and by hodoscopes which measure the transverse coordinate of the electron, hence its energy (see Figure 2.3.2). The apparatus acceptance, expressed as ratio between the radiated photon energy and the primary electron energy, is limited to the range $\sim 0.35 < E_\gamma/E_e < 0.9$, meaning that the range where the photon energy can be measured is restricted to $\sim 122\ GeV < E_\gamma < 315\ GeV$.

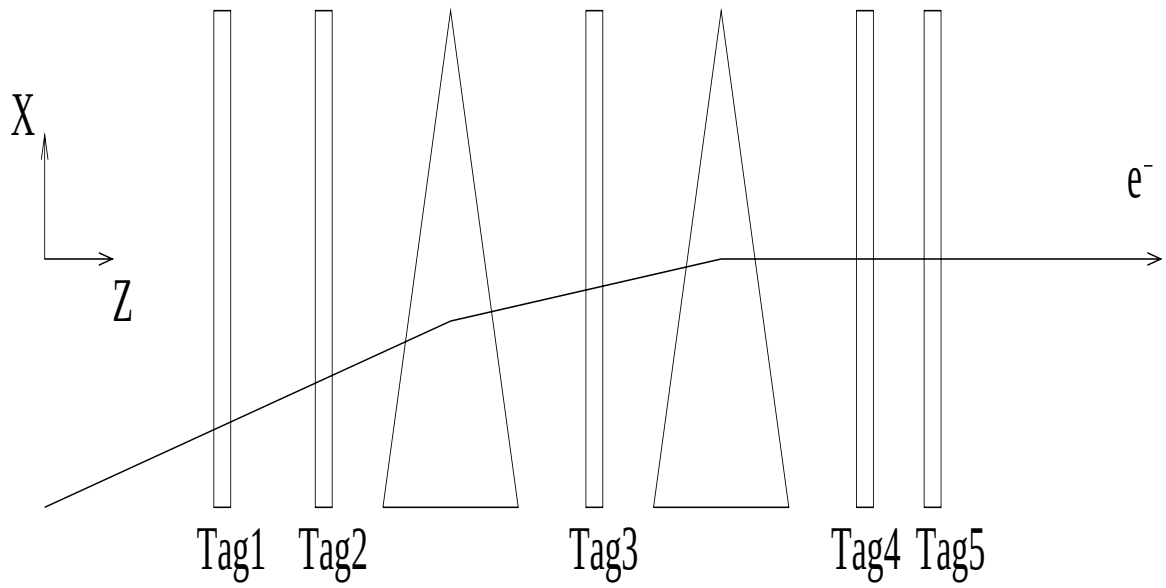

Figure 2.3.1 Schematic drawing of the location of the five planes of the Silicon Microstrip Tagging detector and the two deflecting dipoles.

2.3.3 The Beam Gamma Monitor

The Beam Gamma Monitor (BGM) is a small calorimeter located near the end of the E687 spectrometer. Specially designed to operate at high rate, its purpose is to measure the total electromagnetic energy in a small cone around the beam direction, and thus monitor the beam flux. Of all the photons emitted by the electron inside the radiator, only one has a considerable probability of producing a hadronic event in the Beryllium target. The others either do not interact and travel undisturbed through the hollow central portion of the IE to be arrested in the BGM, or they convert in the target into an e^+e^- pair, which is also arrested in the BGM. The BGM had to be removed during the 1991 run to let the photon beam reach the E683 experimental apparatus, located after the E687 spectrometer. It was replaced by a similar calorimeter (the BCAL) operated by the E683 collaboration.

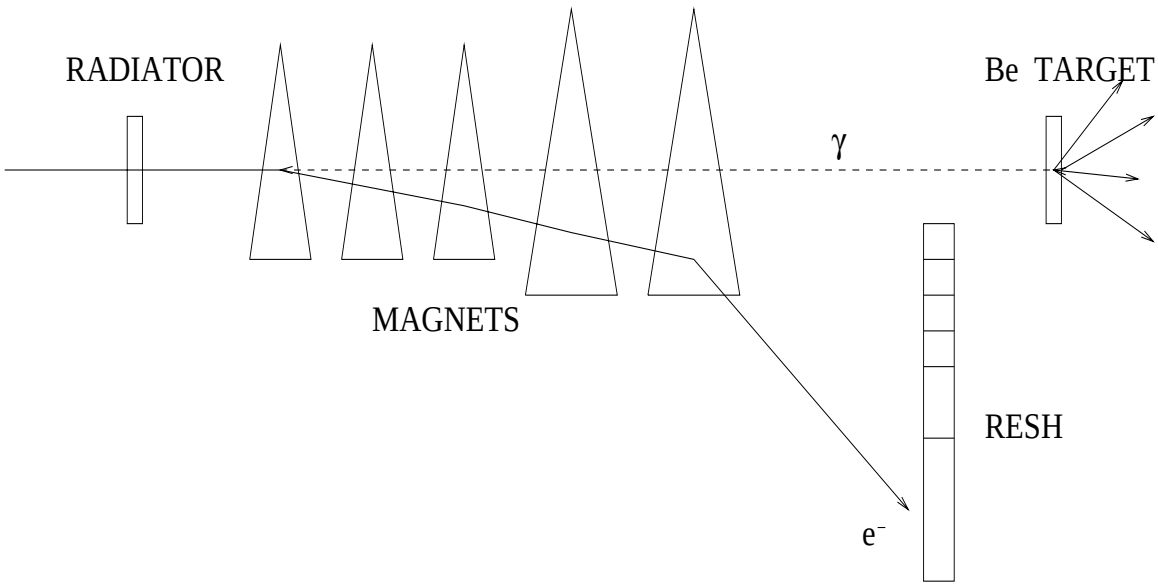

Figure 2.3.2 Schematic drawing of the Recoil Electron Shower Hodoscope detector.

In conclusion, the energy of the interacting photon is given, on an event by event basis, by the following equation:

$$E_\gamma = E_e - E'_e - \sum E_\gamma^{BGM}.$$

The mean *tagged* photon energy is $\overline{E}_\gamma \sim 210\ GeV$, for a resolution of $\Delta E_\gamma / E_\gamma \sim 2\%$. Because of geometrical acceptance, only $\sim 60\%$ of the events have a recorded tagged photon energy.

The Beam Tagging System is not used in any of the analyses presented in this thesis.

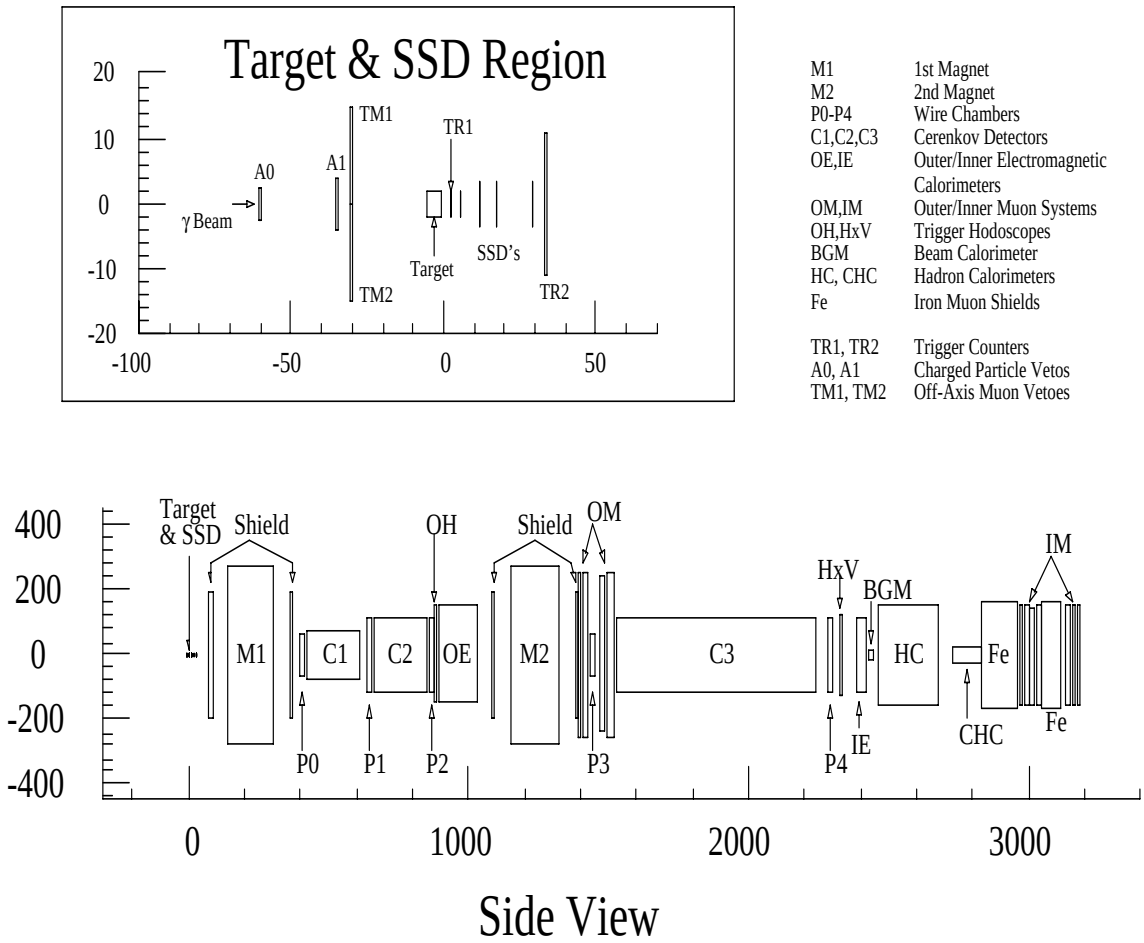

Figure 2.3.3 Schematic drawing of the E687 spectrometer (dimensions on both axes are in centimeters).

2.4 The interaction target

The interaction target was composed of several Beryllium segments, adding up to a total length of about $\sim 4\ cm$, corresponding to both a radiation length and an interaction length of approximately $\sim 10\%$. Two slightly different target configurations were used during the run: see Table 2.4.1 for more details.

Table 2.4.1 Target configurations for the 1990 and 1991 runs

	1st configuration	2nd configuration
% data taken	37%	63%
# Be segments	9	11
total length	3.6 cm	4.4 cm
interaction length	8.8%	10.8%
radiation length	10%	12.5%

The choice of Beryllium as target material was motivated by the necessity of maximizing the ratio between hadronic and electromagnetic interactions. Since the charm photoproduction cross section is approximately proportional to A and the e^+e^- pairs production is proportional to Z^2, the hadronic/electromagnetic ratio goes as $A/Z^2 \sim 2/Z$. The lowest possible Z materials (H,D,He) are found at ordinary temperature in the gaseous state; an interaction target composed of these materials would have had to be several meters long (in order to give an appreciable interaction length), causing problems of geometrical acceptance and loss of resolution due to increased multiple Coulomb scattering. The next lowest Z material is Li, but this is subject to easy oxidation. Following is Be, for which $A/Z^2 = \frac{1}{2}$, which was consequently chosen as target material.

Impacting on the Beryllium target, the photon beam produces approximately 1 hadronic event for every 500 electromagnetic events.

2.5 The silicon microstrip detector

The Silicon Strip Detector (SSD) (see Figure 2.5.1) is used to perform high resolution tracking of charged particles in the region immediately downstream of the production point.

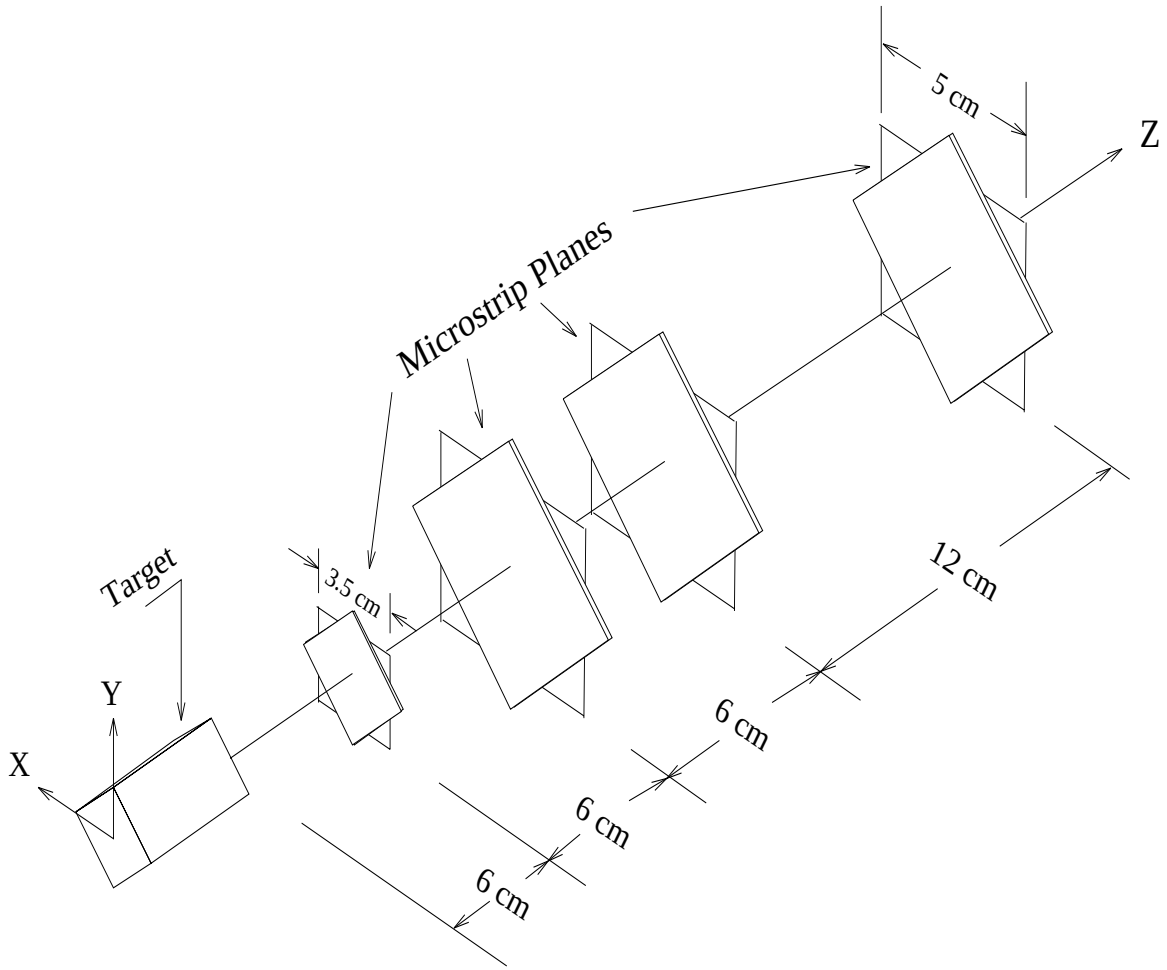

Figure 2.5.1 Schematic drawing of the silicon microstrip detector.

The detector is composed of four stations of three planes each, which are oriented at angles of -135, -45 and -90 degrees with respect to the vertical (U,V and Y views, respectively). In order to maximize the spatial resolution

while limiting the number of electronic channels, the pitch of the silicon strips in the central region of each plane was chosen to be half the size of the pitch in the outer region. This is because the central region is typically crossed by the most energetic tracks, which are closer to one another and less deflected by Coulomb scattering. Furthermore, the pitch on the three planes of the triplet closest to the target was chosen to be half the pitch of the other triplets (see Table 2.5.1).

Table 2.5.1 Microstrip detector characteristics

Property	I Station	II Station	III Station	IV Station
z position	0.0 cm	6.0 cm	12.0 cm	24.0 cm
Active Area (cm^2)	2.5×3.5	5.0×5.0	5.0×5.0	5.0×5.0
High Res. Area (cm^2)	1.0×3.5	2.0×5.0	2.0×5.0	2.0×5.0
Pitch (High/Low Res.)	25/50 μm	50/100 μm	50/100 μm	50/100 μm
# Channels	3×688	3×688	3×688	3×688

The high resolution tracking performed by the microstrip detector allows us to determine the point of origin of a track in the target region with a precision of about $\sim 500\mu m$ in the beam direction and $\sim 10\mu m$ in the transverse direction. This is enough to separate the production and decay vertices of charm particles, which typically have a lifetime $\tau \sim 10^{-12}\ sec$ and at the energy they are produced in E687 ($\gamma = \frac{E}{m_0 c^2} \sim 50$) travel a distance $L = c\tau\gamma \sim 15\ mm$. The identification of a production vertex and a decay vertex is the most typical signature of a charm event with respect to a non-charm or noise event. Requiring a minimum significance of separation between the two reconstructed vertices allows us to dramatically enhance a

charm signal over the background. Also, the capability of separating the two vertices makes the measurement of charm particle lifetimes possible.

2.6 The Analysis Magnets

Momentum analysis of charged particles is accomplished by measuring the deflection in the fields of two large magnets (M1 and M2, see Table 2.6.1). The two magnets are operated with opposite polarities, so that they bend charge tracks in opposite directions on the transverse plane (Y-view). This arrangement was chosen to reduce the geometrical size of all the detectors with respect to the case where the magnets bend particles in the same direction. The ratio of the transverse kicks is such that the tracks come back to their original undeflected position toward the downstream end of the spectrometer. This feature allows us to measure the total energy of the event through the use of downstream hadronic and electromagnetic calorimeters.

Table 2.6.1 Analysis magnets characteristics

	M1	M2
Z position	$\sim 225\ cm$	$\sim 1240\ cm$
transverse kick	$0.400\ GeV/c$	$0.850\ GeV/c$
current	$1020\ amps$	$2000\ amps$

2.7 The Multi-Wire Proportional Chambers

Charged particle tracking after M1 is performed by five stations of Multi-Wire Proportional Chambers (PWC), each composed of four planes arranged in different views (X,Y,U and V, where the U,V views make angles of ± 11.3 degrees with the horizontal). The first three chambers (P0, P1 and P2) are

located between the two analysis magnets, while the last two (P3 and P4) are positioned after M2. This arrangement, together with the SSD detector, allows for two independent measurements of the particle momentum.

Table 2.7.1 PWC characteristics

Property	P0	P1	P2	P3	P4
Aperture (in^2)	30×50	60×90	60×90	30×50	60×90
Wire Spacing (mm)	2.0	3.0	3.0	2.0	3.0
No. X–view Wires	376	512	512	352	512
No. U–view Wires	640	832	800	640	800
No. V–view Wires	640	832	832	608	832
No. Y–view Wires	624	752	752	624	752
Gas used	Argon–Ethane(65/35) Bubbled through 0° C ethyl alcohol				
Voltage Plateau	2–4 kilovolts				

2.8 The Čerenkov Counters

Three multicell Čerenkov counters are used for charged hadron identification: C1 and C2 (located between the two magnets) and C3 (located downstream of M2). The counters are filled with gas at atmospheric pressure and operate in threshold mode (see Table 2.8.1).

Table 2.8.1 Čerenkov counters characteristics

Detector	# of Cells	Length (cm)	Gas	$P_{threshold}$ (GeV/c)		
				pion	kaon	proton
C1	90	188	57% He/43% N_2	8.4	29.8	56.5
C2	110	188	N_20	4.5	16.0	30.9
C3	100	711	He	17.4	61.8	117.0

A charged particle traversing a material with index of refraction n will emit Čerenkov radiation if its velocity is above the threshold value:

$$\beta = \frac{Pc}{E} \geq \beta_{threshold} = \frac{1}{n},$$

or equivalently if its momentum is such that:

$$P \geq P_{threshold} = \frac{m_0 c}{\sqrt{n^2 - 1}}.$$

Since the particle momentum is known (from the track deflection in the fields of M1 and M2), it is possible to infer the mass of the particle by examining whether or not Čerenkov radiation was emitted in each of the three counters. The threshold values for C1, C2 and C3 were chosen in such a way to maximize the momentum range of identification of $K^{\pm}$ and $p^{\pm}$ (the so called *heavy* particles), which are typical decay products of charm hadrons (see Table 2.8.2).

Table 2.8.2 Momentum range of particle identification

Definite Čerenkov Identification Momentum Range GeV/c				
	$e^{\pm}$	$\pi^{\pm}$	$K^{\pm}$	p
3–chamber	0.16-8.4	4.5-8.4	16.0-29.8	16.0-56.5
5–chamber	0.16-17.4	4.5-17.4	16.0-56.5	16.0-56.5 and 61.8-117.0
Ambiguous Čerenkov Identification Momentum Range GeV/c				
	e/π	K/p	$e/\pi/K$	$\pi/K/p$
3–chamber	8.4-29.8	4.5-16.0	29.8-56.5	0.16-4.5
5–chamber	17.4-61.8	4.5-16.0	61.0-117.0	0.16-4.5

2.9 The calorimeters

The E687 spectrometer includes several calorimeters, hadronic and electromagnetic. The calorimetry information was not used for the analysis presented in this thesis (except at the trigger level), so this system of detectors will be discussed only briefly.

2.9.1 The electromagnetic calorimeters

The purpose of the electromagnetic calorimeters is to detect electrons and photons. The Outer Electromagnetic calorimeter (OE) is located between M1 and M2 and it samples wide angle particles which are outside the acceptance of M2. The Inner Electromagnetic calorimeter (IE), located downstream of M2 and after the last PWC station, is meant to cover the central solid angle region. Both detectors are composed of alternating planes of lead and scintillators, summing up to a depth of 18.4 (OE) and 25 (IE) radiation lengths. In

addition another small electromagnetic calorimeter, the Beam Gamma Monitor (BGM), was located during the 1990 run after the IE to monitor the beam flux (see section § 2.3.3).

2.9.2 The hadron calorimeters

The main purpose of the hadron calorimeters in E687 is to identify hadronic events from electromagnetic events. Since electromagnetic showers are mainly contained in the electromagnetic calorimeters (located upstream), this task is performed by measuring the total energy deposited by the hadronic showers and using this information at the trigger level.

The main Hadron Calorimeter (HC) is placed immediately downstream of the IE and covers the angular region from ± 5 $mrad$ to ± 30 $mrad$. It is composed of iron planes (for a total of 8 proton interaction lengths) alternated with sense planes. Each sense plane contains an array of pads which measure the ionization produced by hadronic showers in a gas mixture of 50/50 argon-ethane (see Figure 2.9.1).

The Central Hadronic Calorimeter (CHC) is located downstream of the HC to detect hadronic showers passing through the central hole in the HC. During the 1990 run, its energy information was added to that of the HC to provide trigger selection.

2.10 The muon detectors

The muon detectors take advantage of the high penetration power of muons (the highest among subnuclear particles, with the exception of neutrinos) to distinguish them from other charged particles (electrons and hadrons). Interesting charm events containing muons are semileptonic decays of charm mesons and baryons and fully leptonic decays of ψ and ψ'.

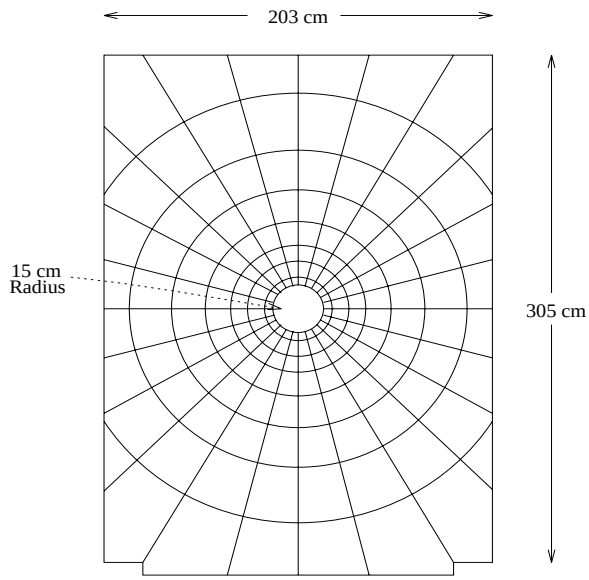

Figure 2.9.1 Schematic drawing of the main Hadron Calorimeter, showing the concentric pad geometry.

2.10.1 The Inner Muon system

The Inner Muon system (IM) is located after the HC and CHC and covers an angular region of ± 40 $mrad$ with respect to the beam direction. It consists of four planes of proportional tubes and three planes of scintillators, arranged in two stations. The counters of each plane are oriented to measure alternatively the horizontal or vertical coordinate. The scintillator planes, having a faster response but lower spatial resolution than the proportional tubes, are meant to rapidly provide the muon information to the trigger logic; the proportional tubes, slower but more accurate, are used to give the point of impact of the muon. The shielding is provided by the upstream detectors (mainly the IE and HC) and by two additional blocks of steel, one located before the first station and the other placed between the two stations (see Figure 2.10.1 and Table 2.10.1).

Table 2.10.1 Inner muon system characteristics

Plane	Channels (1990/1991)	Counter size (cm^2)	Gas
IM1V	21/21	30×100	none
IM1H	20/20	30×100	none
IM1X	64/56	5×256	$(80/20)ArCO_2$
IM1Y	96/88	5×276	$(80/20)ArCO_2$
IM2H	20/20	30×100	none
IM2X	64/56	5×256	$(80/20)ArCO_2$
IM2Y	96/88	5×276	$(80/20)ArCO_2$

During part of the 1990 run, a read-out problem caused the loss of the information from the proportional tubes; approximately 45% of the 1990 data was affected (the so called "bad muon runs"). During the 1991 run the inner muon system had to be modified to allow for the passage of the non-interacting portion of the photon beam through the spectrometer. Holes were placed in the center of each detector plane. The resultant decrease in efficiency was approximately 40%.

2.10.2 The Outer Muon system

The Outer Muon system is located after M2 and covers the angular region outside the geometrical acceptance of the magnet, approximately from ± 40 $mrad$ to ± 125 $mrad$. It consists of two planes of proportional tubes and two planes of scintillators. The shielding to filter out electrons and muons is provided by the magnet material. The performance of this detector is still under investigation and therefore it was not used for this analysis.

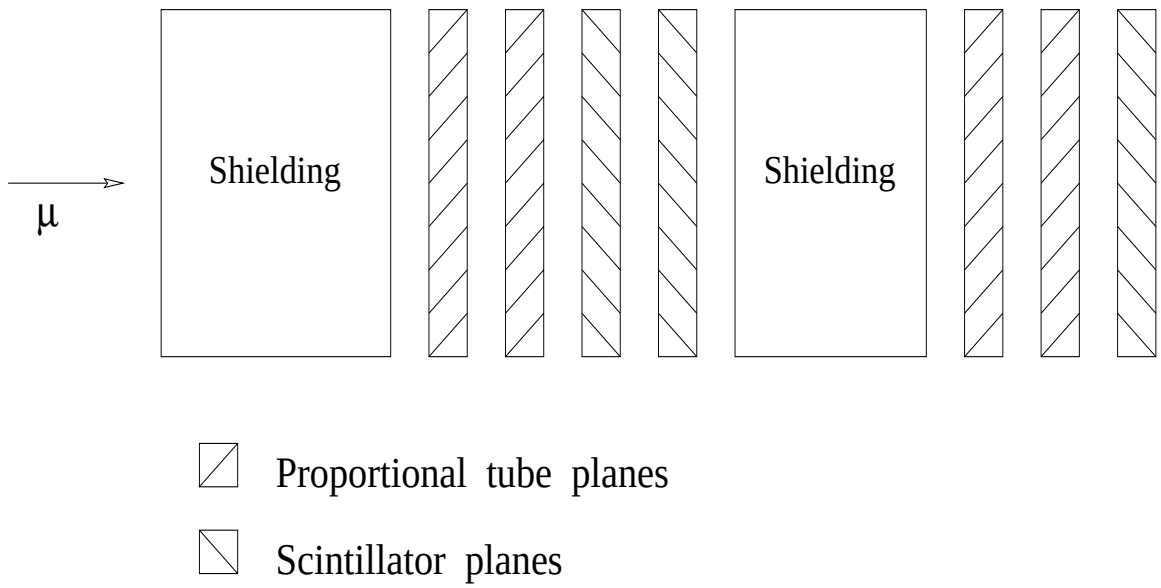

Figure 2.10.1 Schematic drawing of the inner muon detector.

2.11 The Trigger

The purpose of the trigger is to select the interesting events. In E687 the number of interactions/spill produced by the photon beam impacting on the target is extremely high: $\sim 10^6$, of which only $\sim 1/500$ are hadronic interactions, the rest being electromagnetic. Since the data acquisition system was unable to operate at such high rate, the trigger must make a decision about which events be recorded on tape. This process is performed in two successive steps.

2.11.1 The First Level Trigger

In the First Level Trigger or Master Gate (MG), hadronic and electromagnetic events are separated on a purely topological basis. The e^+e^- pairs photoproduced in the target have a very small transverse momentum, so they travel along the spectrometer inside a narrow cone which has approximately the dimensions of the beam. The first magnet opens the pair in the Y-view,

while the second magnet bends it in the opposite direction so that near the IE the two tracks are again confined within a small cross section around the beam direction. On the other hand a hadronic event typically includes some tracks at much wider angles.

The First Level Trigger system is composed of several detectors, all of which are made up of scintillators counters (see also Figure 2.3.3 for the location of the first of these detectors):

- $\underline{A0,\ A1}$: A0 and A1 are small detectors located three and two meters upstream of the target (respectively) along the beam direction. A signal from either one would imply the presence of a charged particle traveling with the beam and would therefore cause the event to be rejected.

- $\underline{TM1,\ TM2}$: TM1 and TM2 are two much larger detectors located upstream of the target with a big central hole. The purpose of these counters was to detect undesired charged particles (especially muons) travelling outside the beam halo. It was found though that this kind of contamination was small, so that TM1 and TM2 were used for only about $\sim 20\%$ of the run.

- $\underline{TR1,\ TR2}$: TR1 and TR2 are two scintillators placed downstream of the target, respectively before and after the microvertex detector, and covering the same angular acceptance of the detector. A simultaneous signal from TR1 and TR2 would indicate the presence of a charged particle crossing the microvertex detector.

- $\underline{OH}$: OH is a plane of scintillators located in front of the OE (see Figure 2.11.1). It is used to detect the presence of wide angle charged tracks outside the acceptance of M2. Besides the central hollow region which matches the M2 acceptance, it has a vertical central cut which allows the e^+e^- pairs to pass undetected.

• $\underline{H \times V}$: $H \times V$ is a system of two planes of scintillators (oriented along X and Y, respectively) cut by a narrow vertical slit (see Figure 2.11.1). Placed in front of the IE, where the e^+e^- pairs are refocalized by the combined action of M1 and M2, they are used to detect charged tracks outside the pair region. During the 1991 run, the V plane was replaced by a V$'$ plane situated behind the IE, in an attempt to further reduce the pair contamination by making advantage of the shielding power of the IE.

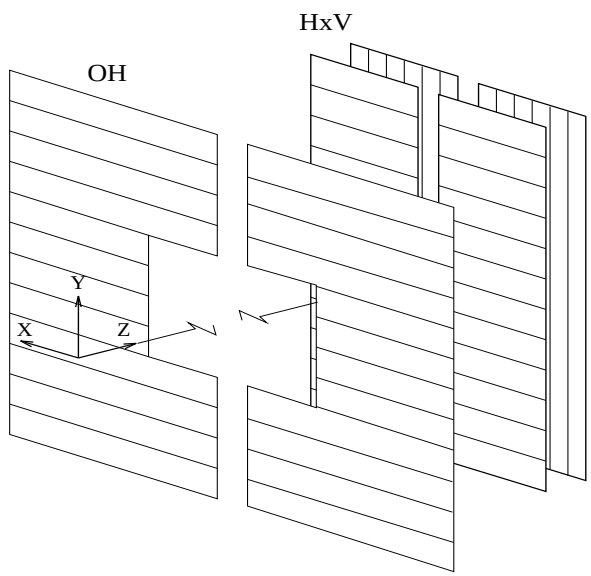

Figure 2.11.1 Schematic drawing of the OH and $H \times V$ scintillator planes used by the First Level Trigger.

The First Level Trigger makes use of the information coming from all of the above detectors to select events satisfying the following conditions:

• the event is produced by the interaction of a photon in the target (no signals from A0 or A1);

• there is at least one charged track crossing the microvertex detector (simultaneous signals from TR1 and TR2);

• there are at least two charged tracks outside the pair region, either both detected by $H \times V$ (inner-inner trigger), or one detected by $H \times V$ and the other by OH (inner-outer trigger).

The logic used by the First Level Trigger is summarized in Table 2.11.1 for the various run periods. The MG requirement rejects $\sim 90\%$ of the e^+e^- pairs, while being $> 90\%$ efficient in retaining hadronic events. The rate of events passing the MG is $\sim 10^5$ per spill, i.e. ~ 5000 per second. This rate is still too high for the data acquisition system, making it necessary to implement a second level event selection.

Table 2.11.1 First Level Trigger

Mastergate	Duration
$TR1 \cdot TR2 \cdot (H \times V)_{2body} \cdot \overline{(A0 + A1)}$	26% of 1990
$TR1 \cdot TR2 \cdot [(H \times V)_{2body} + (OH \cdot (H \times V)_{1body})] \cdot \overline{(A0 + A1)}$	74% of 1990
$TR1 \cdot TR2 \cdot [(H \times V)_{2body} + (OH \cdot (H \times V)_{1body})] \cdot \overline{(A0 + A1)}$	8% of 1991
$TR1 \cdot TR2 \cdot [(H \times V)_{2body}] \cdot \overline{(A0 + A1)}$	5% of 1991
$TR1 \cdot TR2 \cdot [(H \times V') + (OH \cdot (H \times V')_{1body})] \cdot \overline{(A0 \cdot A1)}$	86% of 1991

2.11.2 The Second Level Trigger

The Second Level Trigger achieves a further selection of the hadronic events by combining topological and kinematic requests. In the basic configuration, events are selected on the following basis:

• the pattern of hits detected by the first station of PWC is consistent with at least three tracks outside the pair region;

• the energy deposited in the hadron calorimeters is at least 50 GeV.

The Second Level Trigger rejects $\sim 98\%$ of the pairs surviving the MG. The rate of accepted events is ~ 2000 per spill, i.e. ~ 100 per second. The ratio of hadronic to electromagnetic events is approximately one to one, but of all the hadronic events only $\sim 1\%$ is a charm event!

2.12 Data acquisition

For each event of interest, the signals of all the detectors of the E687 spectrometer are collected and transferred to tape by the Data Acquisition system (DAQ).

If the event satisfies the MG requirements, all the detectors in the spectrometer are put on hold and further MG inhibited until the event has been processed by the Second Level Trigger. The time required by the Second Level Trigger to take a decision is $\sim 1.2\ \mu sec$. If a positive response is achieved, the signals from all the detectors are transferred to Lecroy Fastbus Memories in an additional time of $\sim 1.3\ \mu sec$; if the response is negative, a *fast-clear* signal is sent to all the detectors so that they can start taking data again (this takes $\sim 1\ \mu sec$). Because of the dead time generated by the trigger logic, approximately 30% of the MG signals are lost for further processing. During the 20 second spill time about 3000 events satisfy the Second Level Trigger and are stored in the memories. During the 40 second inter-spill time, data from the memories are then transferred to tape. A total of four 8mm tape drives may be written in parallel. Each tape can contain up to 2 Gb of data corresponding to $\sim 500K$ E687 raw events.

The experiment E687 took data in two approximately equal periods of time (from May to August 1990 and from July 1991 to January 1992), which

are known as the 1990 and 1991 runs. During this period of time, a total of $\sim 510\ M$ events were written to ~ 1000 raw tapes.

CHAPTER 3

DATA RECONSTRUCTION

The first stage of data analysis consists in using all the information recorded by the detectors of the spectrometer to reconstruct the basic elements which compose a charm event: tracks, vertices, particle identification and electromagnetic showers. This process, globally called *PASS1 data reconstruction*, is very CPU intensive and was performed at Fermilab in the period from November 1991 to August 1992 using farms of IBM and SGI computers. About ~ 2000 reconstructed tapes were produced from the ~ 1000 raw data tapes. In this chapter we discuss some of the most important reconstruction algorithms which were run as part of the PASS1 software package.

3.1 Track reconstruction

Charged particle tracks are reconstructed by pattern recognition algorithms from the hits produced in the SSD and PWC detectors. First, tracks are reconstructed separately in the two detectors, then the two sets are compared to look for possible matches.

3.1.1 SSD track reconstruction

The SSD pattern recognition algorithm is composed of several steps.

First, a *pulse height analysis* is performed, which transforms hits in hit coordinates. In the case of an isolated hit, the coordinate of the middle strip line is considered. In the case of a cluster of hits, by analyzing the pulse height of each strip of the cluster it is possible to distinguish between single crossing (in which case the centroid of the cluster is considered) and multiple crossing (in which case the coordinate assignment depends on the track multiplicity

and the pulse height distribution between strips). No more than clusters of three adjacent hits are considered at one time.

Next, tracks are reconstructed separately in the three two-dimensional views UZ, VZ and YZ. A track projection is defined as a system of three or four alignerΦd hits with a χ^2 per degrees of freedom less than 3.0. Hits may be shared between different track projections. The necessity of this approach comes from the difficulty of defining a point in space in a structure of detectors where the distance between planes is considerably larger than the resolution in each view.

Track projections are then combined to reconstruct tracks in space. All possible triplets of projections are considered and a global least-squares fit is performed; if the χ^2 is less than 8.0, the triplet is accepted as a space track.

Finally, clusters of very closely spaced tracks (composed of shared or adjacent hits) are reduced to a single equivalent track by computing the χ^2-weighted mean of the cluster.

The reconstruction efficiency of the SSD detector is a function of the track momentum: it ranges from $\sim$ 90% at $P = 2.5\ GeV/c$ to $\sim$ 99% at $P \geq 10\ GeV/c$ (the average efficiency being $\sim$ 96%). The spatial resolution of the detector is also a function of the particle momentum, because tracks with lower momentum are more affected by multiple Coulomb scattering and therefore have worse resolution. For each track, the spatial resolution can be expressed as the errors in the transverse coordinates when the track is extrapolated to the center of the target. In the case of a track crossing the

high resolution region of each plane:

$$\sigma_x = 11\mu m\sqrt{1+\left(\frac{17.5\ GeV/c}{P}\right)^2}$$
$$\sigma_y = 7.7\mu m\sqrt{1+\left(\frac{25\ GeV/c}{P}\right)^2}$$

while the resolution is approximately twice as big for a track which goes through the low resolution regions of all the planes (the formula takes into account multiple Coulomb scattering in all the SSD planes, the target and TR1). The constant contributions to σ_x, σ_y are due to the strip granularity. The resolution is better in the Y coordinate than in X because all the three SSD views (U,V,Y) give some Y information, while only two of them give X information.

3.1.2 PWC track reconstruction

The first step in PWC track reconstruction consists in forming track projections in the four views. In the X view (the only non-bending view), we extend already reconstructed SSD tracks to look for hits in the PWC planes; in the U,V, and Y views (all bending) track projections are formed independently as systems of at least three hits lying in a straight line. The X projections are then matched to U,V,Y projections to form tracks in space. After all PWC tracks originating from an SSD extension are found, unused hits in the X view are considered for construction of new X projections, which in turned are matched to unused projections in the other views.

At this stage, tracks are required to extend through at least three PWC stations, starting from P0 (the most upstream). A maximum of four missing hits per track over all the PWC stations used is allowed, and no more than

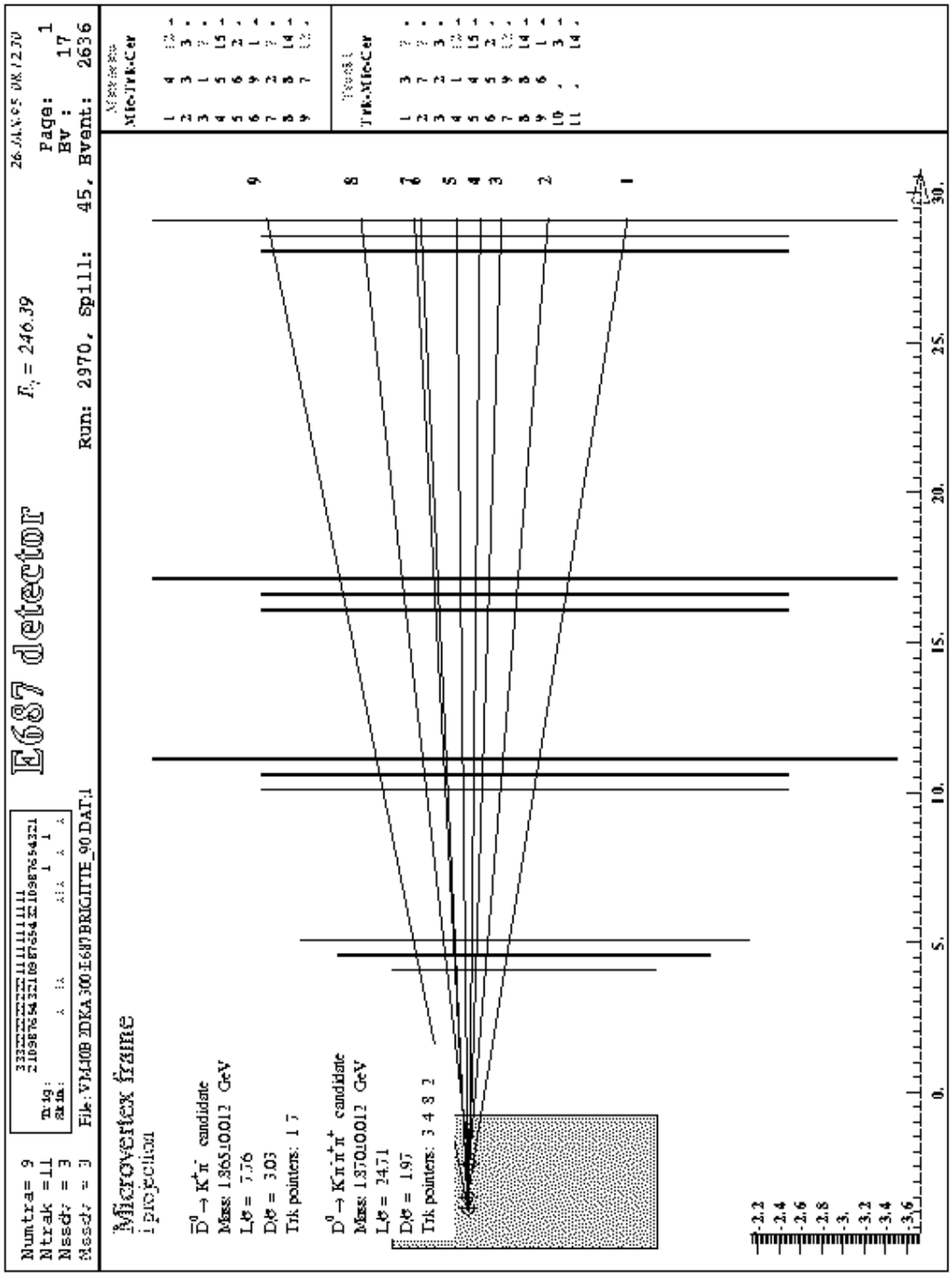

Figure 3.1.1 Display[26] of a completed reconstructed $c\overline{c}$ data event ($\overline{D}^0 \rightarrow K^+\pi^-$, $D^0 \rightarrow K^-\pi^+\pi^+\pi^-$). The microvertex region is shown with the reconstructed SSD tracks and vertices.

two missing hits per station. For each track, a least-squared fit is performed, using as fit parameters the slopes and intercepts at the M2 position and, in the case of 5-chamber tracks, the change in Y slope through the M2 magnetic field. An upper cut to the χ^2/DOF returned by the fit is imposed.

After the main set of PWC tracks is formed, the algorithm tries to recover tracks which left the PWC geometrical acceptance cone before P2, i.e. tracks which crossed only one or two PWC stations. SSD track extensions are used to look for unused hits in the X-view of P0 and P1, which are then combined with unused hits in the U,V,Y views. Tracks extending only to P0 are required to have hits in all the four views, tracks extending to P0 and P1 may have one missing hit in each station.

The efficiency of the PWC pattern recognition algorithm was studied using a Monte Carlo simulation of the detector which included the individual efficiencies of each plane (but not the noise caused by spurious hits). The efficiency was determined to be $\sim 98\%$ for tracks with momentum $P \geq 5\ GeV/c$, and the contamination of spurious tracks to be 0.5%.

The reconstructed PWC tracks are divided in two categories: *tracks* and *stubs*. *Tracks* are reconstructed in at least four PWC stations, i.e. they are composed of a segment between the two magnets and a segment after M2. *Stubs* are tracks reconstructed in only the first three PWC stations, i.e. composed of only one segment between M1 and M2. These are typically low momentum or wide angle tracks which do not make it through the angular acceptance of M2.

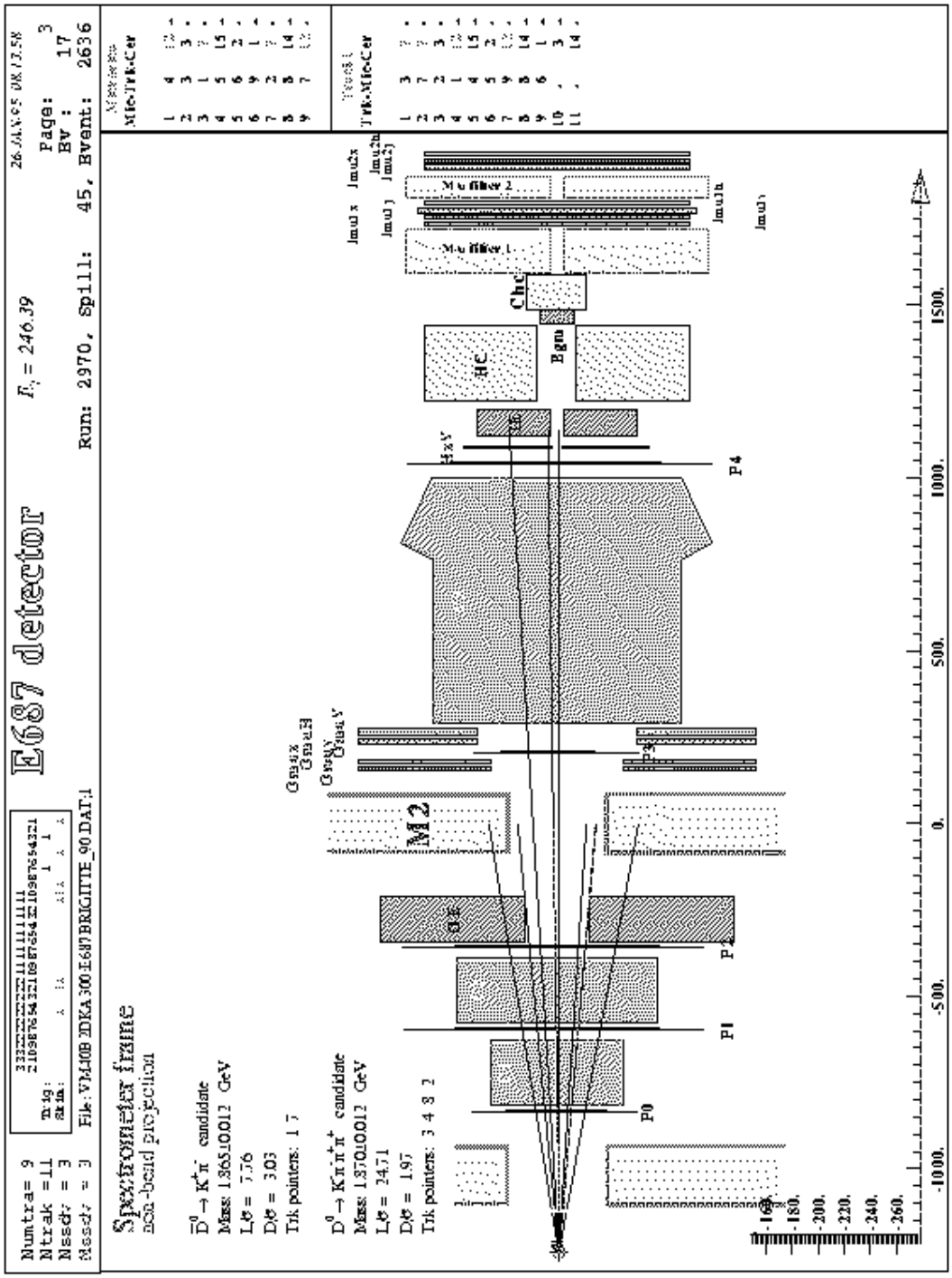

Figure 3.1.2 Display of the same event of Figure 3.1.1 in the XZ (non-bend) spectrometer view.

3.1.3 Linking of SSD and PWC tracks

Once tracks have been reconstructed in both the SSD and PWC detectors, it is necessary to *link* them, or match which PWC track is an extension of each SSD track. In the analysis of a charm decay we need both the momentum information (conveyed by the PWC tracking) and the vertexing information (conveyed by the SSD tracking).

The linking is accomplished by extending both SSD and PWC tracks in opposite directions to the center of M1. For candidate links, the X and Y intercepts and the X slopes (i.e. the slopes in the non-bend view) must match. Furthermore,in the case of five chambers tracks, the bend angles in the fields of M1 and M2 must be consistent. At this stage, multiple PWC tracks are allowed to link to the same SSD track. Next, candidate links are subject to a global least-squares fit which uses all the SSD and PWC hits associated with the track. Multiple links are then arbitrated on the basis of the χ^2/DOF. At most two PWC tracks are allowed to be linked to the same SSD track (this is because e^+e^- pairs are produced with a very small opening angle, so that they are reconstructed as the same track in the SSD detector, but as different tracks in the PWC system after they have been separated in the M1 field).

The linking efficiency is $\sim$ 98% for high momentum *tracks*, and about $\sim$ 94% for high momentum *stubs*. The efficiency is considerably lower at low momentum because the track direction in the SSD detector is smeared by multiple Coulomb scattering effects.

SSD tracks which fail the linking process are generally wide angle tracks which fall outside of the acceptance of M1. Unlinked PWC tracks may originate from non-charm particles which decayed downstream of the microvertex,

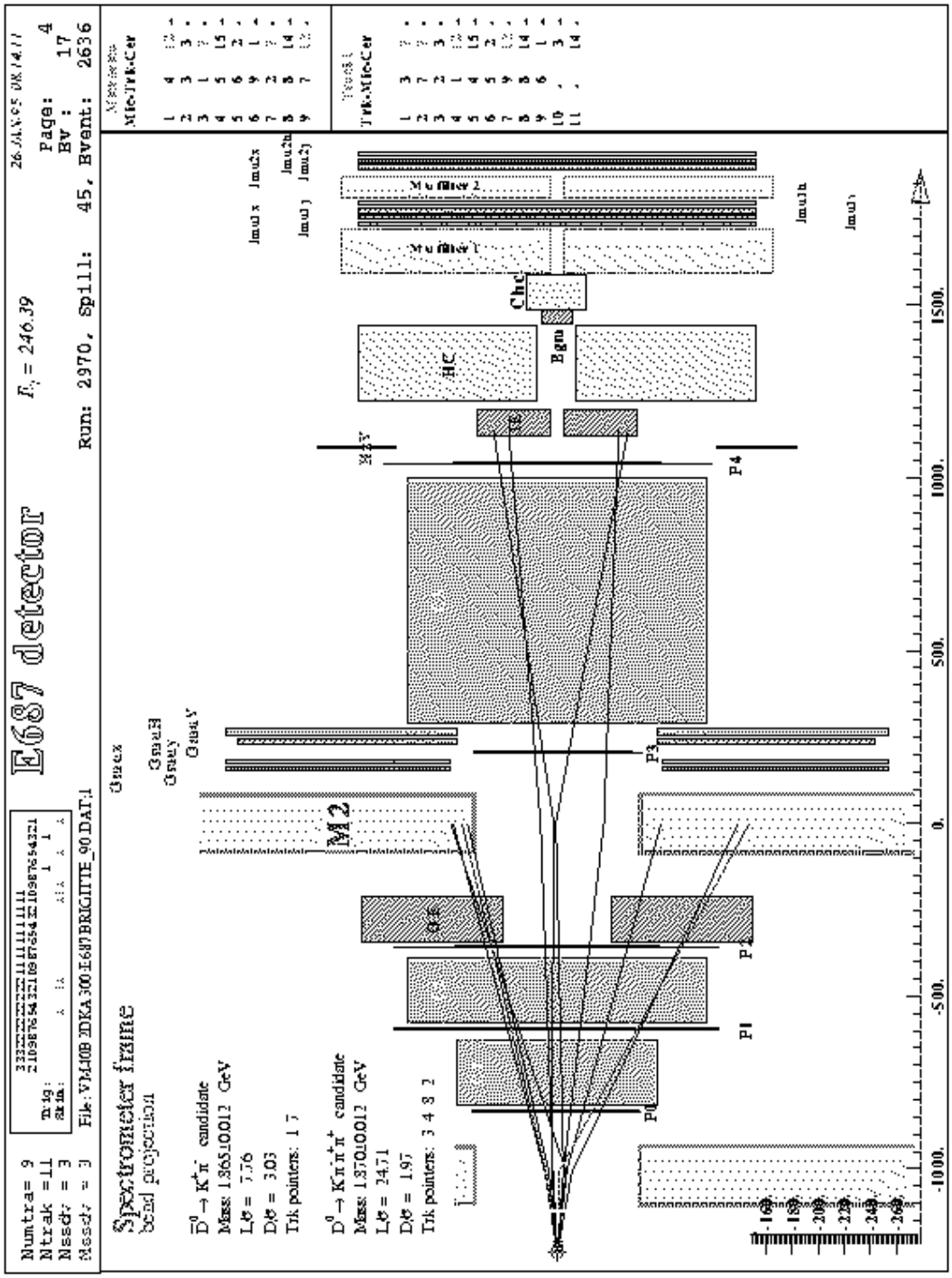

Figure 3.1.3 Display of the same event of Figure 3.1.1 in the YZ (bend) spectrometer view.

and are considered as candidates in the reconstruction algorithms for *vees* (K_s^0 and Λ), Ξ and Ω particles, and *kinks*.

3.2 SSD vertices reconstruction

A basic vertex algorithm using only the SSD information is implemented in the first stages of data reconstruction. This is necessary to provide some form of vertex information to be used by later reconstruction codes. The algorithm uses the reconstructed SSD tracks to determine the complete vertex topology of the event.

The common vertex of two or more tracks is defined as the point in space which minimize their distance of closest approach in the transverse plane. Specifically, the minimized quantity is:

$$\chi^2 = \sum_{i=1}^{n} \left(\frac{x - (x_i + a_i{}' z)}{\sigma_{x,i}} \right)^2 + \left(\frac{y - (y_i + b_i{}' z)}{\sigma_{y,i}} \right)^2$$

where x, y, z are the coordinates of the vertex (which are taken as parameters of the fit), $a_i{}', b_i{}', x_i, y_i$ are the slopes and intercepts of the i-th track, $\sigma_{x,i}, \sigma_{y,i}$ are the errors returned by the purely geometric track fit to the hits (without any multiple Coulomb scattering effects included).

The vertexing algorithm starts by assigning all the SSD tracks to a common vertex and by computing the corresponding χ^2. If the χ^2 is above a threshold value, tracks are subtracted one at a time, starting with the one which gives the biggest contribution, and each time the vertex is refitted. The subtraction process continues until the χ^2 falls below the threshold. At this point, since the space location of the vertex may have changed in the process, all the disregarded tracks are tested, one at a time, to check whether they

originate from the formed vertex, and are definitely included in it if the χ^2 of the fit allows it. Once the construction of the first vertex is completed, the procedure is iterated for the set of unassigned tracks. At the end, the complete vertex topology of the event is constructed, and all the SSD tracks are either assigned to one (and only one) vertex, or remain unassigned.

Some reconstruction codes use as primary vertex of the event (i.e. the point in space where the photon-nucleon interaction took place) the most upstream SSD vertex within the target region. If no SSD vertices are reconstructed, the center of the target is used.

3.3 Momentum determination

Particle momentum is determined by measuring the track deflection in the magnetic fields of M1 and M2. Different track topologies require different techniques. In the case of 5-chamber tracks, the track parameters upstream and downstream of M2 are used to determine the bend angle in the field of M2. For linked three- or four-chamber tracks, the SSD segment and the PWC segment of the track are used to compute the bend through M1. Finally, unlinked three- or four-chamber tracks are assumed to originate from the reconstructed SSD vertex which lies closest to the track projection in the XZ (non-bend) view; the momentum is then determined from the deflection through M1. In all cases, a full simulation of the M1 or M2 magnetic field (including fringe effects) is used.

The momentum resolution for tracks passing through M1 or M2 is found as:

$$\frac{\sigma_p}{P} = 3.4\% \left(\frac{P}{100\ GeV/c} \right) \sqrt{1 + \left(\frac{17\ GeV/c}{P} \right)^2} \quad \text{for M1}$$

$$\frac{\sigma_p}{P} = 1.4\% \left(\frac{P}{100\ GeV/c} \right) \sqrt{1 + \left(\frac{23\ GeV/c}{P} \right)^2} \quad \text{for M2}$$

where the momentum dependent term under the radical is due to multiple Coulomb scattering. For linked five-chamber tracks, it is possible to improve the momentum resolution by combining the M1 and M2 measurement.

3.4 Čerenkov identification

The Čerenkov algorithm makes use of the light patterns observed in the Čerenkov counters and the momentum analysis performed by the magnet-PWC system to identify the type of particle corresponding to each track. Particle identification is a fundamental step in charm analysis, since it allows a drastic reduction of combinatorics when forming invariant mass combinations.

PWC parameters are used to compute the point of impact of each track on the Čerenkov counters. For each counter, the cell hit by the track and all the adjacent cells are checked for the presence (or absence) of a signal of emitted Čerenkov radiation (online pedestal suppression assures that only signals above the background noise are recorded). If a signal is found in at least one cell, the counter is considered *on* for that track; if no signals are found, the counter is considered *off*; if the only cells containing a signal are shared by some other track predicted light cone, the counter is considered *confused*. Since the track momentum is known (from the magnetic field analysis), it is possible to compare the observed light pattern to the expected behavior for a track with that momentum under different particle hypothesis ($e^{\pm}, \pi^{\pm}, K^{\pm}, p^{\pm}$). Particle

identifications which are inconsistent to the observed pattern may therefore be excluded. Information from the three Čerenkov counters are then combined to further restrict the identification possibilities (C3 may be used only for 5-chamber tracks). If the information from any two detectors are contradictory, the Čerenkov identification for that track is said to be *inconsistent*.

For example, let's consider a 5-chamber track with a momentum of $P = 50\ GeV/c$. If all the three counters are on, the track would have to be a $\pi^{\pm}$ (see Table 2.8.1); if C1 and C2 are on but C3 is off, the particle is a $K^{\pm}$; if C2 is on but C1 and C3 are off, the particle is a $p^{\pm}$; all other light patterns are inconsistent with any particle hypothesis.

The result of the Čerenkov algorithm is encoded in a variable (*istatp*) which gives for each track all the possible particle identifications consistent with the observed pattern of light (see Table 3.4.1).

Table 3.4.1 Particle identification variable

istatp = 0	inconsistent information
istatp = 1	e definite
istatp = 2	π definite
istatp = 3	e, π ambiguous
istatp = 4	K definite
istatp = 7	π, K ambiguous
istatp = 8	p definite
istatp = 12	K, p ambiguous
istatp = 14	π, K, p ambiguous
istatp = 15	e, π, K, p ambiguous

3.5 Vee reconstruction

K_s^0 and Λ^0 (usually referred to as "vees") are often found among the decay products of charm mesons and baryons. In E687, these particles are reconstructed through the charged decay modes:

$$K_s^0 \rightarrow \pi^+\pi^- \quad (BR = 68.6\%)$$
$$\Lambda^0 \rightarrow p\ \pi^- \quad (BR = 63.9\%)$$

These particles are relatively long lived with respect to charm particles, and may travel several meters within the spectrometer before decaying. According to the region of decay, they leave topologically distinct tracks, and must be reconstructed with different algorithms (see Figures 3.5.1, 3.5.2 and 3.5.3). In all, vees are reconstructed over a decay length of about 10 meters.

Despite the differences, all vee-reconstruction codes have in common the search for a pair of oppositely charged tracks which originate from a common point in space, the vee decay vertex. The invariant mass of the pair is computed, first assigning to both tracks the pion mass to test the K_s^0 hypothesis; next the proton mass is assigned to the faster particle and the pion mass to the slower particle to check for Λ^0. Initially, no Čerenkov identification is applied, and the vee requirements are intentionally left loose to allow for different degrees of signal to noise in individual analysis.

3.5.1 SSD vees

SSD vees are reconstructed from pairs of oppositely charged linked SSD-PWC tracks originating from a common vertex. These are therefore K_s^0 and Λ^0 which decay upstream of the second SSD station. The vee vertex is required to lie at least 20 σ_z downstream of the reconstructed SSD primary vertex and the

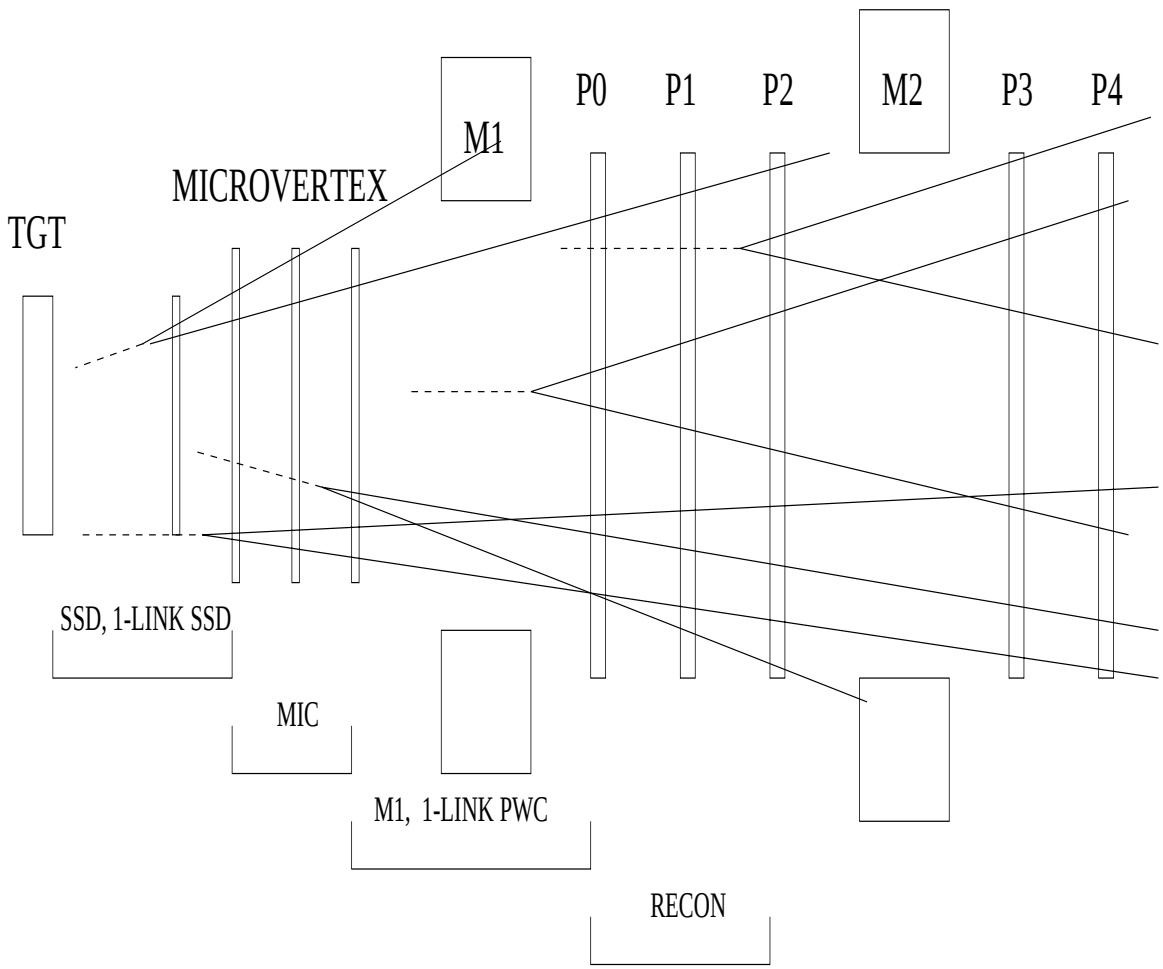

Figure 3.5.1 Schematic drawing of the regions of the spectrometer where vees are reconstructed by the different algorithms.

vee momentum must point back to the primary within 1 mm in the transverse plane (XY). The SSD vees are the cleanest and best defined category of vees: the vee track for this category has a resolution comparable to the composing SSD tracks.

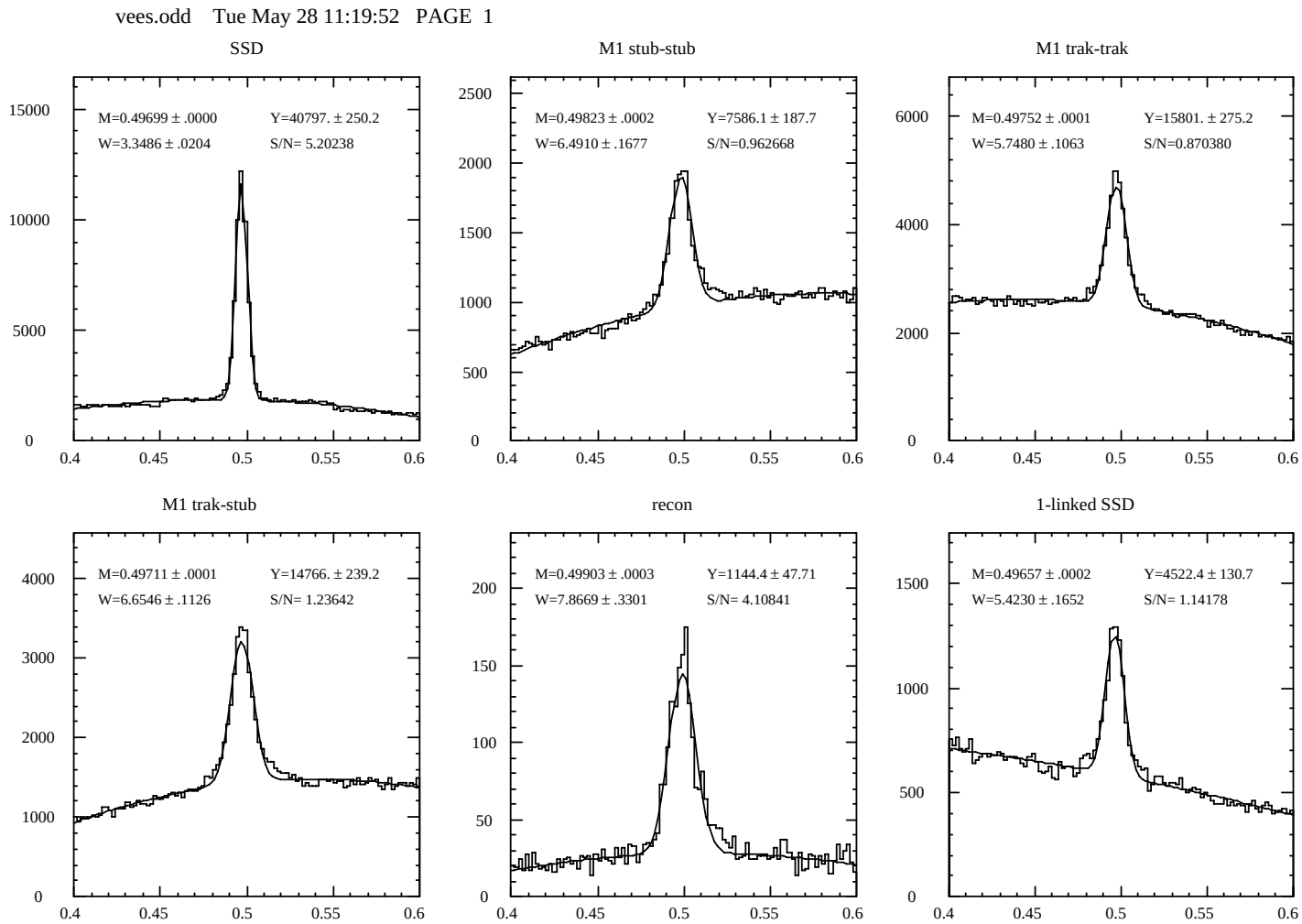

Figure 3.5.2 $K_s^0 \rightarrow \pi^+\pi^-$ candidates for different reconstructed topologies.[27]

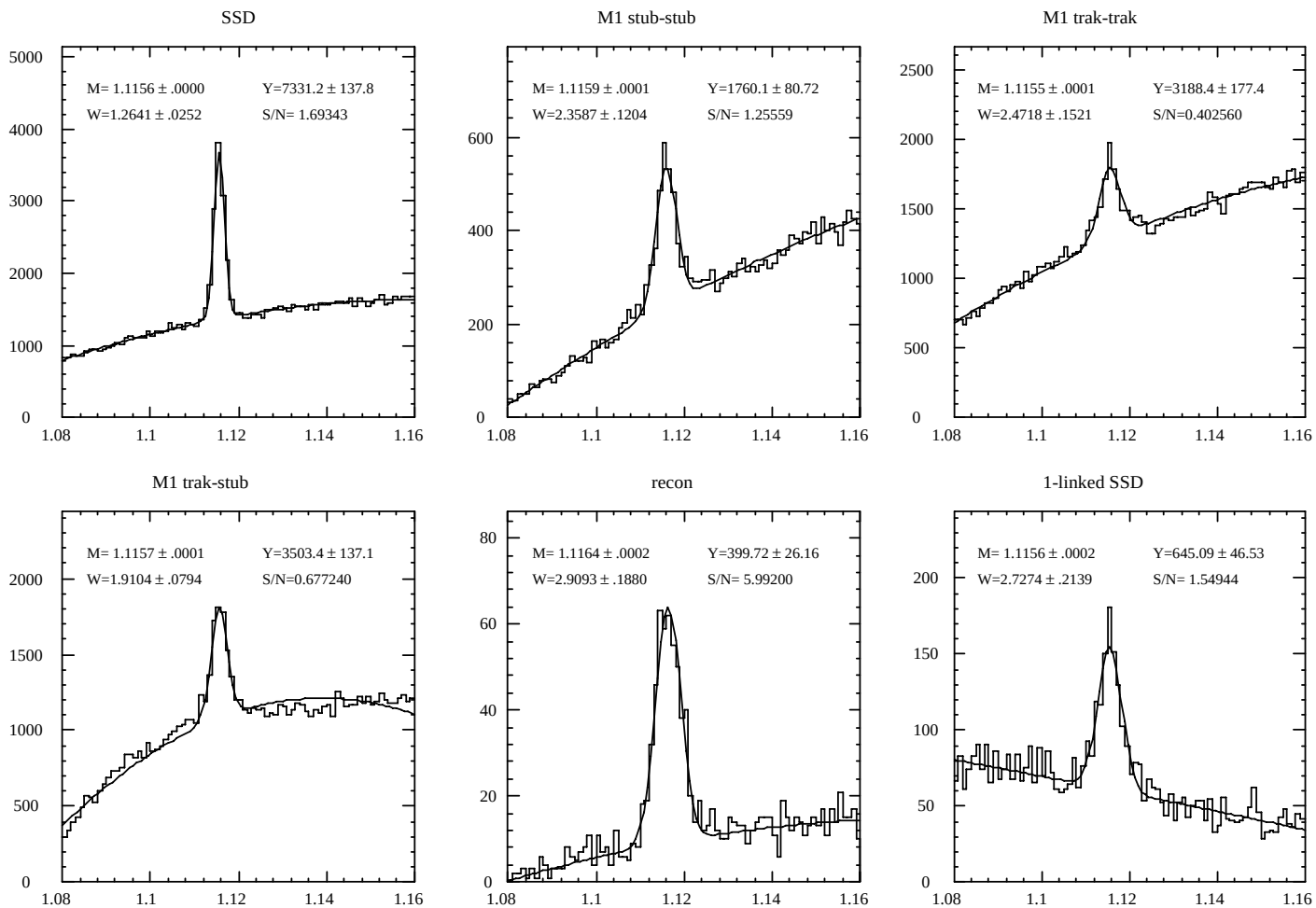

Figure 3.5.3 $\Lambda^0 \to p\pi^-$ candidates for different reconstructed topologies[27].

3.5.2 M1 vees

The M1 vees are composed of K_s^0 and Λ^0 which decayed between the last SSD plane and the first PWC station P0. They are reconstructed with pairs of unlinked PWC tracks and are divided in three subcategories, according to the nature of their components: *track-track*, *track-stub* and *stub-stub*.

The reconstruction algorithm is substantially the same for the three topologies. For each candidate pair of unlinked PWC tracks, the intersection in the XZ plane (non-bend) is first found; an iterative procedure then traces the two prongs through the M1 field and determines the Y location of the vee vertex. In the case of a track-stub vee, the tracing also allows for the computation of the unknown momentum of the stub prong. For a stub-stub vee, it is necessary to further constrain the vee vector to originate from the SSD primary vertex and then both unknown momenta can be computed. Finally, a global fit using the full covariance matrices of the tracks (including multiple Coulomb scattering effects) is applied to each vee candidate to provide a better estimate of the vee decay vertex and the vee momentum. The requirement that the vee points back to the primary vertex is also included in the fit through a contribution to the χ^2.

M1 vees are the most copious vee category, accounting for over 70% of the total reconstructed vee sample. Their resolution is not as good as for SSD vees, for the obvious reason that they lack any SSD information.

3.5.3 Recon vees

Recon vees are vees which decayed between P0 and P2. Because their decay region is the most downstream considered, they tend to be the vee category with the highest momentum.

Recon vees are reconstructed using hits in P1, P2, P3, P4 which have not been already used by the general PWC pattern reconstruction algorithm (which only reconstructs tracks originating in P0). First, track projections in the XZ (non-bend) view are constructed and checked two at a time for intersecting between P0 and P2. Projections which don't intersect in the desired region with any other projection are disregarded. Then, projections in the U,V,Y views are formed and matched to the X projections to form tracks in space, with only loose requirements on the χ^2/DOF of the track. Several track topologies are allowed: P1234 (i.e. tracks with hits in P1, P2, P3 and P4), P123, P234 and P23. In any case, only one missing hit per station is allowed. Finally, tracks are combined pairwise and a global fit to the vee hypothesis is performed. The parameters of the fit are the five parameters for each track (X and Y slopes and intercepts and Y bend angle in the field of M2) plus the three coordinate of the vee vertex. In the case of P23 candidates (for which the prongs are defined by a single point on each side of the magnet) it is also necessary to assume that the vee originates from the SSD primary vertex in target. Recon vees sharing the same X projections are arbitrated on the basis of their χ^2/DOF.

3.5.4 Single-linked SSD vees

Single-linked SSD vees are reconstructed from the combination of a linked SSD+PWC track with an unlinked SSD track. These are K_s^0 and Λ^0 which decayed before the second SSD station like the (double-linked) SSD vees, but for which one of the decay prongs fall out of the M1 geometrical acceptance and therefore was not traced in the PWC. The single-linked vees reconstruction code was only recently implemented and therefore this type of vee has not been used in any analysis.

The reconstruction code uses the *SDVERT* vertexing algorithm, described in section § 2.6. The linked SSD+PWC track and the unlinked SSD track are required to verticize in space with a confidence level greater than 1%. A primary vertex is found as the most upstream vertex in target reconstructed by *DVFREE*. The separation between primary and secondary vertex is computed and it is required to have $L/\sigma > 10$. Also, the primary-secondary vector is required to lie in the plane of the two decay prongs. By knowing the momentum of the linked track, the primary-secondary direction and the unlinked track direction, it is possible to balance the transverse momentum and to compute the total momentum of the unlinked track (there is no two-fold ambiguity in the kinematics). Finally, the invariant mass of the two tracks is computed for the K_s^0 hypothesis and the Λ^0 hypothesis. In the K_s^0 case no Čerenkov requirements on the two prongs are imposed, while in the Λ^0 case the linked prong is required to be identified by the Čerenkov counters as either proton or kaon/proton ambiguous. The Λ^0 candidates where the pion is linked and the proton is unlinked are not reconstructed, since this kind of vee proved to contain very little signal over an overwhelming background.

3.5.5 MIC vees

MIC vees have the decay vertex between the second and the fourth (last) SSD station. The reconstruction algorithm starts by projecting unlinked PWC tracks backward onto the SSD detector to look for unused hits in the last two stations. If one or two matching triplets of hits are found, the parameters of the track are recomputed by a global fit which uses both the SSD and PWC hits. The new reconstructed tracks are then checked two at a time for originating from the same vertex in space, and a cut on the distance of closest approach (DCA) is imposed. Candidate vees sharing one prong are arbitrated on the basis of the minimum DCA.

Although this type of vee proved to be copious and to have high resolution, a software error caused them to be lost in the skim stage of data reconstruction, so that they were never used for any analysis.

3.5.6 Single-linked PWC vees

Single-linked PWC vees share the same decay region of the M1 vees (between the SSD detector and P0), but are composed of one linked SSD+PWC track and one unlinked PWC track. The reconstruction algorithm is essentially the same as for the M1 vees, and they are divided in three subcategories: *track-track*, *track-stub* and *stub-stub*. Unfortunately, this type of vee proved to contain mostly background, so that they were never used in any analysis.

3.6 Candidate-driven vertexing algorithm

In any charm analysis it is absolutely fundamental to determine and separate the production or primary vertex, where the charm particle was produced by the photon-nucleon interaction, from the secondary or decay vertex, where the charm particle decayed into its daughter particles. The reconstruction of

two separate vertices is the single most compelling signature of a charm event, as opposed to a non-charm hadronic event or an electromagnetic event, where all particles originate from the same vertex. In E687, it is the high resolving power of the microvertex detector which makes this separation possible.

The vertexing algorithm most commonly used in E687 data analysis, including the analysis presented in this thesis, is called "SDVERT". SDVERT is a *candidate driven* algorithm. Rather than reconstructing the whole vertex topology of the event, the routine reconstructs only that portion of the event which is compatible with the charm decay of interest. It is therefore a highly flexible (and highly efficient) algorithm, suitable to the analysis of a large variety of charm decays (hadronic, semileptonic, fully leptonic), which may include a large variety of decay objects: charged hadrons and leptons ($\pi^{\pm}$, $K^{\pm}$, $p^{\pm}$, $e^{\pm}$, $\mu^{\pm}$), neutral particles reconstructed in the calorimeters (π^0, γ), "slow" decaying particles (K_s^0, Λ^0, Ξ, Ω), weakly interacting (therefore missing) neutrinos.

The vertex reconstruction performed by SDVERT is accomplished in three stages (see Figure 3.6.1) :

3.6.1 Secondary vertex reconstruction

A combination of objects compatible with the charm decay of interest is selected and fed to SDVERT. For example, this could be a combination of charged linked tracks as in the decay $\Lambda_c^+ \to pK^-\pi^+$, or a combination of some charged linked tracks and some neutral or longer living particles, such as in the decays $\Lambda_c^+ \to pK^-\pi^+\pi^0$, $\Lambda_c^+ \to pK_s^0\pi^+\pi^-$. SDVERT tests the hypothesis that all the objects of the combination *which contain SSD information* (i.e linked tracks, SSD vees and SSD Ξ and Ω) are compatible with coming from

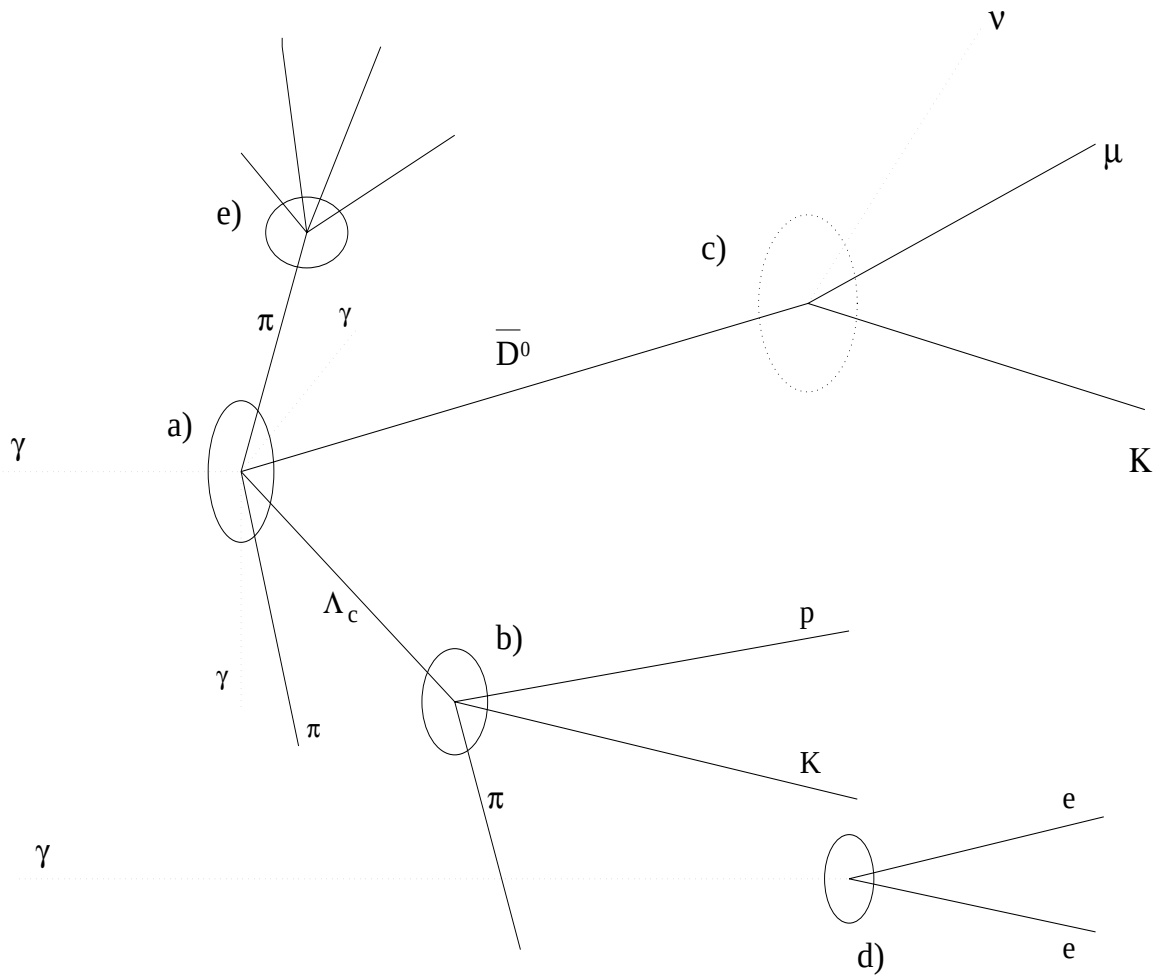

Figure 3.6.1 Schematic diagram for a typical E687 charm event: a) is the primary or production vertex, where the beam photon-target nucleon interaction takes place; in this case a charm baryon Λ_c^+ and a charm meson $\overline{D^0}$ are produced, together with other non-charm particles which originate in the fragmentation process; b) is the secondary vertex for the Λ_c^+, which in this case decays to $pK^-\pi^+$; c) is the secondary vertex for the $\overline{D^0} \rightarrow K^+\mu^-\nu_\mu$; in d) an embedded photon (for example originating from multiple bremsstrahlung) converts to an e^+e^- pair; in e) one of the fragmentation pions undergoes a secondary interaction.

the same point in space, the candidate secondary vertex. The probability that this happens is expressed through the secondary vertex confidence level, which is required to be greater than some threshold value (typically $cls > 1\%$).

Decay objects not containing SSD information (like π^0, spectrometer vees, Ξ and Ω) are not used in the construction of the secondary vertex. Typically, the invariant mass and the total momentum of the combination of decay objects is also computed.

3.6.2 Primary vertex reconstruction

The way the production vertex of the candidate charm is reconstructed depends on the topology of the decay.

- The most common case is where all the decay daughters are reconstructed and at least two of them have SSD information (for example, $\Lambda_c^+ \rightarrow pK^-\pi^+$ or $D^0 \rightarrow K^-\pi^+$). In this case the total momentum of the decay objects equals the momentum of the candidate parent charm, and a secondary vertex has been constructed in the previous stage. It is therefore possible to attach the total momentum to the secondary vertex and use it as a *seed* to look for the primary vertex.

The primary vertex construction begins by selecting all of the SSD tracks which intersect in space with the charm seed (the daughter objects are excluded from the process). A minimum cut on the confidence level of the vertex ($clp > 1\%$) is required for an intersection to be accepted. If only one intersecting track is found, its intersection with the seed is assumed to be the primary vertex. If more than one track is found, the algorithm first checks if any two of these tracks make a common vertex with the seed (always requiring $clp > 1\%$). If no pair is found, the primary vertex location is given by the highest confidence level intersection between a single track and the seed. If at least one pair is found, the primary vertex is given by the intersection of the two tracks of the pair. At this point all the other SSD tracks (which intersect the seed) are

added one at a time to the vertex, and are included if the confidence level of the object remains above 1%.

• In the case of a *one-prong decay*, where only one decay daughter contains SSD information (such as $\Lambda_c^+ \to pK_s^0$, if the K_s^0 is reconstructed in the spectrometer), no secondary vertex has been reconstructed in the previous stage. However, the two decay daughters define a plane which must contain the primary vertex. It is therefore possible to reconstruct the primary vertex with an algorithm similar to the one previously described, but clustering SSD tracks around a *seed plane* instead of a seed track. Since any given track will intersect the seed plane, the algorithm must start by looking for a pair of tracks making a common vertex in the seed plane (therefore no single-track primaries are accepted). Then, other SSD tracks in the event are clustered around the best pair so long as the confidence level of the vertex remains above 1%.

• The last scenario we consider is that of a semileptonic decay (for example $D^0 \to K^-\mu^+\nu$). Because of the missing neutrino we do not reconstruct all the decay daughters of the parent charm. It is still possible to define a secondary vertex in space by verticizing the charged component of the decay (in our example, the K^- and the μ^+), but it is not possible to use the total charged momentum (which does *not* equal the charm momentum) as a seed in the primary vertex search. The primary vertex is then reconstructed by a *standalone* vertexing algorithm called *DVFREE* which makes use of all the SSD tracks in the event, excluding those associated with the decay object. DVFREE starts by considering any pair of tracks which form a vertex in space with a confidence level greater than 1%. All other tracks in the event are then added to this vertex if the confidence level of the total object remains above 1%. Once the construction of the first vertex has ended, the process is repeated

with another pair of intersecting tracks. In constructing the second vertex, all other tracks are considered, even those already assigned to the first vertex. At the end of the process, several vertices may have been constructed, and a track may belong to one or more vertices or to no vertex at all. The primary vertex is then defined as either the most upstream or the highest multiplicity reconstructed vertex within the target region.

Once the primary and secondary vertices are reconstructed, the distance in space L is computed and divided by its error σ_L: L/σ_L is therefore the *significance of separation* between the two vertices. Requiring L/σ_L to be greater than a threshold value exploits the finite lifetime nature of charm particles in order to reject hadronic and combinatoric background. L/σ_L is the primary selection tool used in E687 analysis (and fixed target experiments in general).

3.6.3 Isolation

Once a vertex topology compatible with the decay of interest has been reconstructed, an effective way of improving signal to noise is to check whether this topology is compatible with a higher multiplicity charm decay, or with the inclusion of fragments in a lower multiplicity charm decay.

The first isolation tool determines whether the daughter tracks are compatible with coming from the primary vertex. Tracks from the secondary vertex are assigned one at a time to the primary, the global fit for the primary vertex is performed again and a confidence level for the new object is computed. The highest confidence level found in the process ($iso1$) is retained and required to be less than a certain value. This cut is intended to reject events where one (or more) track from the primary vertex is unintentionally assigned

to a lower multiplicity charm decay vertex, making it appear as a vertex with the desired multiplicity.

The second isolation tool determines whether other SSD tracks in the event (excluding the ones coming from the primary) are compatible with originating in the secondary vertex. Again, these tracks are assigned one at a time to the secondary vertex and the highest confidence level of the new objects thus formed is retained ($iso2$). By requiring $iso2$ to be less than some value we reject higher multiplicity charm events which have been partially reconstructed by the vertexing algorithm.

In Figure 3.6.2 we show the power of the topological cuts L/σ_L, $iso1$ and $iso2$ in extracting a charm signal from the background.

3.7 Muon reconstruction

The standard E687 muon reconstruction algorithm uses PWC parameters to compute the point of impact of the track on each of the seven planes of the inner muon system and then searches for hits within a 3σ radius around that point. If a hit is found, the track is said to have a match on that plane. Tracks having matches in at least four planes are identified as muons. The standard algorithm does not use a large fraction (about 45%) of the 1990 data which were affected by a read-out problem of the proportional tube planes of the inner muon detector (the so called *"bad runs"*). The outer muon detector is not used at all.

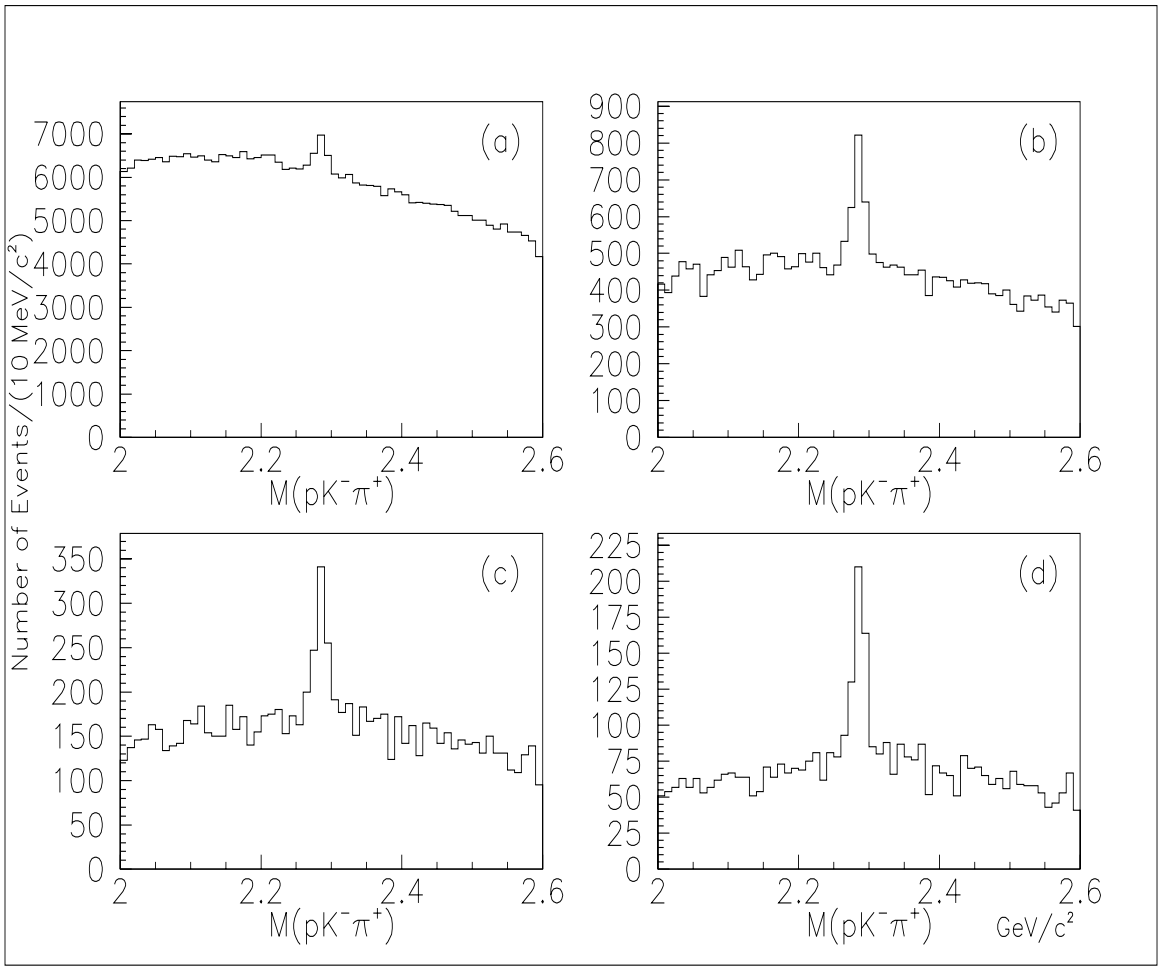

Figure 3.6.2 Invariant mass distributions for $\Lambda_c^+ \to pK^-\pi^+$ candidates. In (a) minimal topological cuts are applied: $L/\sigma_L > 3$, $cls > 1\%$, $clp > 1\%$; in (b) and (c) we tighten the L/σ_L cut to $L/\sigma_L > 7, 10$ respectively; in (d) we also add some isolation requirements: $iso1 < 90\%$ and $iso2 < 1\%$.

For the semileptonic analysis presented in this thesis, the standard muon identification had to be tightened in order to reduce the background due to hadrons (mostly pions) misidentified as muons. There are two major sources of this background: hadron showers penetrating the muon shields, and hadronic particles (K, π) decaying into muons. In order to establish $D^0 \to \pi^-\mu^+\nu$ and $D^+ \to \varrho^0\mu^+\nu$ signals (see Chapters 4 and 5), it is essential to reduce the hadron

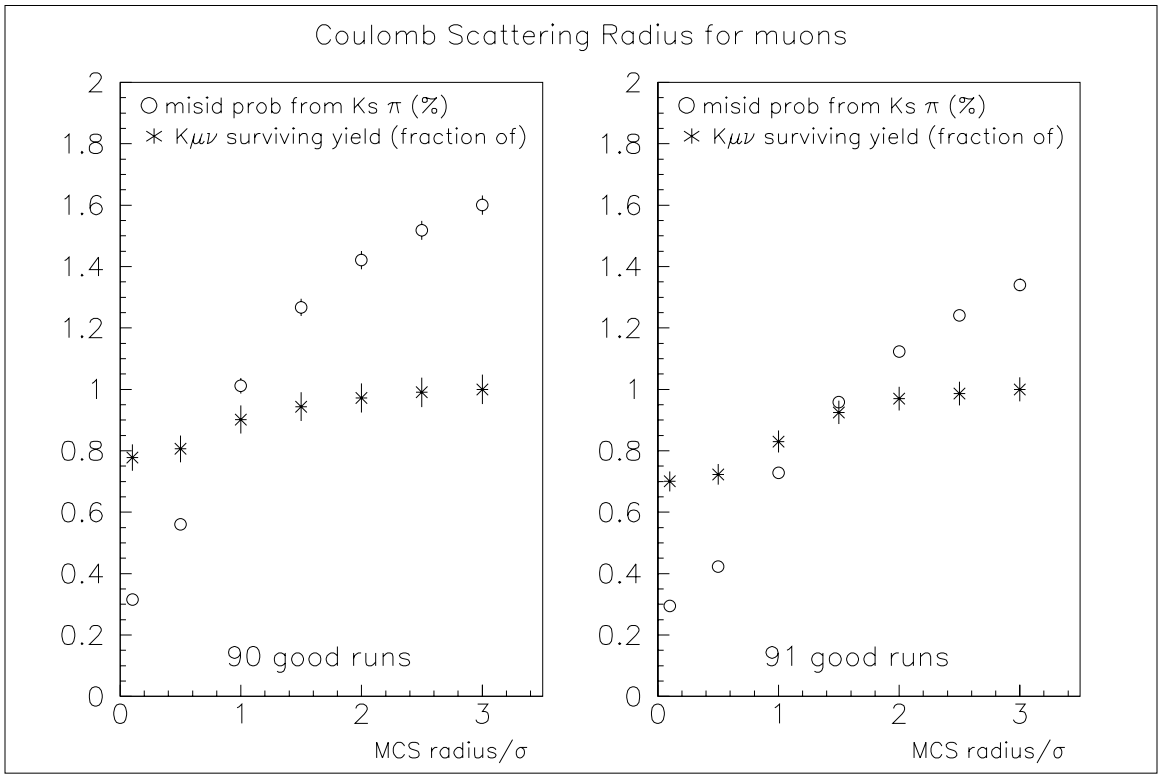

Figure 3.7.1 Effect of reducing the multiple Coulomb scattering radius on the hadron misidentification probability and on a real charm muonic signal ($D^{*+} \to D^0\tilde{\pi}^+,\ D^0 \to K^-\mu^+\nu$). Data are plotted separately for the 1990 and 1991 good runs. Only tracks with at least 5 matches are used in this study.

misidentification background below 1%. This goal could be accomplished by means of two additional tools: reducing the Coulomb scattering radius around the track projection, and using the energy deposited by the track in the HC and IE.

Furthermore, an effort was made to recover part of the signal contained in the 1990 bad runs, always keeping in mind the necessity for low misidentification probability.

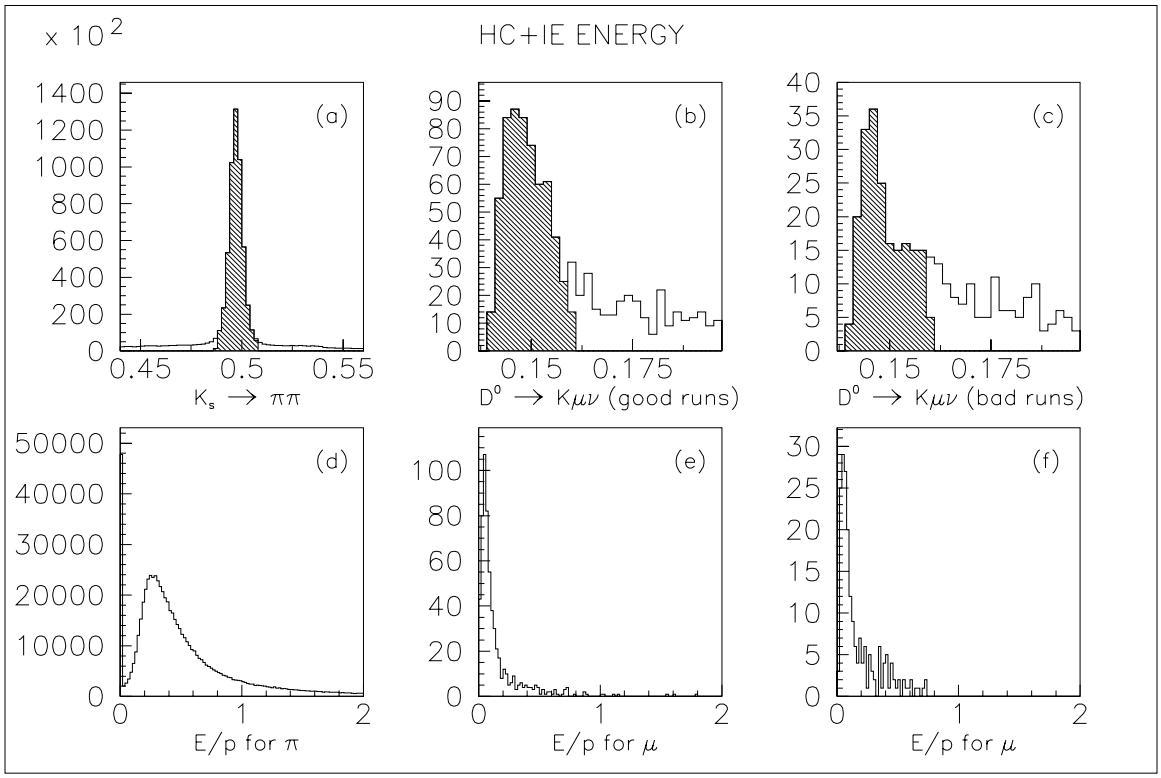

Figure 3.7.2 E/p distributions for $K_s \rightarrow \pi^+\pi^-$ pions (d) and $D^0 \rightarrow K^-\mu^+\nu$ muons (e) and (f) (good and bad runs, respectively). Plots (a), (b), (c) show the corresponding data samples.

3.7.1 The Coulomb scattering radius

It is possible to use the proportional tube planes of the muon detector to cut on the Coulomb scattering radius used by the muon reconstruction algorithm. In Figure 3.7.1 we show the effect on the misidentification probability of reducing the radius from the standard 3σ value down to almost zero (perfect match). The data come from a high statistics sample of pions from K_s^0 decays. The decrease in misidentification probability is compared to the reduction in yield caused by the same cut on a reconstructed $D^{*+} \rightarrow D^0\tilde{\pi}^+$, $D^0 \rightarrow K^-\mu^+\nu$ charm signal. As a compromise between low misidentification probability and high efficiency, we require $r/\sigma_r < 1$.

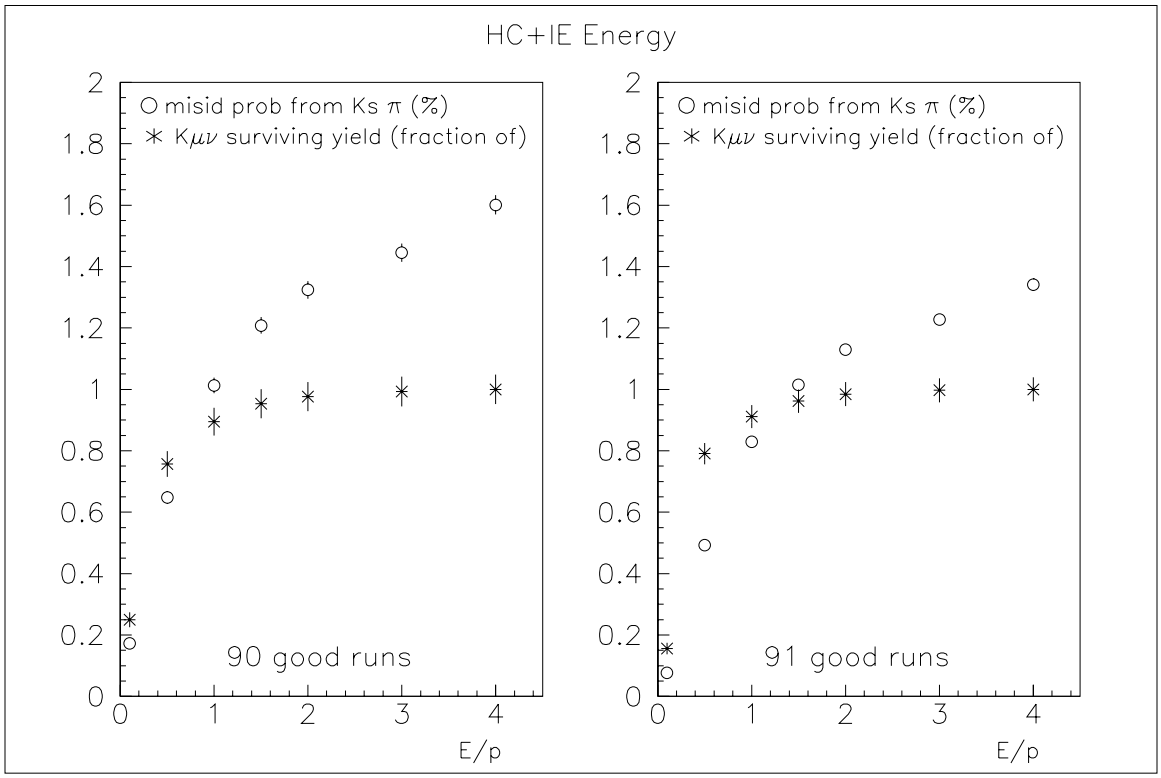

Figure 3.7.3 Reduction in misid probability ($K_s^0 \to \pi^+\pi^-$ pions) and effect on a real charm signal (for $D^0 \to K^-\mu^+\nu$ data candidates) when an upper limit on E/p is imposed.

3.7.2 HC+IE energy

In the E687 spectrometer, the HC and IE calorimeters are located upstream of the inner muon detector. If the misidentified hadron comes from a hadronic shower, we expect the total energy deposited by the track in the HC and IE to be larger than for a real muon track. In Figure 3.7.2 we plot the E/P distributions (E = sum of HC and IE energies associated to the track, P = track momentum) for a sample of candidate hadrons (π from K_s^0 decays) and muons (μ from $D^0 \to K^-\mu^+\nu$ decays): the hadron distribution is indeed shifted to much higher values than for muons, showing that we can reduce the hadronic background by imposing an upper limit on E/P.

In Figure 3.7.3 we compare the reduction in hadronic misidentification probability (for pions from $K_s^0 \rightarrow \pi^+\pi^-$) to the reduction in charm yield (for $D^0 \rightarrow K^-\mu^+\nu$ data candidates), when increasingly tighter E/P cuts are applied. In the analysis we require $E/P < 1$.

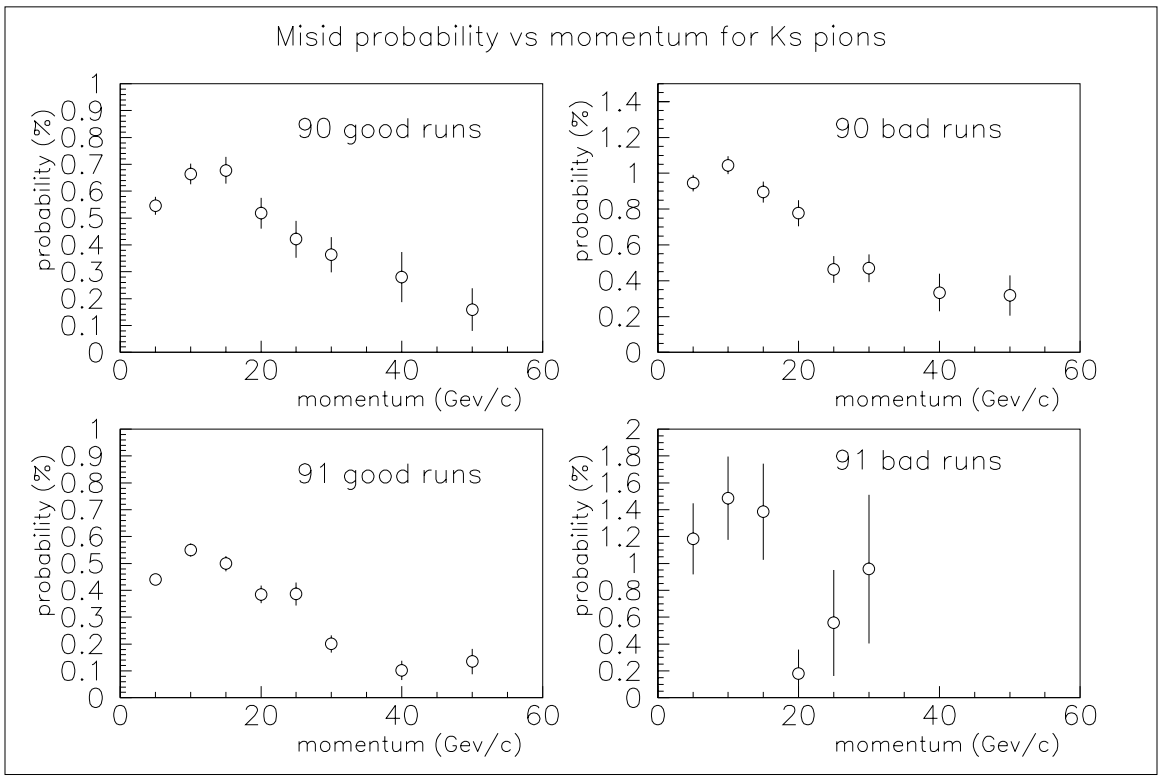

Figure 3.7.4 Hadronic misidentification probability as function of the particle momentum when the final set of analysis cuts is applied. The misidentification probability is computed separately for 1990 and 1991 and for good and bad runs. In all cases, the first point in the plots represents the misidentification probability averaged over all momenta.

3.7.3 Muon identification

In the *good muon runs*, where both the proportional tubes and the scintillator planes of the inner muon detector were working, we define as muon candidates tracks which have at least five matches (out of seven) within a Coulomb scattering radius of 1σ. In the *bad muon runs*, where we only have the information from the three scintillator planes, muon candidates are: tracks which either have three matches; or tracks with one or two matches that are positively identified as muons by the HC. In all cases, we require the total energy deposited in the HC+IE calorimeters to be within the limits $0.01 < E/P < 1.0$. Also, to reduce contamination from $K^+ \rightarrow \mu^+\nu$ decays, we require the Čerenkov identification of the track to be inconsistent with being either proton or kaon definite or kaon/proton ambiguous (istatp(μ)$\neq 4, 8, 12$). In Figure 3.7.4 we show the final hadronic misidentification probabilities when all the requirements identifying a muon candidate are applied.

CHAPTER 4

PSEUDOSCALAR D^0 SEMILEPTONIC DECAYS

In this chapter we analyze the two semileptonic decays of the charm meson D^0 into scalar meson final states, namely $D^0 \to K^-\mu^+\nu$ (Cabibbo-favored) and $D^0 \to \pi^-\mu^+\nu$ (Cabibbo-suppressed). In order to reduce background and obtain cleaner reconstructed samples, we concentrate on events where the D^0 is not directly photoproduced, but rather originates from the decay of an excited charm meson: $D^{*+} \to D^0\tilde{\pi}^+$ ("tag" analysis). We measure the relative branching ratio of the two decays $D^0 \to \pi^-\mu^+\nu$ and $D^0 \to K^-\mu^+\nu$ and use this result to compute the ratio of form factor normalizations $\frac{|f_+^\pi(0)|}{|f_+^K(0)|}$.

4.1 Analysis algorithm

We want to reconstruct the decay chain $D^{*+} \to D^0\tilde{\pi}^+$, $D^0 \to h^-\mu^+\nu$, where $h^- = K^-, \pi^-$ is the daughter hadron originating in the decay $D^0 \to K^-\mu^+\nu$ or $D^0 \to \pi^-\mu^+\nu$, respectively, and $\tilde{\pi}^+$ is the soft pion resulting from the D^{*+} decay (see Figure 4.1.1 (a)).

We first select a combination of two linked $SSD + PWC$ tracks compatible with being a $h^-\mu^+$ pair. The hadron candidate track h^- is required to be reconstructed in at least three PWC stations, while the muon candidate track must be reconstructed in all five PWC stations since it has to penetrate the Inner Muon detector. Both tracks must have momentum $P(h^-)$, $P(\mu^+) > 10\ GeV/c$. The hadron is required to be identified by the Čerenkov counters as either kaon definite or proton/kaon ambiguous (istatp(K^-)= 4, 12) in the case of a $D^0 \to K^-\mu^+\nu$ candidate, or as either pion

definite or pion/electron ambiguous (istatp(π^-)= 2, 3) for a $D^0 \to \pi^-\mu^+\nu$ candidate. The muon is identified as described in section § 2.7; in addition, we require that the muon candidate is *not* identified by the Čerenkov counters as either kaon or proton definite or kaon/proton ambiguous (istatp(μ)$\neq$ 4, 8, 12). The two prongs h^- and μ^+ are required to have opposite charge and to originate from a common vertex in space (secondary vertex) with a confidence level $cls > 1\%$. We compute the invariant mass of the $h^-\mu^+$ pair and we restrict it to be contained within the limits $0.95\ GeV/c^2 < M(K^-\mu^+) < 1.85\ GeV/c^2$ and $1.1\ GeV/c^2 < M(\pi^-\mu^+) < 1.85\ GeV/c^2$ in order to reduce contamination from other D^0 tag decays (see section § 4.3). To reduce background from higher multiplicity semileptonic decays, we require that no other track in the event, excluding those coming from the primary vertex (see below), be compatible with originating from the secondary vertex with a confidence level greater than 1%, i.e. we require $iso2 < 1\%$.

Next, we look for the primary vertex of the event, i.e. the point where the D^{*+} was produced. Because of the missing neutrino, it is not possible to compute the total D^0 momentum from its daughter tracks and use it as a *seed* to be combined with other SSD tracks to construct the primary vertex. Instead, we use the *standalone* DVFREE code which uses all the SSD tracks in the event (excluding those already associated to the $h^-\mu^+$ pair) to construct all the possible vertices (with a confidence level $clp > 1\%$). We then define the primary vertex as the highest multiplicity vertex in target which is separated by a distance of at least $L/\sigma_L > 4$ from the already reconstructed secondary vertex (ties are arbitrated by choosing the vertex with the best L/σ_L).

The primary and secondary vertex positions define a direction of flight for the candidate D^0. Using the flight direction, it is possible to compute the

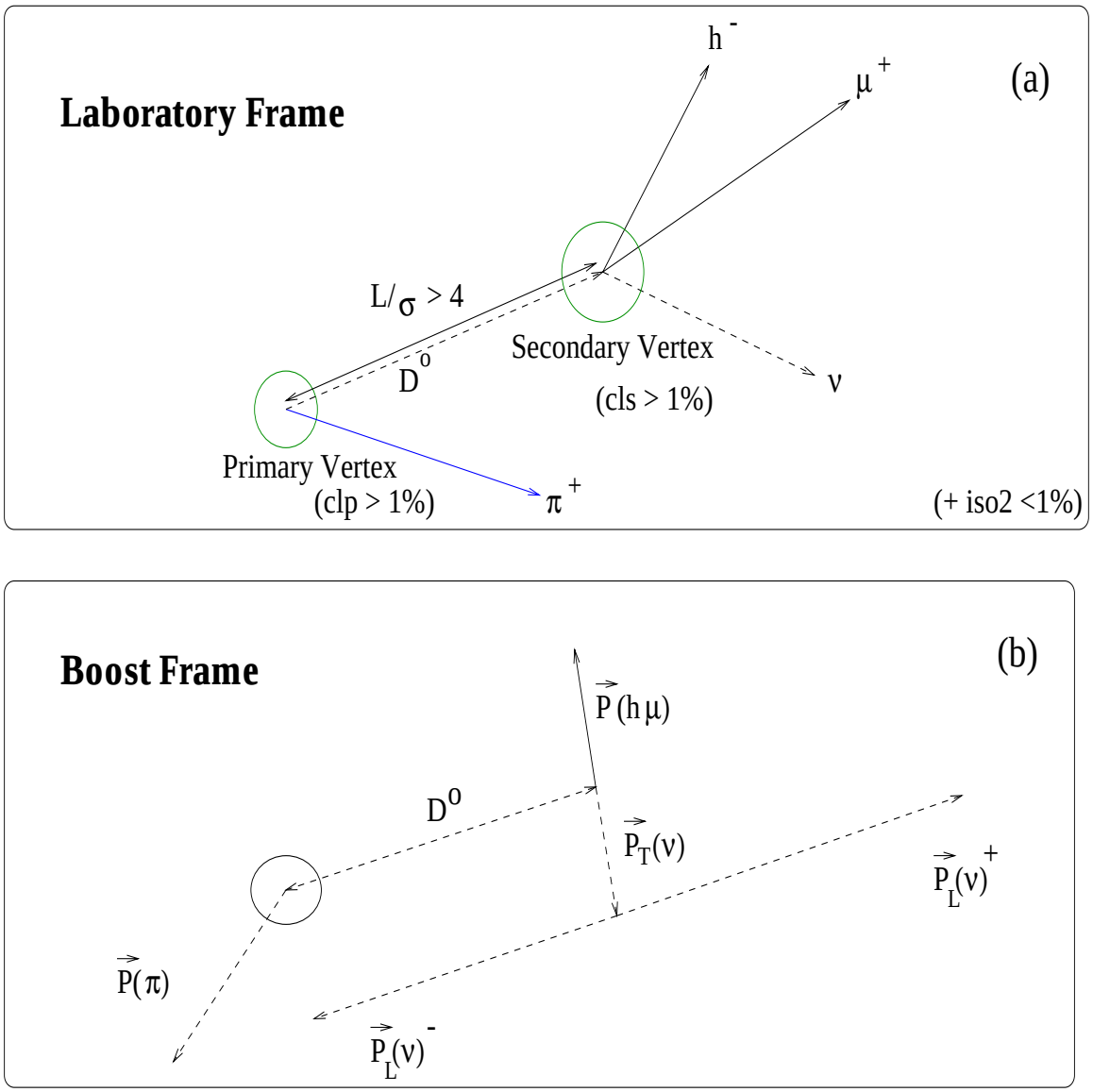

Figure 4.1.1 Schematic diagram for the $D^{*+} \to D^0 \tilde{\pi}^+$, $D^0 \to h^- \mu^+ \nu$ decay, in the laboratory frame (a) and the boost frame (b).

D^0 momentum by assuming the D^0 mass. Following the technique developed by E691[28], we perform the calculation in a boosted frame where the total charged momentum (i.e. the momentum of the $h^- \mu^+$ pair) is perpendicular

to the D^0 direction of flight $\hat{r}$, and consequently is equal to the transverse component of the neutrino momentum (see Figure 4.1.1 (b)):

$$\vec{P}_T^{\prime}(\nu) = \vec{P}_T^{\prime}(h^-\mu^+)$$

(primed quantities refer to the boosted frame). Assuming the D^0 mass, we can compute the neutrino energy with the formula:

$$E^{\prime}(\nu) = P^{\prime}(\nu) = \frac{M^2(D) - E^{\prime 2}(h^-\mu^+) - P^{\prime 2}(h^-\mu^+)}{2E^{\prime}(h^-\mu^+)}$$

and require it to be positive $E^{\prime}(\nu) \geq 0$ (see Figure 4.1.2 (a)). The longitudinal component squared of the neutrino momentum is given by:

$$P_L^{\prime 2}(\nu) = E^{\prime 2}(\nu) - P_T^{\prime 2}(\nu).$$

This quantity should always be positive, but resolution effects allow it to be negative about 40% of the time (see Figure 4.1.2 (b)): nevertheless, we can still recover these events by setting $P_L^{\prime 2}(\nu) = 0$. We extract the square root to compute the *absolute value* of the longitudinal momentum of the neutrino, which in the boost frame coincides with the D^0 momentum:

$$|P^{\prime}(D^0)| = |P_L^{\prime}(\nu)| = \sqrt{E^{\prime 2}(\nu) - P_T^{\prime 2}(\nu)}.$$

The sign of $P^{\prime}(D^0)$ is not determined by the calculation, since physically we do not know the direction of flight of the D^0 in the boost frame (forward or backward). This *two-fold ambiguity* persists when the D^0 momentum is boosted back to the laboratory frame, giving a lower and a higher D^0 momentum solution (if $P_L^{\prime}(\nu) = 0$, the two solutions coincide).

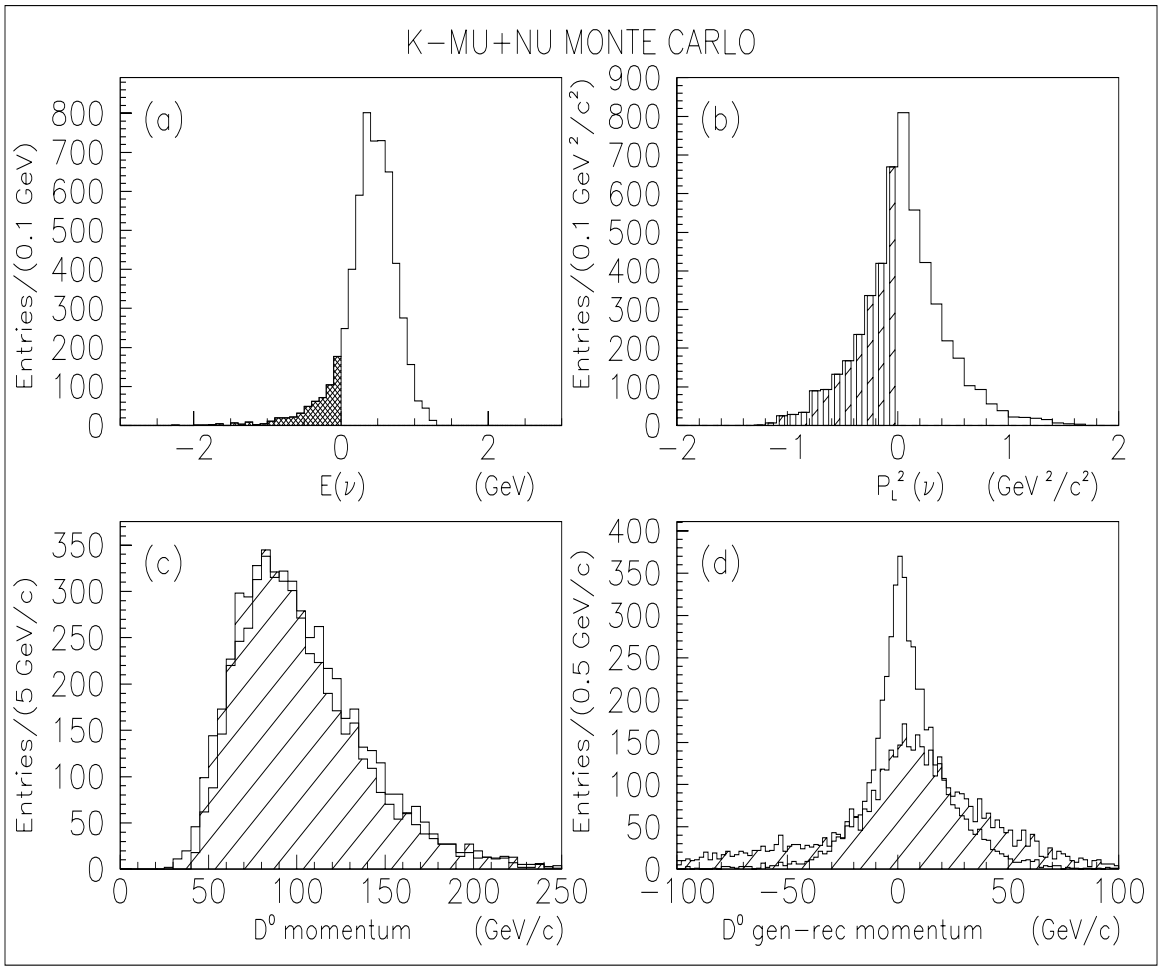

Figure 4.1.2 (a) Neutrino energy in the boost frame. Candidates with $E'(\nu) < 0$ (hatched area, about 10% of total sample) are disregarded. (b) Longitudinal component squared of neutrino momentum in boost frame. Candidates with $P_L'^2(\nu) < 0$ (hatched area) are set to $P_L'^2(\nu) = 0$. (c) Comparison between magnitude of the generated D^0 momentum (unhatched area) and magnitude of the reconstructed D^0 momentum for the lowest D^* mass solution (hatched area): agreement is good. (d) Difference between generated D^0 momentum and *lowest mass solution* (unhatched area) or *highest mass solution* (hatched area) D^0 reconstructed momentum: the lowest mass solution gives a better answer most of the time.

The final step of the analysis algorithm consists in selecting a soft pion candidate $\tilde{\pi}^+$ from all the tracks assigned to the primary vertex. The $\tilde{\pi}^+$

candidate must be a linked $SSD + PWC$ track reconstructed in at least 3 stations of PWC, must have the same charge as the daughter muon, and its Čerenkov identification must *not* be kaon or proton definite or kaon/proton ambiguous (istatp($\tilde{\pi}^+$)$\neq$ $4, 8, 12$). No momentum cut is applied to the soft pion.

Finally, we combine the $\tilde{\pi}^+$momentum with the two reconstructed D^0 momenta and obtain two solutions for the D^{*+} mass. We solve the ambiguity by always choosing the lowest mass solution: Monte Carlo study shows that this approach gives the correct answer in $\sim$ 80% of the cases (see Figures 4.1.2 (c), (d)). The cuts used in this analysis are summarized in Table 4.1.1.

4.2 The data signals

The data sample used for this analysis is the Global Vertex Skim. This skim (performed on the whole data sample collected during the 1990-1991 run) requires the presence in the event of at least two vertices, each composed of at least two SSD tracks: therefore it does not introduce any bias in our semileptonic analysis. Running the analysis algorithm on the Global Vertex Skim, we obtain the $D^0 \to K^-\mu^+\nu$ and $D^0 \to \pi^-\mu^+\nu$ signals presented in Figure 4.2.1, where for historical reasons we plot the $M(D^{*+}) - M(D^0)$ mass difference instead of the D^{*+} mass (the D^0 mass is assumed in the reconstruction algorithm and therefore it is fixed to its nominal value $M(D^0) = 1.8645\ GeV/c^2$).

4.3 Discussion of backgrounds

For a quantitative evaluation of the amount of signal present in the plots of Figure 4.2.1, it is important to understand all possible sources of backgrounds which may contaminate the invariant mass distributions.

Table 4.1.1 Analysis cuts

tracking	all tracks linked $SSD + PWC$ $\mu^+ = 5$ PWC, h^- and $\tilde{\pi}^+$= at least 3 PWC $P(h^-), P(\mu^+) > 10\ GeV/c$
Čerenkov	istatp$(K^-) = 4, 12$, istatp$(\pi^-) = 2, 3$ istatp$(\tilde{\pi}^+) \neq 4, 8, 12$ istatp$(\mu^+) \neq 4, 8, 12$
μ identification	$0.01 < E/p < 1.0$ Good Runs: at least 5 out of 7 planes + $r/\sigma_r < 1$ Bad Runs: 1 or 2 scint. planes + HC μ id or 3 scint. planes with no further request
kinematics	$P_L^{l2}(\nu) > -2\ GeV^2/c^2$, $E'(\nu) > 0\ GeV$
vertexing	$cls > 1\%$, $clp > 1\%$, $iso2 < 1\%$ $L/\sigma_L > 4$ $\tilde{\pi}^+$must be found in primary vertex
hadron-lepton invariant mass	$0.95\ GeV/c^2 < M(K^-\mu^+) < 1.85\ GeV/c^2$ $1.1\ GeV/c^2 < M(\pi^-\mu^+) < 1.85\ GeV/c^2$

It is incorrect to estimate the amount of background present in the *right sign* (RS) mass difference distributions by looking at *wrong sign* (WS) mass plots. WS mass plots are produced with the same analysis cuts used for the RS but with charge requirements on the prongs not compatible with a $D^{*+} \rightarrow D^0\tilde{\pi}^+$, $D^0 \rightarrow h^-\mu^+\nu$ decay ($D^{*+} \rightarrow D^0\tilde{\pi}^-$, $D^0 \rightarrow h^-\mu^+\nu$ and $D^{*+} \rightarrow D^0\tilde{\pi}^+$, $D^0 \rightarrow h^-\mu^-\nu$ are both examples of WS combinations; see Figure 4.3.1). Although random combinatoric background is expected to contaminate both RS and WS in the same way, other sources of background

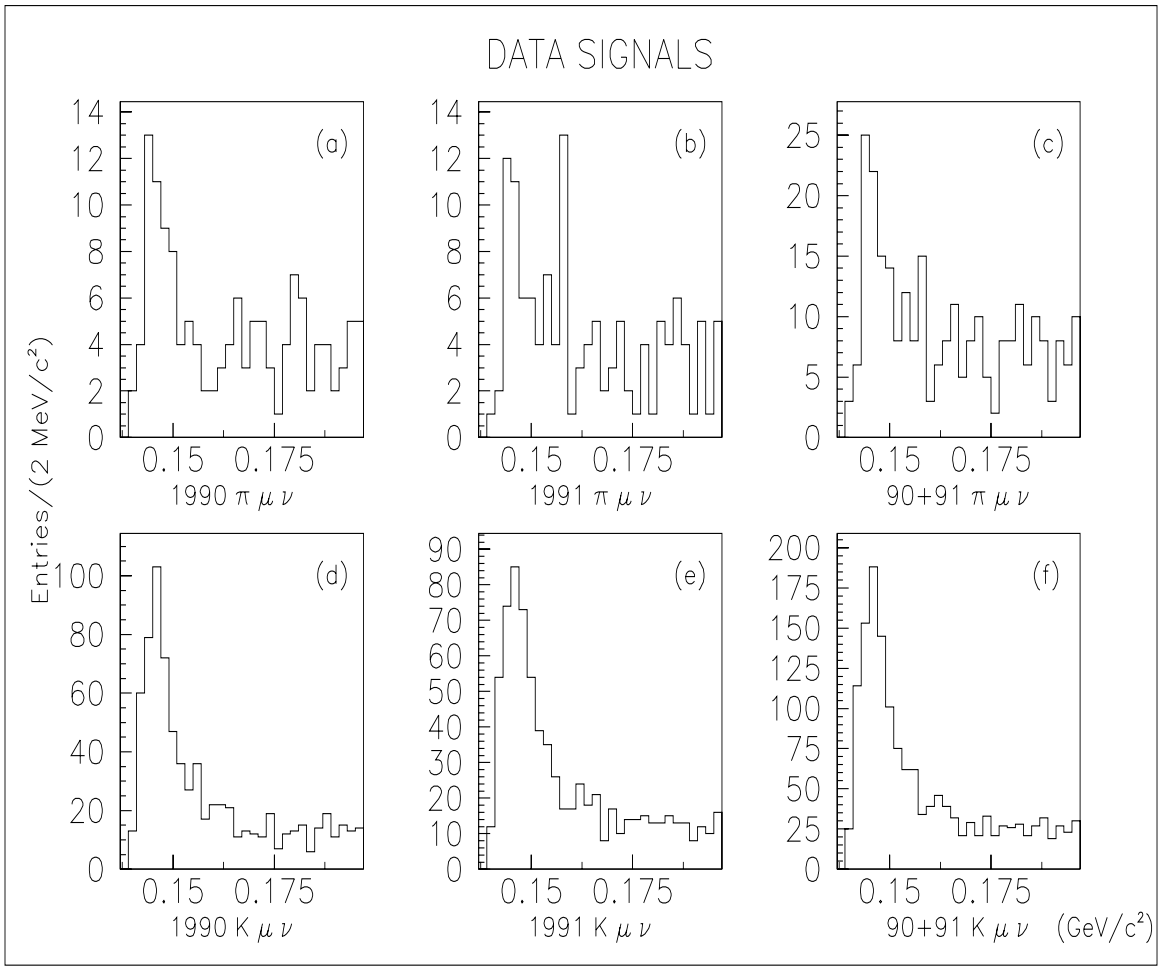

Figure 4.2.1 $D^{*+} \rightarrow D^0\tilde{\pi}^+$, $D^0 \rightarrow \pi^-\mu^+\nu$ and $D^{*+} \rightarrow D^0\tilde{\pi}^+$, $D^0 \rightarrow K^-\mu^+\nu$ signals obtained with the analysis cuts described in the text. Signals for the 1990, 1991 and the combined 1990+1991 samples are presented.

originating from physical charm decays will contaminate preferentially either the RS or the WS mass distributions. We do not utilize WS distributions to parameterized the background in the RS distributions, but rather we try to estimate quantitatively all the possible sources of background which are known to contaminate the signals.

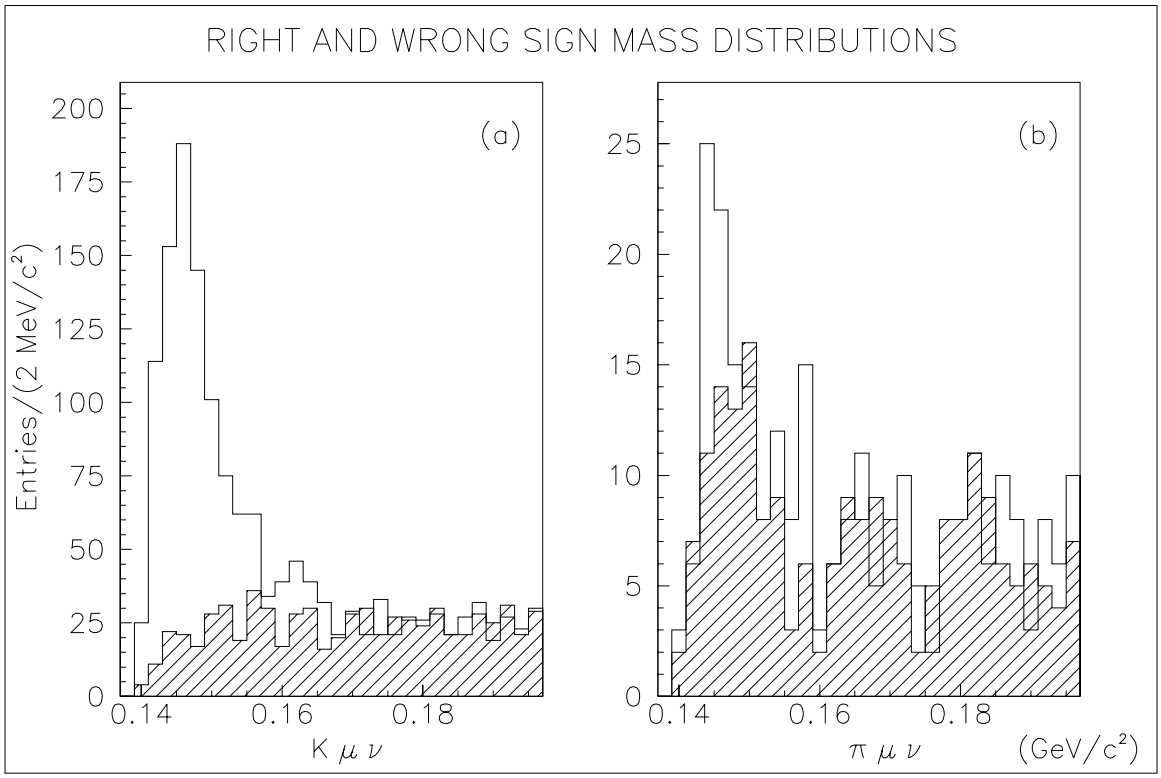

Figure 4.3.1 $M(D^{*+}) - M(D^0)$ mass difference plots for combinations with right sign ($q(\tilde{\pi}) \neq q(h)$, unhatched areas) and wrong sign ($q(\tilde{\pi}) = q(h)$, hatched areas). In both cases the two secondary prongs have opposite charge ($q(h) \neq q(\mu)$).

4.3.1 D^0 tag semileptonic decays

The first source of background is given by other possible D^0 tag semileptonic decays. When reconstructed as $K^-\mu^+\nu$ or $\pi^-\mu^+\nu$, these decays produce RS mass difference distributions which peak at the nominal $M(D^{*+}) - M(D^0)$ mass difference (see Figure 4.3.2).

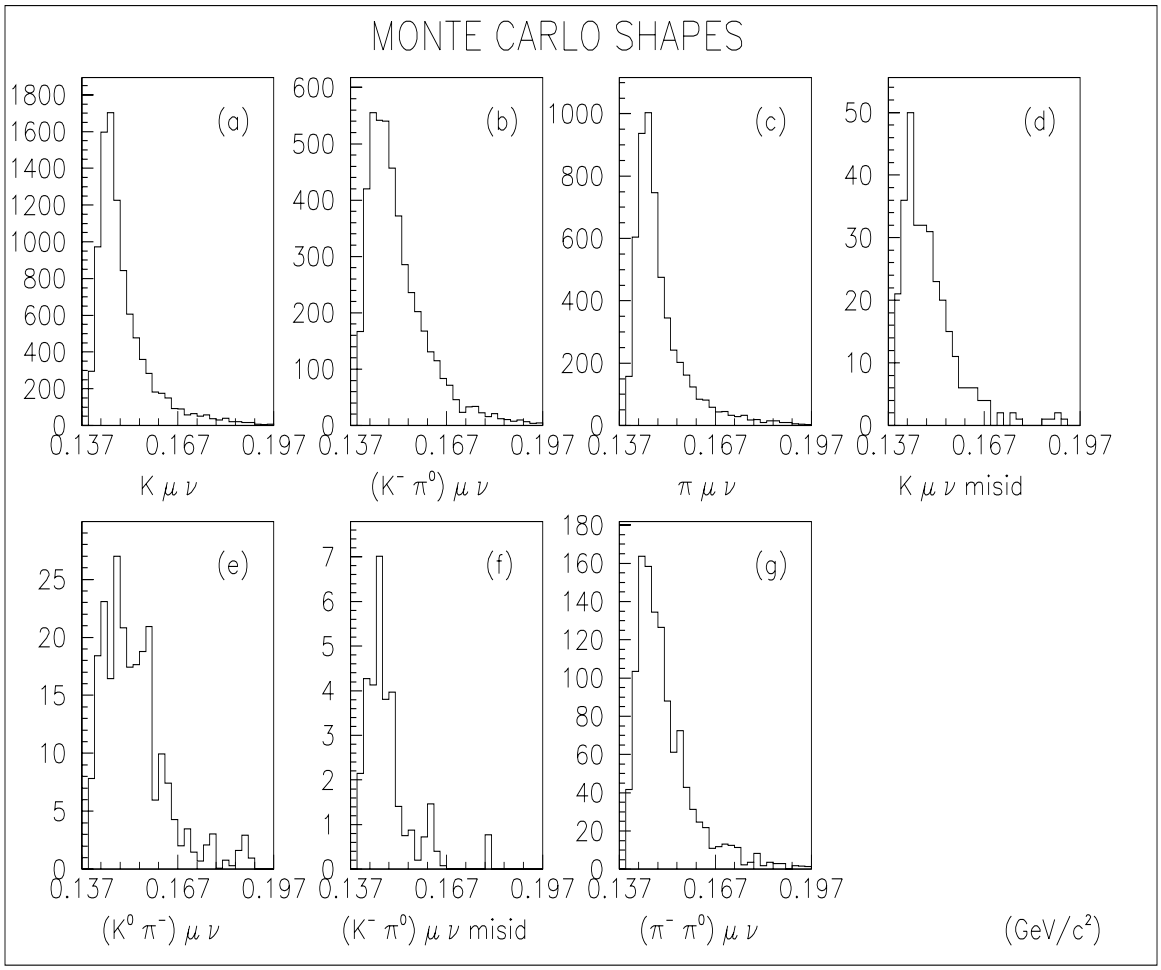

Figure 4.3.2 $M(D^{*+})-M(D^0)$ mass difference distributions for several Monte Carlo simulated D^0 tag semileptonic decays, after all analysis cuts are applied.

- $\underline{D^{*+} \to D^0\pi^+,\ D^0 \to K^{*-}\mu^+\nu,\ K^{*-} \to K^-\pi^0}$.

This decay is a major source of background for the $K^-\mu^+\nu$ tag signal. Since the π^0 is not reconstructed, the topology of the event looks exactly like that of a $D^{*+} \to D^0\tilde{\pi}^+,\ D^0 \to K^-\mu^+\nu$ event. Furthermore the reconstructed $M(D^{*+}) - M(D^0)$ mass difference, although it looks broader than in a $K^-\mu^+\nu$ event because one additional particle is missing (see Figure 4.3.2 (a) and (b)), peaks at approximately the same mass, making

$K^{*-}\mu^+\nu$ events virtually indistinguishable from $K^-\mu^+\nu$ events. Assuming equal efficiency for the reconstruction of the charged prongs in the two decays, the amount of $K^{*-}\mu^+\nu$ contamination expected to the $K^-\mu^+\nu$ signal is given by $\frac{Y(K^{*-}\mu^+\nu)}{Y(K^-\mu^+\nu)} = \frac{BR(D^0\to K^{*-}\mu^+\nu)\times BR(K^{*-}\to K^-\pi^0)}{BR(D^0\to K^-\mu^+\nu)} \sim 0.6^{[29][30][31]} \times\frac{1}{3} \sim 0.2$. Fortunately we can reduce the amount of $K^{*-}\mu^+\nu$ contamination by imposing a lower limit on the two-body $K^-\mu^+$ invariant mass. In Figure 4.3.3 (a) we show the $K^-\mu^+$ invariant mass reconstructed from Monte Carlo $K^-\mu^+\nu$ and $K^{*-}\mu^+\nu$ samples. Because of the missing π^0, the distribution from $K^{*-}\mu^+\nu$ is shifted at much lower masses. By requiring $M(K^-\mu^+) > 0.95\ GeV/c^2$ we eliminate mostly $K^{*-}\mu^+\nu$ events so that the contamination to the $K^-\mu^+\nu$ signal reduces to $\sim 10\%$.

Table 4.3.1 Mass cut efficiency and global reconstruction efficiency

D^0 decay	Mass Cut	Mass Cut Eff.	Global Efficiency
$K^-\mu^+\nu$	0.95	85.7 %	1.185%
$K^{*-}\mu^+\nu,\ K^{*-}\to K^-\pi^0$	0.95	39.9%	0.574%
$\pi^-\mu^+\nu$	1.10	50.6 %	0.689 %
$K^-\mu^+\nu$ (K^- misid as π^-)	1.10	41.0 %	0.038%
$K^{*-}\mu^+\nu,\ K^{*-}\to K^-\pi^0$ (K^- misid as π^-)	1.10	6.3 %	0.004%
$K^{*-}\mu^+\nu,\ K^{*-}\to K^0\pi^-$	1.10	1.7 %	0.029 %
$\varrho^-\mu^+\nu,\ \varrho^-\to\pi^0\pi^-$	1.10	9.8%	0.145 %

The $D^{*+}\to D^0\tilde{\pi}^+,\ D^0\to K^{*-}\mu^+\nu,\ K^{*-}\to K^-\pi^0$ decay can also affect the $\pi^-\mu^+\nu$ signal if the π^0 is not reconstructed *and* the K^- is misidentified by the Čerenkov counters as a π^-. The misidentified $\pi^-\mu^+$ mass distribution is shifted at even lower values (see Figure 4.3.3 (c)), and our cut on the two-body

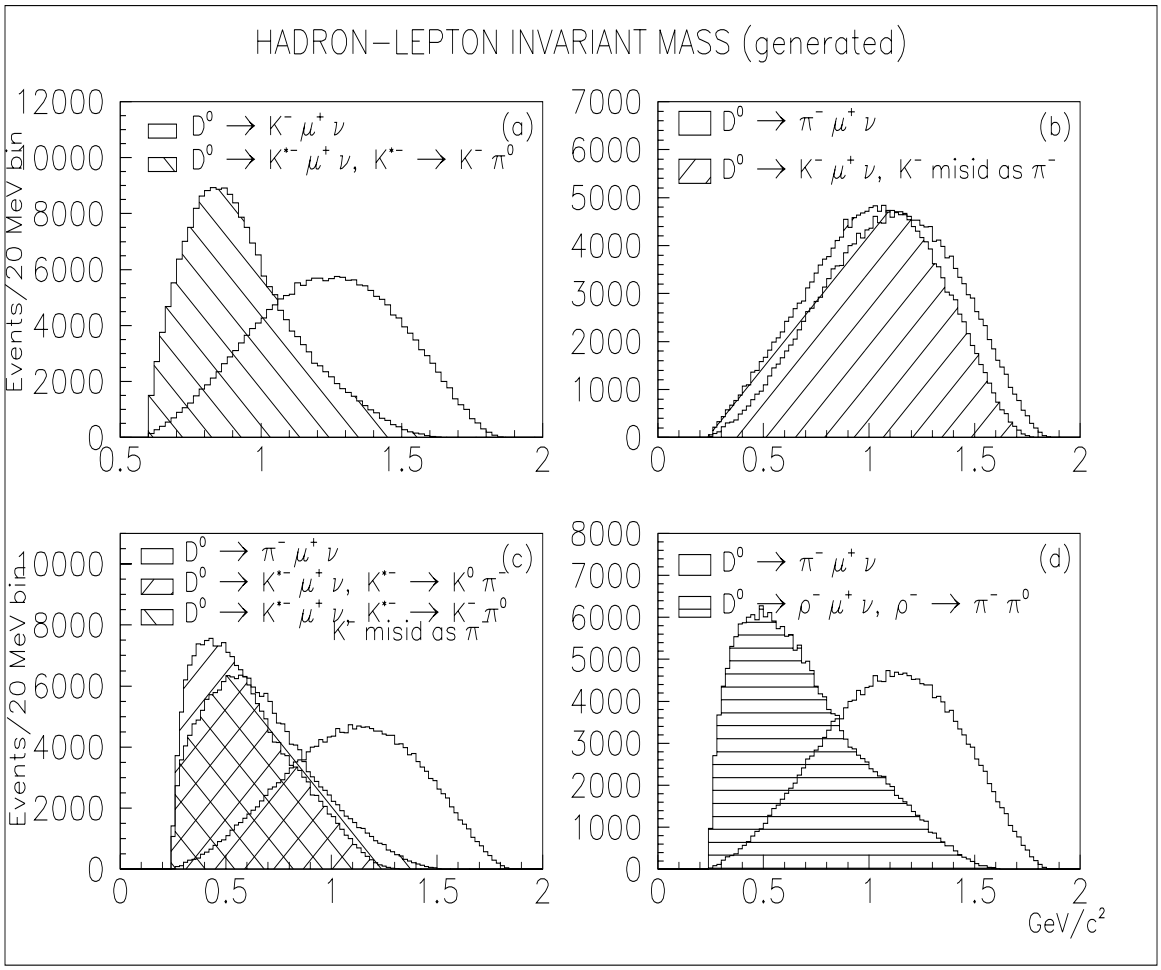

Figure 4.3.3 Hadron-lepton invariant mass $M(h^-\mu^+)$ for various Monte Carlo D^0 semileptonic decays. The distributions are normalized to the same number of generated events. No cuts are applied to sample the generated events. For each channel, the efficiency of the mass cut used in the analysis is listed in Table 4.3.1.

invariant mass $M(\pi^-\mu^+) > 1.1\ GeV/c^2$ reduces this background by a factor of ~ 15. The contamination to the $\pi^-\mu^+\nu$ signal due to this channel can be estimated as: $\frac{Y(K^{*-}\mu^+\nu, K^{*-}\to K^-\pi^0,\ K^- mis)}{Y(\pi^-\mu^+\nu)} = \frac{BR(D^0\to K^{*-}\mu^+\nu)\times BR(K^{*-}\to K^-\pi^0)}{BR(D^0\to K^-\mu^+\nu)} \times \frac{BR(D^0\to K^-\mu^+\nu)}{BR(D^0\to\pi^-\mu^+\nu)} \times \frac{\epsilon(K^{*-}\mu^+\nu,\ K^{*-}\to K^-\pi^0, K^- mis)}{\epsilon(\pi^-\mu^+\nu)} \sim 0.6 \times \frac{1}{3} \times 10 \times 0.005 \sim 0.01$, where we have assumed $\frac{BR(D^0\to\pi^-\mu^+\nu)}{BR(D^0\to K^-\mu^+\nu)} \sim 10\%$. Although small compared to the statistical error involved, this contribution is inserted in the fit.

- $\underline{D^{*+} \to D^0\pi^+,\ D^0 \to K^{*-}\mu^+\nu,\ \ K^{*-} \to \overline{K}^0\pi^-}$.

Also this channel can contaminate the $\pi^-\mu^+\nu$ signal, since the $\overline{K}^0$ is not reconstructed. In this case the fraction of events surviving the two-body mass cut is only $\sim 1.7\%$ (see Figure 4.3.3 (c)), but since there is no misidentification involved, the efficiency of all the other kinematic and topological cuts is about the same for the two channels. As a result, contamination from this channel is much higher and is roughly estimated to be: $\frac{Y(K^{*-}\mu^+\nu,\ K^{*-}\to\overline{K}^0\pi^-)}{Y(\pi^-\mu^+\nu)} = \frac{BR(D^0\to K^{*-}\mu^+\nu)\times BR(K^{*-}\to\overline{K}^0\pi^-)}{BR(D^0\to K^-\mu^+\nu)} \times \frac{BR(D^0\to K^-\mu^+\nu)}{BR(D^0\to\pi^-\mu^+\nu)} \times \frac{\epsilon(K^{*-}\mu^+\nu,\ K^{*-}\to\overline{K}^0\pi^-)}{\epsilon(\pi^-\mu^+\nu)} \sim 0.6 \times \frac{2}{3} \times 10 \times 0.04 \sim 0.16$.

(The contamination to the $K^-\mu^+\nu$ signal due to the $K^{*-} \to \overline{K}^0\pi^-$ channel is negligible, because of the two-body mass cut efficiency and the π/K misidentification probability).

- $\underline{D^{*+} \to D^0\pi^+,\ D^0 \to K^-\mu^+\nu}$

The major source of background to the $\pi^-\mu^+\nu$ signal is given by the $D^{*+} \to D^0\tilde{\pi}^+,\ D^0 \to K^-\mu^+\nu$ decay, where the daughter K^- is misidentified by the Čerenkov counters as a π^-. In Figure 4.3.3 (b) we compare the Monte Carlo generated two-body invariant mass for the $\pi^-\mu^+\nu$ and misidentified $K^-\mu^+\nu$ decays. It can be seen that the two distributions are nearly identical, making it impossible to separate the two decays by means of an invariant mass cut (except in the very high mass region $M(\pi^-\mu^+) > 1.5\ GeV/c^2$). Also the final $M(D^{*+}) - M(D^0)$ mass difference distribution for misidentified $D^{*+} \to D^0\tilde{\pi}^+,\ D^0 \to K^-\mu^+\nu$ events is almost identical to the $D^{*+} \to D^0\tilde{\pi}^+,\ D^0 \to \pi^-\mu^+\nu$ distribution (see Figure 4.3.2 (c) and (d)).

The level of contamination to the $\pi^-\mu^+\nu$ signal depends on the total number of $D^{*+} \rightarrow D^0\tilde{\pi}^+,\ D^0 \rightarrow K^-\mu^+\nu$ decays generated in the experiment and the relative efficiency for reconstructing the two channels, which is dominated by the K/π misidentification probability. Roughly we estimate: $\frac{Y(K^-\mu^+\nu,\ K^-msd)}{Y(\pi^-\mu^+\nu)} = \frac{BR(D^0\rightarrow K^-\mu^+\nu)}{BR(D^0\rightarrow \pi^-\mu^+\nu)} \times \frac{\epsilon(K^-\mu^+\nu,\ K^-msd)}{\epsilon(\pi^-\mu^+\nu)} \sim 10 \times 0.05 \sim 0.5$, i.e. one out of three events in the $\pi^-\mu^+\nu$ signal is a misidentified $K^-\mu^+\nu$ event!

- $\underline{D^{*+} \rightarrow D^0\pi^+,\ D^0 \rightarrow \varrho^-\mu^+\nu,\ \varrho^- \rightarrow \pi^-\pi^0}$

The $D^0 \rightarrow \varrho^-\mu^+\nu,\ \varrho^- \rightarrow \pi^-\pi^0$ decay is another possible source of contamination for the $\pi^-\mu^+\nu$ signal, since the π^0 is not reconstructed. A priori we may expect this channel to have a branching ratio of the same order of magnitude of the $\pi^-\mu^+\nu$ decay, since both decays are Cabibbo suppressed and involve similar final states (the only difference being that the $\varrho^-\mu^+\nu$ decay requires the creation of an additional $u\overline{u}$ or $d\overline{d}$ pair from the quark sea).

The only tool we have to distinguish between the two channels is the hadron-lepton invariant mass, which for the $\varrho^-\mu^+\nu$ decay is shifted towards lower values than for $\pi^-\mu^+\nu$ (see Figure 4.3.3 (d)). With the mass cut used in this analysis, $M(\pi^-\mu^+) > 1.1\ GeV/c^2$, the reconstruction efficiency for $\varrho^-\mu^+\nu$ is about five times smaller than for $\pi^-\mu^+\nu$. If the mass cut is increased, the ratio of the two efficiencies becomes increasingly smaller, until the possible $\varrho^-\mu^+\nu$ contamination can be neglected (see Table 4.3.2). In section § 4.5.3 we will show that the measured branching ratio $\frac{BR(D^0\rightarrow \pi^-\mu^+\nu)}{BR(D^0\rightarrow K^-\mu^+\nu)}$ remains stable when the mass cut is increased (see Figure 4.5.3), indicating that the $\varrho^-\mu^+\nu$ contamination is not large.

We obtain a rough estimate of the $\varrho^-\mu^+\nu$ contamination by using the E653 result $\frac{BR(D^+\rightarrow \varrho^0\mu^+\nu)}{BR(D^+\rightarrow \overline{K}^{*0}\mu^+\nu)} = 0.044^{+0.031}_{-0.025} \pm 0.014$[32]. Because of isospin con-

Table 4.3.2 Increasing mass cut for $\pi^-\mu^+\nu$ and $\varrho^-\mu^+\nu$

Mass cut (GeV/c^2)	$\epsilon(\varrho^-\mu^+\nu)$	$\epsilon(\pi^-\mu^+\nu)$	$\frac{\epsilon(\varrho^-\mu^+\nu)}{\epsilon(\pi^-\mu^+\nu)}$
1.1	9.8 %	50.6 %	19.4 %
1.2	5.6 %	39.0 %	14.3 %
1.3	2.6 %	27.9 %	9.3 %
1.4	0.9 %	19.0 %	4.7 %
1.5	0.2 %	10.0 %	2.0 %

siderations, we can assume $\frac{BR(D^0\to\varrho^-\mu^+\nu)}{BR(D^0\to K^{*-}\mu^+\nu)} \sim 2\times \frac{BR(D^+\to\varrho^0\mu^+\nu)}{BR(D^+\to\overline{K}^{*0}\mu^+\nu)} \sim 0.088$. The amount of $\varrho^-\mu^+\nu$ contamination is then $\frac{Y(\varrho^-\mu^+\nu)}{Y(\pi^-\mu^+\nu)} = \frac{BR(D^0\to\varrho^-\mu^+\nu)}{BR(D^0\to K^{*-}\mu^+\nu)} \times\frac{BR(D^0\to K^{*-}\mu^+\nu)}{BR(D^0\to K^-\mu^+\nu)} \times\frac{BR(D^0\to K^-\mu^+\nu)}{BR(D^0\to\pi^-\mu^+\nu)} \times\frac{\epsilon(D^0\to\varrho^-\mu^+\nu)}{\epsilon(D^0\to\pi^-\mu^+\nu)} \sim 0.088\times 0.6\times 10\times 0.20 \sim 0.1$.

4.3.2 Misidentified D^0 tag hadronic decays

D^0 (tag) hadronic decays may contaminate the $K^-\mu^+\nu$ or $\pi^-\mu^+\nu$ signals if one of the daughter hadrons is misidentified as a muon. For example, three D^0 decays with large branching fraction (compared to $D^0 \to K^-\mu^+\nu$, for which BR=$3.2\pm 0.4\%$[33]) are:

- $D^0 \to K^-\pi^+$ (BR = $4.01\pm 0.14\%$[33])
- $D^0 \to K^-\pi^+\pi^0$ (BR = $13.8\pm 1.0\%$[33])
- $D^0 \to K^-\pi^+\pi^0\pi^0$ (BR = $15\pm 5\%$[33]).

All these decays can contaminate the RS $K^-\mu^+\nu$ mass distributions if the π^+ is misidentified as a μ^+. The corresponding misidentified two-body invariant mass distributions are shown in Figure 4.3.4 . It can be seen that our mass cut $0.95\ GeV/c^2 < M(K^-\mu^+) < 1.85\ GeV/c^2$ strongly reduces contamination from the $K^-\pi^+$ decay, but it does not reduce significantly the $K^-\pi^+\pi^0$ and

$K^-\pi^+\pi^0\pi^0$ channels. In the case of the $\pi^-\mu^+\nu$ signal, these decays contaminate mostly the WS distributions (if the K^- is misidentified for a μ^-), and only at lower order the RS distributions (if the K^- is taken for a π^- and the π^+ for a μ^+).

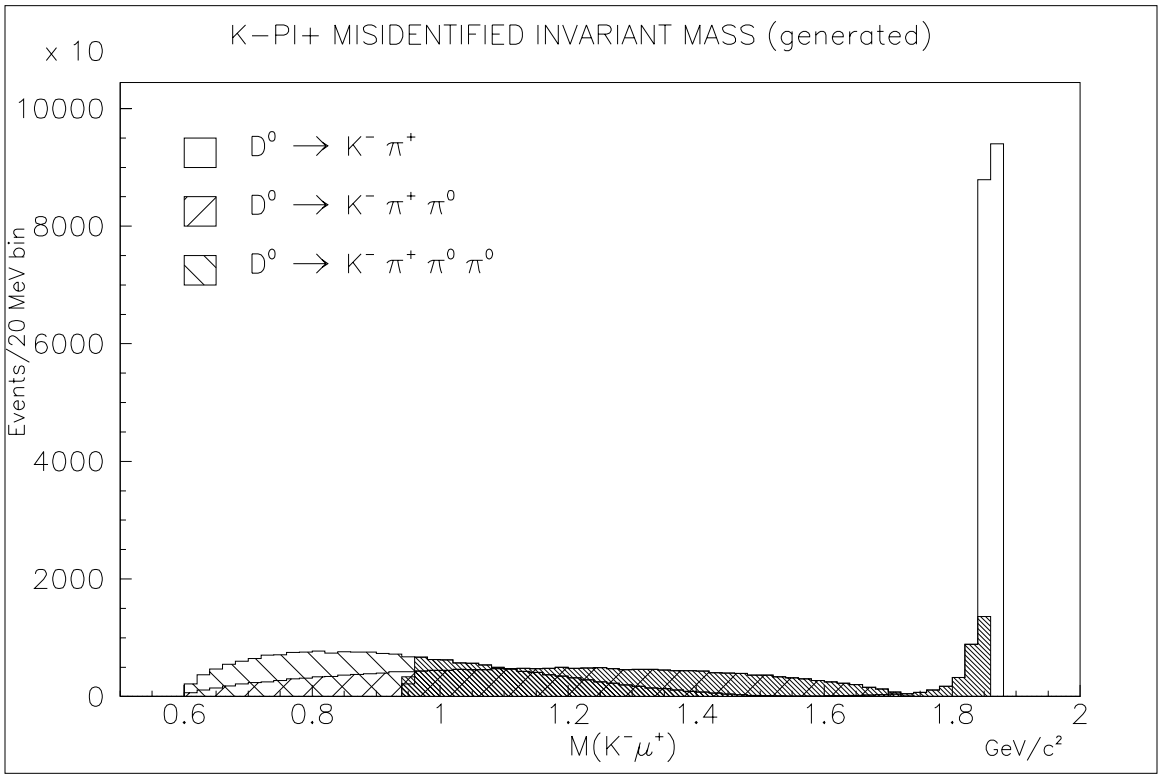

Figure 4.3.4 Monte Carlo generated two-body invariant mass from various D^0 tag decays, where in every case the daughter π^+ is misidentified as μ^+. The shaded region indicates the portion of phase space which lies inside our invariant mass cut $0.95\ GeV/c^2 < M(K^-\mu^+) < 1.85\ GeV/c^2$.

The total amount of background from hadron/muon misidentification affecting the data signal is estimated as follows. We run the analysis algorithm used to reconstruct the $K^-\mu^+\nu$ and $\pi^-\mu^+\nu$ signals on a subset of our data sample (about 10%), but instead of requiring a $h^-\mu^+$ secondary vertex, we require that the track companion of the h^- *be not* identified as a μ^+. In this way

we obtain an estimate of the background from hadronic decays if no muon identification was used. We then weight each event by the momentum-dependent probability of misidentifying the hadron for a muon (see Figure 3.7.4), separately for the 1990 and 1991 runs and for the bad and good run periods. Finally, we boost the background contamination obtained from the data subset to simulate the contamination level from the whole data set. The boost factor is calculated as the ratio of the $D^{*+} \rightarrow D^0\tilde{\pi}^+$, $D^0 \rightarrow K^-\pi^+$ yield reconstructed from the whole data set to that from the data subset. The final distributions obtained for the hadron misidentification background are shown in Figures 4.3.5. These background distributions are considered a *fixed* component in the fit of the $K^-\mu^+\nu$ and $\pi^-\mu^+\nu$ data signals.

4.3.3 Non-tag semileptonic decays

The last source of background to consider consists of random combinatoric, for example originating from non-tag semileptonic decays such as:

- $D^+ \rightarrow \overline{K}^{*0}\mu^+\nu$,
- $D^+ \rightarrow \varrho^0\mu^+\nu$,
- $D_s^+ \rightarrow \phi\mu^+\nu$,

etc. If some of the decay prongs are not reconstructed or are misidentified, and a random pion in the event is mistakenly assigned to the primary vertex, these decays can contaminate the data signals. In order to simulate this kind of background, we run our analysis algorithm on *non-tag* $D^0 \rightarrow K^-\mu^+\nu$ and $D^0 \rightarrow \pi^-\mu^+\nu$ Monte Carlo samples, and fit the produced $M(D^{*+}) - M(D^0)$ mass distributions with a third degree polynomial (see Figure 4.3.6). The polynomial shape is then introduced in the fit of the data signals with a variable amplitude.

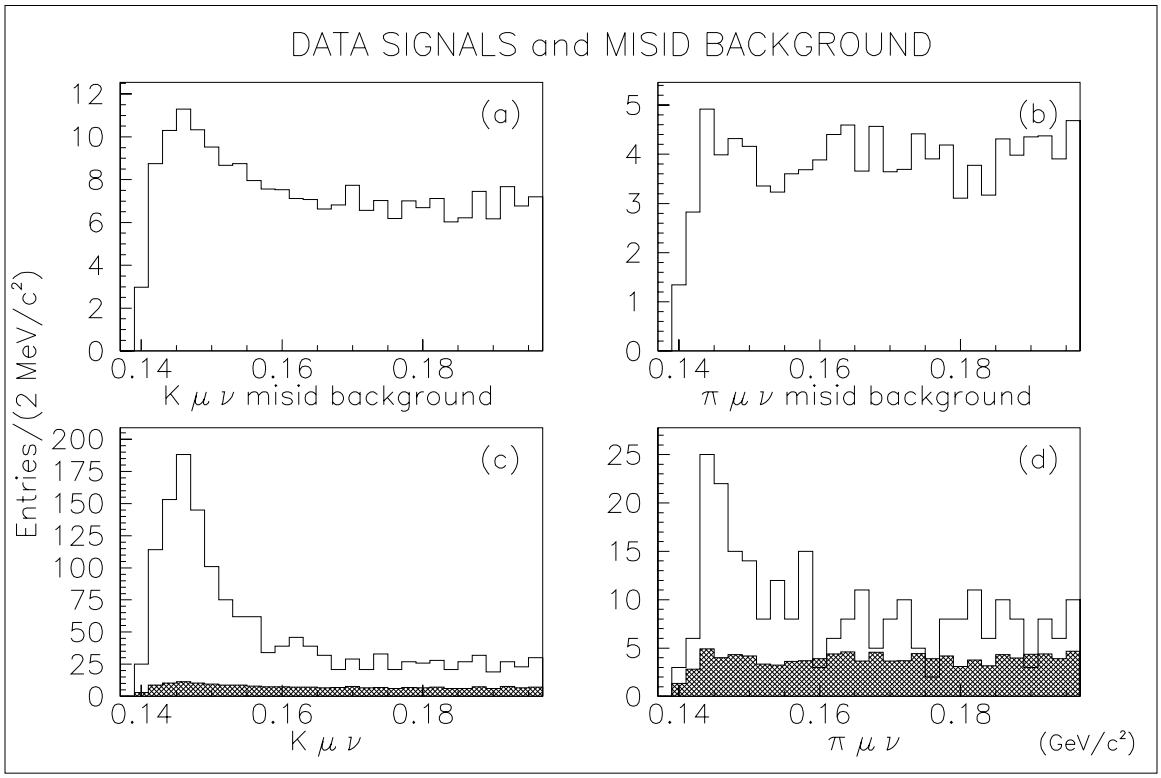

Figure 4.3.5 Estimated background due to hadronic misidentification affecting the $K^-\mu^+\nu$ (a) and $\pi^-\mu^+\nu$ (b) signals. The peak at low mass in the $K^-\mu^+\nu$ plot is due to misidentified $K^-\pi^+$, $K^-\pi^+\pi^0$ and $K^-\pi^+\pi^0\pi^0$ tag events. In Figures (c) and (d) the misidentification background is overlaid on the data signals.

4.4 The fit

4.4.1 Fitting technique

To fit the data histograms and to extract the amount of $D^0 \to K^-\mu^+\nu$ and $D^0 \to \pi^-\mu^+\nu$ signal present, we use a *binned maximum likelihood* technique. For either the $K^-\mu^+\nu$ or $\pi^-\mu^+\nu$ histogram, the likelihood is constructed as:

$$\mathcal{L} = \prod_{i=1}^{\#\text{bins}} \frac{n_i^{s_i} e^{-n_i}}{s_i!},$$

where:

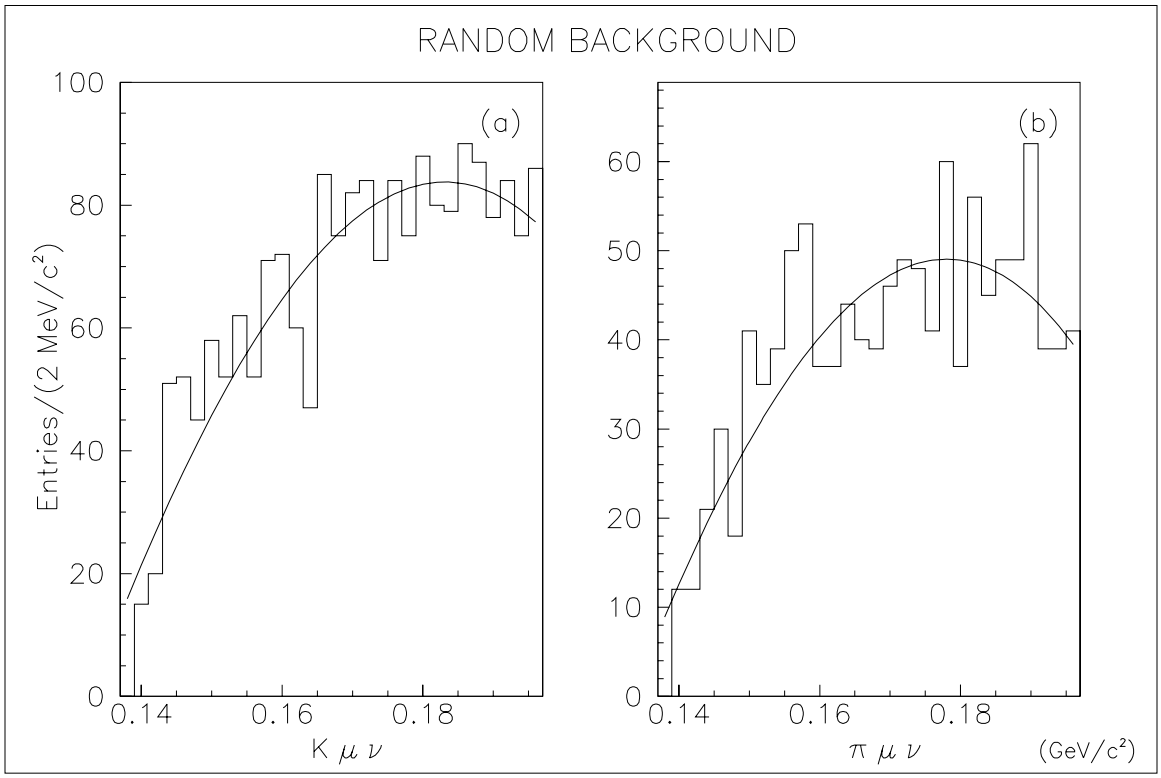

Figure 4.3.6 Shapes for random combinatoric background, obtained by fitting with a third degree polynomial the mass difference distributions $M(D^{*+}) - M(D^0)$ originating from *non-tag* $D^0 \to K^-\mu^+\nu$ and $D^0 \to \pi^-\mu^+\nu$ decays.

s_i = number of events in bin i of data histogram;

n_i = number of events in bin i of fit histogram.

The likelihood is the product over all bins of the Poisson probabilities of observing s_i entries in bin i when the expected number of entries is n_i.

The fit histogram is constructed using our knowledge of the decay processes involved: the shape of the $K^-\mu^+\nu$ or $\pi^-\mu^+\nu$ signals from Monte Carlo, the shape and level of the D^0-tag charm background known to contaminate the signal, and the shape of the non-tag charm background producing random combinatoric.

4.4.2 The $K^-\mu^+\nu$ fit histogram

The $D^{*+} \to D^0\tilde{\pi}^+$, $D^0 \to K^-\mu^+\nu$ fit histogram is composed of the following components:

1. the $D^{*+} \to D^0\tilde{\pi}^+$, $D^0 \to K^-\mu^+\nu$ signal, with the shape fixed by the Monte Carlo and yield which is a parameter of the fit;
2. the $D^{*+} \to D^0\tilde{\pi}^+$, $D^0 \to K^{*-}\mu^+\nu$, $K^{*-} \to K^-\pi^0$ background, with the shape fixed by its own Monte Carlo and with the relative yield to the $K^-\mu^+\nu$ signal known;
3. the background coming from hadron misidentification, whose shape and level have been previously estimated and are assumed fixed in the fit;
4. the background coming from random combinatoric, with the shape given by the fit to the $D^0 \to K^-\mu^+\nu$ non-tag Monte Carlo and with the level allowed to fluctuate.

The number of entries in bin i of the fit histogram is constructed as:

$$\begin{aligned} n_i &= Y_{k\mu\nu} S_{1i} + Y_{k^*\mu\nu}\ \alpha\ S_{2i} + \boldsymbol{\mathcal{M}} S_{3i} + \boldsymbol{\mathcal{X}} S_{4i} \\ &= Y_{k\mu\nu}\left[\ S_{1i} + \frac{\epsilon(K^*\mu\nu, K^* \to K^-\pi^0)}{\epsilon(K\mu\nu)}\ \alpha\boldsymbol{\mathcal{A}}\ S_{2i}\right] + \boldsymbol{\mathcal{M}} S_{3i} + \boldsymbol{\mathcal{X}} S_{4i} \end{aligned}$$

where:

Y denotes a yield;

ϵ denotes an efficiency;

S_{ji} is the fraction of Monte Carlo events in bin i for the j decay (for each fixed j: $\sum_{i=1}^{\#\text{bins}} S_{ji} = 1$);

$\alpha = BR\ (K^{*-} \to K^-\pi^0) = \frac{1}{3}$;

$\boldsymbol{\mathcal{A}} = \frac{BR\ (D^0 \to K^{*-}\mu^+\nu)}{BR\ (D^0 \to K^-\mu^+\nu)}$;

$\mathcal{M}$ = Number of $K^-\mu^+\nu$ background events from μ misidentification;

$\mathcal{X}$ = Number of $K^-\mu^+\nu$ random combinatoric background events.

4.4.3 The $\pi^-\mu^+\nu$ fit histogram

The $D^{*+} \to D^0\tilde{\pi}^+$, $D^0 \to \pi^-\mu^+\nu$ fit histogram is composed of the following components:

5. the $D^{*+} \to D^0\tilde{\pi}^+$, $D^0 \to \pi^-\mu^+\nu$ signal, with the shape fixed by the Monte Carlo and with the yield determined by the fit;
6. the $D^{*+} \to D^0\tilde{\pi}^+$, $D^0 \to K^-\mu^+\nu$ feedthrough due to K/π misidentification, with the shape fixed by the Monte Carlo and with the yield given by the fitted yield for the $K^-\mu^+\nu$ signal and the efficiency for reconstructing $K^-\mu^+\nu$ as $\pi^-\mu^+\nu$;
7. the $D^{*+} \to D^0\tilde{\pi}^+$, $D^0 \to K^{*-}\mu^+\nu$, $K^{*-} \to K^-\pi^0$ background, whose the shape is given by the Monte Carlo and with the yield fixed by the $K^-\mu^+\nu$ fitted yield and the corresponding reconstruction efficiencies;
8. the $D^{*+} \to D^0\tilde{\pi}^+$, $D^0 \to K^{*-}\mu^+\nu$, $K^{*-} \to \overline{K}^0\pi^-$ background, with the shape and yield determined as in the $K^{*-} \to K^-\pi^0$ case;
9. the $\varrho^-\mu^+\nu$ background, with the shape fixed by the Monte Carlo and with the yield which ultimately depends on the $K^-\mu^+\nu$ signal;
10. the hadron/muon misidentification background, with the shape and level fixed;
11. the random combinatoric background, with the shape fixed to the polynomial fit and variable amplitude.

The number of entries in bin i of the fit histogram is constructed as:

$$
\begin{aligned}
n_i &= Y_{\pi\mu\nu}\ S_{5i} + \frac{Y_{k\mu\nu}}{\epsilon(K\mu\nu)}\ \epsilon(K\mu\nu \to \pi\mu\nu)\ S_{6i} \\
&+ Y_{k^*\mu\nu}\ \alpha\ \epsilon(K^{*-}\mu\nu, K^{*-} \to K^-\pi^0)\ S_{7i} \\
&+ Y_{k^*\mu\nu}\ \beta\ \epsilon(K^{*-}\mu\nu, K^{*-} \to \overline{K}^0\pi^-)\ S_{8i} \\
&+ Y_{\varrho\mu\nu}\ \epsilon(\varrho^-\mu^+\nu)\ S_{11i}\ + \boldsymbol{\mathcal{M}}'\ S_{9i} + \ \boldsymbol{\mathcal{X}}'\ S_{10i} \\
&= Y_{\pi\mu\nu}\ S_{5i} + \ \frac{Y_{k\mu\nu}}{\epsilon(K\mu\nu)} \times \Bigg[\ \epsilon(K\mu\nu \to \pi\mu\nu)\ S_{6i} \\
&+ \ \frac{1}{5}\ \epsilon(K^{*-}\mu\nu, K^{*-} \to K^-\pi^0)\ S_{7i} + \ \frac{2}{5}\ \epsilon(K^{*-}\mu\nu, K^{*-} \to \overline{K}^0\pi^-)\ S_{8i} \\
&+ \ \boldsymbol{\mathcal{A}}\,\boldsymbol{\mathcal{B}}\ \epsilon(D^0 \to \varrho^-\mu^+\nu)\ S_{9i}\ \Bigg] + \boldsymbol{\mathcal{M}}'\ S_{10i} + \ \boldsymbol{\mathcal{X}}'\ S_{11i}
\end{aligned}
,
$$

where:

$\beta = BR\ (K^{*-} \to \overline{K}^0\pi^-) = \frac{2}{3}$;

$\boldsymbol{\mathcal{B}} = \frac{BR(D^0 \to \varrho^-\mu^+\nu)}{BR(D^0 \to K^{*-}\mu^+\nu)} \equiv 2 \times \frac{BR(D^+ \to \varrho^0\mu^+\nu)}{BR(D^+ \to \overline{K}^{*0}\mu^+\nu)}$;

$\boldsymbol{\mathcal{M}}' =$ Number of $\pi^-\mu^+\nu$ background events from μ misidentification;

$\boldsymbol{\mathcal{X}}' =$ Number of $\pi^-\mu^+\nu$ random combinatoric background events.

4.4.4 Fit results

We construct separate likelihoods for the $K^-\mu^+\nu$ and $\pi^-\mu^+\nu$ data histograms, then maximize the combined quantity:

$$
\boldsymbol{\mathcal{L}} = \boldsymbol{\mathcal{L}}_{k\mu\nu} \times \boldsymbol{\mathcal{L}}_{\pi\mu\nu} \times exp\left\{-\frac{1}{2}\left[\frac{\boldsymbol{\mathcal{A}} - A_0}{\sigma_{A_0}}\right]^2\right\} \times exp\left\{-\frac{1}{2}\left[\frac{\boldsymbol{\mathcal{B}} - B_0}{\sigma_{B_0}}\right]^2\right\}
$$

(or rather we minimize the negative logarithm of the likelihood). The Gaussian terms have been added to the likelihood to let the two ratios $\boldsymbol{\mathcal{A}} = \frac{BR\ (D^0 \to K^{*-}\mu^+\nu)}{BR\ (D^0 \to K^-\mu^+\nu)}$, $\boldsymbol{\mathcal{B}} = \frac{BR(D^0 \to \varrho^-\mu^+\nu)}{BR(D^0 \to K^{*-}\mu^+\nu)}$ fluctuate within their error around their measured value $A_0 = 0.60 \pm 0.06$[29] [30] [31] and $B_0 = 0.088 \pm 0.056$[32],

respectively. The final likelihood $\mathcal{L}$ depends on six unknown quantities, which are assumed as parameters of the fit: $Y_{k\mu\nu}$, $Y_{\pi\mu\nu}$, $\mathcal{X}$, $\mathcal{X}'$, $\mathcal{A}$ and $\mathcal{B}$ ($\mathcal{M}$ and $\mathcal{M}'$ are fixed). With our technique, we fit *simultaneously* for the $D^0 \to K^-\mu^+\nu$ and $D^0 \to \pi^-\mu^+\nu$ yields.

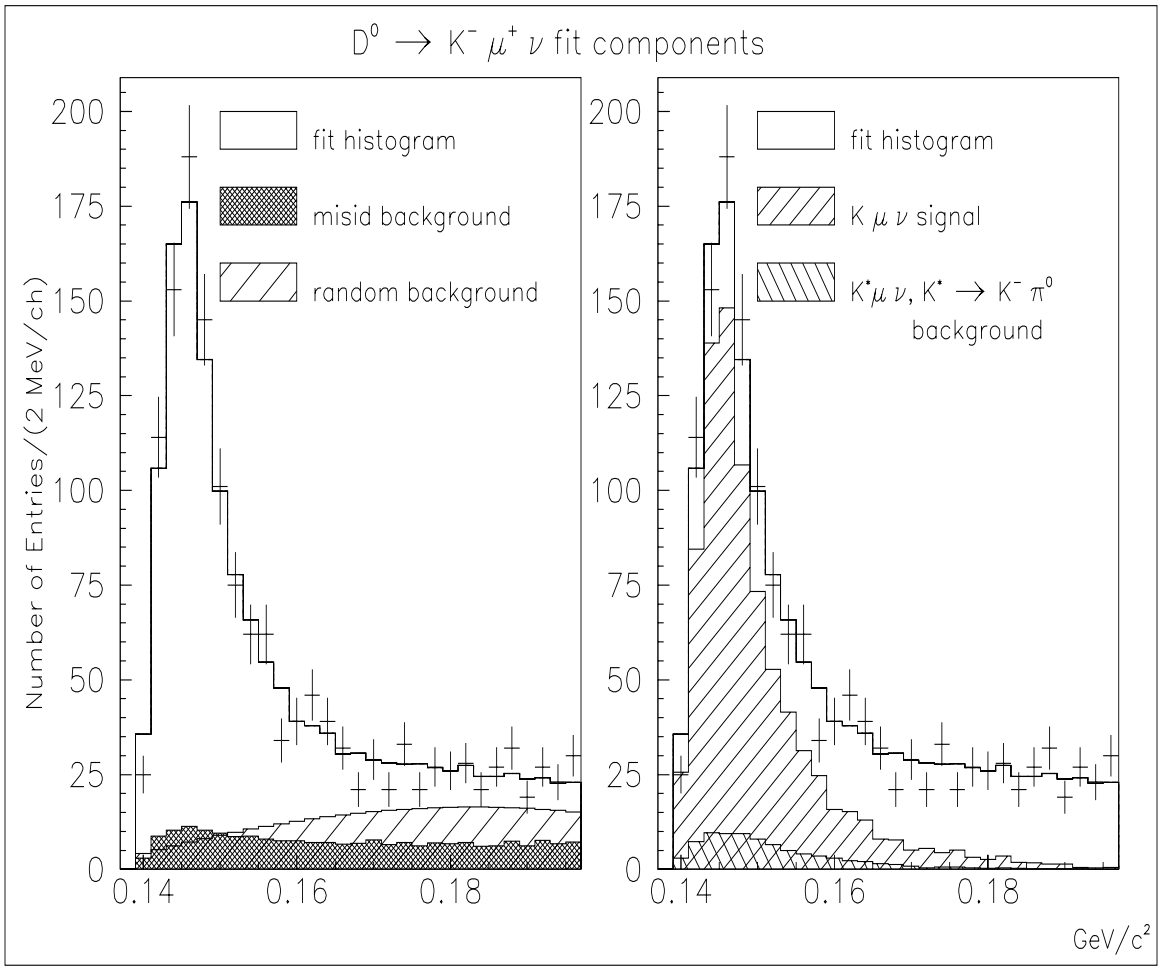

Figure 4.4.1 Components of the $K^-\mu^+\nu$ fit. Data points are indicated by crosses, the fit by a solid line. The various backgrounds components are shown in two plots for easier presentation.

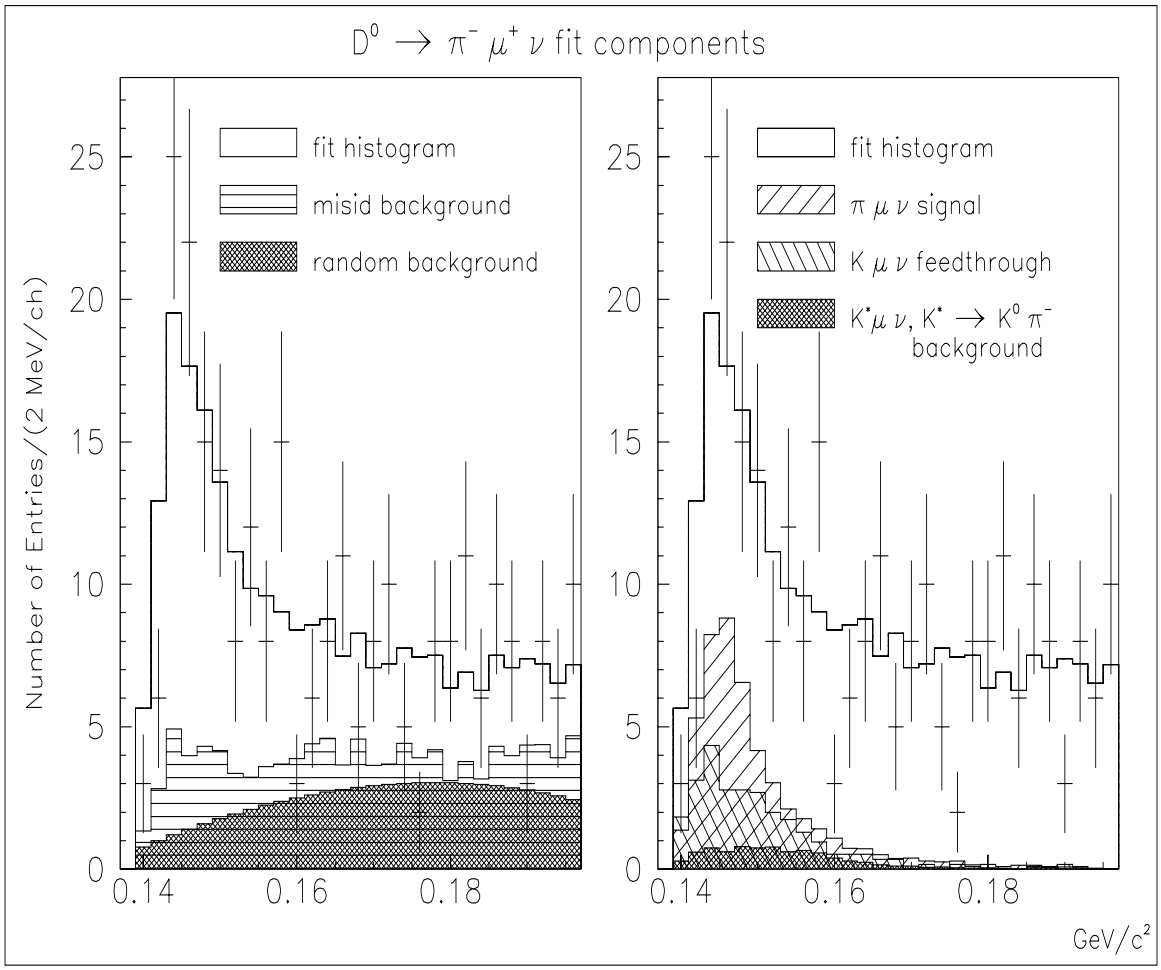

Figure 4.4.2 Components of the $\pi^-\mu^+\nu$ fit. Data points are indicated by crosses, the fit by a solid line. The various backgrounds components are shown in two plots for easier presentation.

The experimental conditions changed between the 1990 and the 1991 runs. The Inner Muon detector was modified to allow the delivery of the beam to the E683 experimental area, and changes in the Čerenkov system resulted in a different K/π misidentification probability. To account for these changes, we fit the 1990 and 1991 data sets separately, then we combine the results treating them independently.

For the $K^-\mu^+\nu$ signal, we find 416.2±23.6 events in 1990 and 408.3±23.0 in 1991, for a total of $Y_{k\mu\nu} = 824.5 \pm 33.0$ (after the backgrounds have been subtracted). The contamination to the signal due to the $D^+ \to \overline{K}^{*0}\mu^+\nu$, $K^{*-} \to K^-\pi^0$ decay is found to be 9.6%. The various components of the $K^-\mu^+\nu$ fit are shown in Figure 4.4.1.

For the $\pi^-\mu^+\nu$ signal, we find 22.7 ± 8.9 events in 1990 and 23.0 ± 7.9 events in 1991, for a combined yield of $Y_{\pi\mu\nu} = 45.6 \pm 11.8$ (after background subtraction). The statistical significance of the signal is $Y_{\pi\mu\nu}/\delta Y = 3.9$. Contamination due to other decays is estimated to be 58.3% from $K^-\mu^+\nu$ feedthrough, 17.9% from $K^{*-}\mu^+\nu$, $K^{*-} \to \overline{K}^0\pi^-$, 1.2% from $K^{*-}\mu^+\nu$, $K^{*-} \to K^-\pi^0$, and 11.4% from $\varrho^-\mu^+\nu$. The components of the $\pi^-\mu^+\nu$ fit are shown in Figure 4.4.2. The fitted yields for the $K^-\mu^+\nu$ and $\pi^-\mu^+\nu$ histograms are summarized in Table 4.4.1. The values returned by the fit for the two branching ratios A, B are listed in Table 4.4.2.

Table 4.4.1 Fitted yields for D^0 decays

Decay	1990	1991	90+91
$K^-\mu^+\nu$	416.2 ± 23.6	408.3 ± 23.0	824.5 ± 33.0
$K^{*-}\mu^+\nu$, $K^{*-} \to K^-\pi^0$	40.0 ± 4.7	39.6 ± 4.6	79.6 ± 6.6
$\pi^-\mu^+\nu$	22.7 ± 8.9	23.0 ± 7.9	45.6 ± 11.8
$K^-\mu^+\nu$, K^- misid as π^-	13.6 ± 1.3	13.0 ± 1.4	26.6 ± 1.9
$K^{*-}\mu^+\nu$, $K^{*-} \to \overline{K}^0\pi^-$	4.1 ± 0.6	4.1 ± 0.6	8.2 ± 0.8
$K^{*-}\mu^+\nu$, $K^{*-} \to K^-\pi^0$, K^- misid as π^-	0.3 ± 0.1	0.3 ± 0.1	0.5 ± 0.1
$\varrho^-\mu^+\nu$	2.6 ± 1.8	2.5 ± 1.7	5.2 ± 2.4

Table 4.4.2 Other fit parameters

fit parameter	1990	1991
$\mathcal{A} = \frac{BR\ (D^0 \to K^{*-}\mu^+\nu)}{BR\ (D^0 \to K^-\mu^+\nu)}$	0.595 ± 0.060	0.600 ± 0.059
$\mathcal{B} = \frac{BR(D^0 \to \varrho^-\mu^+\nu)}{BR(D^0 \to K^{*-}\mu^+\nu)}$	0.085 ± 0.056	0.088 ± 0.057

4.5 Branching ratio measurement

The branching ratio of the $D^0 \to \pi^-\mu^+\nu$ decay relative to the $D^0 \to K^-\mu^+\nu$ decay is computed by use of the fitted yields and the reconstruction efficiencies for the two channels:

$$\frac{BR\ (D^0 \to \pi^-\mu^+\nu)}{BR\ (D^0 \to K^-\mu^+\nu)} = \frac{Y_{\pi\mu\nu}/\epsilon(\pi\mu\nu)}{Y_{k\mu\nu}/\epsilon(K\mu\nu)}$$

The branching ratios for the 1990 and 1991 runs are computed separately (see Table 4.5.1); then the two results are combined using a weighted average. The combined result is:

$$\frac{BR\ (D^0 \to \pi^-\mu^+\nu)}{BR\ (D^0 \to K^-\mu^+\nu)} = 0.0953 \pm 0.0251\ .$$

The statistical error in the quoted result includes the effect of correlation between the two parameters of the fit $Y_{\pi\mu\nu}$ and $Y_{k\mu\nu}$ (about $\sim 6.0\%$), the uncertainty due to the finite size of the Monte Carlo samples produced (about $\sim 2\%$), and the statistical uncertainty in the assumed values $A_0 = 0.60 \pm 0.06$ (about 0.1%) and $B_0 = 0.088 \pm 0.056$ (about 6%). All these contributions are small compared to the statistical error associated with the $\pi^-\mu^+\nu$ yield, which for either the 1990 or 1991 sample is $\sim 36\%$. The large error in the assumed value for B_0 does not significantly affect our measurement because

the $\varrho^-\mu^+\nu$ efficiency is much smaller than the $\pi^-\mu^+\nu$ efficiency, limiting the $\varrho^-\mu^+\nu$ contamination. The uncertainty in the assumed value for A_0 causes a negligible effect, because the $K^{*-}\mu^+\nu$ contamination is about $\sim 10\%$ for the $K^-\mu^+\nu$ channel and $\sim 15\%$ for the $\pi^-\mu^+\nu$ channel, and both corrections go in the same direction.

Table 4.5.1 1990 and 1991 measurements

Decay	1990 Yield	1990 Efficiency	1991 Yield	1991 Efficiency
$K^-\mu^+\nu$	416.2 ± 23.6	$1.412 \pm 0.019\%$	408.3 ± 23.0	$0.958 \pm 0.015\%$
$\pi^-\mu^+\nu$	22.7 ± 8.9	$0.821 \pm 0.014\%$	23.0 ± 7.9	$0.557 \pm 0.012\%$
$\frac{BR\ (D^0 \to \pi^-\mu^+\nu)}{BR\ (D^0 \to K^-\mu^+\nu)}$	0.0937 ± 0.0376		0.0967 ± 0.0338	

4.6 Systematic error on branching ratio measurement

We now present several studies designed to investigate possible systematic biases in our measurement of the branching ratio $B = \frac{BR\ (D^0 \to \pi^-\mu^+\nu)}{BR\ (D^0 \to K^-\mu^+\nu)}$. Since the two decays are topologically and kinematicaly very similar and the analysis cuts used are almost the same, we expect that most systematics will cancel out.

4.6.1 Split sample systematic error

To check for possible systematic errors associated with any of the cuts used in the analysis, we use the *split sample technique* described in the Appendix. For each analysis cut, we divide the total data sample into four statistically independent subsamples: events above or below a discriminating value of the analysis cut, and events belonging to the 1990 or 1991 run. For each cut, the discriminating value is chosen in such a way to split the total data

sample in approximately equal parts. The analysis cuts used for this study and the corresponding discriminating values are listed in Table 4.6.1.

Table 4.6.1 Split samples cuts

Variable	Cut value
L/σ_L	$L/\sigma_L < 15$; $L/\sigma_L > 15$
cls	$cls < 50\%$; $cls > 50\%$
$iso2$	$iso2 < 10^{-12}$; $iso2 > 10^{-12}$
$M(h^-\mu^+)$	$M(K^-\mu^+) < 1.30\ GeV/c^2$, $M(\pi^-\mu^+) < 1.35\ GeV/c^2$; $M(K^-\mu^+) > 1.30\ GeV/c^2$, $M(\pi^-\mu^+) > 1.35\ GeV/c^2$
$p(\tilde{\pi}^+)$	$p(\tilde{\pi}^+) < 8\ GeV/c$; $p(\tilde{\pi}^+) > 8\ GeV/c$
$p(h^-\mu^+)$	$p(h^-\mu^+) < 80\ GeV/c$; $p(h^-\mu^+) > 80\ GeV/c$
$p(h^-)$	$p(\pi^-) < 20\ GeV/c$, $p(K^-) < 35\ GeV/c$; $p(\pi^-) > 20\ GeV/c$, $p(K^-) > 35\ GeV/c$
$p(\mu^+)$	$p(\mu^+) < 45\ GeV/c$; $p(\mu^+) > 45\ GeV/c$

For each analysis cut, we compute the branching ratio for the four independent subsamples, and then we compare its variation to the standard deviation of the full data set measurement (see Figure 4.6.1). We find that the variation of the branching ratio over the split samples is always compatible with our statistical error. Therefore, we conclude that the systematic uncertainty associated with the analysis cuts is small.

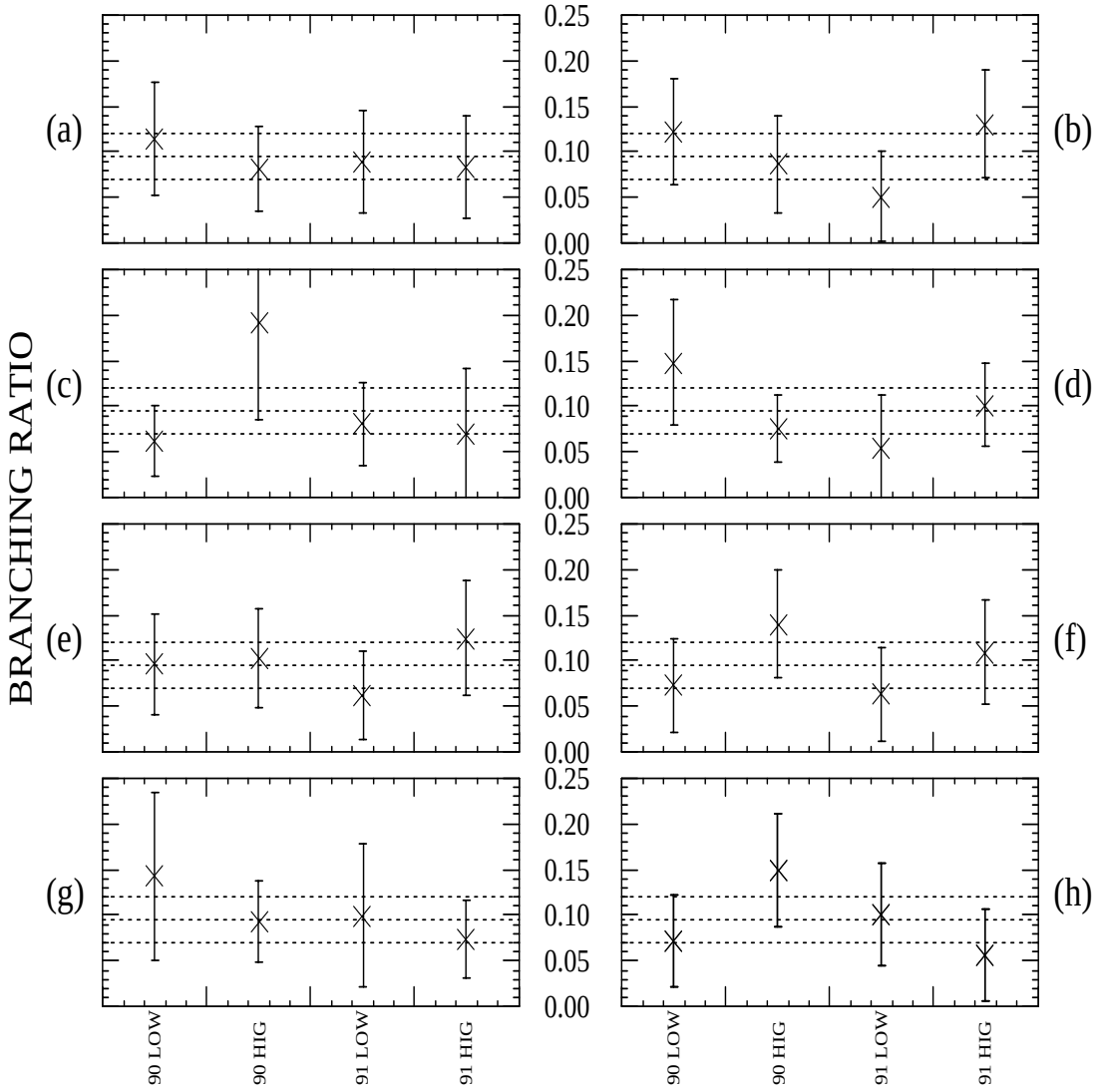

Figure 4.6.1 Branching ratios for various split samples:
(a) L/σ_L;
(b) secondary vertex confidence level cls;
(c) isolation of the secondary vertex $iso2$;
(d) hadron-lepton invariant mass $M(h^-\mu^+)$;
(e) soft pion momentum $p(\tilde{\pi}^+)$;
(f) total charged momentum $p(h^-\mu^+)$;
(g) daughter hadron momentum $p(h^-)$;
(h) daughter muon momentum $p(\mu^+)$.

4.6.2 Fit variants

In order to investigate possible biases in our fit to the experimental data, we use the technique described in the Appendix, and recompute the branching ratio by varying some of the significant parameters involved in the fitting process. For fit variants we considered the bin size of the $M(D^{*+}) - M(D^0)$ histograms, the mass range of the histograms used in the fit, and the functional form used to fit to the random combinatoric background (see Figure 4.3.6). The fit variants used, and the corresponding measured branching ratios, are listed in Table 4.6.2. We conservatively estimate that the systematic error associated with the fit process is:

$$\frac{\sigma_{B,fit}}{B} = \pm 4.7\% \ .$$

4.6.3 Hadron-lepton misidentification background

When performing the fit to the $\pi^-\mu^+\nu$ and $K^-\mu^+\nu$ signals, we *fix* the amount of background from hadrons misidentified as muons. The misidentification background is obtained by running the analysis program with *inverted* muon requirements on a subsample of the full data set, by weighting each event according to the momentum-dependent misidentification probability, and finally by boosting the amount of background by the scale factor obtained with the $D^0 \to K^-\pi^+$ yield estimator (see section § 4.3.2 for details). We checked the correctness of our estimate for the level of misidentification background in two different ways. First, we conservatively increased or decreased each point of the momentum-dependent misidentification probability within $\pm 1\sigma$ of its value. We found that the corresponding relative variation of the branching ratio is $\sigma_B/B = \pm 3.82\%$. Also, we varied within $\pm 1\sigma$ the value used for

Table 4.6.2 Fit variants

Fit variant	branching ratio (%)
none [$*$]	9.53 ± 2.51
mass range: $0.137 - 0.187\ GeV/c^2$	9.22 ± 2.72
mass range: $0.137 - 0.177\ GeV/c^2$	10.30 ± 2.85
bin size: $1\ (MeV/c^2)/ch$	9.50 ± 2.70
bin size: $3\ (MeV/c^2)/ch$	9.41 ± 2.69
bin size: $4\ (MeV/c^2)/ch$	8.74 ± 2.66
2nd degree polynomial	9.52 ± 2.56
4th degree polynomial	9.52 ± 2.72
data shape (no fit)	8.87 ± 2.72

[$*$] The standard fit conditions are: $2\ (MeV/c^2)/ch$ bin size, $0.137 - 0.197\ GeV/c^2$ mass range, third degree polynomial used to fit the random combinatoric background.

the $D^0 \rightarrow K^-\pi^+$ scale factor, and found that the branching ratio is affected by $\sigma_B/B = \pm 2.58\%$. Combining the two errors in quadrature, we conservatively estimate the systematic uncertainty associated with the level of hadronic misidentification background to be:

$$\frac{\sigma_{B,misid}}{B} = \pm 4.6\%.$$

4.6.4 Particle identification

We do not expect any systematic bias in the Čerenkov identification of the soft pion produced in the $D^{*+} \to D^0\tilde{\pi}^+$ decay, since the same criteria are used for the $K^-\mu^+\nu$ and $\pi^-\mu^+\nu$ channels, and the momentum spectrum of the soft pion does not depend on the subsequent D^0 decay (see Figure 4.6.2).

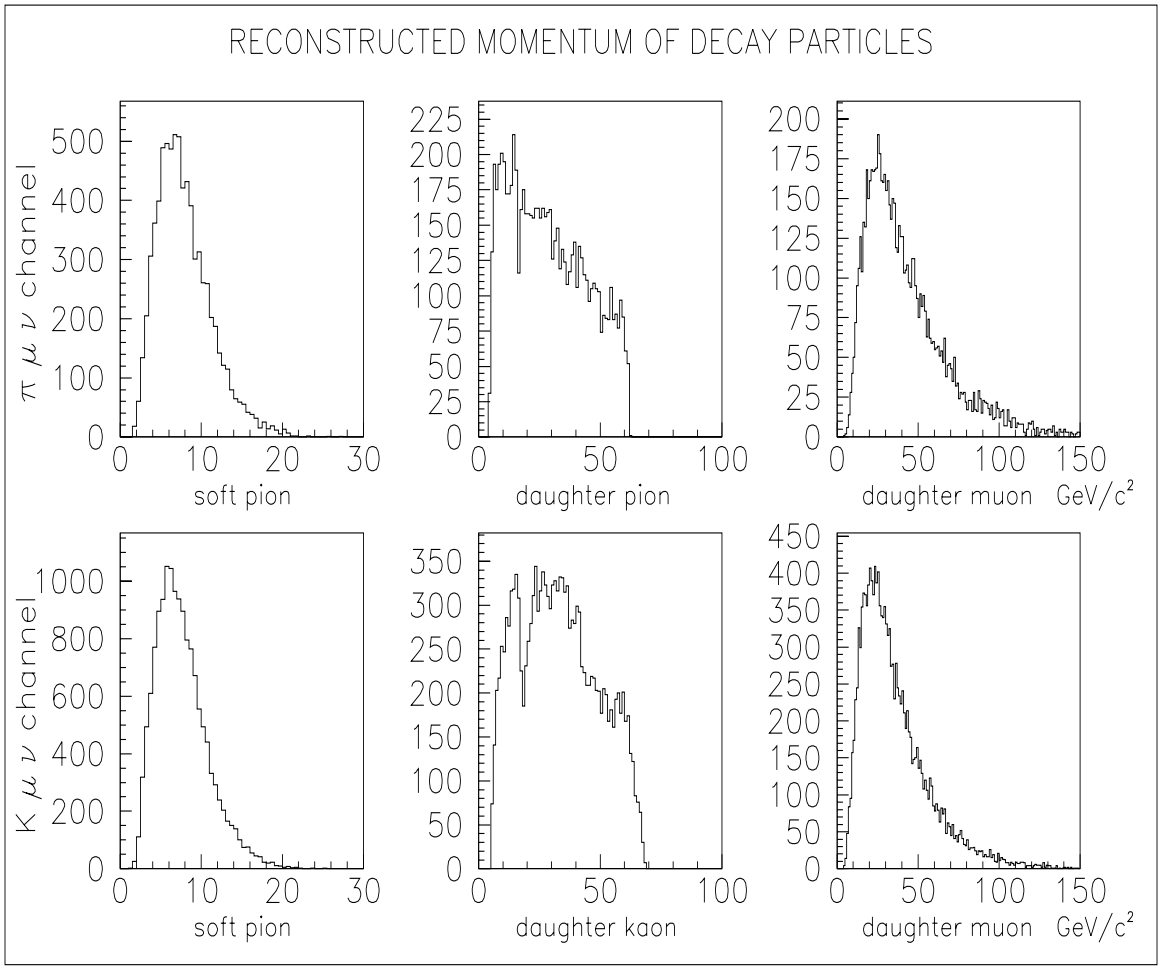

Figure 4.6.2 Monte Carlo reconstructed momentum for the decay prongs from $D^{*+} \to D^0\tilde{\pi}^+$, $D^0 \to K^-\mu^+\nu$ and $D^{*+} \to D^0\tilde{\pi}^+$, $D^0 \to \pi^-\mu^+\nu$. The daughter hadron distributions (π or K) are limited by the Čerenkov requirements.

No systematic variation is expected from muon identification, since the same requirements are applied to the daughter muon from both channels, and the two channels are kinematicaly very similar.

As for the Čerenkov identification of the daughter hadron (K or π, the only particle being different between the two decays), we conservatively quote a systematic error of:

$$\frac{\sigma_{B,cer}}{B} = \pm 2.5\%$$

associated with our Monte Carlo simulation of the Čerenkov detectors[34].

4.6.5 $D^0 \to \varrho^- \mu^+ \nu$ background

As discussed previously, the $\varrho^- \mu^+ \nu$ contamination to the $\pi^- \mu^+ \nu$ signal is estimated in the fit using the E653 result $\frac{BR(D^+ \to \varrho^0 \mu^+ \nu)}{BR(D^+ \to \overline{K}^{*0} \mu^+ \nu)} = 0.044^{+0.031}_{-0.025} \pm 0.014$[32]. Because of the large uncertainty of this measurement, it is useful to check that this source of background is not greatly underestimated (or overestimated).

We can do so by varying the two-body mass cut used to select the $D^0 \to \pi^- \mu^+ \nu$ signal, since the $M(\pi\mu)$ invariant mass distributions for the two decays $D^0 \to \pi^- \mu^+ \nu$ and $D^+ \to \varrho^0 \mu^+ \nu$ are significantly different (see Figure 4.3.3 (d)). Because the $M(\pi\mu)$ mass distribution drops off faster for $D^+ \to \varrho^0 \mu^+ \nu$ than for $D^0 \to \pi^- \mu^+ \nu$, if there was a large unaccounted $\varrho^- \mu^+ \nu$ contamination in our signal, we would expect the $\frac{BR(D^0 \to \pi^- \mu^+ \nu)}{BR(D^0 \to K^- \mu^+ \nu)}$ branching ratio to decrease with increasing mass cuts. In Figure 4.6.3 we plot the branching ratio versus the $M(\pi\mu)$ mass cut. No downward systematic trend is observed, suggesting there is no large residual $\varrho^- \mu^+ \nu$ contamination.

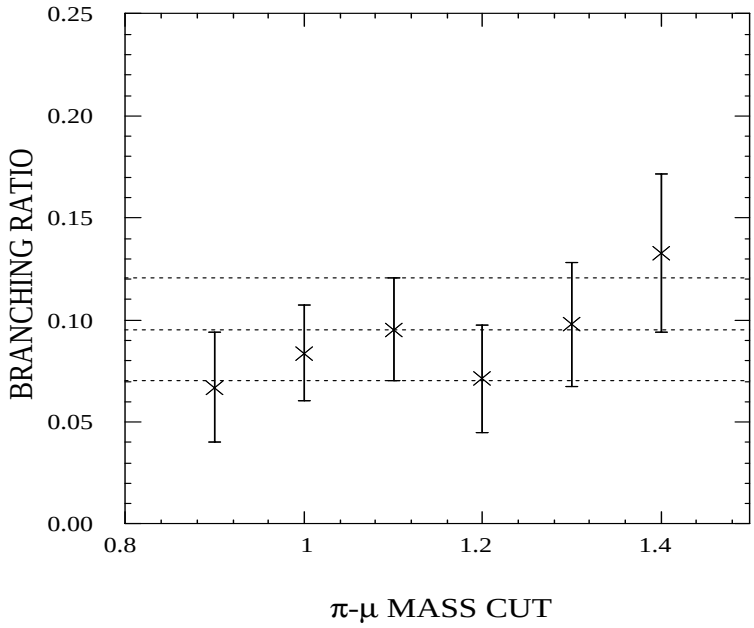

Figure 4.6.3 $\frac{BR(D^0 \to \pi^- \mu^+ \nu)}{BR(D^0 \to K^- \mu^+ \nu)}$ as a function of the $M(\pi\mu)$ mass cut for the $\pi^- \mu^+ \nu$ decay (the nominal cut is $M(\pi\mu) > 1.1\ GeV/c^2$).

4.6.6 Pole mass variation

As described in Chapter 1, the decay amplitude for a semileptonic decay contains the two form factors $f_{\pm}^{h}(q^2)$ (where $h = \pi, K$), which express the unknown hadronic part of the interaction (q is the four momentum carried by the virtual W boson, i.e. the invariant mass squared of the lepton-neutrino pair). The form factor $f_{-}^{h}(q^2)$ enters in the computation only through terms proportional to m_{μ}^2, so it drops out if the muon mass is neglected. The remaining form factor is generally parameterized according to a *single pole mass*

dependence:

$$f_+^h(q^2) = \frac{f_+^h(0)}{1 - q^2/\mathrm{M}_{pole}^2} \ ,$$

where $f_+^h(0)$ is the form factor at $q = 0$ (zero momentum transfer) and M_{pole} is the pole mass. The pole mass is expected to be equal to the mass of the nearest vector resonance of the two quarks involved in the weak decay. Therefore we expect $M_{pole}^K = M(D_s^{*+}) \sim 2.11\ GeV/c^2$ for the $K^-\mu^+\nu$ decay, and $M_{pole}^\pi = M(D^{*+}) \sim 2.01\ GeV/c^2$ for the $\pi^-\mu^+\nu$ decay.

We find that the value used for the pole mass in Monte Carlo generation affects the hadron-lepton invariant mass distribution for the $\pi^-\mu^+\nu$ decay, while having a negligible effect for the $K^-\mu^+\nu$ decay (this is because the allowed q^2 range for $D^0 \to K^-\mu^+\nu$ is much smaller then for $D^0 \to \pi^-\mu^+\nu$). In Figure 4.6.4 (a) we show the hadron-lepton invariant mass for the $K^-\mu^+\nu$ decay in the two cases $M_{pole}^K = 2.11\ GeV/c^2$ (predicted value) and $M_{pole}^K = 1.90\ GeV/c^2$ (measured value[29] [35]); the two distributions are nearly identical. In Figure 4.6.4 (b) we show the hadron-lepton mass for the $\pi^-\mu^+\nu$ decay in the two cases $M_{pole}^\pi = 2.01\ GeV/c^2$ (predicted value) and $M_{pole}^\pi = 1.80\ GeV/c^2$ (a somewhat arbitrary value below $1.90\ GeV/c^2$); this time the two distributions are significantly different, and the relative efficiency of the mass cut $M(\pi^-\mu^+) > 1.1\ GeV/c^2$ changes by $\sim 10\%$ between the two. In Figures 4.6.4 (c) and (d) we plot the variation in the hadron-lepton mass cut efficiency when the pole mass is varied from $M_{pole}^h = 1.80\ GeV/c^2$ to $M_{pole}^h = 2.11\ GeV/c^2$, for the $K^-\mu^+\nu$ and $\pi^-\mu^+\nu$ decay (respectively). In Figure 4.6.5 (a) we show how the branching ratio measurement is affected by the pole mass induced variation of the $D^0 \to \pi^-\mu^+\nu$ efficiency. Since the efficiency of the mass cut increases with M_{pole}^π, the branching ratio goes down.

The value of M^K_{pole} instead does not significantly affect the branching ratio measurement.

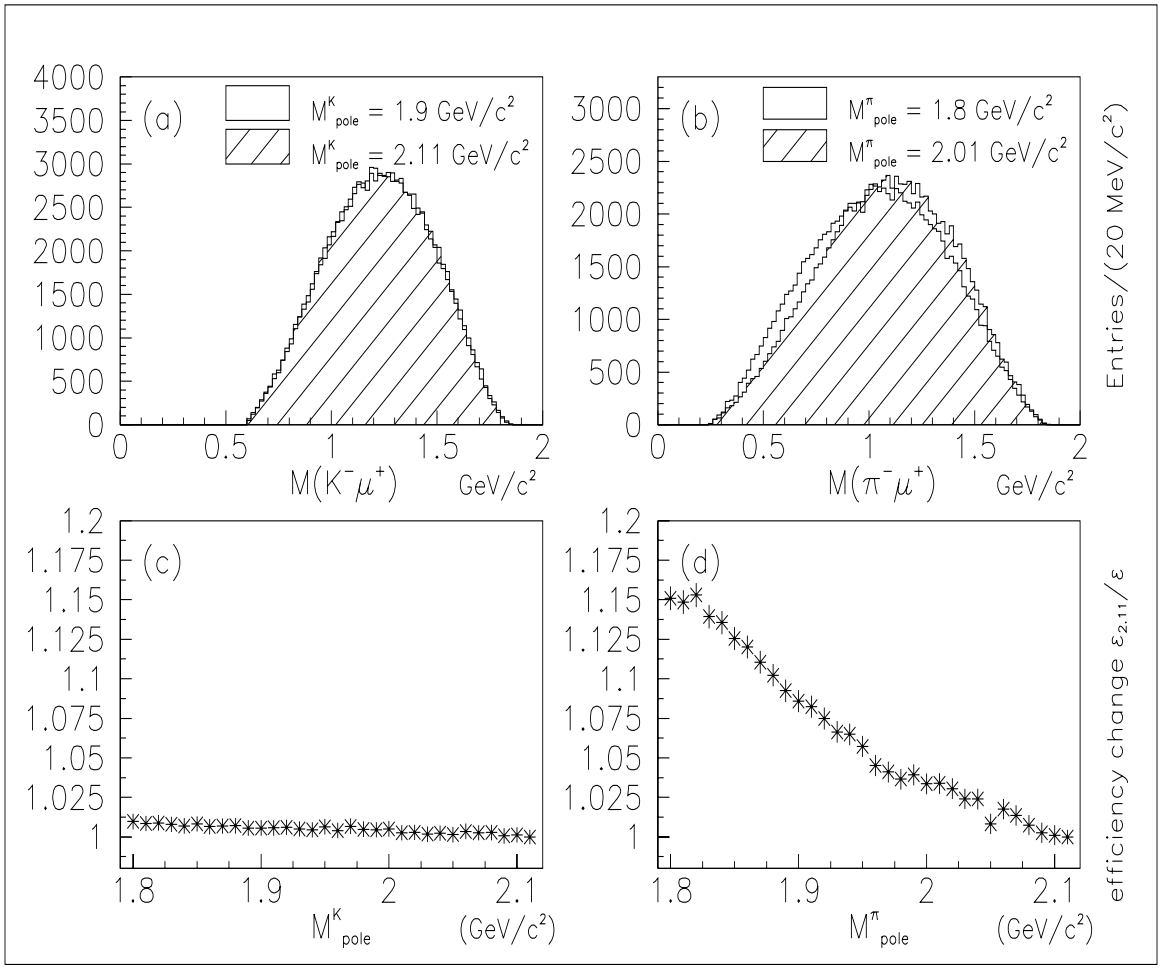

Figure 4.6.4 (a) hadron-lepton invariant mass for the $K^-\mu^+\nu$ decay, generated with $M^K_{pole} = 2.11\ GeV/c^2$ and $M^K_{pole} = 1.90\ GeV/c^2$; (b) hadron-lepton invariant mass for the $\pi^-\mu^+\nu$ decay, generated with $M^\pi_{pole} = 2.01\ GeV/c^2$ and $M^\pi_{pole} = 1.80\ GeV/c^2$; (c), (d) variation of the hadron-lepton mass cut efficiency for the two decays, when the pole mass is varied from $M^h_{pole} = 1.80\ GeV/c^2$ to $M^h_{pole} = 2.11\ GeV/c^2$. The variations have been normalized on the value used in the Monte Carlo generation, which is $M^h_{pole} = 2.11\ GeV/c^2$ for both decays.

Table 4.6.3 Variation of branching ratio with pole mass

M^{π}_{pole} pole mass	Eff. change $\epsilon_{2.11}(\pi\mu\nu)/\epsilon(\pi\mu\nu)$	Branching ratio
$2.11 GeV/c^2$	1	$B = 9.53 \pm 2.51\%$
$2.01 GeV/c^2$	1.0338 ± 0.0065	$B = 9.86 \pm 2.60\%$
$1.80 GeV/c^2$	1.1510 ± 0.0075	$B = 10.97 \pm 2.89\%$

When generating the Monte Carlo samples, we used the value $M^{h}_{pole} = 2.11\ GeV/c^2$ for both the $K^-\mu^+\nu$ and $\pi^-\mu^+\nu$ decays. If we had used for the $\pi^-\mu^+\nu$ decay the theoretically "correct" value $M^{\pi}_{pole} = 2.01\ GeV/c^2$, the $\pi^-\mu^+\nu$ reconstruction efficiency would have changed by $\epsilon_{2.11}/\epsilon_{2.01} = 1.0338 \pm 0.0065$. Therefore we correct our measured value for the branching ratio by this amount, obtaining:

$$\frac{BR\ (D^0 \to \pi^-\mu^+\nu)}{BR\ (D^0 \to K^-\mu^+\nu)} = 0.0986 \pm 0.0260\ .$$

In Table 4.6.3 we report the value of the branching ratio when the $\pi^-\mu^+\nu$ pole mass is varied between $M^{\pi}_{pole} = 1.80\ GeV/c^2$ and $M^{\pi}_{pole} = 2.11\ GeV/c^2$. The total variation of the branching ratio is:

$$\frac{\sigma_{B,pole}}{B} = ^{+10.7}_{-3.3}\ \%$$

around the value quoted for $M^{\pi}_{pole} = 2.01\ GeV/c^2$ (and $M^{K}_{pole} = 2.11\ GeV/c^2$). We do *not* include this source of theoretical uncertainty in our systematic error.

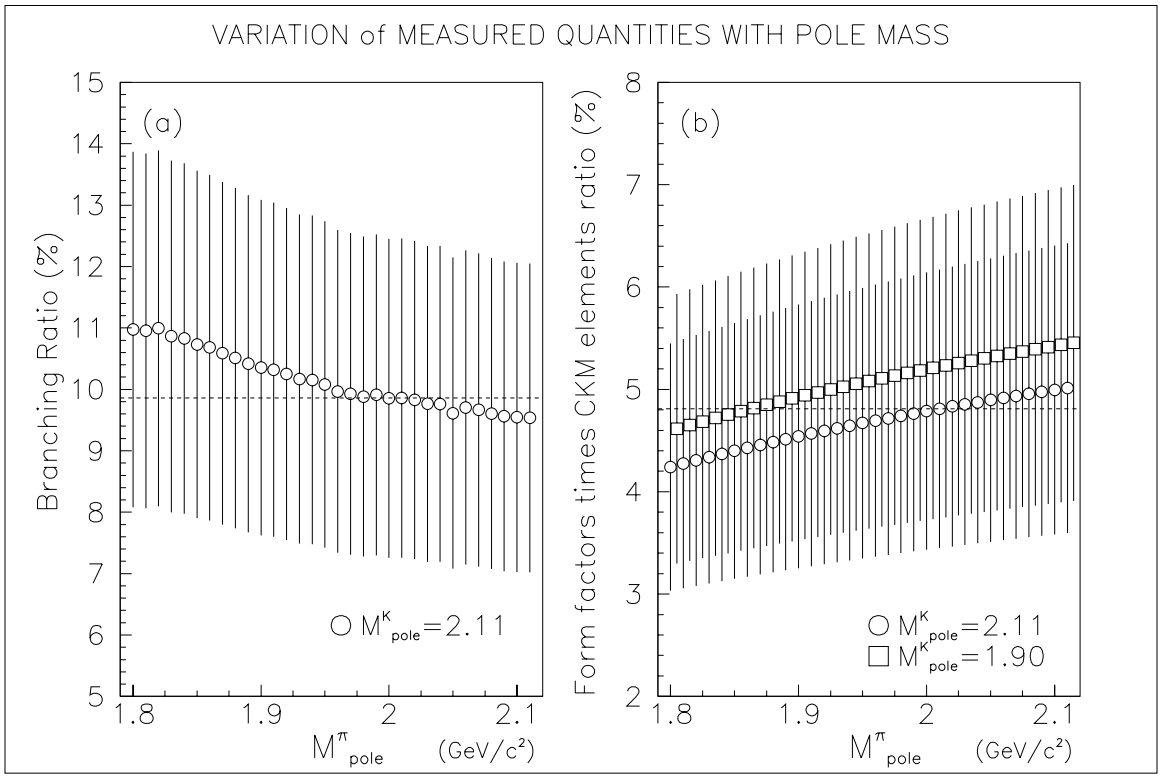

Figure 4.6.5 Variation of branching ratio (a) and form factors times CKM matrix elements ratio (b) with the value of the $D^0 \to \pi^- \mu^+ \nu$ pole mass used in Monte Carlo generation, for a reasonable range of M^{π}_{pole}. The value of the $D^0 \to K^- \mu^+ \nu$ pole mass does not significantly affect the measurement of the branching ratio, while it does affect the form factors ratio measurement, and was considered as a parameter in plot (b).

4.6.7 Total systematic error

We summarize all our sources of systematic error for the branching ratio measurement in Table 4.6.4 . Adding all contributions incoherently, we compute a total systematic error of:

$$\frac{\sigma_{B,sys}}{B} = 7.1\% \ .$$

Table 4.6.4 Branching Ratio systematic errors

Source	Error on branching ratio σ_B/B
fit variants	$\pm 4.72\%$
split samples	0%
misidentification level	$\pm 4.61\%$
Čerenkov identification	$\pm 2.50\%$
total systematic error	7.05%

4.7 Form factor ratio measurement

In Chapter 1 we saw that the differential decay rate for a pseudoscalar semileptonic decay can be written as[13]:

$$\frac{d^2,(D \to h\mu\nu)}{dq^2 dm^2_{h\mu}} = \frac{G^2}{64\pi^3 M_D^2}|V_{cq}|^2 \ |f_+^h(q^2)|^2 \left\{ A + B \ Re\xi + C \ |\xi|^2 \right\}$$

where $\xi \equiv \frac{f_-^h(q^2)}{f_+(q^2)}$ is the ratio of the two form factors entering the hadronic current, and A, B, C are kinematic functions of the two variables $q^2 = m^2_{\mu\nu}$ (the four momentum transfer) and $m^2_{h\mu}$ (the hadron-lepton invariant mass).

The above equation gives the probability density according to which $D^0 \to h^-\mu^+\nu$ decay events are distributed over the allowed region of the Dalitz plot q^2 vs $m^2_{h\mu}$ (see Figure 4.7.1). Since the probability density contains the two form factors $f_\pm(q^2)$, a study of the distribution of real events over the Dalitz plot region could give information on the functional dependence of the form factors[35]. The form factors are functions of q^2 only (and not of $m^2_{h\mu}$), consequently the choice of the pole mass (or more generally, of the form factor parameterization) may influence the Dalitz plot density only along the Y axis, but not along the X direction. Here we are interested in measuring the ratio

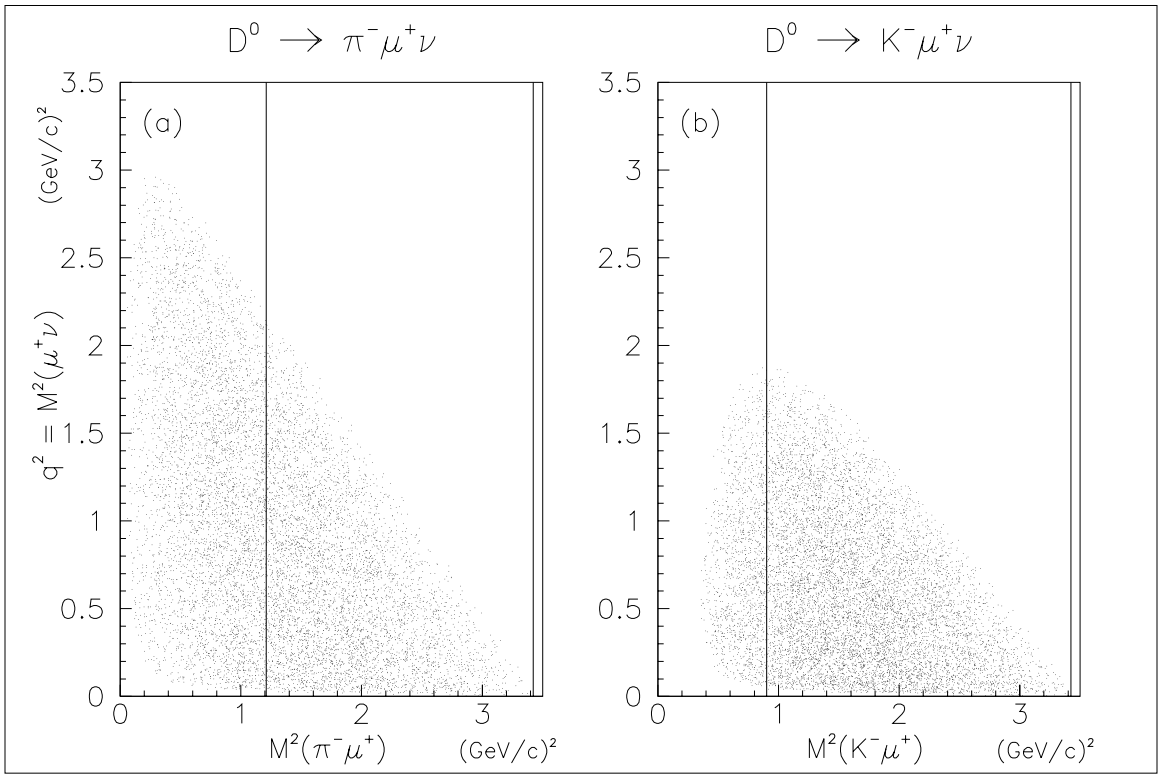

Figure 4.7.1 Distribution of generated Monte Carlo events for the two decays $D^0 \to \pi^-\mu^+\nu$ (a) and $D^0 \to K^-\mu^+\nu$ (b). In both cases, a single pole mass dependence with $M_{pole} = 2.11\ GeV/c^2$ was assumed for the decay matrix element. The two vertical lines indicate the position of the hadron-lepton mass cut used in the analysis, and define the portion of the Dalitz plot over which the integration described in the text is performed.

of the two dominant form factors for $D^0 \to \pi^-\mu^+\nu$ and $D^0 \to K^-\mu^+\nu$ at zero momentum transfer $q^2 = 0$. Taking the ratio of the differential decay rates for the two channels, we obtain:

$$\begin{aligned}\frac{d^2,\,(\pi\mu\nu)}{d^2,\,(K\mu\nu)} &= \frac{dY_{\pi\mu\nu}/\epsilon_{\pi\mu\nu}(q^2)}{dY_{k\mu\nu}/\epsilon_{k\mu\nu}(q^2)} \\ &= \left|\frac{V_{cd}}{V_{cs}}\right|^2 \left|\frac{f_+^\pi(0)}{f_+^K(0)}\right|^2 \frac{\left|\frac{f_+^\pi(q^2)}{f_+^\pi(0)}\right|^2 \left[A + BRe\xi + C|\xi|^2\right]_{\pi\mu\nu} dq^2 dm^2_{\pi\mu}}{\left|\frac{f_+^K(q^2)}{f_+^K(0)}\right|^2 \left[A + BRe\xi + C|\xi|^2\right]_{k\mu\nu} dq^2 dm^2_{k\mu}}\ ,\end{aligned}$$

where for each decay we have expressed the differential decay rate through

the differential corrected yield, and we have assumed that the reconstruction efficiency is only a function of q^2 and does not depend on $m^2_{h\mu}$. For each decay, we can integrate this expression over the region of the Dalitz plot which is defined by the hadron-lepton mass cut:

$$\frac{Y_{\pi\mu\nu}}{Y_{k\mu\nu}} = \left|\frac{V_{cd}}{V_{cs}}\right|^2 \left|\frac{f_+^\pi(0)}{f_+^K(0)}\right|^2 \times \frac{\int_{(1.1)^2}^{(1.85)^2} dm^2_{\pi\mu} \int_{q^2_{min}}^{q^2_{max}} dq^2 \left|\frac{f_+^\pi(q^2)}{f_+^\pi(0)}\right|^2 \left[A + BRe\xi + C|\xi|^2\right]_{\pi\mu\nu} \epsilon_{\pi\mu\nu}(q^2)}{\int_{(0.95)^2}^{(1.85)^2} dm^2_{k\mu} \int_{q^2_{min}}^{q^2_{max}} dq^2 \left|\frac{f_+^K(q^2)}{f_+^K(0)}\right|^2 \left[A + BRe\xi + C|\xi|^2\right]_{k\mu\nu} \epsilon_{k\mu\nu}(q^2)}$$

where the two limits in the inner integration q^2_{min},q^2_{max} are functions of $m^2_{h\mu}$.

We use this equation to measure the ratio of the two form factors at $q^2 = 0$ times the corresponding CKM matrix elements, i.e. the quantity

$$FV \equiv \left|\frac{V_{cd}}{V_{cs}}\right|^2 \left|\frac{f_+^\pi(0)}{f_+^K(0)}\right|^2 .$$

For each decay, we measure the reconstruction efficiency by segmenting the Dalitz plot into horizontal strips of q^2 and counting the number of reconstructed and generated Monte Carlo events which are contained in the portion of the strip between the two mass cuts. We then fit the efficiency curves to a second degree polynomial (see Figure 4.7.2).

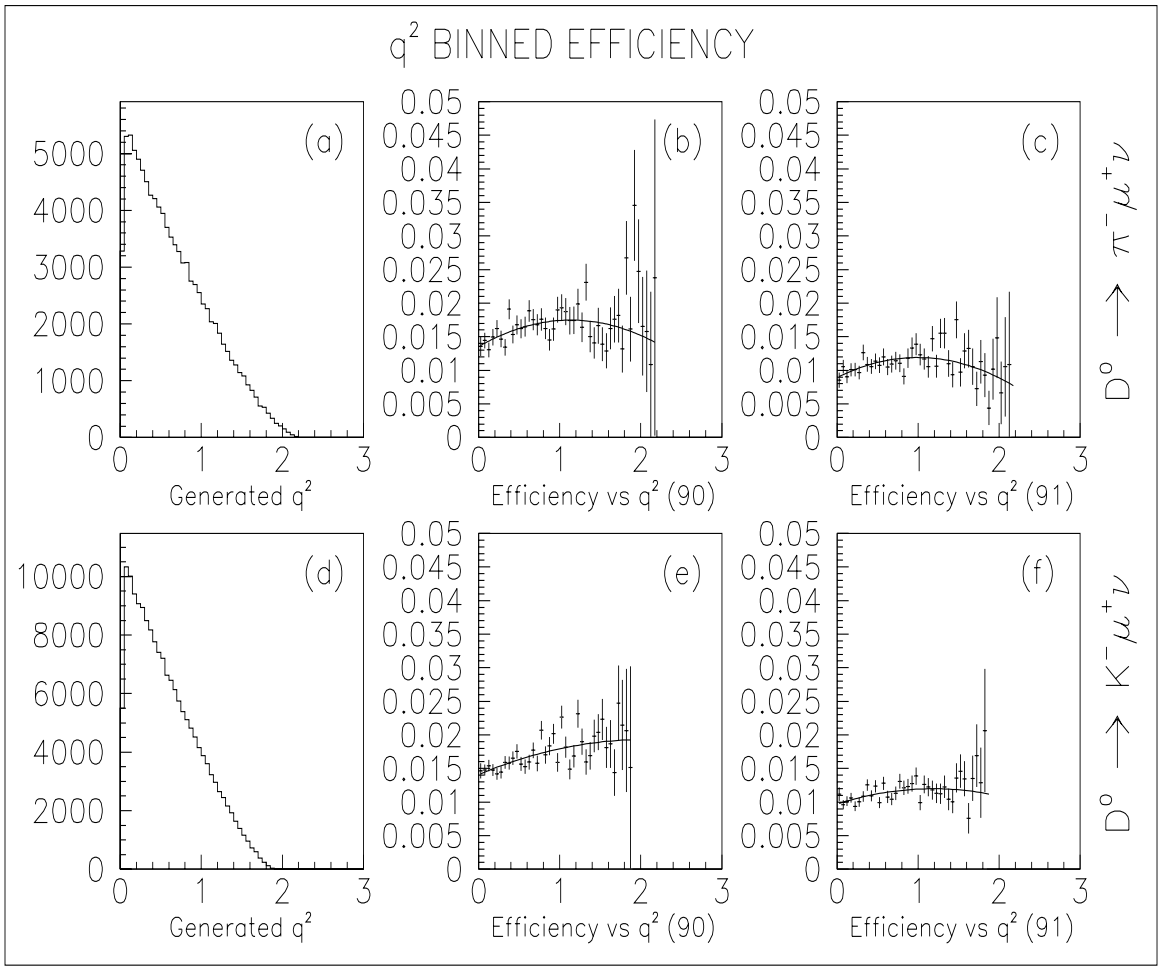

Figure 4.7.2 Figures (a) and (d) show the number of Monte Carlo generated events which pass the hadron-lepton mass cut for the two decays $D^0 \rightarrow \pi^-\mu^+\nu$ and $D^0 \rightarrow K^-\mu^+\nu$, respectively, plotted in bins of q^2 ($50\ MeV/bin$). Figures (b), (c), (e), (f) show the reconstruction efficiency versus q^2 for the two decays, separately for the 1990 and 1991 runs.

The efficiency thus measured in bins of q^2 is independent of the value of the pole mass used in the form factor parameterization. This is because in each small cell of the Dalitz plot (or, in this case, in each strip, since we do not consider $m^2_{h\mu}$ dependence), the form factor affects in the same way both reconstructed and generated events, so that its effect cancels out. In the equation considered, the only pole mass dependence left is contained in

the form factors themselves. If instead we performed our measurement using global reconstruction efficiencies, these latter would also depend on the choice of the pole mass value, since the pole mass determines how many of the total number of generated events fall in the Dalitz plot to the left or to the right of the mass cut (see Figure 4.6.4 (d)).

We assume $\xi = -1$[35] and perform numerically the integrations on the right hand side of the equation, inserting in the form factors the values $M^{\pi}_{pole} = 2.01\ GeV/c^2$ and $M^{K}_{pole} = 2.11\ GeV/c^2$. On the left hand side of the equation, we use the (background subtracted) yields $Y_{\pi\mu\nu}$ and $Y_{K\mu\nu}$ returned by the fit. We thus measure:

$$FV \;=\; \left|\frac{V_{cd}}{V_{cs}}\right|^2 \left|\frac{f^{\pi}_{+}(0)}{f^{K}_{+}(0)}\right|^2 \;=\; 0.0481 \pm 0.0136$$

(the results for the 1990 and 1991 runs separately are 0.0472 ± 0.0199 and 0.0488 ± 0.0186, respectively). The statistical error quoted is obtained by propagating the errors on the two fitted yields $Y_{\pi\mu\nu}$, $Y_{K\mu\nu}$ (including their correlation term) and the errors on the fit to the q^2 binned efficiencies (a $\sim 10\%$ effect).

Assuming unitarity for the CKM matrix (and the existence of only three generations of leptons and quarks), the ratio of the matrix elements involved in the two decays is constrained to be:

$$\left|\frac{V_{cd}}{V_{cs}}\right|^2 = 0.051 \pm 0.001^{[33]}\ .$$

We can use this result to compute the ratio of the two form factors at zero

momentum transfer:

$$F \equiv \left| \frac{f_+^\pi(0)}{f_+^K(0)} \right| = 0.971 \pm 0.138 \ .$$

4.8 Systematic error on form factor measurement

The form factor ratio measurement is affected by all the sources of systematic error which have been previously discussed for the branching ratio measurement. We assumed that the relative errors due to yields fit variants, estimate of hadron/muon misidentification level, and Čerenkov identification are the same for the two measurements. Furthermore, we estimated additional error to the form factor measurement originating from the use of q^2 binned efficiencies. We applied the *fit variants* technique by modifying the size of the q^2 bins and by using the bin by bin efficiency instead of the fit to the distribution. The results of this study are summarized in Table 4.8.1. The resultant systematic error is very small:

$$\frac{\sigma_{FV}}{FV} = 0.3\% \ .$$

Combining all sources of systematic error in quadrature, we obtain a total systematic error of:

$$\frac{\sigma_{FV,syst}}{FV} = 7.1\% \ ,$$

corresponding to an error on the form factor ratio alone of:

$$\frac{\sigma_{F,syst}}{F} = 3.5\% \ .$$

Table 4.8.1 Form factors fit variants

Fit variant	FV
50 MeV/bin, fit function [$*$]	0.04810 ± 0.01361
50 MeV/bin, step function	0.04777 ± 0.01268
75 MeV/bin, fit function	0.04804 ± 0.01358
75 MeV/bin, step function	0.04778 ± 0.01269
100 MeV/bin, fit function	0.04789 ± 0.01354
100 MeV/bin, step function	0.04777 ± 0.01269

[$*$] Standard conditions.

Since the Dalitz plot density for the two decays contains the square of the form factors, our measurement for $\left|\frac{V_{cd}}{V_{cs}}\right|^2 \left|\frac{f_+^\pi(0)}{f_+^K(0)}\right|^2$ depends on the choice of the pole mass used in Monte Carlo generation. The dependence is more pronounced than for the branching ratio measurement, since this time the two form factors enter the expression with a square (as discussed earlier, pole mass dependence in the efficiency has been eliminated by measuring it in bins of q^2). In Figure 4.6.5 (b) we show how the measured quantity changes when the $D^0 \to \pi^- \mu^+ \nu$ pole mass is varied from $M^\pi_{pole} = 1.80$ to $M^\pi_{pole} = 2.11\ GeV/c^2$; the study is performed for two different choices of the $D^0 \to K^- \mu^+ \nu$ pole mass: $M^K_{pole} = 1.90\ GeV/c^2$ and $M^K_{pole} = 2.11\ GeV/c^2$. As for the branching measurement, we do not include this source of theoretical uncertainty in the computation of the total systematic error.

Finally we investigated how sensitive our measurement is to the ratio $\xi = \left|\frac{f_-^h(q^2)}{f_+^h(q^2)}\right|$ which is assumed to be -1 in the computation. We used the

measurement $\left|\frac{f_-^K(0)}{f_+^K(0)}\right| = -1.3^{+3.6}_{-3.4} \pm 0.6$[35] and varied ξ within $\pm 1\sigma$ of its central value. The corresponding variation of the measured quantity was found to be

$$\frac{\sigma_{FV,\xi}}{FV} = \pm 1.4\%$$

(see Table 4.8.2). The effect is so small because the factor ξ enters in the computation only through terms which are proportional to the muon mass squared.

Table 4.8.2 Variation of $\xi = \left|\frac{f_-^h(q^2)}{f_+^h(q^2)}\right|$

ξ	FV
+2.3	0.04884 ± 0.01387
-1.0	0.04810 ± 0.01361
-4.7	0.04745 ± 0.01348

4.9 Summary of results

We investigated the two semileptonic decays $D^0 \to \pi^-\mu^+\nu$ and $D^0 \to K^-\mu^+\nu$ using a D^*-tag technique. We observed 45.6 ± 11.8 $\pi^-\mu^+\nu$ events and 824.5 ± 33.0 $K^-\mu^+\nu$ events. We measured the relative branching ratio of the two decays to be:

$$\frac{BR\ (D^0 \to \pi^-\mu^+\nu)}{BR\ (D^0 \to K^-\mu^+\nu)} = 0.0986 \pm 0.0260\ (stat)\ \pm 0.0069\ (syst)\ .$$

Integrating the differential decay rates over the significant region of the Dalitz plot q^2 vs $m^2_{h\mu}$, we measured the ratio of the two form factor normalizations

times the ratio of the corresponding CKM matrix elements:

$$\left|\frac{V_{cd}}{V_{cs}}\right|^2 \left|\frac{f_+^\pi(0)}{f_+^K(0)}\right|^2 = 0.0481 \pm 0.0136 \pm 0.0034 \ .$$

Assuming unitarity for the CKM matrix, we computed the ratio of the two form factors alone to be:

$$\left|\frac{f_+^\pi(0)}{f_+^K(0)}\right| = 0.971 \pm 0.138 \pm 0.034 \ .$$

CHAPTER 5

VECTOR D^+ SEMILEPTONIC DECAYS

In this chapter we analyze the vector meson semileptonic decays $D^+ \to \overline{K}^{*0}\mu^+\nu$ and $D^+ \to \varrho^0\mu^+\nu$ and measure the relative branching ratio. The major problem with this analysis is represented by background from other D^+ and D_s^+ semileptonic decays. In order to reduce D_s^+ contamination, we will exploit the longer D^+ lifetime to require a large separation between the reconstructed primary and secondary vertex; we will further require that the secondary position is outside the target region. Contamination from other incompletely reconstructed D^+ semileptonic decays will be either suppressed by tight three-body invariant mass cuts ($D^+ \to \eta'\mu^+\nu$), or inserted as another possible charm signal in the fit to the data ($D^+ \to \eta\mu^+\nu$). Finally, because of our low reconstruction efficiency for π^0, we will not be able in this analysis to impose a D^{*+}-tag requirement on the decay candidates.

5.1 Analysis algorithm

We want to reconstruct the decay $D^+ \to h^*\,\mu^+\,\nu$, where h^* is a neutral vector meson decaying into two bodies $h^* \to h^-h^+$. In particular, we are interested in the two decays $D^+ \to \overline{K}^{*0}\mu^+\nu$, $\overline{K}^{*0} \to K^-\pi^+$ and $D^+ \to \varrho^0\mu^+\nu$, $\varrho^0 \to \pi^+\pi^-$. The analysis algorithm we employ is very similar to the one used to reconstruct $D^0 \to h^-\mu^+\nu$ events. The major differences are the number of decay prongs (three instead of two) and the absence of a D^*-tag.

We start by selecting a combination of three linked $SSD + PWC$ tracks compatible with originating from the decay $D^+ \to h^*\mu^+\nu$, $h^* \to h^-h^+$. The muon candidate is required to be traced through all five PWC stations

(in order to hit the Inner Muon detector), it must not be identified by the Čerenkov counters as a heavy particle (i.e. it must not be a kaon, a proton or kaon/proton ambiguous: istatp$\neq 4, 8, 12$), and it is subject to the same muon identification requirements which have been used for the $D^0 \to h^-\mu^+\nu$ analysis (including the cut $P(\mu^+) > 10\ GeV/c$ which reduces hadron misidentification). The two hadron candidates h^-, h^+ must be traced in at least three PWC stations and must have opposite charge. The candidate with opposite sign to the muon, h^-, is required to be kaon definite or kaon/proton ambiguous (istatp$= 4, 12$) for $D^+ \to \overline{K}^{*0}\mu^+\nu$ candidates, while it is required to be pion definite or electron/pion ambiguous (istatp$= 2, 3$) for $D^+ \to \varrho^0\mu^+\nu$ candidates. The same sign hadron $h^+ = \pi^+$ (in both cases) has a looser requirement of not being identified as a heavy particle. No momentum cut is applied to the hadrons. The three-body invariant mass of the combination is computed and is required to be satisfy $1.0 < M(K^-\pi^+\mu^+) < 1.8\ GeV/c^2$ and $1.2 < M(\pi^-\pi^+\mu^+) < 1.8\ GeV/c^2$. This cut is applied to reduce contamination from other non-tag charm decays. We also compute the two-body invariant mass of the muon candidate with the opposite sign hadron and we impose the condition $M(h^-h^+\mu^+) - M(h^-\mu^+) > 0.25\ GeV/c^2$. This cut reduces contamination from charm D^*-tag semileptonic decays. Both cuts will be discussed in much more detail in section § 5.3. The three tracks are tested for a common origin, the secondary vertex, with a confidence level $cls > 1\%$. Contamination from higher multiplicity charm decays is reduced by requiring the secondary vertex to be isolated from any other track in the event ($iso2 < 1\%$). We take advantage of the fact that the D^+ has a longer lifetime than the D^0 (two and a half times bigger) and we require the reconstructed secondary vertex to be *outside the target* region. Monte Carlo studies show that the percentage of

D^+ and D_s^+ which decay outside the target is on average 42% and 25%, respectively (due to absorption in the target region, there is a small dependence on the number of decay prongs). The out-of-target requirement not only enhances the D^+ signals with respect to the D_s^+'s, but it also rejects background originating from secondary interactions.

As in the $D^0 \rightarrow h^-\mu^+\nu$ analysis, we construct the primary vertex of the event by using a standalone vertexing algorithm, which combines all the SSD tracks of the event (except those composing the secondary vertex) to form all possible vertices with a confidence level $clp > 1\%$. We then choose as the primary vertex the highest multiplicity vertex reconstructed within the target region. To reduce the shorter-living combinatorial background, we require the significance of separation between primary and secondary vertex to satisfy $L/\sigma_L > 20$. The hard L/σ_L cut also contributes in suppressing the D_s^+ component with respect to the D^+.

In the $D^0 \rightarrow h^-\mu^+\nu$ analysis, we use the direction in space defined by the primary and secondary vertex position to compute the D^0 momentum by assuming the D^0 mass. The D^0 momentum was then combined with the soft pion momentum from the primary vertex to form the D^{*+} invariant mass. In this analysis there is no D^* mass to compute, so we could avoid calculating the D^+ momentum by assuming the D^+ mass. Nevertheless, we perform the computation because it allows us to impose some kinematic constraints on the reconstructed neutrino energy and longitudinal momentum. Boosting as before to a reference frame where the total charged momentum (i.e. the momentum of the $h^-h^+\mu^+$ combination) is perpendicular to the D^+ direction of flight, we require $P_L'^2(\nu) > -2\ GeV/c$ and $E'(\nu) > -1\ GeV$ (quantities are

allowed to be slightly negative because of resolution effects). These constraints help reduce background from non semileptonic decays.

The complete set of analysis cuts used to select the $D^+ \to \overline{K}^{*0}\mu^+\nu$ and $D^+ \to \varrho^0\mu^+\nu$ signals is summarized in Table 5.1.1. For the decay candidates satisfying the analysis requirements, we plot the two-hadron invariant mass $M(h^-h^+)$ and look for a peak at the parent vector meson h^* mass. Since we are not interested in the computed D^+ momentum, there is no twofold ambiguity to be solved (as in the $D^0 \to h^-\mu^+\nu$ analysis), and for each decay candidate there is only one $M(h^-h^+)$ value to be plotted.

5.2 The data signals

The analysis algorithm was run on the full data set collected during the 1990 and 1991 runs. Events were ambiguous by the Global Vertex routine, which requires the presence in the event of at least two vertices, each composed of at least two SSD tracks. In Figure 5.2.1 we show the two-body reconstructed invariant mass $M(K^-\pi^+)$ for $D^+ \to \overline{K}^{*0}\mu^+\nu$ candidates (increasing L/σ_L cuts are applied). The distribution is dominated by the $\overline{K}^{*0}(892)$ mass peak. In Figure 5.2.2 we show the two-body $M(\pi^-\pi^+)$ invariant mass for $D^+ \to \varrho^0\mu^+\nu$ candidates. The broad peak in the center of the plot is the $\varrho^0(770)$ signal. Other peaks at lower mass values may be interpreted as due to other incompletely reconstructed resonant semileptonic decays, which contain two oppositely charged pions among their decay products.

Table 5.1.1 Analysis cuts

	$D^+ \to \overline{K}^{*0}\mu^+\nu$	$D^+ \to \varrho^0\mu^+\nu$	$D_s^+ \to \phi\mu^+\nu$
tracking	all tracks linked $SSD + PWC$		
	$\mu^+ = 5$ PWC, $h^-, h^+ =$ at least 3 PWC		
	$P(\mu^+) > 10\ GeV/c$		
Čerenkov (istatp)	$\mu^+ \neq 4, 8, 12$		
	$\pi^+ \neq 4, 8, 12$		$K^+ = 4, 12$
	$K^- = 4, 12$	$\pi^- = 2, 3$	$K^- = 4, 12$
μ identification	$0.01 < E/p < 1.0$		
	Good Runs: at least 5 out of 7 planes + $r/\sigma_r < 1$		
	Bad Runs: 1 or 2 scint. planes + HC μ id		
	or 3 scint. planes with no further request		
vertexing	$cs > 1\%$, $cp > 1\%$, $iso2 < 1\%$		
	$L/\sigma_L > 20$, Z_{sec} out of target		$L/\sigma_L > 5$
kinematics	$P_L^{l2}(\nu) > -2\ GeV/c$, $E'(\nu) > -1\ GeV/c^2$		
invariant mass	$1.0 < M(K^-\pi^+\mu^+) < 1.80$	$1.2 < M(\pi^-\pi^+\mu^+) < 1.80$	no cut
	$0.25 < M(h^-\pi^+\mu^+) - M(h^-\mu^+)$		no cut

5.3 Discussion of backgrounds

The two-body invariant mass $M(\pi^+\pi^-)$ reconstructed from $\pi^+\pi^-\mu^+$ combinations is a very rich, and therefore a complicated, distribution. Several D^+, D^0 and D_s^+ semileptonic decay channels may in principle contribute to the distribution.

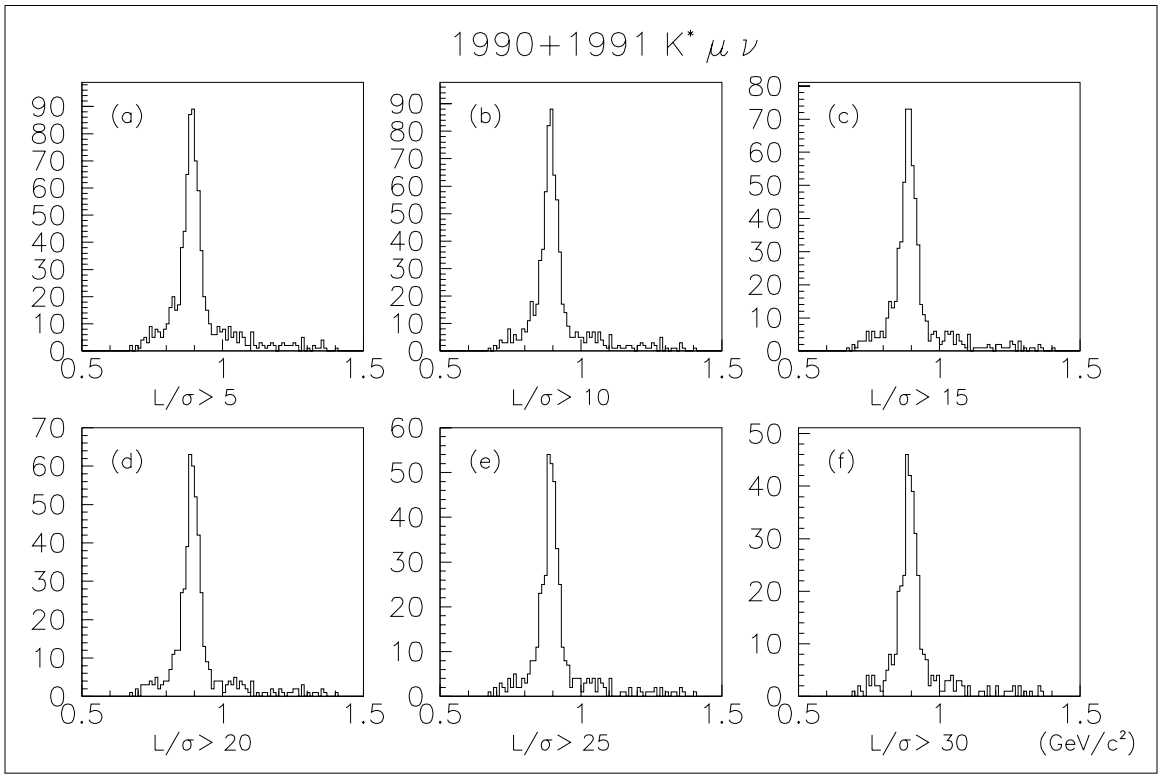

Figure 5.2.1 $M(K^-\pi^+)$ invariant mass for $D^+ \to \overline{K}^{*0}\mu^+\nu$ candidates, reconstructed with the cuts described in the text and increasing L/σ_L cuts.

5.3.1 $D^+ \to \overline{K}^{*0}\mu^+\nu$

The first source of contamination to the $D^+ \to \varrho^0\mu^+\nu$ signal originates from $D^+ \to \overline{K}^{*0}\mu^+\nu$ events where the opposite sign kaon is misidentified as a pion. If the K^- from the $K^{*0}(892)$ is given the pion mass, the misidentified $K^-\pi^+$ mass peak is broadened and shifted in the $\varrho^0(770)$ region (see Figure 5.3.1 (b)). It is because of this source of contamination that in the $D^+ \to \varrho^0\mu^+\nu$ decay, the Čerenkov identification of the opposite sign pion π^- is required to be tighter than that of the same sign pion π^+. The lower limit imposed on the three-body mass also helps in reducing the contamination, since the distribution for misidentified $\overline{K}^{*0}\mu^+\nu$ events is shifted to lower values than

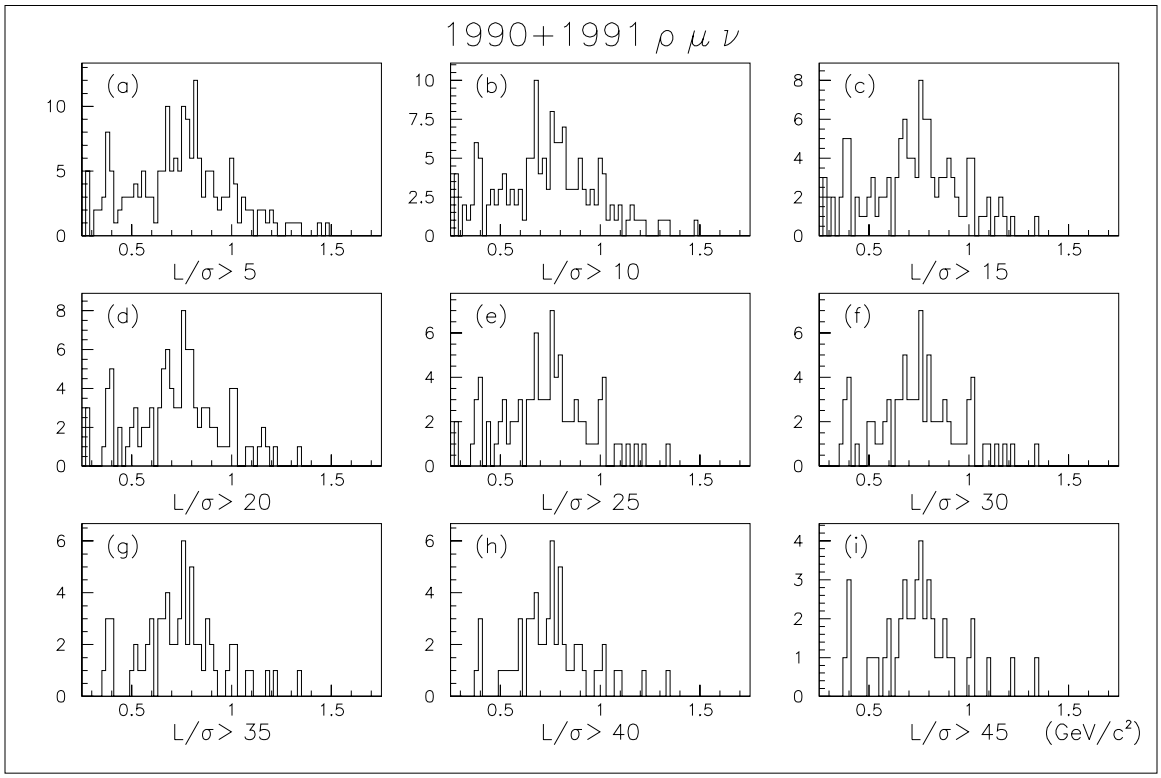

Figure 5.2.2 $M(\pi^-\pi^+)$ invariant mass for $D^+ \to \varrho^0\mu^+\nu$ candidates, reconstructed with the cuts described in the text and increasing L/σ_L cuts.

for $\varrho^0\mu^+\nu$ events (see Figure 5.3.2 (b)). The total amount of feedthrough depends on the number of $D^+ \to \overline{K}^{*0}\mu^+\nu$ events generated in our experiment and the efficiency to misidentify them as $D^+ \to \varrho^0\mu^+\nu$. Roughly we can estimate: $\frac{Y(\overline{K}^{*0}\mu^+\nu,msd)}{Y(\varrho^0\mu^+\nu)} = \frac{BR(D^+\to K^{*0}\mu^+\nu)}{BR(D^+\to\varrho^0\mu^+\nu)} \times \frac{\epsilon(\overline{K}^{*0}\mu^+\nu,msd)}{\epsilon(\varrho^0\mu^+\nu)} \sim 10\times0.05\times0.5 \sim 0.25$, where 5% is the K/π misidentification probability, 50% is the relative efficiency of the mass cuts, and we have assumed $\frac{BR(D^+\to\varrho^0\mu^+\nu)}{BR(D^+\to\overline{K}^{*0}\mu^+\nu)} \sim 10\%$.

5.3.2 Non-tag D^+, D_s^+ inclusive semileptonic decays

A priori, many D^+ and D_s^+ semileptonic decays with two oppositely charged pions in the final state are possible (see Table 5.3.1). If these decays are only partially reconstructed, they will contaminate the $M(\pi^+\pi^-)$ mass distribution for the $\varrho^0\mu^+\nu$ signal. In Figure 5.3.1 (c)-(i) we show for each decay the two two-body $M(\pi^+\pi^-)$ mass distributions reconstructed from Monte Carlo.

Only two of these decays have been observed. Namely, the CLEO collaboration[36] fully reconstructed the decay chains $D_s^+ \to \eta e^+\nu,\ \eta \to \gamma\gamma$ and $D_s^+ \to \eta' e^+\nu,\ \eta' \to \eta\pi^+\pi^-$, and measured $\frac{BR(D_s^+ \to \eta e^+\nu)}{BR(D_s^+ \to \phi e^+\nu)} = 1.24 \pm 0.12 \pm 0.15$ and $\frac{BR(D_s^+ \to \eta' e^+\nu)}{BR(D_s^+ \to \phi e^+\nu)} = 0.43 \pm 0.11 \pm 0.07$.

Table 5.3.1 Inclusive D^+, D_s^+ semileptonic decays into $\pi^+\pi^-$

decay	sub-decay	sub-decay BR[33]
$\eta(547)\mu^+\nu$	$\eta \to \pi^+\pi^-\pi^0$	0.236 ± 0.006
	$\eta \to \pi^+\pi^-\gamma$	0.0488 ± 0.0015
$\eta'(958)\mu^+\nu$	$\eta' \to \gamma\varrho^0$	0.302 ± 0.013
	$\eta' \to \eta\pi^+\pi^-,\ \eta \to X$	0.437 ± 0.015
	$\eta' \to \eta\pi^0\pi^0,\ \eta \to \pi^+\pi^-\pi^0$	$(0.208 \pm 0.013) \times (0.236 \pm 0.006)$
	$\eta' \to \eta\pi^0\pi^0,\ \eta \to \pi^+\pi^-\gamma$	$(0.208 \pm 0.013) \times (0.0488 \pm 0.0015)$
$\omega^0(782)\mu^+\nu$	$\omega^0 \to \pi^+\pi^-\pi^0$	0.888 ± 0.007

In this analysis, two tools are employed to reduce contamination from these decays. First, contamination from D_s^+ decays is suppressed by the large L/σ_L cut and the out-of-target requirement. Because of the combined action of these two cuts, the reconstruction efficiency for D_s^+ is about half that for

D^+ for the same final state (see Tables 5.3.2, 5.3.4). Second, the lower limit imposed on the three-body mass $M(\pi^-\pi^+\mu^+) > 1.2\ GeV/c^2$ removes almost completely any contribution from $D^+, D_s^+ \to \eta'\mu^+\nu,\ \eta' \to \eta X$, while suppressing contributions from $D^+, D_s^+ \to \eta\mu^+\nu$ and $D^+ \to \omega^0\mu^+\nu$ (see Table 5.3.3 for the efficiency of the invariant mass cuts for each decay).

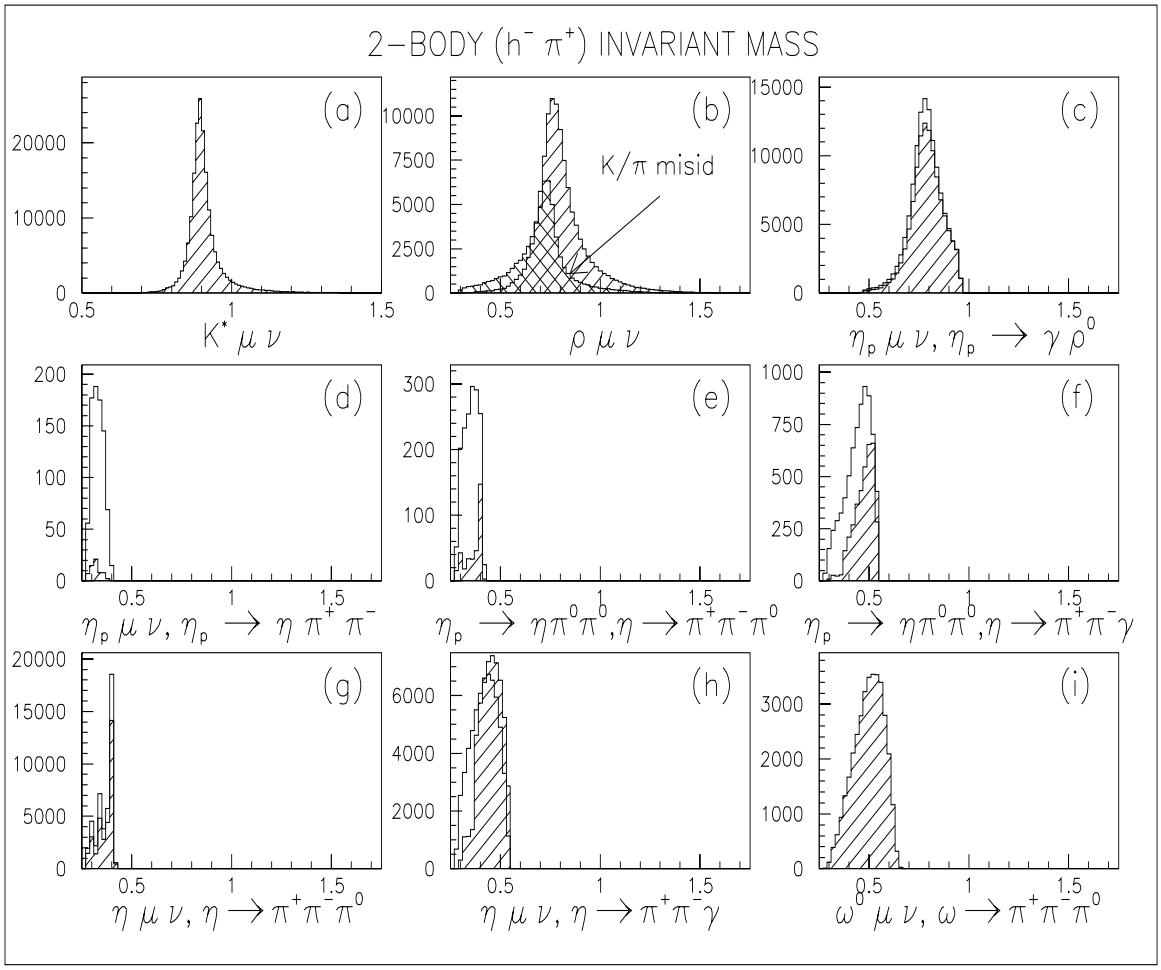

Figure 5.3.1 Two-body $M(h^-\pi^+)$ invariant mass for various D^+ (hatched style) and D_s^+ (unhatched style) decay channels. The relative size of D^+ and D_s^+ distributions reflect the relative efficiency of the invariant mass cuts applied. No other analysis cuts have been used to produce these distributions. In plot (b), the additional distribution represents $\overline{K}^{*0}\mu^+\nu$ events where the K^- is misidentified as a π^-.

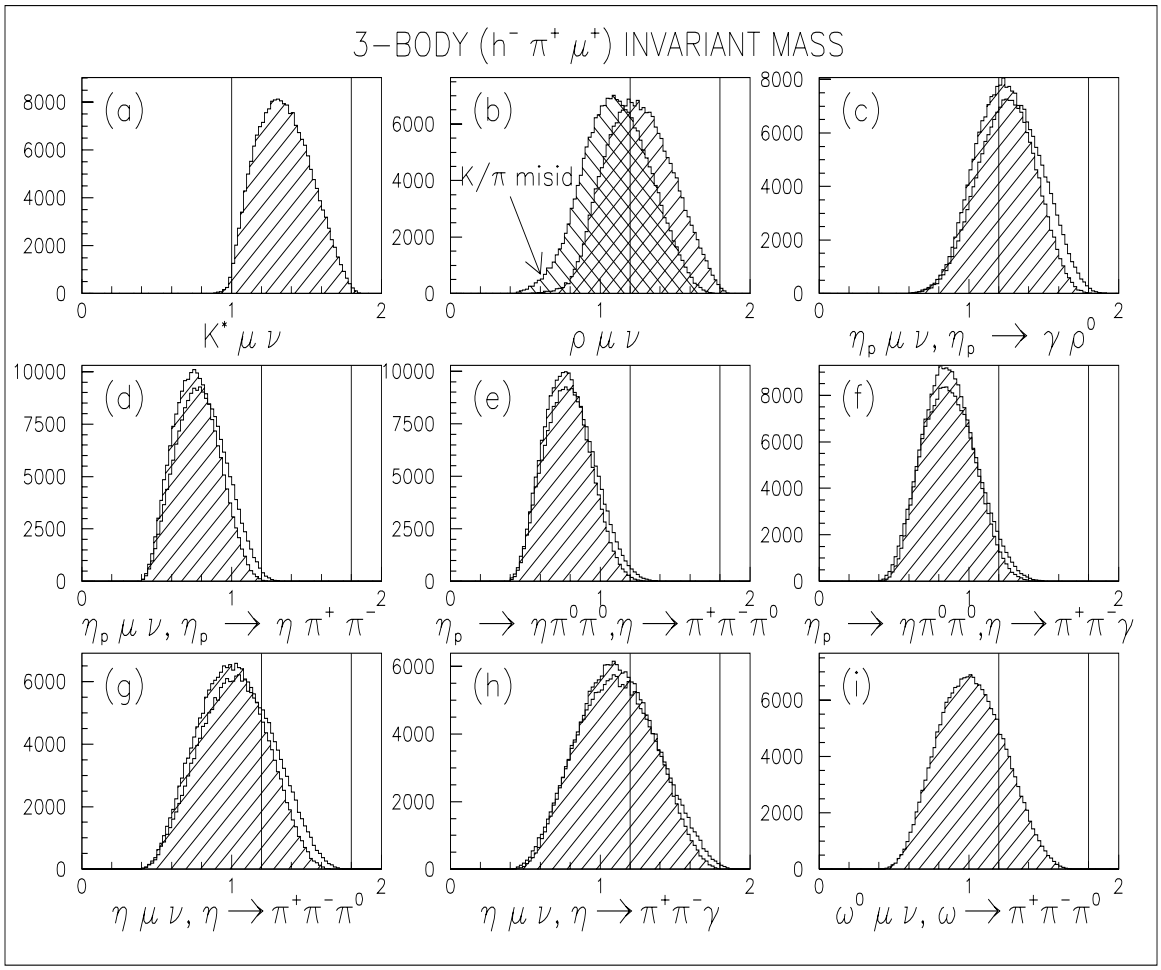

Figure 5.3.2 Three-body $M(h^-\pi^+mu^+)$ invariant mass distributions for various D^+ (hatched style) and D_s^+ (unhatched style) decay channels. In plot (b), the additional distribution represents $\overline{K}^{*0}\mu^+\nu$ events where the K^- is misidentified as a π^-. The two vertical lines indicate the position of the mass cuts.

Table 5.3.2 Efficiency of L/σ_L and out of target cut for some D^+ and D_s^+ decays [*]

decay	out of target	L/σ_L	both cuts
$D^+ \to K^{*0}\mu^+\nu$	41.0%	53.5%	31.7%
$D^+ \to \varrho^0\mu^+\nu$	41.6%	59.7%	34.9%
$D^+ \to \eta'\mu^+\nu,\ \eta' \to \gamma\varrho^0$	41.9%	59.8%	35.3%
$D^+ \to \eta\mu^+\nu,\ \eta \to \pi^+\pi^-\pi^0$	42.7%	57.1%	35.4%
$D_s^+ \to \phi\mu^+\nu$	24.9%	18.9%	10.0%
$D_s^+ \to \eta'\mu^+\nu,\ \eta' \to \gamma\varrho^0$	24.9%	35.2%	16.4%
$D_s^+ \to \eta\mu^+\nu,\ \eta \to \pi^+\pi^-\pi^0$	26.1%	33.4%	15.8%

[*] The cut efficiency is normalized to $L/\sigma_L > 0$; all the other analysis cuts have been applied.

Residual contamination from $D_s^+ \to \eta\mu^+\nu$ is computed using the CLEO branching ratio for $\frac{BR(D_s^+\to\eta e^+\nu)}{BR(D_s^+\to\phi e^+\nu)}$ and fully reconstructing the decay $D_s^+ \to \phi\mu^+\nu$ from E687 data. The estimated number of $D_s^+ \to \eta\mu^+\nu$ events is entered as a fixed components in the fit. Any residual signal from partially reconstructed $\eta\mu^+\nu$ decays is then interpreted as originating from D^+ and included in the fit.

Contamination from $D_s^+ \to \eta'\mu^+\nu,\ \eta' \to \varrho^0\gamma$ can also be estimated using the CLEO result $\frac{BR(D_s^+\to\eta' e^+\nu)}{BR(D_s^+\to\phi e^+\nu)}$ and is then inserted as a fixed component in the fit. On the other hand, decay events from $D^+ \to \eta'\mu^+\nu,\ \eta' \to \varrho^0\gamma$ are indistinguishable, from the point of view of our reconstruction algorithm, from decay events of the form $D^+ \to \varrho^0\mu^+\nu$. (We can not separately measure the decay $D^+ \to \eta'\mu^+\nu,\ \eta' \to \varrho^0\gamma$ because of our low reconstruction efficiency for γ). Therefore, in what follows, the decay $D^+ \to \varrho^0\mu^+\nu$ will always have to

Table 5.3.3 Mass cut efficiency for D^+ decays

decay	$1.0/1.2 < M(h\pi\mu) < 1.8$	$0.25 < M(h\pi\mu) - M(h\mu)$	both cuts
$K^{*0}\mu^+\nu$	99.2%	92.9%	92.2%
$\varrho^0\mu^+\nu$	59.0%	95.2%	55.3%
$\eta'\mu^+\nu,\ \eta' \to \gamma\varrho^0$	56.5%	97.5%	55.3%
$\eta'\mu^+\nu,\ \eta' \to \eta\pi^+\pi^-$	0.03%	48.2 %	0.03%
$\eta'\mu^+\nu,\ \eta' \to \eta\pi^0\pi^0$ $\eta \to \pi^+\pi^-\pi^0$	0.2%	49.7%	0.2 %
$\eta'\mu^+\nu,\ \eta' \to \eta\pi^0\pi^0$ $\eta \to \pi^+\pi^-\gamma$	2.4%	66.1%	1.9 %
$\eta\mu^+\nu,\ \eta \to \pi^+\pi^-\pi^0$	20.1 %	66.0 %	16.3 %
$\eta\mu^+\nu,\ \eta \to \pi^+\pi^-\gamma$	35.7 %	73.1%	28.6%
$\omega^0\mu^+\nu,\ \omega^0 \to \pi^+\pi^-\pi^0$	21.4%	75.0%	18.0%
$K^{*0}\mu^+\nu,\ K/\pi$ misid	34.6%	91.1 %	30.5%
$K^-\mu^+\nu$ tag	74.4%	0.04%	0%
$\pi^-\mu^+\nu$ tag	56.0%	3.5%	0%

be considered in an *inclusive* sense, since the reconstructed ϱ^0 may originate from the decay $\eta' \to \varrho^0\gamma$.

Background from $D^+ \to \omega^0\mu^+\nu,\ \omega^0 \to \pi^+\pi^-\pi^0$ can also contaminate the $M(\pi^+\pi^-)$ distribution in the region between the partially reconstructed η and the ϱ^0. Unfortunately, this source of contamination can not be estimated a priori, since the decay has never been observed. Because of the invariant mass cuts, the reconstruction efficiency for $D^+ \to \omega^0\mu^+\nu$ is about three times lower than for $D^+ \to \varrho^0\mu^+\nu$. In the data plots in Figure 5.2.2, a large ω^0 contamination is not apparent. However, it is not possible to make a precise

Table 5.3.4 Global reconstruction efficiency for D^+, D_s^+ decays [*]

decay	D^+	D_s^+
$K^{*0}\mu^+\nu$	$6.3 \cdot 10^{-3}$	
$\varrho^0\mu^+\nu$	$4.7 \cdot 10^{-3}$	
$\eta'\mu^+\nu,\ \eta' \to \gamma\varrho^0$	$4.7 \cdot 10^{-3}$	$1.9 \cdot 10^{-3}$
$\eta'\mu^+\nu,\ \eta' \to \eta\pi^+\pi^-$	$3.7 \cdot 10^{-6}$	$5 \cdot 10^{-6}$
$\eta'\mu^+\nu,\ \eta' \to \eta\pi^0\pi^0,\ \eta \to \pi^+\pi^-\pi^0$	$1.2 \cdot 10^{-5}$	$1.9 \cdot 10^{-5}$
$\eta'\mu^+\nu,\ \eta' \to \eta\pi^0\pi^0,\ \eta \to \pi^+\pi^-\gamma$	$1.7 \cdot 10^{-4}$	$8.6 \cdot 10^{-5}$
$\eta\mu^+\nu,\ \eta \to \pi^+\pi^-\pi^0$	$1.2 \cdot 10^{-3}$	$5.4 \cdot 10^{-4}$
$\eta\mu^+\nu,\ \eta \to \pi^+\pi^-\gamma$	$2.4 \cdot 10^{-3}$	$8.2 \cdot 10^{-4}$
$\omega^0\mu^+\nu,\ \omega^0 \to \pi^+\pi^-\pi^0$	$1.5 \cdot 10^{-3}$	
$K^{*0}\mu^+\nu,\ \ K/\pi$ misid	$2.0 \cdot 10^{-4}$	

[*] Average of 1990 and 1991 runs. All analysis cuts are applied, including $L/\sigma_L > 20$.

estimate of the contamination, since we can not fit to the broad $M(\pi^+\pi^-)$ mass peak from $\omega^0 \to \pi^+\pi^-\pi^0$. Therefore, we ignore this possible source of contamination.

5.3.3 Tag D^0 semileptonic decays

D^*-tag semileptonic decays such as $D^{*+} \to D^0\tilde{\pi}^+,\ D^0 \to K^-\mu^+\nu$ and $D^{*+} \to D^0\tilde{\pi}^+,\ D^0 \to \pi^-\mu^+\nu$ can contaminate the $D^+ \to \overline{K}^{*0}\mu^+\nu$ and $D^+ \to \varrho^0\mu^+\nu$ distributions, respectively, if the soft pion $\tilde{\pi}^+$ from the primary vertex is erroneously assigned to the secondary. This kind of background could be reduced by applying some $iso1$ cut, i.e. requiring that tracks from the primary not be compatible with coming from the secondary. We found that this cut,

although effective in rejecting some contamination, is not as efficient as one would hope.

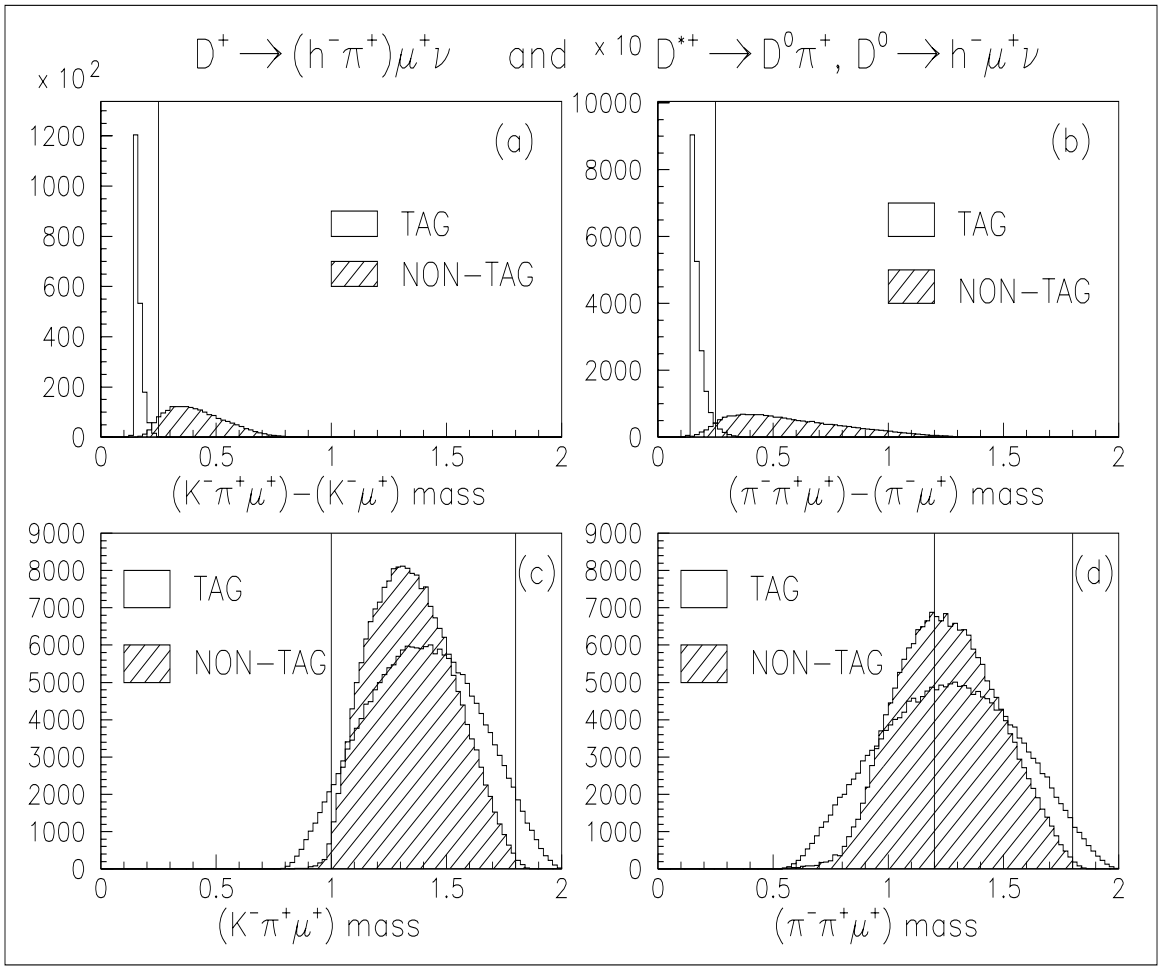

Figure 5.3.3 Comparison of mass distributions for D^* tag and non-tag decays. The vertical lines indicate the position of the mass cuts. The combined effect of the two cuts $M(h^-\pi^+\mu^+) - M(h^-\mu^+) > 0.25\ GeV/c^2$ and $1.0/1.2 < M(h^-\pi^+\mu^+) < 1.8\ GeV/c^2$ removes any D^*-tag background.

A better tool to suppress D^*-tag background consists in imposing a lower limit on the mass difference $M(h^-\pi^+\mu^+)-M(h^-\mu^+)$. If the π^+ assigned to the secondary is indeed a soft pion from the primary, the mass difference would

peak around the value $M(D^{*+}) - M(D^0)$. (The mass difference peaks are broader than those reconstructed in the $D^0 \to h^-\mu^+\nu$ tag analysis, because here we do not attempt to reconstruct the neutrino momentum, and therefore we are missing a portion of the "D^* mass".) If the π^+ truly originates from the secondary vertex, the mass difference will be more broadly distributed. In Figure 5.3.3 (a), (b) we compare the two distributions for tag and non-tag decays, for both cases $h^- = K^-$ and $h^- = \pi^-$. Our cut $M(h^-\pi^+\mu^+) - M(h^-\mu^+) > 0.25\ GeV/c^2$ eliminates all contamination from D^*-tag sources.

The effectiveness of this cut for a real data signal can also be observed in Figure 5.3.4. Plot (a) shows the $D^{*+} \to D^0\tilde{\pi}^+$, $D^0 \to K^{*-}\mu^+\nu$ signal reconstructed with all the analysis cuts described in the text except for the cut on the mass difference (and $L/\sigma_L > 5$ instead of $L/\sigma_L > 20$). The big bump on the left side of the $\overline{K}^{*0}(892)$ peak is due to tag decays $D^{*+} \to D^0\tilde{\pi}^+$, $D^0 \to K^-\mu^+\nu$, where the K^- and the $\tilde{\pi}^+$ are combined to form the two-body invariant mass. (The bump is significantly reduced if higher L/σ_L cuts are applied, because of the shorter lifetime of the D^0 relative to the D^+.) Plot (b) shows the same distribution after the cut $M(h^-\pi^+\mu^+) - M(h^-\mu^+) > 0.25\ GeV/c^2$ has been applied: the bump has disappeared.

5.3.4 Hadron-lepton misidentification background

Charm meson hadronic decays, where one of the decay products is misidentified as a muon, may contaminate the invariant mass distributions of $(h^-\pi^+)\mu^+$ candidates. The h/μ misidentification background is estimated with exactly the same technique which was applied to the $D^0 \to h^-\mu^+\nu$ tag analysis (see section § 4.3.2). Briefly, we run the analysis algorithm on a subsample of the full data set, with identification requirements on the "μ^+"

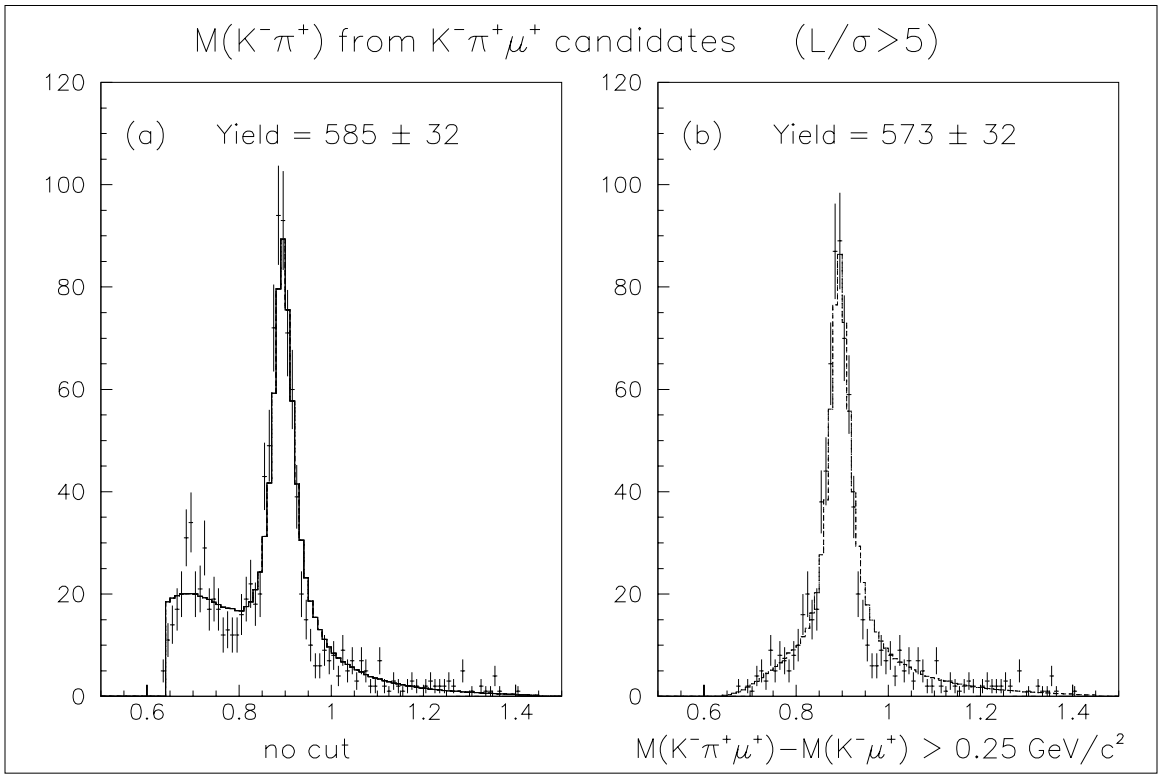

Figure 5.3.4 Effect of the cut $M(h^-\pi^+\mu^+) - M(h^-\mu^+) > 0.25\ GeV/c^2$ on the $D^+ \to \overline{K}^{*0}\mu^+\nu$ signal. The bump on the left of plot (a) is due to tag decays $D^{*+} \to D^0\tilde{\pi}^+$, $D^0 \to K^-\mu^+\nu$, and disappears when the cut is imposed. The efficiency of the cut on data matches quite well with the Monte Carlo computed efficiency listed in Table 5.3.3. In the plots, the crosses represent the data points and the solid line is the result of the fit.

prong exactly opposite to our standard muon identification. We thus obtain a mass distribution for the h/μ misidentification background. Each entry in the distribution is then scaled according to the momentum-dependent misidentification probability, and multiplied by a boosting factor to scale to the full data sample. In Figures 5.3.5 (a)-(d) we show the estimated misidentification background for both the $\overline{K}^{*0}\mu^+\nu$ and $\varrho^0\mu^+\nu$ mass distributions, and compare it to the signal level.

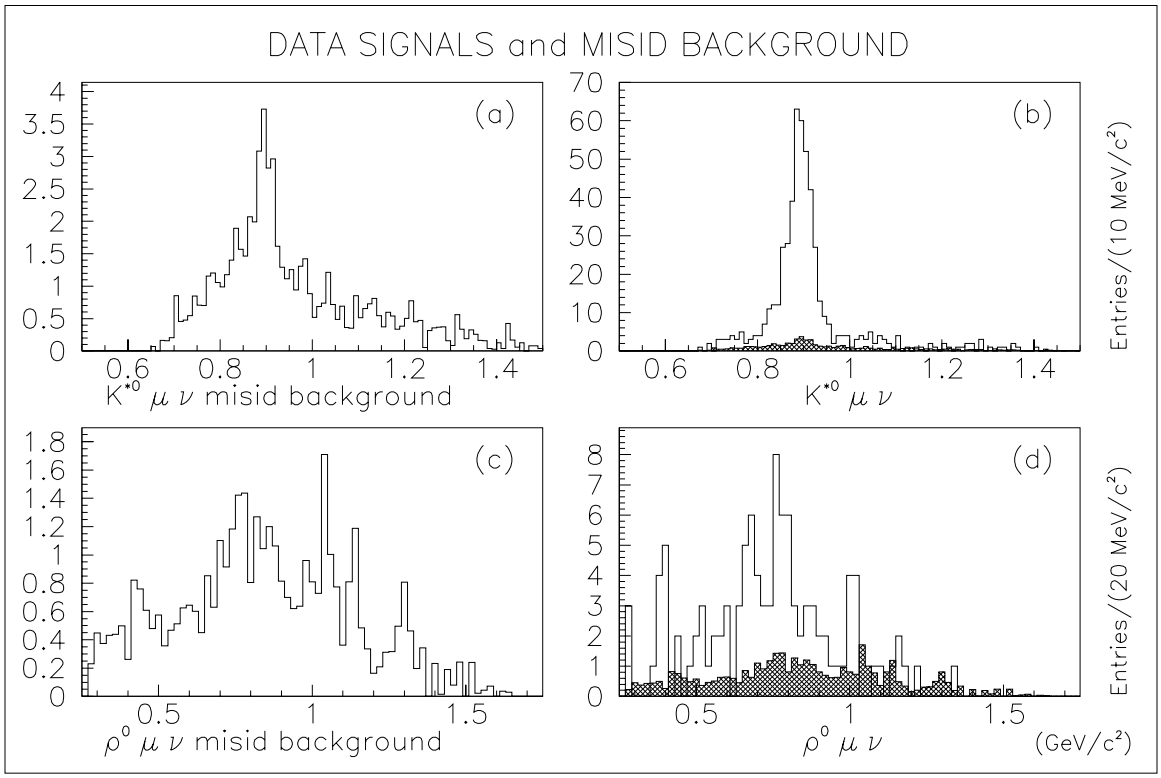

Figure 5.3.5 Estimated h/μ misidentification background for the $\overline{K}^{*0}\mu^+\nu$ (a) and $\varrho^0\mu^+\nu$ (c) data histograms. In plots (b) and (d) we compare the level of the misid background (hatched style) to that of the signals.

5.4 The fit

5.4.1 Fitting technique

To fit the data histograms, we use the same *binned maximum likelihood* technique which was employed for the $D^0 \to h^-\mu^+\nu$ tag analysis (see section § 4.4). The likelihood is defined as:

$$\mathcal{L} = \prod_{i=1}^{\#\text{bins}} \frac{n_i^{s_i} e^{-n_i}}{s_i!},$$

where

s_i = number of events in bin i of data histogram,

n_i = number of events in bin i of fit histogram.

We construct separate likelihood functions for the $D^+ \to \overline{K}^{*0}\mu^+\nu$, $D_s^+ \to \phi\mu^+\nu$ and $D^+ \to \varrho^0\mu^+\nu$ data histograms, and for the 1990 and 1991 runs. In each case, the fit histogram is constructed using the signal shape from Monte Carlo[37] (see Figure 5.4.1) and our best knowledge of all the background sources involved.

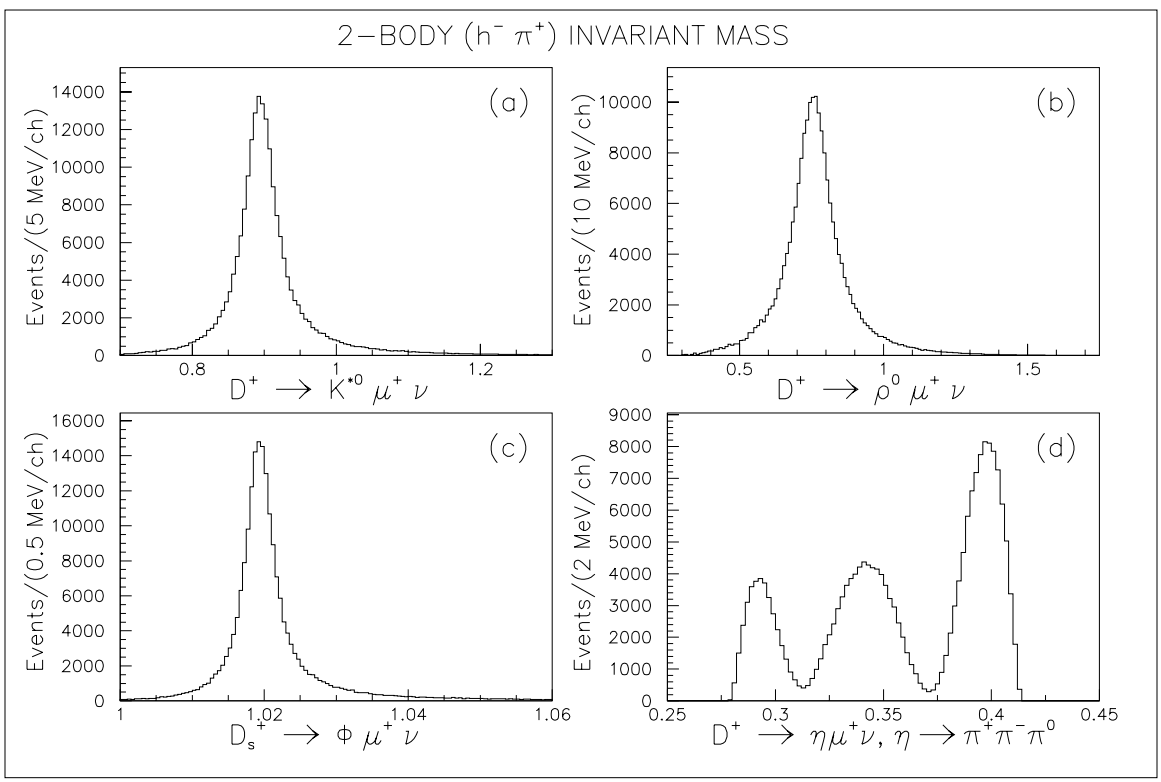

Figure 5.4.1 Two body $M(h^-\pi^+)$ mass distribution for several semileptonic decays. In plots (a), (b), (c) the mass spectrum of the vector meson resonance was produced according to a p-wave Breit-Wigner parameterization[37]. In plot (d), the full matrix element for the three-body decay $\eta \to \pi^+\pi^-\pi^0$ was used; when binned at 20 MeV/ch, this distribution appears as shown in Figure 5.3.1 (g).

5.4.2 The $\overline{K}^{*0}\mu^+\nu$ fit

The $\overline{K}^{*0}\mu^+\nu$ fit histogram is composed of only two components:

1. The $D^+ \to \overline{K}^{*0}\mu^+\nu$ signal, with shape given by the Monte Carlo (see Figure 5.3.1 (a)) and yield which is a parameter of the fit;
2. Background from h/μ misidentification, which is fixed in the fit.

The number of entries in bin i of the fit histograms is then defined as:

$$n_i = Y_{K^*\mu\nu} S_{1i} + \mathcal{M} S_{2i}$$

where $Y_{K^*\mu\nu}$ is the $D^+ \to \overline{K}^{*0}\mu^+\nu$ yield, S_i are the normalized Monte Carlo shapes and $\mathcal{M}$ is the h/μ misidentification background.

The result of the fit is shown in Figure 5.4.2 for $L/\sigma_L > 20$. We find 228.8 ± 16.2 events in 1990 and 214.2 ± 15.3 events in 1991, for a combined yield of $Y_{K^*\mu\nu} = 443.0 \pm 22.3$. In Figure 5.4.3 (a) we show the surviving $Y_{K^*\mu\nu}$ for increasing L/σ_L requirements, and compare it to the Monte Carlo prediction.

5.4.3 The $\phi\mu^+\nu$ fit

$D_s^+ \to \phi\mu^+\nu$ decay candidates are reconstructed with the same analysis algorithm used for $D^+ \to \overline{K}^{*0}\mu^+\nu$ and $D^+ \to \varrho^0\mu^+\nu$ candidates, but with slightly different analysis cuts. Both kaons from the decay $\phi \to K^+K^-$ are required to be either kaon definite or kaon/proton ambiguous (istatp$= 4, 12$). Due to the shorter D_s^+ lifetime, no out of target requirement is imposed, and a looser detachment between primary and secondary vertex is required: $L/\sigma_L > 5$. Also, no requirement on the three-body mass $M(K^+K^-\mu^+)$ or on the mass difference $M(K^+K^-\mu^+) - M(K^-\mu^+)$ is imposed, as there is not a large charm semileptonic background which needs to be suppressed.

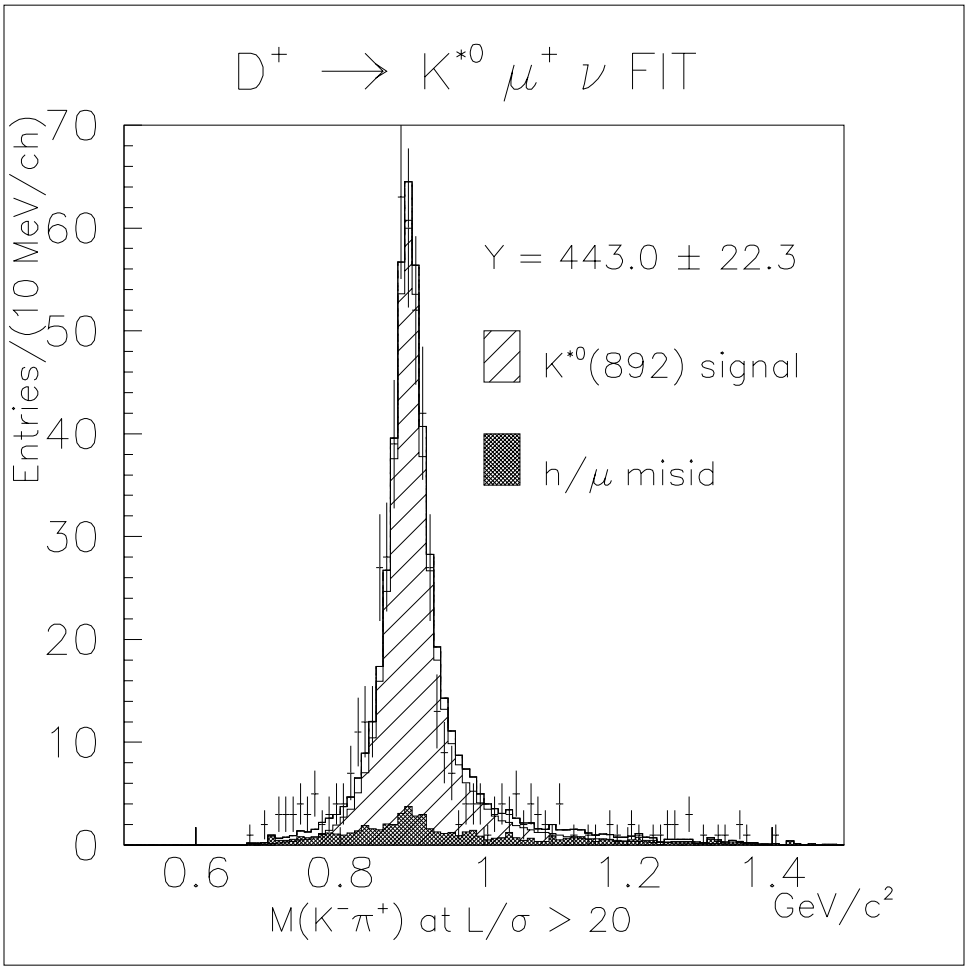

Figure 5.4.2 Fit to the $\overline{K}^{*0}\mu^+\nu$ histogram (1990 and 1991 data are combined). The crosses are the data points, the solid line is the fit.

The $D_s^+ \to \phi\mu^+\nu$ fit histogram is composed of two components:

1. The $D_s^+ \to \phi\mu^+\nu$ signal, with shape given by the Monte Carlo and yield which is a parameter of the fit;
2. A linear function for the background.

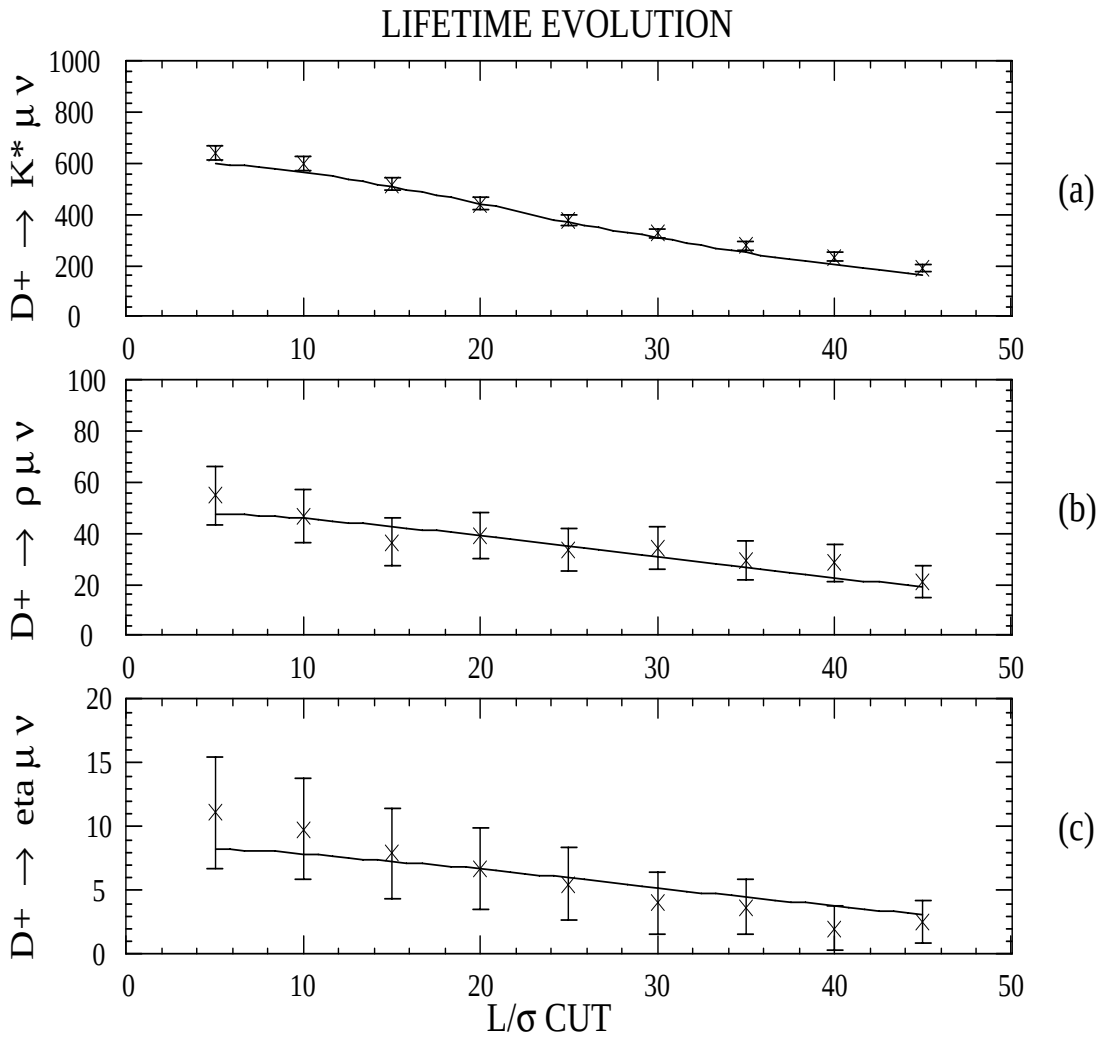

Figure 5.4.3 Surviving yield as function of the L/σ_L cut, for different D^+ decay signals. The crosses indicate the fitted data yield, the solid line represents the Monte Carlo prediction. The two curves are normalized at $L/\sigma_L > 20$.

The number of entries in bin i of the fit histograms is then defined as:

$$n_i = Y_{\phi\mu\nu} S_i + (b_1 + b_2\ x_i)\ ,$$

where $Y_{\phi\mu\nu}$ is the $D_s^+ \to \phi\mu^+\nu$ yield, $x = M(K^-K^+) - (M(K^-) + M(K^+))$

(the fixed threshold value is subtracted) and b_1, b_2 are the two additional fit parameters for the background.

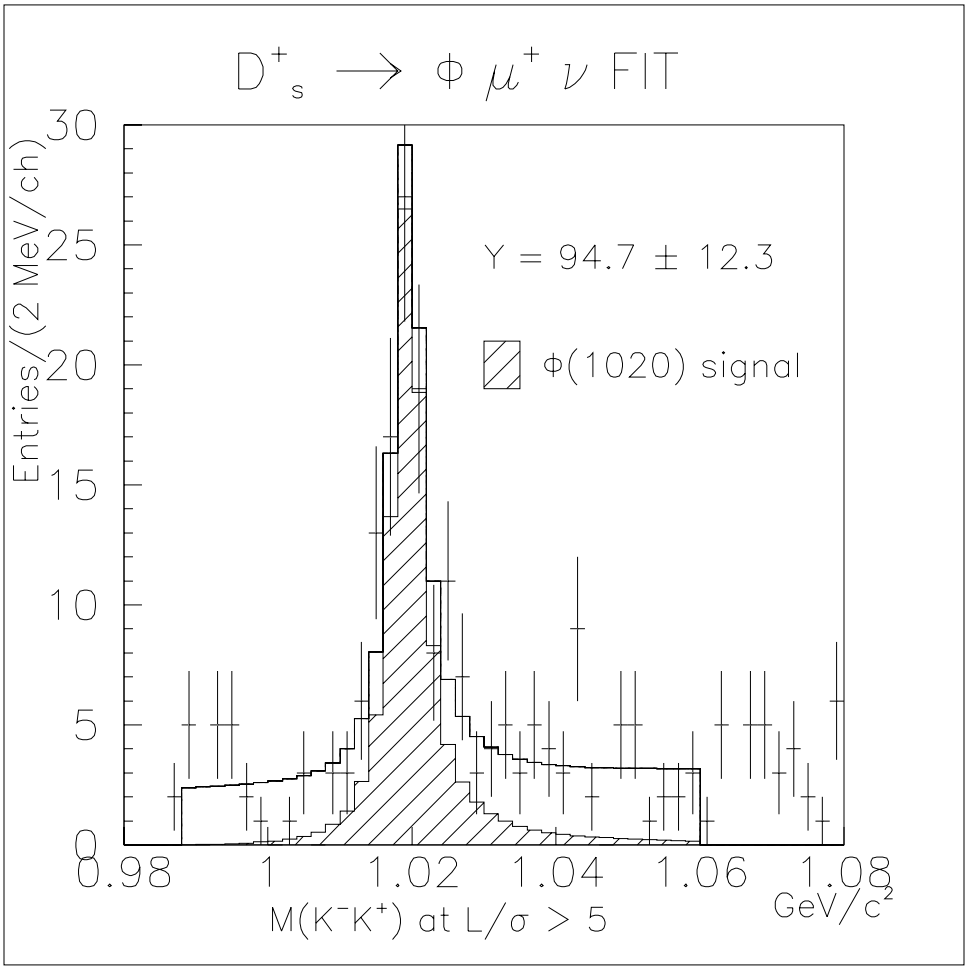

Figure 5.4.4 Fit to the $\phi\mu^+\nu$ histogram (1990 and 1991 data are combined). The crosses are the data points, the solid line is the fit. A second degree polynomial is used to parameterize the background.

The result of the fit is shown in Figure 5.4.4 for $L/\sigma_L > 5$. We find 52.7 ± 9.2 events in 1990 and 42.0 ± 8.1 events in 1991, for a combined yield of $Y_{\phi\mu\nu} = 94.7 \pm 12.3$.

5.4.4 The $\varrho^0\mu^+\nu$ fit

The $\varrho^0\mu^+\nu$ data histogram is more complicated than the $\overline{K}^{*0}\mu^+\nu$ and $\phi\mu^+\nu$ histograms. The corresponding fit histogram is composed of the following components:

1. The $D^+ \to \varrho^0\mu^+\nu$ signal, with the shape given by the Monte Carlo (see Figure 5.3.1 (b)) and a yield which is a parameter of the fit;
2. The feedthrough from the $D^+ \to \overline{K}^{*0}\mu^+\nu$ signal (where the K^- is misidentified as a π^-), with the shape fixed by the Monte Carlo (see Figure 5.3.1 (b)) and a yield which depends on the previously fitted value for $Y_{K^*\mu\nu}$;
3. Background from $D_s^+ \to \eta'\mu^+\nu,\ \eta' \to \gamma\varrho^0$, with the shape given by the Monte Carlo (see Figure 5.3.1 (c)) and a yield which depends on the fitted value for $Y_{\phi\mu\nu}$ through the branching ratio $\frac{BR(D_s^+\to\eta' e^+\nu)}{BR(D_s^+\to\phi e^+\nu)}$ measured by CLEO.
4. Various background contributions from $D_s^+ \to \eta'\mu^+\nu$, $\eta' \to \pi^+\pi^-X$, with the shapes taken from Monte Carlo (see Figures 5.3.1 (d)-(f)) and the yields which depend on $Y_{\phi\mu\nu}$ and $\frac{BR(D_s^+\to\eta'\ e^+\ \nu)}{BR(D_s^+\to\phi\ e^+\ \nu)}$.
5. Background from $D_s^+ \to \eta\mu^+\nu$, where $\eta \to \pi^+\pi^-\pi^0$ or $\eta \to \pi^+\pi^-\gamma$, with the shapes taken from Monte Carlo (see Figures 5.3.1 (g),(h)) and the yields depending on $Y_{\phi\mu\nu}$ and $\frac{BR(D_s^+\to\eta\ e^+\ \nu)}{BR(D_s^+\to\phi\ e^+\ \nu)}$.
6. Background from $D^+ \to \eta\mu^+\nu$, $\eta \to \pi^+\pi^-\pi^0$ or $\eta \to \pi^+\pi^-\gamma$, with the shapes taken from Monte Carlo (see Figures 5.3.1 (g),(h)) and a yield which is considered as a parameter of the fit.
7. Background from h/μ misidentification, which is fixed in the fit.

The number of entries in bin i of the fit histogram is then defined as:

$$
\begin{aligned}
n_i = {} & Y_{\varrho\mu\nu}\ S_{1i} + \frac{Y_{K^*\mu\nu}}{\epsilon(K^*\mu\nu)}\ \epsilon(K^*\mu\nu \to \varrho\mu\nu)\ S_{2i} \\
& + \frac{Y_{\phi\mu\nu}}{\epsilon(\phi\mu\nu, K^-K^+)} \frac{1}{BR(\phi \to K^-K^+)} \times \\
& \Bigg\{ \boldsymbol{\mathcal{A}} \cdot \Bigg[BR(\eta' \to \gamma\varrho^0)\ \epsilon(\eta'\mu^+\nu,\ \gamma\varrho^0)\ S_{3i} \\
& + BR(\eta' \to \eta\pi^+\pi^-)\ \epsilon(\eta'\mu^+\nu,\ \eta\pi^+\pi^-)\ S^a_{4i} \\
& + BR(\eta' \to \eta\pi^0\pi^0)\ BR(\eta \to \pi^+\pi^-\pi^0)\ \epsilon(\eta'\mu^+\nu,\ \eta\pi^0\pi^0,\ \pi^+\pi^-\pi^0)\ S^b_{4i} \\
& + BR(\eta' \to \eta\pi^0\pi^0)\ BR(\eta \to \pi^+\pi^-\gamma)\ \epsilon(\eta'\mu^+\nu,\ \eta\pi^0\pi^0,\ \pi^+\pi^-\gamma)\ S^c_{4i} \Bigg] \\
& + \boldsymbol{\mathcal{B}} \cdot \Bigg[BR(\eta \to \pi^+\pi^-\pi^0)\ \epsilon(\eta\mu^+\nu,\ \pi^+\pi^-\pi^0)\ S^a_{5i} \\
& + BR(\eta \to \pi^+\pi^-\gamma)\ \epsilon(\eta\mu^+\nu,\ \pi^+\pi^-\gamma)\ S^b_{5i} \Bigg] \Bigg\} \\
& + Y_{\eta\mu\nu} \Bigg[S^a_{6i} + \frac{\epsilon(\eta\mu\nu,\ \pi^+\pi^-\gamma)}{\epsilon(\eta\mu\nu, \pi^+\pi^-\pi^0)} \frac{BR(\eta \to \pi^+\pi^-\gamma)}{BR(\eta \to \pi^+\pi^-\pi^0)}\ S^b_{6i} \Bigg] + \boldsymbol{\mathcal{M}}\ S_{7i}\ ,
\end{aligned}
$$

where: $Y_{\varrho\mu\nu}$ is the fitted yield for $D^+ \to \varrho^0\mu^+\nu$; $Y_{\eta\mu\nu}$ is the fitted yield for $D^+ \to \eta\mu^+\nu$, $\eta \to \pi^+\pi^-\pi^0$; $\boldsymbol{\mathcal{A}} = \frac{BR(D_s^+ \to \eta' e^+\nu)}{BR(D_s^+ \to \phi e^+\nu)}$; $\boldsymbol{\mathcal{B}} = \frac{BR(D_s^+ \to \eta e^+\nu)}{BR(D_s^+ \to \phi e^+\nu)}$; $\boldsymbol{\mathcal{M}}$ is the number of $\varrho^0\mu^+\nu$ background events from h/μ misidentification, and as usual ϵ denotes an efficiency, S_i a normalized Monte Carlo shape and BR a branching ratio.

The total likelihood function for the $\varrho^0\mu^+\nu$ histogram is constructed as:

$$
\boldsymbol{\mathcal{L}}_{\varrho\mu\nu} = \left\{ \prod_{i=1}^{\#\text{bins}} \frac{n_i^{s_i} e^{-n_i}}{s_i!} \right\} \times exp\left\{ -\frac{1}{2} \left[\frac{\boldsymbol{\mathcal{A}} - A_0}{\sigma_{A_0}} \right]^2 \right\} \times exp\left\{ -\frac{1}{2} \left[\frac{\boldsymbol{\mathcal{B}} - B_0}{\sigma_{B_0}} \right]^2 \right\}
$$

to allow the two ratios $\boldsymbol{\mathcal{A}}$, $\boldsymbol{\mathcal{B}}$ to fluctuate within the error around the measured value $A_0 = 0.43 \pm 0.11 \pm 0.07$ and $B_0 = 1.24 \pm 0.12 \pm 0.15$[36], respectively.

Overall, the likelihood depends on four unknown parameters: $Y_{\varrho\mu\nu}$, $Y_{\eta\mu\nu}$, $\mathcal{A}$ and $\mathcal{B}$.

The various components of the fit are shown in Figures 5.4.5 (a) and (b) for $L/\sigma_L > 20$. The corresponding fitted yields are listed in Table 5.4.1. In particular, the fit returns 16.1 ± 6.5 $D^+ \to \varrho^0\mu^+\nu$ events in 1990 and 23.0 ± 6.3 events in 1991, for a combined yield of $Y_{\varrho\mu\nu} = 39.2 \pm 9.0$. The combined fitted yield for the decay $D^+ \to \eta\mu^+\nu$, $\eta \to \pi^+\pi^-\pi^0$ is $Y_{\eta\mu\nu} = 6.7 \pm 3.1$. The values returned for the two fitting parameters $\mathcal{A}$, $\mathcal{B}$ in 1990 and 1991 can be found in Table 5.4.2.

Table 5.4.1 Fitted yields

decay	1990	1991	90+91
$D^+ \to \overline{K}^{*0}\mu^+\nu$	228.8 ± 16.2	214.2 ± 15.3	443.0 ± 22.3
$D^+ \to \varrho^0\mu^+\nu$	16.1 ± 6.5	23.0 ± 6.3	39.2 ± 9.0
$D^+ \to \overline{K}^{*0}\mu^+\nu$, K/π misid	7.9 ± 1.0	6.2 ± 0.9	14.1 ± 1.3
$D_s^+ \to \eta'\mu^+\nu$, $\eta' \to \gamma\varrho^0$	2.4 ± 0.9	1.8 ± 0.6	4.2 ± 1.1
$D_s^+ \to \eta\mu^+\nu$, $\eta \to \pi^+\pi^-\pi^0$	1.6 ± 0.4	1.2 ± 0.3	2.8 ± 0.5
$D_s^+ \to \eta\mu^+\nu$, $\eta \to \pi^+\pi^-\gamma$	0.5 ± 0.1	0.4 ± 0.1	0.9 ± 0.1
$D^+ \to \eta\mu^+\nu$, $\eta \to \pi^+\pi^-\pi^0$	3.0 ± 2.3	3.7 ± 2.1	6.7 ± 3.1
$D^+ \to \eta\mu^+\nu$, $\eta \to \pi^+\pi^-\gamma$	1.1 ± 0.9	1.6 ± 0.9	2.7 ± 1.3

Table 5.4.2 Other fit parameters

fit parameter	1990	1991
$\mathcal{A} = \frac{BR\ (D_s^+ \to \eta'\mu^+\nu)}{BR\ (D_s^+ \to \phi\mu^+\nu)}$	0.43 ± 0.13	0.42 ± 0.13
$\mathcal{B} = \frac{BR(D_s^+ \to \eta\mu^+\nu)}{BR(D_s^+ \to \phi\mu^+\nu)}$	1.23 ± 0.19	1.24 ± 0.19

In Figures 5.4.3 (b), (c) we compare the surviving yields for $D^+ \to \varrho^0\mu^+\nu$ and $D^+ \to \eta\mu^+\nu$ (respectively) to the corresponding Monte Carlo samples, for increasing L/σ_L cuts. It can be noticed that in both cases the fitted yield agrees well with the predicted D^+ lifetime evolution.

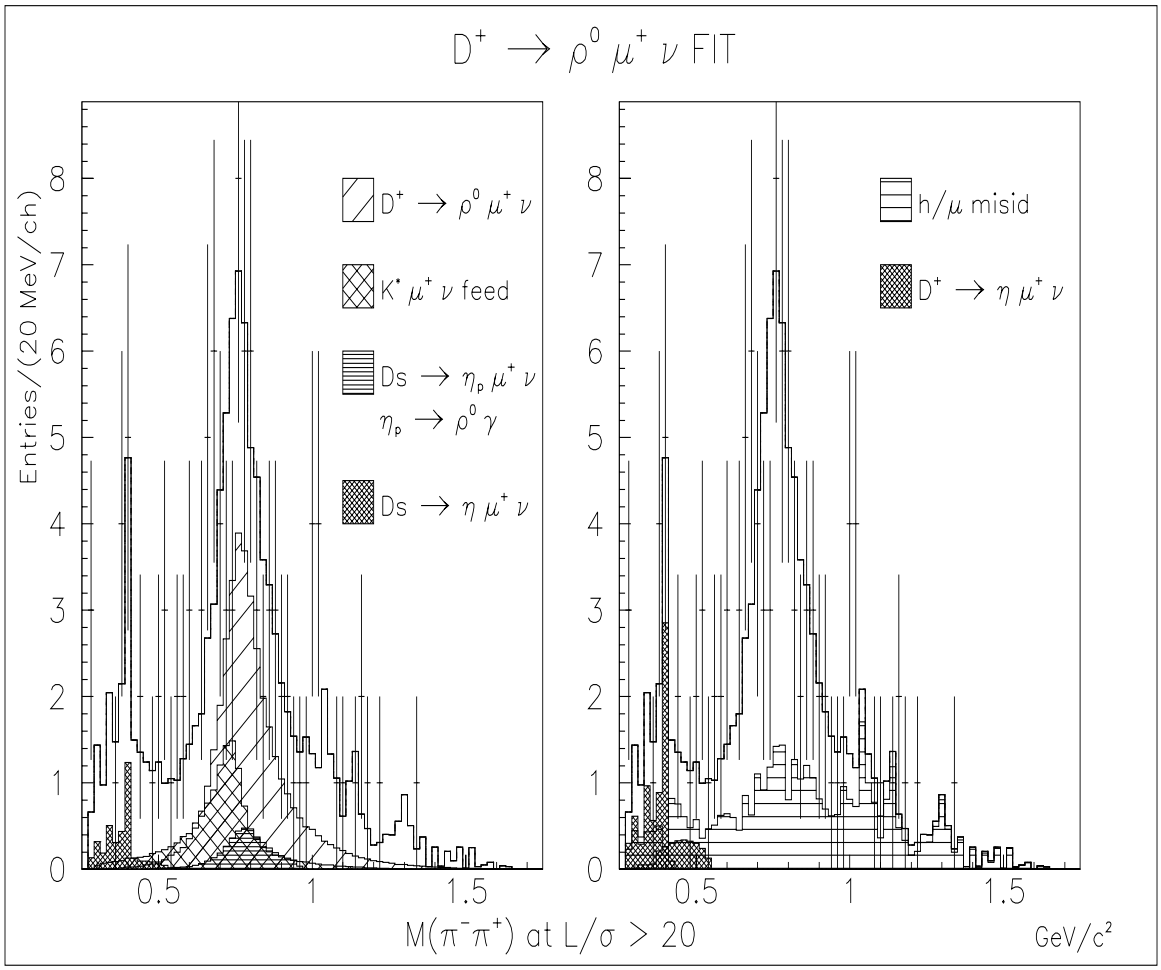

Figure 5.4.5 Fit to the $\varrho^0\mu^+\nu$ histogram (1990 and 1991 data are combined). The crosses are the data points, the solid line is the fit. The various fit components are superimposed with different hatching styles.

5.5 Branching ratio measurements

We use the fitted yields and the Monte Carlo computed efficiencies to measure the relative branching ratios of the D^+ decay channels $D^+ \to \overline{K}^{*0}\mu^+\nu$, $D^+ \to \varrho^0\mu^+\nu$ and $D^+ \to \eta\mu^+\nu$. We find:

$$\frac{BR\ (D^+ \to \varrho^0\mu^+\nu)}{BR\ (D^+ \to \overline{K}^{*0}\mu^+\nu)} = \frac{Y_{\varrho\mu\nu}/\epsilon(\varrho\mu\nu)}{Y_{K^*\mu\nu}/\epsilon(K^*\mu\nu,\ K^* \to K^-\pi^+)}\ BR(\overline{K}^{*0} \to K^-\pi^+)$$
$$= \ 0.0790 \pm 0.0188$$

$$\frac{BR\ (D^+ \to \eta\mu^+\nu)}{BR\ (D^+ \to \varrho^0\mu^+\nu)} = \frac{Y_{\eta\mu\nu}/\epsilon(\eta\mu\nu,\ \eta \to \pi^+\pi^-\pi^0)}{Y_{\varrho\mu\nu}/\epsilon(\varrho\mu\nu)}\frac{1}{BR(\eta \to \pi^+\pi^-\pi^0)}$$
$$= \ 2.83 \pm 1.45$$

In Tables 5.5.1 we report the fitted yields, the Monte Carlo efficiencies and the measured branching ratios for the 1990 and 1991 runs. The 1990 and 1991 branching ratios are combined with a weighted average to obtain the final result.

Table 5.5.1 1990 and 1991 branching ratios

	1990 Yield	1990 Efficiency	1991 Yield	1991 Efficiency
$\overline{K}^{*0}\mu^+\nu$	228.8 ± 16.2	$0.742 \pm 0.014\%$	214.2 ± 15.3	$0.526 \pm 0.011\%$
$\varrho^0\mu^+\nu$	16.1 ± 6.5	$0.550 \pm 0.012\%$	23.0 ± 6.3	$0.392 \pm 0.010\%$
$\eta\mu^+\nu$	3.0 ± 2.3	$0.148 \pm 0.006\%$	3.7 ± 2.1	$0.097 \pm 0.005\%$
$\frac{BR\ (D^+\to\varrho^0\mu^+\nu)}{BR\ (D^+\to\overline{K}^{*0}\mu^+\nu)}$	0.0634 ± 0.0260		0.0960 ± 0.0272	
$\frac{BR\ (D^+\to\eta\mu^+\nu)}{BR\ (D^+\to\varrho^0\mu^+\nu)}$	2.92 ± 2.54		2.79 ± 1.77	

In Figures 5.5.1 (a), (b) we show the two measured branching ratios for increasing L/σ_L cuts. In both cases the agreement between the 1990 and 1991 values is not very good, except in the region around $L/\sigma_L > 20$, where the measurement is performed. Nevertheless, the combined 1990+1991 branching ratios appear to be reasonably stable with L/σ_L.

5.6 Systematic error studies

In order to evaluate a possible systematic bias in our measurements, we apply the same techniques which were used for the $D^0 \to h^- \mu^+ \nu$ tag analysis. Because of the nearly identical topology, most of the systematic uncertainty will cancel out when computing the branching ratio of the two decays (this should be true at least for the two completely reconstructed decays $D^+ \to \varrho^0 \mu^+ \nu$ and $D^+ \to \overline{K}^{*0} \mu^+ \nu$). In the case of the $\frac{BR\ (D^+ \to \eta \mu^+ \nu)}{BR\ (D^+ \to \varrho^0 \mu^+ \nu)}$ measurement, the reliability of our systematic checks will be limited by the poor statistical significance of the signal.

5.6.1 Split sample systematic errors

In order to investigate possible bias originating from specific analysis cuts, we divide the total data sample into two approximately equal, statistically independent subsamples, below and above a particular value of the cut. We perform the measurement for the two independent subsamples and compare the results to the value obtained with the total data sample. In Table 5.6.1 we list the analysis cuts considered and the corresponding discriminating values.

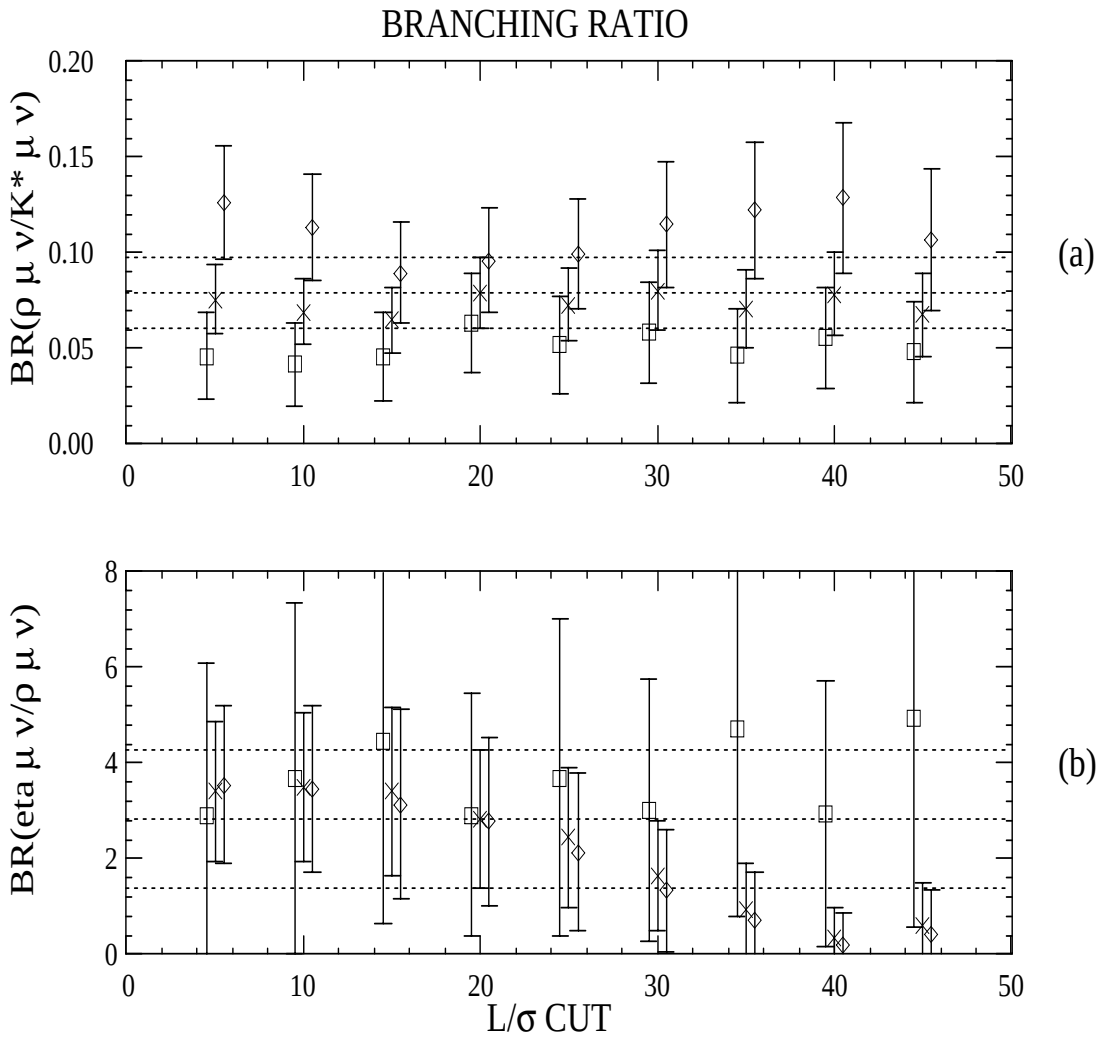

Figure 5.5.1 Measured ratio of branching fractions as function of the L/σ_L cut. Squares are the 1990 values, diamonds are the 1991 values, and crosses are the weighted-average combined results.

In Figure 5.6.1 we plot the branching ratio measured with each subsample, for both $\frac{BR\ (D^+ \to \varrho^0 \mu^+ \nu)}{BR\ (D^+ \to \overline{K}^{*0} \mu^+ \nu)}$ and $\frac{BR\ (D^+ \to \eta \mu^+ \nu)}{BR\ (D^+ \to \varrho^0 \mu^+ \nu)}$. It can be seen that all the

Table 5.6.1 Split samples cuts

Variable	Cut value
L/σ_L	$L/\sigma_L < 45$; $L/\sigma_L > 45$
cls	$cls < 50\%$; $cls > 50\%$
$iso2$	$iso2 = 0$; $iso2 \neq 0$
$M(h^-\pi^+\mu^+)$	$M(h^-\pi^+\mu^+) < 1.4\ GeV/c^2$; $M(h^-\pi^+\mu^+) > 1.4 GeV/c^2$
$M(h^-\pi^+\mu^+)$	$M(K^-\pi^+\mu^+) - M(K^-\mu^+) < 0.45$; $M(K^-\pi^+\mu^+) - M(K^-\mu^+) > 0.45\ GeV/c^2$
$-M(h^-\mu^+)$	$M(\pi^-\pi^+\mu^+) - M(\pi^-\mu^+) < 0.70$; $M(\pi^-\pi^+\mu^+) - M(\pi^-\mu^+) > 0.70\ GeV/c^2$
$p\ (h^-\pi^+\mu^+)$	$p\ (h^-\pi^+\mu^+) < 80\ GeV/c$; $p\ (h^-\pi^+\mu^+) > 80\ GeV/c$
run period	1990 ; 1991

split sample measurements are consistent with the quoted values. We therefore estimate no systematic uncertainty from the particular choice of analysis conditions.

5.6.2 Fit variants

In order to estimate any systematic uncertainty originating from our fitting technique, we perform N reasonable variations of the fitting process, and remeasure the branching ratio each time (see Appendix). The considered variations are listed in Table 5.6.2. These tests involve the variation of the bin size in the data histograms, the variation of the mass range over which the fit is performed, and the combined fitting for the 1990 and 1991 runs (instead of averaging the two results independently). Another variation performed was letting the h/μ misidentification level vary freely in both the $\overline{K}^{*0}\mu^+\nu$ and $\varrho^0\mu^+\nu$ data histograms, so that this time (as opposed to the $D^0 \to h^-\mu^+\nu$ tag analysis) any possible uncertainty in the misid background level is included in

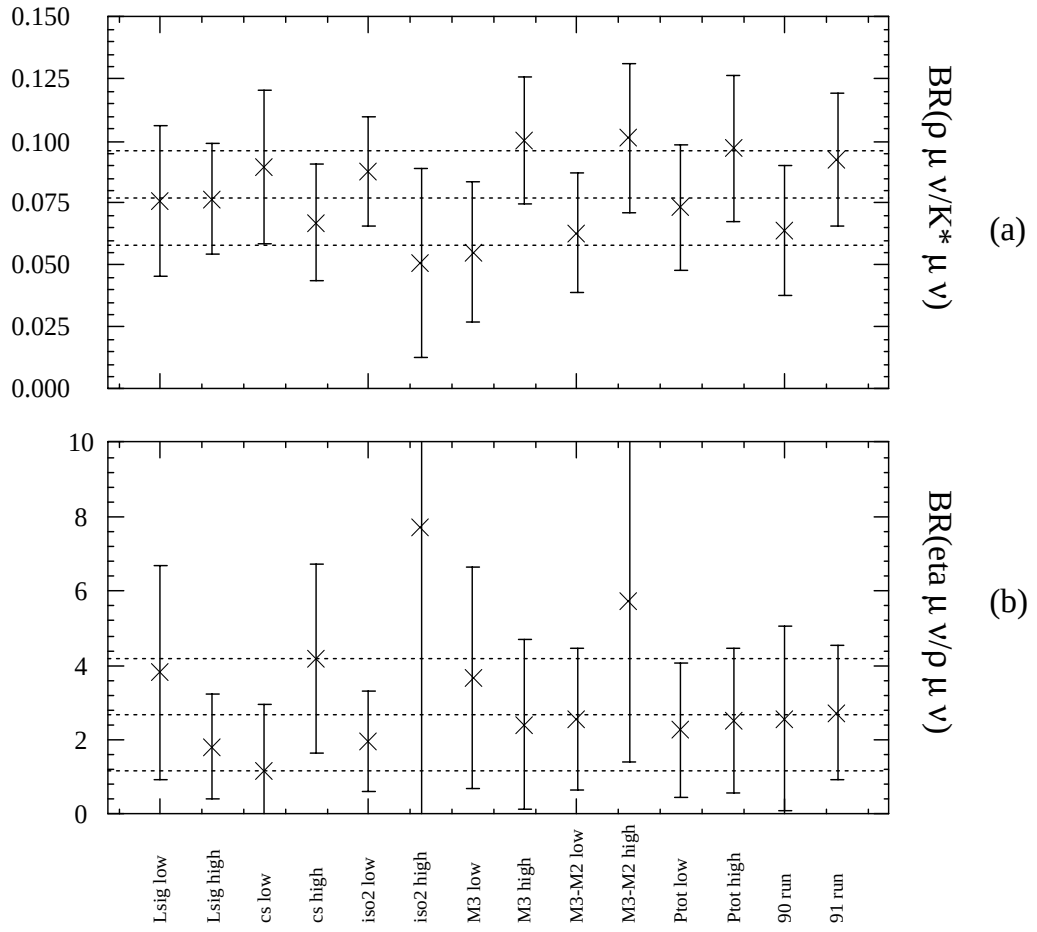

Figure 5.6.1 Relative branching ratio measured for various split samples (combined 1990 and 1991 Monte Carlo efficiencies were used). The dotted lines indicate the full data sample value and the corresponding 1σ statistical fluctuation.

the fit variant systematic. Finally, we tried different parameterizations of the background under the $\overline{K}^{*0}\mu^+\nu$ and $\varrho^0\mu^+\nu$ data histograms.

Table 5.6.2 Fit variants

Fit variant	$\frac{BR\ (D^+ \to \varrho^0 \mu^+ \nu)}{BR\ (D^+ \to \overline{K}^{*0} \mu^+ \nu)}$	$\frac{BR\ (D^+ \to \eta \mu^+ \nu)}{BR\ (D^+ \to \varrho^0 \mu^+ \nu)}$
(1) none (*)	0.0790 ± 0.0188	2.82 ± 1.51
(2) reconstructed MC shapes	0.0742 ± 0.0189	2.67 ± 1.50
(3) recon. MC shapes, $90 + 91$ MC	0.0770 ± 0.0190	2.67 ± 1.50
(4) $30 MeV/bin$,$0.25 - 1.75\ GeV/c^2$	0.0706 ± 0.0188	2.80 ± 1.58
(5) $15 MeV/bin$,$0.25 - 1.75\ GeV/c^2$	0.0767 ± 0.0189	2.68 ± 1.49
(6) $10 MeV/bin$,$0.25 - 1.25\ GeV/c^2$	0.0800 ± 0.0190	2.26 ± 1.40
(7) $20 MeV/bin$,$0.25 - 1.45\ GeV/c^2$	0.0788 ± 0.0188	2.82 ± 1.51
(8) $20 MeV/bin$,$0.25 - 1.25\ GeV/c^2$	0.0787 ± 0.0189	2.81 ± 1.51
(9) variable misid level	0.1183 ± 0.0255	2.64 ± 1.42
(10) Landau background for $K^* \mu \nu$	0.0853 ± 0.0204	2.78 ± 1.47
(11) fit to $\varrho^0 \mu^+ \nu$ misid used with variable amplitude	0.0743 ± 0.0242	2.56 ± 1.77
(12) fixed misid + variable function	0.0655 ± 0.0262	2.93 ± 2.17

(*) The standard fit conditions are: 20 $(MeV/c^2)/ch$ bin size, $0.25 - 1.75\ GeV/c^2$ mass range, fixed level of h/μ misidentification background.

The various results obtained with each fit variant are plotted in Figure 5.6.2. The total fit variant systematic error is then obtained by combining these results according to the formula reported in the Appendix. For $\frac{BR\ (D^+ \to \varrho^0 \mu^+ \nu)}{BR\ (D^+ \to K^{*0} \mu^+ \nu)}$ we estimate $\frac{\sigma_{B,fit}}{B} = 16.5\%$, while for $\frac{BR\ (D^+ \to \eta \mu^+ \nu)}{BR\ (D^+ \to \varrho^0 \mu^+ \nu)}$ we estimate $\frac{\sigma_{B,fit}}{B} = 6.2\%$.

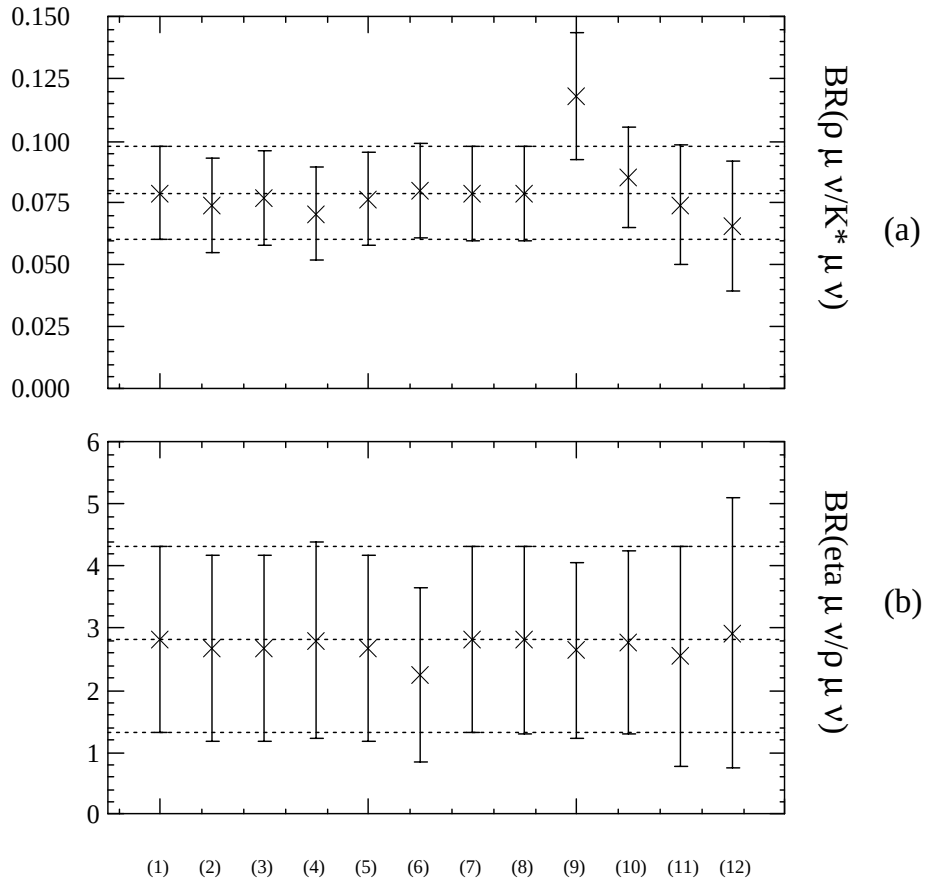

Figure 5.6.2 Branching ratios measured for various fit variants. The dotted lines indicate the value obtained with standard fitting conditions and the corresponding 1σ statistical fluctuation.

5.6.3 Particle identification

We do not expect any systematic bias from the identification of the μ^+ and the same sign pion π^+, because the same requirements are imposed on the prongs of the $D^+ \to \overline{K}^{*0}\mu^+\nu$ and $D^+ \to \varrho^0\mu^+\nu$ candidates, and the two decays are kinematicaly very similar. Different identification requirements are instead imposed on the opposite sign hadron h^- from the two decays (istatp= $2, 3$ for

the π^- and istatp= $4, 12$ for the K^-). For the $\frac{BR\ (D^+ \to \varrho^0 \mu^+ \nu)}{BR\ (D^+ \to \overline{K}^{*0} \mu^+ \nu)}$ measurement, we conservatively quote a systematic error of $\frac{\sigma_{B,cer}}{B} = \pm 2.5\%$ associated with our Monte Carlo simulation of the Čerenkov detectors[34]. For the $\frac{BR\ (D^+ \to \eta \mu^+ \nu)}{BR\ (D^+ \to \varrho^0 \mu^+ \nu)}$ measurement, we do not quote any systematic from particle identification since the requirements are exactly the same on all the three prongs.

5.6.4 Total systematic error

We summarize the sources of systematic error for the branching ratio measurement in Table 5.6.3. All contributions are added incoherently to compute the total systematic error.

Table 5.6.3 Systematic error

	$\frac{\sigma_B}{B}$	
Source	$\frac{BR\ (D^+ \to \varrho^0 \mu^+ \nu)}{BR\ (D^+ \to \overline{K}^{*0} \mu^+ \nu)}$	$\frac{BR\ (D^+ \to \eta \mu^+ \nu)}{BR\ (D^+ \to \varrho^0 \mu^+ \nu)}$
split sample	0%	0%
fit variants (includes misid level)	16.5%	6.2%
Čerenkov identification	2.5%	0%
Total systematic error	16.7%	6.2%

5.7 Form Factor Measurement

In Chapter 1 we saw that in the limit of zero momentum transfer, and neglecting the lepton mass, the rate for a vector meson semileptonic decay can

be expressed in the form[22]:

$$\lim_{q^2\to 0} \frac{d,\ (D \to h^* l\nu)}{dq^2} = \frac{G^2}{192\pi^3 M_D^3} |V_{cq}|^2 (M_D^2 - m_{h^*}^2)^3 |A_3^{h^*}(0)|^2 \ ,$$

where A_3 is the only form factor remaining when the two limits are taken. Considering the ratio of the $D^+ \to \varrho^0 \mu^+ \nu$ mode to the $D^+ \to \overline{K}^{*0} \mu^+ \nu$ mode, we find:

$$\lim_{q^2\to 0} \frac{d,\ (D^+ \to \varrho\mu\nu)/dq^2}{d,\ (D^+ \to \overline{K}^* \mu\nu)/dq^2} \ = \ \left|\frac{V_{cd}}{V_{cs}}\right|^2 \left[\frac{M_D^2 - m_\varrho^2}{M_D^2 - m_{K^*}^2}\right]^3 \left|\frac{A_3^\varrho(0)}{A_3^{K^*}(0)}\right|^2 \ .$$

If we assume that the measured branching ratio $\frac{BR\ (D^+ \to \varrho^0 \mu^+ \nu)}{BR\ (D^+ \to \overline{K}^{*0} \mu^+ \nu)}$ does not depend significantly on q^2, and we use the value for $\left|\frac{V_{cd}}{V_{cs}}\right|^2$ which comes from CKM unitarity, we can compute the ratio of form factor normalizations for the two decays:

$$\left|\frac{A_3^\varrho(0)}{A_3^{K^*}(0)}\right| = 1.29 \pm 0.15\ (stat) \pm\ 0.11\ (syst)\ .$$

Our result is a little larger, although compatible, with unity, which is the value predicted by $SU(3)_F$ symmetry. Various theoretical models exist which predict $SU(3)_F$ symmetry breaking effects of the order of 10-20%, both below and above the unity value (see Table 7.2.1).

5.8 Summary of results

We have investigated the two vector meson semileptonic decays $D^+ \to \overline{K}^{*0}\mu^+\nu$ and $D^+ \to \varrho^0\mu^+\nu$. We observed 443.0 ± 22.3 $\overline{K}^{*0}\mu^+\nu$ events and 39.2 ± 9.0 $\varrho^-\mu^+\nu$ events. We have measured the relative branching ratio of the two decays to be:

$$\frac{BR\ (D^+ \to \varrho^0\mu^+\nu)}{BR\ (D^+ \to K^{*0}\mu^+\nu)} = 0.0790 \pm 0.0188\ (stat)\ \pm 0.0132\ (syst)\ .$$

Assuming that this result holds in the limit of zero momentum transfer $q^2 \to 0$, we have computed the ratio of form factors:

$$\left|\frac{A_3^{\varrho}(0)}{A_3^{K^*}(0)}\right| = 1.29 \pm 0.15\ (stat) \pm\ 0.11\ ,$$

where we used the value of $\left|\frac{V_{cd}}{V_{cs}}\right|^2$ which comes from CKM unitarity and we neglected the lepton mass.

We also observed 6.7 ± 3.1 candidate events for the decay channel $D^+ \to \eta\mu^+\nu$, $\eta \to \pi^+\pi^-\pi^0$ (where the π^0 is not reconstructed). If this fitted yield is interpreted as a signal, the branching ratio with respect to the $D^+ \to \varrho^0\mu^+\nu$ decay is computed to be:

$$\frac{BR\ (D^+ \to \eta\mu^+\nu)}{BR\ (D^+ \to \varrho^0\mu^+\nu)} = 2.83 \pm 1.45\ (stat)\ \pm 0.17\ (syst)\ .$$

CHAPTER 6

CHARM BARYONS DECAYING TO Λ_c^+

In this chapter we use the total Λ_c^+ sample reconstructed through several decay modes to look for higher mass charm baryons decaying to Λ_c^+: $\Lambda_c^{\star+} \to \Lambda_c^+\pi^+\pi^-$and $\Sigma_c \to \Lambda_c^+\pi^\pm$. Mass measurements for the four states $\Lambda_c^{\star+}(2593)$, $\Lambda_c^{\star+}(2625)$, Σ_c^0 and Σ_c^{++} are presented. Furthermore we measure the ratio of the photoproduction cross sections for $\Lambda_c^{\star+}$ and Σ_c with respect to the (inclusive) photoproduction cross section for Λ_c^+.

6.1 Introduction

Several experiments have observed the isospin triplet Σ_c^0, Σ_c^+, Σ_c^{++} which decay strongly to $\Lambda_c^+\pi$. Here we concentrate on the two decays $\Sigma_c^0 \to \Lambda_c^+\pi^-$ and $\Sigma_c^{++} \to \Lambda_c^+\pi^+$ and we do not investigate $\Sigma_c^+ \to \Lambda_c^+\pi^0$, since our reconstruction efficiency for π^0 is considerably lower than for $\pi^\pm$.

Few experiments have observed the $\Lambda_c^{\star+}$ excited states. ARGUS[39], CLEO[40] and E687[41] have reported the existence of one such state, the $\Lambda_c^{\star+}(2625)$, with a mass difference M($\Lambda_c^{\star+}(2625)$)-M(Λ_c^+)$\simeq$ 341 MeV/c^2, reconstructed through its decay to $\Lambda_c^+\pi^-\pi^+$. ARGUS reported a significant resonant component for the decay, $\frac{BR(\Lambda_c^{\star+}(2625)\to\Sigma_c\pi^\pm)}{BR(\Lambda_c^{\star+}(2625)\to\Lambda_c^+\pi^+\pi^-)} = 0.46 \pm 0.14$. CLEO and E687 did not see any resonant decay: E687[41] estimated the total resonant fraction to be less than $\frac{BR(\Lambda_c^{\star+}(2625)\to\Sigma_c\pi^\pm)}{BR(\Lambda_c^{\star+}(2625)\to\Lambda_c^+\pi^+\pi^-)} < 0.36$ (90% c.l.), CLEO[42] measured the two separate upper limits $\frac{BR(\Lambda_c^{\star+}(2625)\to\Sigma_c^0\pi^+)}{BR(\Lambda_c^{\star+}(2625)\to\Lambda_c^+\pi^+\pi^-)} < 0.07$ and $\frac{BR(\Lambda_c^{\star+}(2625)\to\Sigma_c^{++}\pi^-)}{BR(\Lambda_c^{\star+}(2625)\to\Lambda_c^+\pi^+\pi^-)} < 0.08$ at the 90% confidence level.

CLEO[42] has also reported evidence for a lower mass $\Lambda_c^{\star+}$ excited state, which we shall refer to as $\Lambda_c^{\star+}(2593)$, with a mass difference M($\Lambda_c^{\star+}(2593)$)-M(Λ_c^+) $\simeq$ 307.5 MeV/c^2 above the Λ_c^+ mass. The $\Lambda_c^{\star+}(2593)$ was reconstructed from the final state $\Lambda_c^+\pi^-\pi^+$, and the resonant decay $\Lambda_c^{\star+}(2593) \rightarrow \Sigma_c\pi^\pm$, $\Sigma_c \rightarrow \Lambda_c^+\pi^\mp$ (where the Σ_c can either be a Σ_c^0 or a Σ_c^{++}) was reported to be dominant. No other experiment has observed such a state.

The newly discovered $\Lambda_c^{\star+}$states have been interpreted[43] as a fine structure doublet, in which the light diquark ud carries a unit of orbital angular momentum $L = 1$ with respect to the heavy c quark. Combining this orbital angular momentum with the spin $S = \frac{1}{2}$ of the baryon, the two states have been assigned total angular momentum and parity J^P as follows: $\Lambda_c^{\star+}(2593)= \frac{1}{2}^-$, $\Lambda_c^{\star+}(2625)= \frac{3}{2}^-$, while for both states the isospin is expected to be zero. If this is the case, the $\Lambda_c^{\star+}$ can not decay to Λ_c^+ via single pion emission because of isospin conservation, but requires two pions in the final state. If on the other hand the two new states were excited $\Sigma_c^\star$ states, in which the light diquark ud has orbital angular momentum $L = 0$ but isospin $I = 1$, they could decay either to $\Lambda_c^+\pi$ or to $\Lambda_c^+\pi\pi$, with the former decay being favored by phase space. CLEO[42] has searched for the two states in the decay mode $\Lambda_c^+\pi^0$, and reported no evidence for them. Furthermore, the $\Sigma_c^\star$ states are predicted to have higher masses than the $\Lambda_c^{\star+}$states[44].

Assuming the two states to be $\Lambda_c^{\star+}$, angular momentum and parity conservation show that the state $\Lambda_c^{\star+}(\frac{1}{2}^-)$ may decay to the intermediate resonant state $\Sigma_c(\frac{1}{2}^+)$ via an S-wave, but the state $\Lambda_c^{\star+}(\frac{3}{2}^-)$ would have to decay to $\Sigma_c(\frac{1}{2}^+)$ via a D-wave. Therefore in this picture we expect that the resonant decay $\Lambda_c^{\star+}(2625) \rightarrow \Sigma_c\pi^\pm$, $\Sigma_c \rightarrow \Lambda_c^+\pi$ is strongly suppressed, while the decay $\Lambda_c^{\star+}(2593) \rightarrow \Sigma_c\pi^\pm$, $\Sigma_c \rightarrow \Lambda_c^+\pi$ is not. Therefore the analysis of the resonant

Table 6.1.1 Excited Charm Baryons Quantum Numbers and Allowed Decays

baryon	J^P	I	decays
Λ_c^+	$\frac{1}{2}^+$	0	
Σ_c	$\frac{1}{2}^+$	1	$\Lambda_c^+\pi$
$\Lambda_c^{+\star}(2593)$	$\frac{1}{2}^-$	0	$\Lambda_c^+\pi\pi$ $\Sigma_c\pi$ $\Lambda_c^+\gamma$
$\Lambda_c^{+\star}(2625)$	$\frac{3}{2}^-$	0	$\Lambda_c^+\pi\pi$ $\Lambda_c^+\gamma$
$\Sigma_c^\star$	$\frac{1}{2}^-$	1	$\Lambda_c^+\pi$ $\Lambda_c^+\pi\pi$
$\Sigma_c^\star$	$\frac{3}{2}^-$	1	$\Lambda_c^+\pi$ $\Lambda_c^+\pi\pi$

component of the decays of the $\Lambda_c^{\star+}$ is very important in establishing the true nature of the states. Finally the $\Lambda_c^{\star+}$ states could also decay to $\Lambda_c^+\gamma$ via radiative transition, but this decay would be competitive with that to $\Lambda_c^+\pi^-\pi^+$ only if the intrinsic widths of the states are sufficiently narrow.

6.2 Reconstruction of Λ_c^+ in several decay modes

The total Λ_c^+ sample used in the search for higher mass charm baryons is obtained by summing Λ_c^+ candidates reconstructed in five decay modes: $\Lambda_c^+ \to pK^-\pi^+$, $\Lambda_c^+ \to pK_s^0$, $\Lambda_c^+ \to pK_s^0\pi^+\pi^-$, $\Lambda_c^+ \to \Lambda^0\pi^+$, $\Lambda_c^+ \to \Lambda^0\pi^+\pi^-\pi^+$. Neutral vees are reconstructed through their decay modes $K_s^0 \to \pi^+\pi^-$ and $\Lambda^0 \to p\pi^-$ as described in section § 3.5.

The analysis cuts employed for each decay mode are listed in Table 6.2.1.

Table 6.2.1 Analysis cuts for Λ_c^+ decay modes

$pK\pi$	$p\overline{K}_s^0\pi\pi$	$\Lambda^0\pi\pi\pi$	$p\overline{K}_s^0$	$\Lambda^0\pi$
$L/\sigma_L > 4$	$L/\sigma_L > 4$	$L/\sigma_L > 4$	$L/\sigma_L > 2$	$L/\sigma_L > 5$
$cls > 1\%$	$cls > 1\%$	$cls > 1\%$	$cls > 1\%$	$cls > 1\%$
$clp > 1\%$	$clp > 1\%$	$clp > 1\%$	$clp > 1\%$	$clp > 1\%$
$iso1 < 90\%$	$iso1 < 90\%$	$iso1 < 90\%$	$rin < 250\mu m$	$rin < 250\mu m$
$iso2 < 0.5\%$	$iso2 < 0.5\%$	$iso2 < 0.5\%$	$rtr < 25\mu m$	$rtr < 25\mu m$
$P(\Lambda_c^+) > 30GeV$	$P(\Lambda_c^+) > 30GeV$	$P(\Lambda_c^+) > 30GeV$	$P(p) > 20GeV$	
$ct < 323\mu m$	$ct < 323\mu m$	$ct < 323\mu m$	$ct < 323\mu m$	$ct < 323\mu m$
$\Delta M < 20MeV$	$\Delta M < 20MeV$	$\Delta M < 20MeV$	$\Delta M < 25MeV$	$\Delta M < 20MeV$

A special effort was made to use the same requirements for all modes. Protons are required to be identified by the Čerenkov system as either proton definite or kaon/proton ambiguous (istatp(p)= $8, 12$); similarly kaons must be kaon definite, kaon/proton ambiguous (istatp(K)= $4, 12$) or pion/kaon ambiguous (istatp(K)= 7, accepted only if their momentum is $P(K) > 60\ GeV/c$); pions must not be compatible with being electrons, kaons, protons or kaon/proton ambiguous (istatp(π)$\neq$ $1, 4, 8, 12$). For all modes the confidence levels of primary and secondary vertices are required to be greater than 1%. For the multi-prong modes ($pK^-\pi^+$, $p\overline{K}_s^0\pi^+\pi^-$, $\Lambda^0\pi^+\pi^-\pi^+$) we require $L/\sigma_L > 4$ and improve the signal to noise by means of isolation cuts: $iso1 < 90\%$ and $iso2 < 0.5\%$; we also require the total momentum of the Λ_c^+ combination to be greater than 30 GeV/c. For the one-prong modes we require $L/\sigma_L > 2$ ($p\overline{K}_s^0$) and $L/\sigma_L > 5$ ($\Lambda^0\pi^+$) and substitute the isolation requirements (which are ineffective for this kind of topology) with conditions on the impact parameter of the neutral daughter (K_s^0 or Λ^0) to the decay

vertex, both in the decay plane ($rin < 250\mu m$) and in the direction transverse to the decay plane ($rtr < 25\mu m$). Two additional cuts are used for the $p\overline{K}^0_s$ mode: a cut on the proton momentum ($P(p) > 20\ GeV/c$) and a cut on the fractional energies of the two decay daughters ($E(p)/E(\Lambda_c) > 20\%$, $E(\overline{K^0_s})/E(\Lambda_c) < 80\%$). Finally, for all channels we required the proper time of the decay to be less than five times the nominal Λ_c^+ lifetime[45]: $ct = \frac{Lmc}{P} \leq 5 \cdot c\tau = 323\mu m$. According to Monte Carlo simulations, this cut retains 98% of the Λ_c^+ events while rejecting 14% and 45% of the reflections from D_s^+ and D^+ mesons, respectively

In Figures 6.2.1 (a)-(e) we show the Λ_c^+ signals selected in the various decay modes by the conditions described above. In Figure 6.2.1 (f) we sum all the decay modes to obtain the total Λ_c^+ sample used for this analysis. The resulting Λ_c^+ sample is composed of $Y(\Lambda_c^+) = 1564 \pm 101$ events. The $pK^-\pi^+$ mode contributes 64% of the total yield, the $p\overline{K}^0_s$ mode 22%, and the other modes $p\overline{K}^0_s\pi^+\pi^-$, $\Lambda^0\pi^+$, $\Lambda^0\pi^+\pi^-\pi^+$ the remaining 14%.

For each decay mode, we select Λ_c^+ candidates which are contained within approximately $\pm 2\sigma$ of the nominal Λ_c^+ mass and compute the invariant mass of the Λ_c^+ with one or two oppositely charged tracks coming from the primary vertex. These additional tracks have to be linked SSD-PWC tracks and their Čerenkov identification must be compatible with the pion hypothesis (istatp(π)$\neq 1, 4, 8, 12$). In order to reduce systematic errors in the mass measurements, we measure the mass difference between the Λ_c^++pion(s) state and the original Λ_c^+ state.

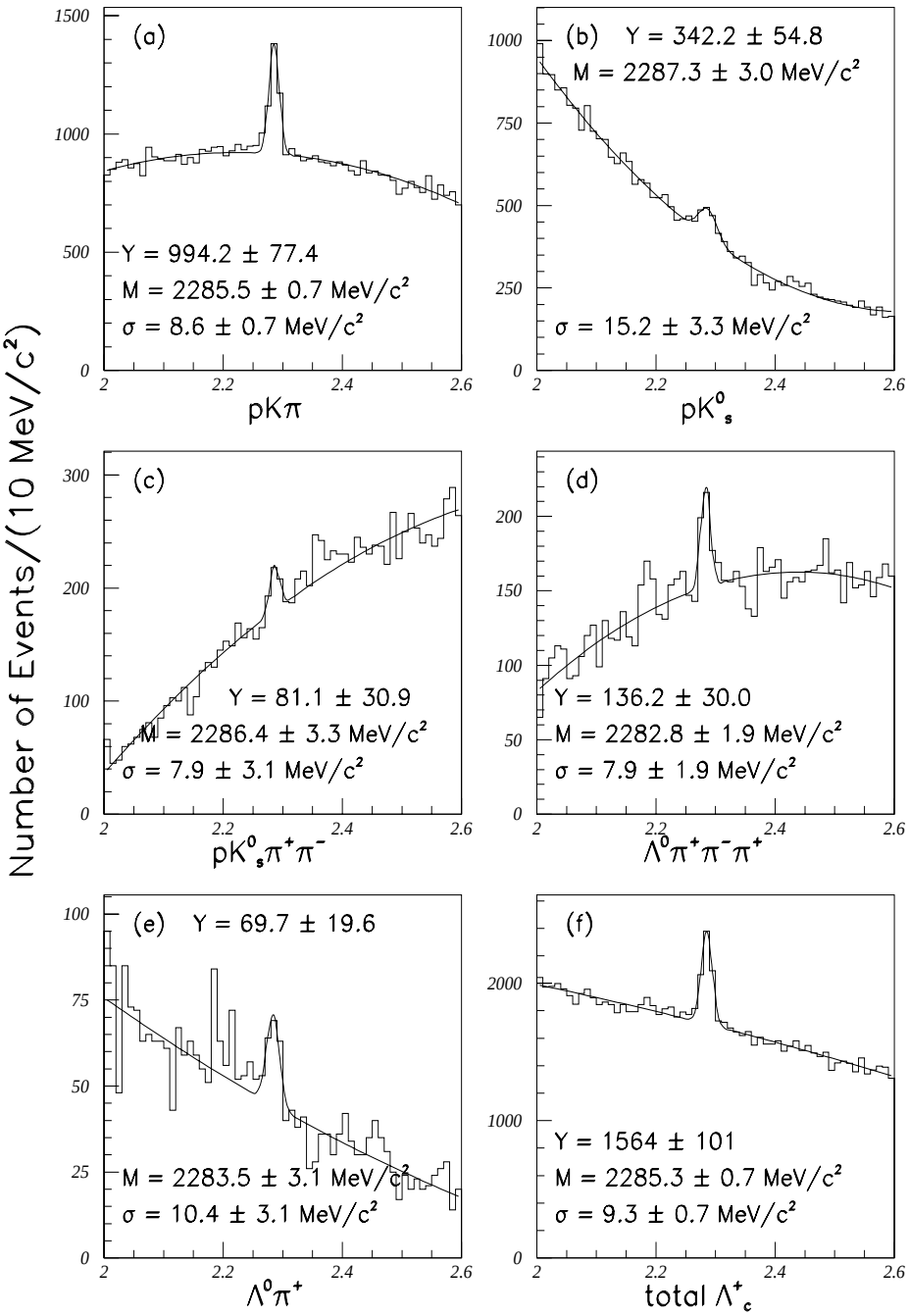

Figure 6.2.1 (a)-(e) Λ_c^+ candidates reconstructed through several decay modes and (f) total Λ_c^+ sample used to look for higher mass charm baryon states.

6.3 $\Lambda_c^{*+}(2593)$ evidence and mass measurement

In Figure 6.3.1 we present the mass difference M($\Lambda_c^+\pi^-\pi^+$)-M(Λ_c^+) reconstructed by use of the total Λ_c^+ sample of Figure 6.2.1 (f); the histogram shows evidence for two peaks above the background. The histogram is fitted with two Gaussian functions for the signals plus a second degree polynomial for the background, using the likelihood estimator. The fitted yield for the lower mass peak is $Y_1 = 13.9 \pm 4.5$ at a mass difference of $\Delta M_1 = 309.2 \pm 0.7\ MeV/c^2$. The statistical significance of the signal $\delta Y_1/Y_1$ is more than 3 σ and the value ΔM_1 is in agreement with the mass difference measured by CLEO[42] for the $\Lambda_c^{\star+}(2593)$ state (see Table 7.3.1): therefore we confirm the existence of such a state. For the higher mass peak the fit returns $Y_2 = 38.8 \pm 8.0$ events at a mass difference of $\Delta M_2 = 341.4 \pm 0.4\ MeV/c^2$, which agrees with the mass difference for the $\Lambda_c^{\star+}(2625)$ state previously measured by E687[41] by use of the $\Lambda_c^+ \to pK^-\pi^+$ decay mode alone and with looser analysis cuts than those employed here (see again Table 7.3.1).

Several checks were performed on the $\Lambda_c^{\star+}(2593)$ signal to make sure it was not a statistical fluctuation. For this purpose we considered only the $\Lambda_c^+ \to pK^-\pi^+$ sample, since it is the only one which has statistical significance when considered alone. Figure 6.3.2 (a) shows the M($\Lambda_c^+\pi^-\pi^+$)-M(Λ_c^+) mass difference for $\Lambda_c^+ \to pK^-\pi^+$candidates, Figure 6.3.2 (b) shows the mass difference for $pK^-\pi^+$combinations belonging to Λ_c^+ sidebands, Figure 6.3.2 (c) shows the mass difference for same-sign $\Lambda_c^+\pi^-\pi^-$ combinations; no evidence of signal can be seen in either plot (b) or (c).

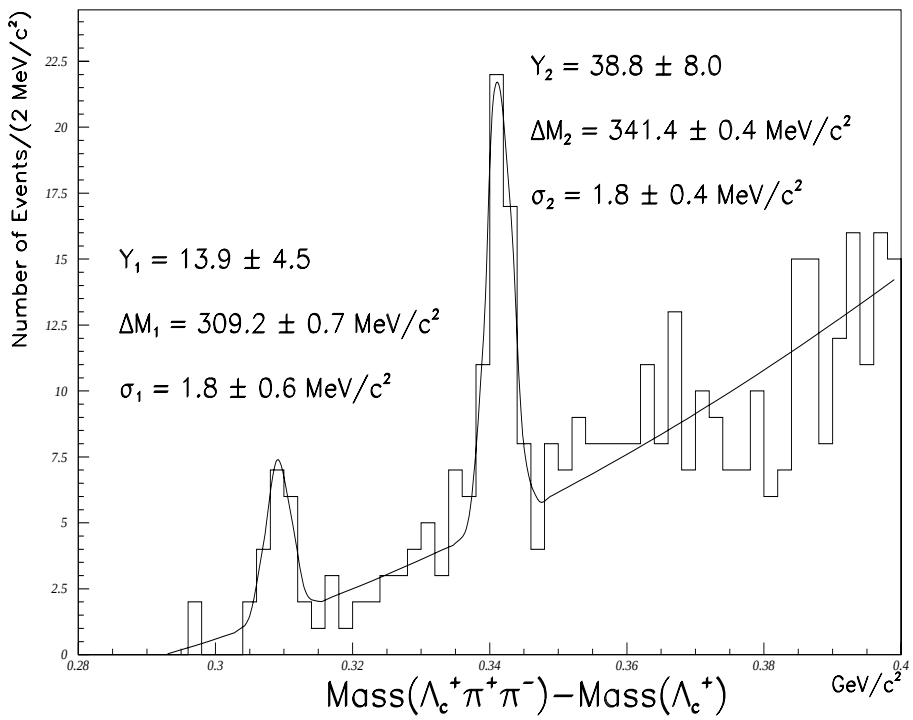

Figure 6.3.1 M($\Lambda_c^+\pi^-\pi^+$)-M(Λ_c^+) invariant mass distribution obtained with the total Λ_c^+ sample of Figure 6.2.1 (f), showing evidence for both the $\Lambda_c^{\star+}(2593)$ and $\Lambda_c^{\star+}(2625)$ states.

In Figure 6.3.3 we plot respectively the $\Lambda_c^{\star+}(2593)$ mass and the ratio of the $\Lambda_c^{\star+}(2593)$ yield to the $\Lambda_c^{\star+}(2625)$ yield, when different analysis conditions are used and when the total $\Lambda_c^{\star+}$ sample is split into 90 and 91 subsamples and low and high momentum subsamples: both quantities appear to be reasonably stable, showing no substantial systematic effects.

In Figure 6.3.4 we show $\Lambda_c^{\star+}(2593) \rightarrow \Lambda_c^+\pi^+\pi^-$ and $\Lambda_c^{\star+}(2625) \rightarrow \Lambda_c^+\pi^+\pi^-$ (where in both cases $\Lambda_c^+ \rightarrow pK^-\pi^+$) Monte Carlo samples, reconstructed with the analysis cuts described in Table 6.3.1. The width of the Monte Carlo signal for the $\Lambda_c^{\star+}(2593)$ state is measured to be $\sigma = 2.30 \pm 0.06\ MeV/c^2$, which agrees well with the value returned by the fit

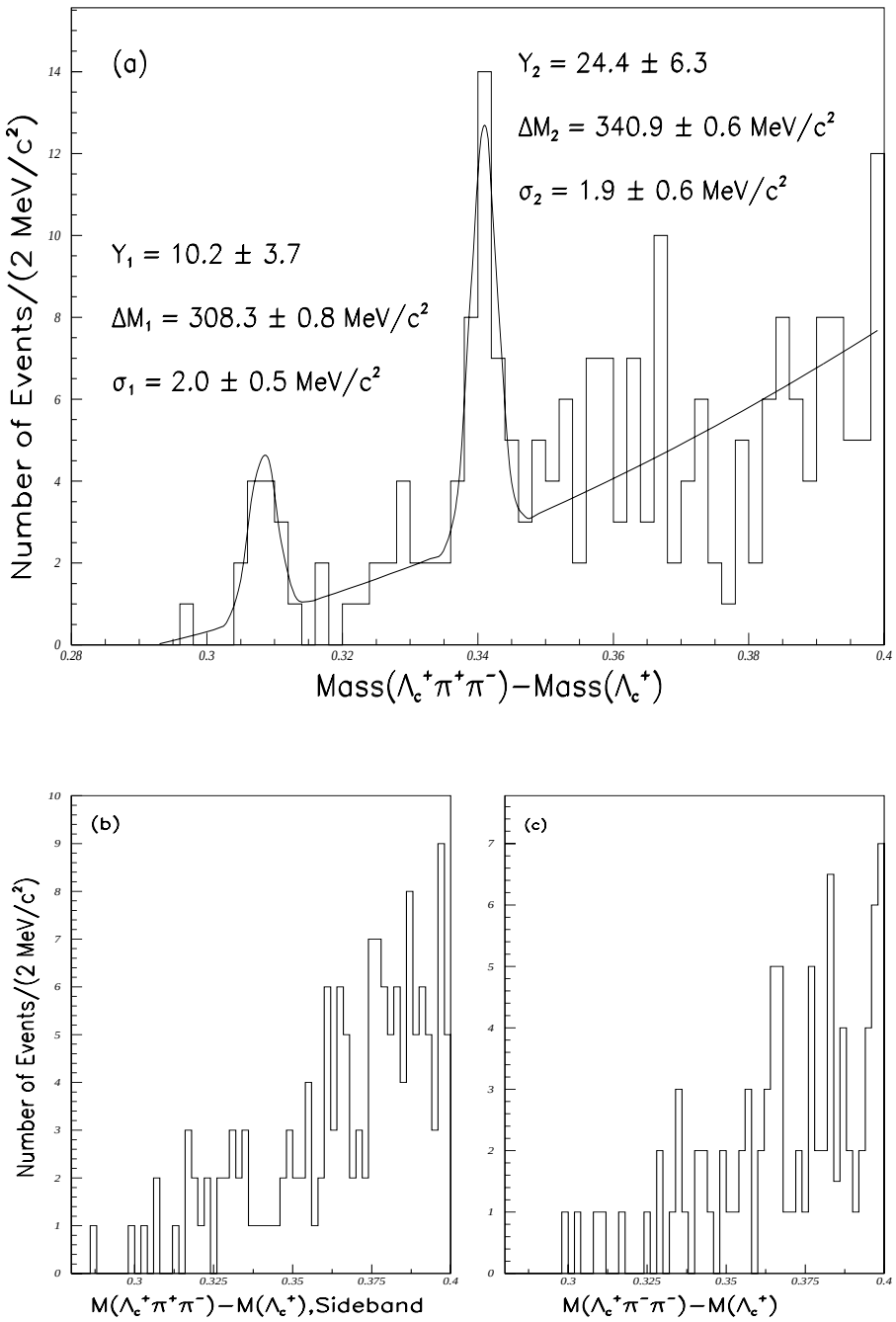

Figure 6.3.2 (a) M($\Lambda_c^+\pi^-\pi^+$)-M(Λ_c^+) for $\Lambda_c^+ \rightarrow pK^-\pi^+$ candidates; (b) M($\Lambda_c^+\pi^-\pi^+$)-M(Λ_c^+) for $pK^-\pi^+$ combinations inside Λ_c^+ sidebands; (c) same sign M($\Lambda_c^+\pi^-\pi^-$)-M(Λ_c^+).

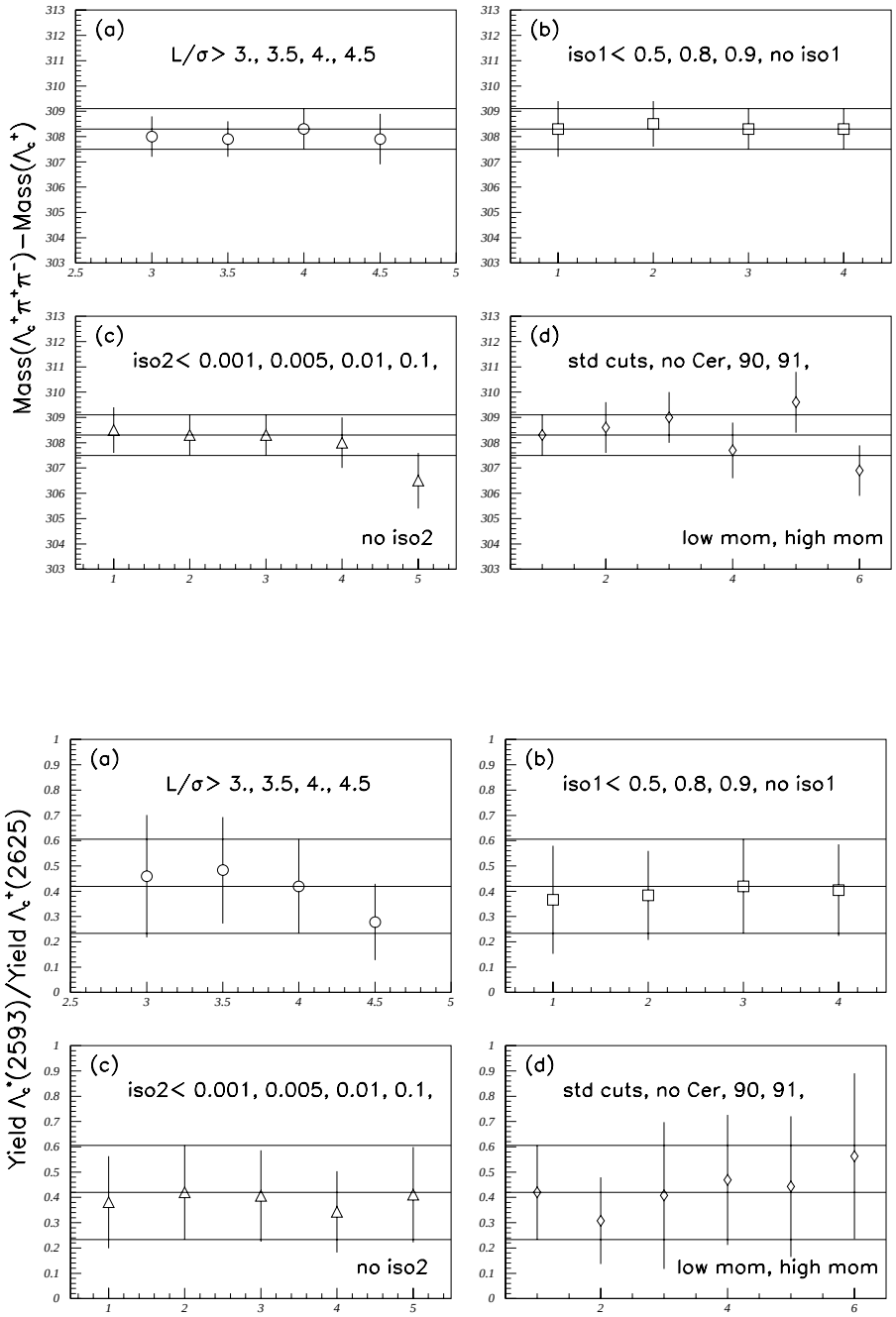

Figure 6.3.3 M($\Lambda_c^+\pi^-\pi^+$)-M(Λ_c^+) invariant mass difference and ratio of yields Y($\Lambda_c^{\star+}$(2593))/Y($\Lambda_c^{\star+}$(2625)) for different analysis cuts.

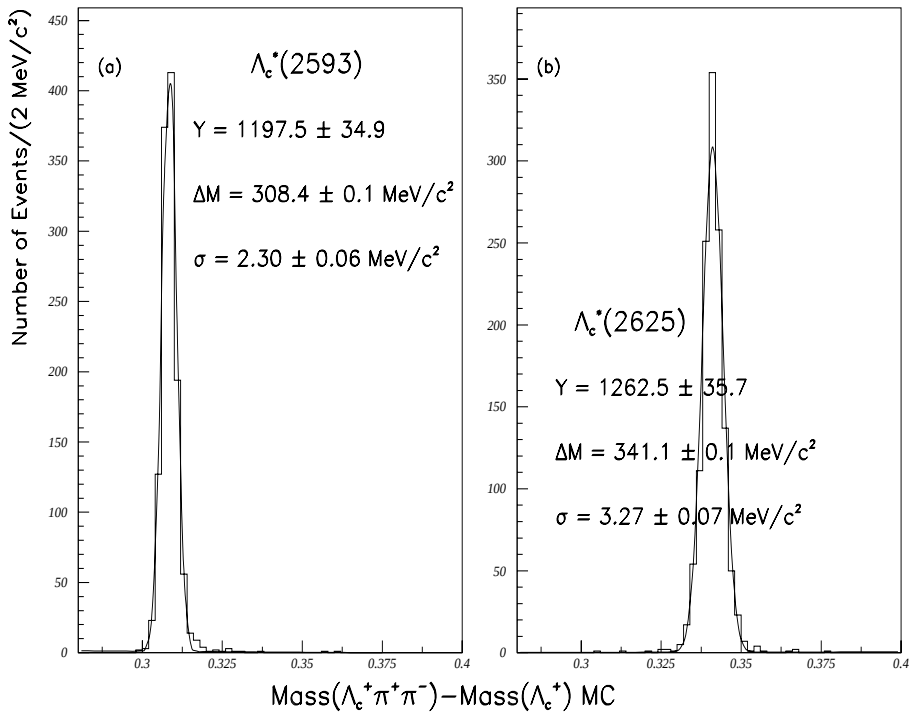

Figure 6.3.4 Monte Carlo $\Lambda_c^{\star+}(2593) \rightarrow \Lambda_c^+\pi^+\pi^-$ (a) and $\Lambda_c^{\star+}(2625) \rightarrow \Lambda_c^+\pi^+\pi^-$ (b) signals, where in both cases $\Lambda_c^+ \rightarrow pK^-\pi^+$.

to the data $\sigma = 2.0 \pm 0.5\ MeV/c^2$ [46]. In Table 6.3.2 we compare the generated and reconstructed mass differences in Monte Carlo for several high mass charm baryon states; in all cases, the shift between the two is very small.

Table 6.3.2 Monte Carlo M(Λ_c^+,Σ_c)-M(Λ_c^+) mass difference

	generated	reconstructed
Σ_c^0	167.50	167.63 ± 0.05
Σ_c^{++}	168.20	168.31 ± 0.05
$\Lambda_c^{+\star}(2593)$	308.20	308.41 ± 0.07
$\Lambda_c^{+\star}(2625)$	340.70	341.12 ± 0.07

We quote a conservative upper limit of 0.3 MeV/c^2 as systematic error in the $\Lambda_c^{\star+}(2593)$ mass measurement. This uncertainty is derived from fluctuations in the fitted mass observed when different fitting techniques or analysis cuts are applied, and when the $pK^-\pi^+$ mode alone is used to reconstruct Λ_c^+candidates, as well as from the small shift observed between Monte Carlo generated and reconstructed mass difference. In conclusion, the $\Lambda_c^{\star+}(2593)$ mass is measured to be:

$$M(\Lambda_c^{\star+}(2593)) - M(\Lambda_c^+) = 309.2 \pm 0.7\ (stat) \pm 0.3\ (syst)\ MeV/c^2\ .$$

6.4 Analysis of the resonant decay $\Lambda_c^{\star+}(2593) \to \Sigma_c\pi^\pm$

The resonant decay chain $\Lambda_c^{\star+}(2593) \to \Sigma_c\pi^\pm$, $\Sigma_c \to \Lambda_c^+\pi^\pm$ (where the Σ_c can be either a Σ_c^0 or a Σ_c^{++}) was investigated, again using only Λ_c^+ candidates reconstructed in the $pK^-\pi^+$ mode. A similar study previously performed on E687 data[41] for the $\Lambda_c^{\star+}(2625)$ state did not observe any significant resonant component, and resulted in the 90% confidence level upper limit:

$$\frac{BR(\Lambda_c^{\star+}(2625) \to \Sigma_c\pi^\pm)}{BR(\Lambda_c^{\star+}(2625) \to \Lambda_c^+\pi^+\pi^-)} < 0.36\ .$$

In Figures 6.4.1 (a), (b) we present a scatter plot of the two mass differences M($\Lambda_c^+\pi^+$)-M(Λ_c^+) and M($\Lambda_c^+\pi^-$)-M(Λ_c^+) for *non resonant* Monte Carlo $\Lambda_c^{\star+}(2593) \to \Lambda_c^+\pi^+\pi^-$and $\Lambda_c^{\star+}(2625) \to \Lambda_c^+\pi^+\pi^-$events, respectively. It can be noticed that the $\Lambda_c^{\star+}(2593)$ and $\Lambda_c^{\star+}(2625)$ states appear as uniform diagonal bands in the plot. In Figure 6.4.1 (c) the same distribution is plotted for a *resonant* $\Lambda_c^{\star+}(2593) \to \Sigma_c\pi^\pm$ Monte Carlo. In this case, the presence of an

intermediate Σ_c^0 or Σ_c^{++} state in the decay causes the $\Lambda_c^{\star+}$ events to concentrate at two regions corresponding to the Monte Carlo generated Σ_c masses. Figure 6.4.1 (d) shows the situation for real data: background events distribute uniformly over the surface of the scatter plot, yet the points in the $\Lambda_c^{\star+}(2593)$ diagonal band appear to be concentrated at the two ends of the band.

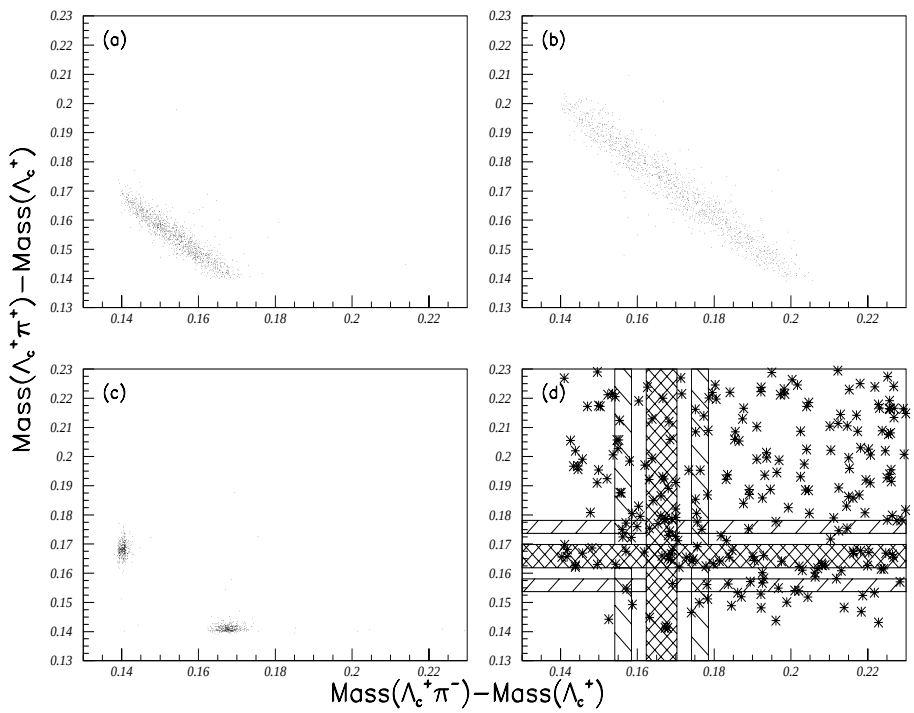

Figure 6.4.1 Scatter plot of the mass difference M($\Lambda_c^+\pi^-$)-M(Λ_c^+) vs. the mass difference M($\Lambda_c^+\pi^+$)-M(Λ_c^+) for:
(a) Non resonant $\Lambda_c^{\star+}(2593) \to \Lambda_c^+\pi^+\pi^-$Monte Carlo;
(b) Non resonant $\Lambda_c^{\star+}(2625) \to \Lambda_c^+\pi^+\pi^-$Monte Carlo;
(c) Resonant $\Lambda_c^{\star+}(2593) \to \Sigma_c\pi^\pm$, $\Sigma_c \to \Lambda_c^+\pi^\pm$Monte Carlo;
(d) Data events (same entries as in Figure 6.3.2 (a)), with superimposed the Σ_c *region* (double-crossed area) and the *sideband region* (single-crossed area).

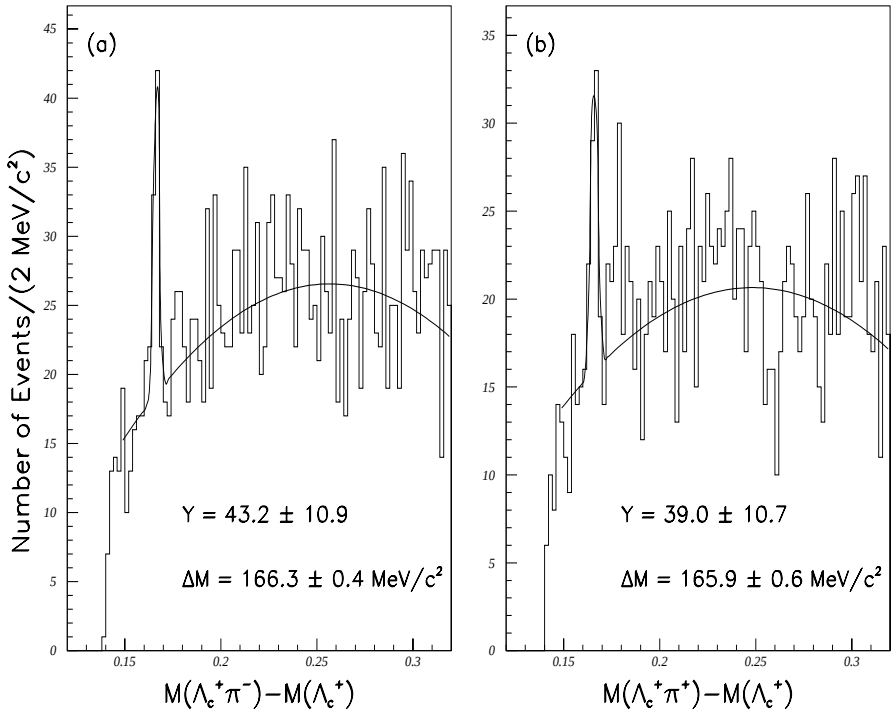

Figure 6.4.2 M($\Lambda_c^+\pi^\mp$)-M(Λ_c^+) mass differences for $\Lambda_c^+ \to pK^-\pi^+$events, showing signals for the Σ_c^0 (a) and Σ_c^{++} (b) states. The analysis cuts for $pK^-\pi^+$ candidates are those listed in Table 6.3.1.

We selected $\Lambda_c^+\pi^-\pi^+$ combinations for which either one of the two sub-masses M($\Lambda_c^+\pi^-$) or M($\Lambda_c^+\pi^+$) is compatible with being a Σ_c^0 or a Σ_c^{++}, respectively. For this purpose we define a Σ_c *signal region* as that portion of the M($\Lambda_c^+\pi^+$)-M(Λ_c^+) vs. M($\Lambda_c^+\pi^-$)-M(Λ_c^+) scatter plot which is contained within two bands of width ± 4 MeV centered around the Σ_c^0 and Σ_c^{++}masses (see double-crossed area in Figure 6.4.1). The values for the Σ_c masses were obtained from a separate fit to the Σ_c^0 and Σ_c^{++} signals reconstructed by combining $\Lambda_c^+ \to pK^-\pi^+$ events with one pion (respectively opposite-sign or like-sign) coming from the primary vertex, using exactly the same analysis conditions

employed to reconstruct the $\Lambda_c^{\star+}$ signals. The $\Sigma_c \to \Lambda_c^+\pi^\pm$, $\Lambda_c^+ \to pK^-\pi^+$ signals are shown in Figures 6.4.2 (a) and (b). The $\Lambda_c^+\pi^-\pi^+$ combinations satisfying the additional Σ_c cut are plotted in Figure 6.4.3. A maximum likelihood fit to the histogram returns the yields $Y_1 = 10.4 \pm 3.4$, $Y_2 = 10.6 \pm 3.7$ events. If the same Σ_c cut is applied to the non resonant $\Lambda_c^{\star+}(2593) \to \Lambda_c^+\pi^+\pi^-$ and $\Lambda_c^{\star+}(2625) \to \Lambda_c^+\pi^+\pi^-$ Monte Carlo samples, it is found that 33.2% and 31.2% (respectively) of the original $\Lambda_c^{\star+}$ yield is retained. This shows that the $\Lambda_c^{\star+}(2593)$ sample is consistent with being completely resonant, while the $\Lambda_c^{\star+}(2625)$ sample (as expected) is consistent with being completely non resonant.

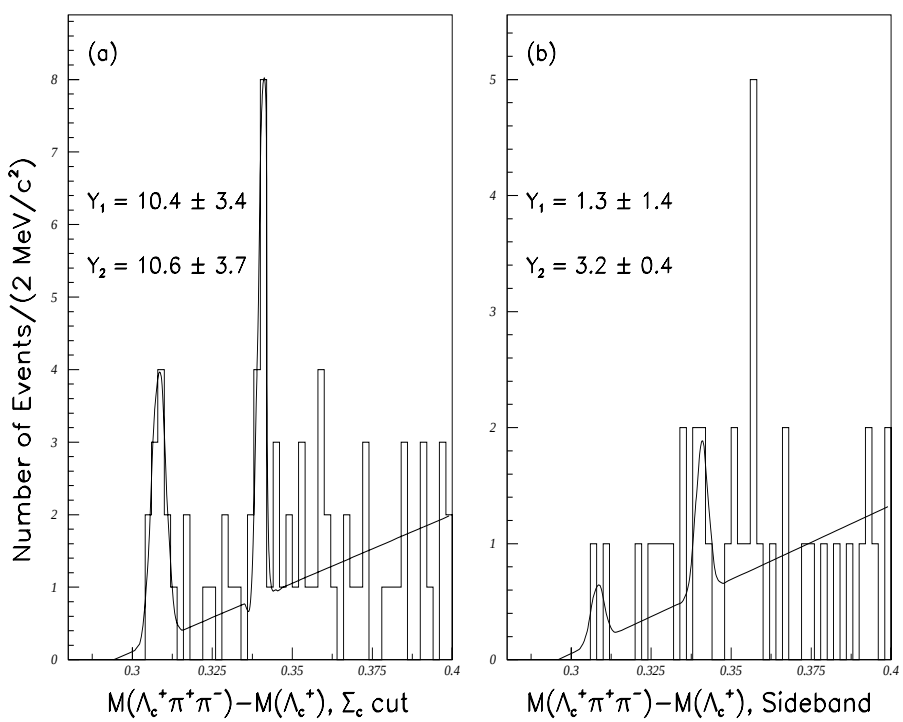

Figure 6.4.3 (a) $M(\Lambda_c^+\pi^-\pi^+)$-$M(\Lambda_c^+)$ mass distribution for the same events as in Figure 6.3.2, but with the additional Σ_c requirement; (b) same distribution for $\Lambda_c^+\pi^-\pi^+$combinations belonging to Σ_c sidebands.

We decided to measure a lower limit on the resonant component of the $\Lambda_c^{\star+}(2593) \to \Lambda_c^+\pi^+\pi^-$ decay. At this purpose we defined a *sideband region* as the portion of the M($\Lambda_c^+\pi^+$)-M(Λ_c^+) vs. M($\Lambda_c^+\pi^-$)-M(Λ_c^+) scatter plot which is composed by two normalized sidebands of the Σ_c^0 mass and two normalized sidebands of the Σ_c^{++} mass (see single-crossed area in Figure 6.4.1). The sidebands were normalized by requiring equal yields in the Σ_c signal region and in the sideband region for a *non resonant* $\Lambda_c^{\star+}(2593) \to \Lambda_c^+\pi^+\pi^-$ Monte Carlo sample. $\Lambda_c^+\pi^-\pi^+$ data combinations lying within the sideband region are plotted in Figure 6.4.3 (b). This last histogram is fitted with two Gaussian curves with centers and widths fixed to the $\Lambda_c^{\star+}(2593)$ and $\Lambda_c^{\star+}(2625)$ values found in Figure 6.3.2 (a), and its contribution to the $\Lambda_c^{\star+}(2593)$ yield is subtracted from that of Figure 6.4.3 (a). The resonant $\Lambda_c^{\star+}(2593)$ yield is therefore: $Y_{res} = Y_{\Sigma_c region} - Y_{sideband} = 9.2 \pm 3.7$. Dividing Y_{res} by the total $\Lambda_c^{\star+}(2593)$ yield of Figure 6.3.2 (a) we obtain the resonant branching ratio of the decay: $\frac{BR(\Lambda_c^{\star+}(2593)\to\Sigma_c\pi^\pm)}{BR(\Lambda_c^{\star+}(2593)\to\Lambda_c^+\pi^+\pi^-)} = 0.90 \pm 0.25$, which is compatible with 1. We thus establish a lower limit on the resonant branching fraction:

$$\frac{BR(\Lambda_c^{\star+}(2593) \to \Sigma_c\pi^\pm)}{BR(\Lambda_c^{\star+}(2593) \to \Lambda_c^+\pi^+\pi^-)} > 51\%$$

at the 90% confidence level.

In conclusion, E687 results for the resonant ratio of the $\Lambda_c^{\star+}(2593) \to \Lambda_c^+\pi^+\pi^-$ and $\Lambda_c^{\star+}(2625) \to \Lambda_c^+\pi^+\pi^-$ decays agree with the results found by CLEO[42] and support the interpretation of the $\Lambda_c^{\star+}(2593)$ to be the $J^P = (1/2)^-$ state and the $\Lambda_c^{\star+}(2625)$ to be the $J^P = (3/2)^-$ state of the orbitally excited $\Lambda_c^{\star+}$ doublet.

6.5 Measurement of photoproduction cross sections

We use the charm baryon signals in Figures 6.3.2 (a) and 6.4.2 (a), (b) to measure the inclusive photoproduction cross sections of $\Lambda_c^{\star+}$ and Σ_c relative to the inclusive photoproduction cross section of Λ_c^+. For Σ_c we use the formula:

$$\frac{\sigma_{\Sigma_c}}{\sigma_{\Lambda_c}} = \frac{Y(\Sigma_c)}{\epsilon(\Sigma_c \to \Lambda_c\pi, \Lambda_c \to pK\pi) \cdot BR(\Sigma_c \to \Lambda_c\pi) \cdot BR(\Lambda_c \to pK\pi)}$$

$$\times \frac{\epsilon(\Lambda_c \to pK\pi) \cdot BR(\Lambda_c \to pK\pi)}{Y(\Lambda_c)}$$

(ϵ denotes the Monte Carlo reconstruction efficiency and BR a Branching Ratio), where we assume $BR(\Sigma_c \to \Lambda_c\pi) = 1$.

In the case of $\Lambda_c^\star$ we use the formula:

$$\frac{\sigma_{\Lambda_c^\star}}{\sigma_{\Lambda_c}} = \frac{Y(\Lambda_c^\star)}{\epsilon(\Lambda_c^\star \to \Lambda_c\pi\pi, \Lambda_c \to pK\pi) \cdot BR(\Lambda_c^\star \to \Lambda_c\pi^+\pi^-)} \times \frac{\epsilon(\Lambda_c \to pK\pi)}{Y(\Lambda_c)} ,$$

but this time $BR(\Lambda_c^{+\star} \to \Lambda_c^+\pi^+\pi^-) \neq 1$ since the $\Lambda_c^{+\star}$ can also decay to $\Lambda_c^+\pi^0\pi^0$. We thus measure the combined quantity:

$$BR(\Lambda_c^{+\star} \to \Lambda_c^+\pi^+\pi^-) \times \frac{\sigma_{\Lambda_c^\star}}{\sigma_{\Lambda_c}} = \frac{Y(\Lambda_c^\star)}{\epsilon(\Lambda_c^\star \to \Lambda_c\pi\pi, \Lambda_c \to pK\pi)} \times \frac{\epsilon(\Lambda_c \to pK\pi)}{Y(\Lambda_c)} .$$

The fitted yield, the Monte Carlo reconstruction efficiency and the measured photoproduction cross section for the four states are listed in Table 6.5.1 (the reconstruction efficiencies are computed with the Monte Carlo yields obtained in Figure 6.3.4 and Figure 6.5.1).

Table 6.5.1 Photoproduction Cross Sections (%)

	Yield	Efficiency (%)	$\sigma_{\Sigma_c}/\sigma_{\Lambda_c}$ or $BR \cdot \sigma_{\Lambda_c^*}/\sigma_{\Lambda_c}$ (%)
Λ_c^+	994.2 ± 77.4	1.98 ± 0.04	
Σ_c^0	43.2 ± 10.9	1.11 ± 0.03	$7.77 \pm 2.07 \pm 0.31$
Σ_c^{++}	39.0 ± 10.7	1.16 ± 0.03	$6.70 \pm 1.92 \pm 0.27$
$\Lambda_c^{\star+}(2593)$	10.2 ± 3.7	0.61 ± 0.02	$3.34 \pm 1.23 \pm 0.27$
$\Lambda_c^{\star+}(2625)$	24.4 ± 6.3	0.69 ± 0.03	$7.01 \pm 1.93 \pm 0.56$

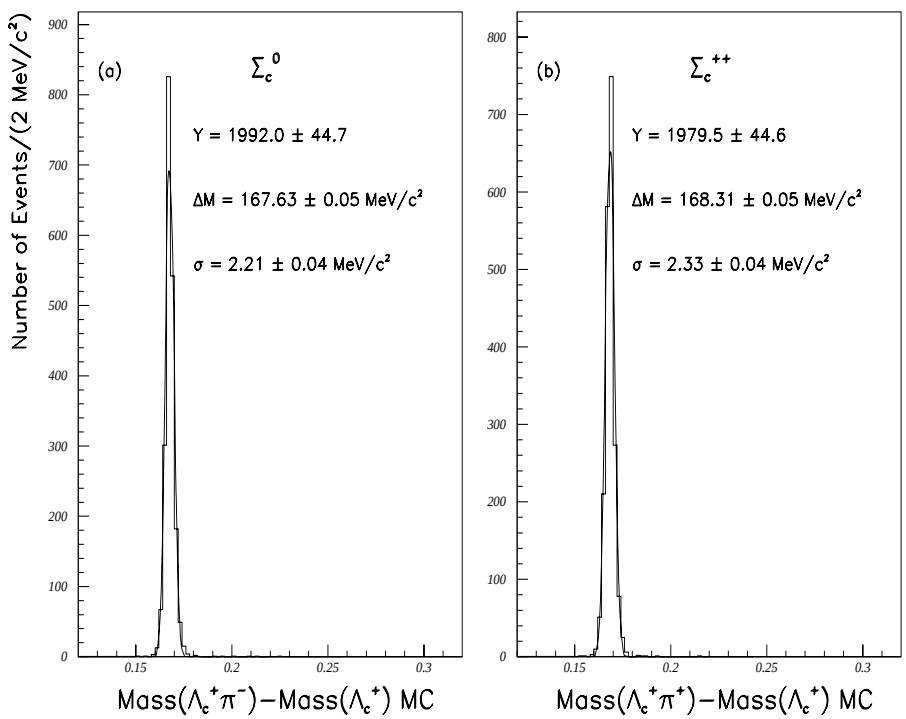

Figure 6.5.1 $\Sigma_c^0 \to \Lambda_c^+\pi^-$ (a) and $\Sigma_c^{++} \to \Lambda_c^+\pi^+$ (b) ($\Lambda_c^+ \to pK^-\pi^+$) Monte Carlo signals reconstructed with the analysis conditions listed in Table 6.3.1

The systematic uncertainty on the measured cross sections is computed by considering a conservative estimate of 4% error per track. We checked the

stability of our results by using different analysis cuts and different fitting techniques and find that the results are consistent within the statistical errors. We also investigate a possible dependence of the measured values on the momentum of the reconstructed Λ_c^+. For this purpose we divide the Λ_c^+ momentum spectrum into three different regions (between 30 and 60 Gev/c, between 60 and 90 GeV/c, above 90 GeV/c). We fit each data histogram separately, computing the Monte Carlo reconstruction efficiency for each momentum range, and sum the three efficiency-corrected yields. The results obtained with this "momentum-binned efficiency" technique proved to be in agreement, within the statistical error, with the ones obtained by use of global reconstruction efficiency.

We can perform a rough estimate of the number of Λ_c^+ originating from higher mass charm baryons by summing the photoproduction cross sections for each of the $\Lambda_c^{\star+}$ and Σ_c states observed. In the case of the Σ_c, we average the two results for Σ_c^0 and Σ_c^{++} and multiply by 3 to take into account the decay mode $\Sigma_c^+ \rightarrow \Lambda_c^+\pi^0$, which is not completely reconstructed in this analysis but nevertheless contributes to the total $\Lambda_c^+ \rightarrow pK^-\pi^+$ sample observed. In the case of the $\Lambda_c^{\star+}$, we assume that the decay $\Lambda_c^{\star+}(2593) \rightarrow \Lambda_c^+\pi^+\pi^-$ is completely dominated by the resonant mode $\Lambda_c^{\star+}(2593) \rightarrow \Sigma_c\pi^\pm, \Sigma_c \rightarrow \Lambda_c^+\pi^\mp$, so that these events are already included in the Σ_c^0, Σ_c^{++} photoproduction cross sections. On the other hand we assume the decay $\Lambda_c^{\star+}(2625) \rightarrow \Lambda_c^+\pi^+\pi^-$ to be completely non resonant and also take BR($\Lambda_c^{\star+}(2625) \rightarrow \Lambda_c^+\pi^+\pi^-$) to be

2/3 (from isospin invariance). Therefore we obtain:

$$\frac{\sigma(\Sigma_c, \Lambda_c^\star)}{\sigma_{\Lambda_c}} \simeq \frac{3}{2}(\frac{\sigma_{\Sigma_c^0}}{\sigma_{\Lambda_c}} + \frac{\sigma_{\Sigma_c^{++}}}{\sigma_{\Lambda_c}}) + \frac{3}{2} BR(\Lambda_c^\star(2625) \to \Lambda_c \pi^+ \pi^-) \cdot \frac{\sigma_{\Lambda_c^\star(2625)}}{\sigma_{\Lambda_c}}$$
$$= (32.2 \pm 5.1 \pm 1.7)\%.$$

Therefore our data indicates that about a third of the photoproduced Λ_c^+ come from some higher mass charm baryon state.

6.6 Measurement of the Σ_c^0, Σ_c^{++} masses

We measure the Σ_c^0 and Σ_c^{++} masses by using a combined sample of Λ_c^+ reconstructed in the two decay modes $pK^-\pi^+$ and $p\overline{K}_s^0$. Figures 6.6.1, 6.6.2 and 6.6.3 show the Σ_c samples reconstructed by using increasingly tighter analysis cuts for the $pK^-\pi^+$ and $p\overline{K}_s^0$ samples. It can be noticed that, as the cuts become more stringent and the signal to noise improves, the Σ_c^0 mass appears to be quite stable, while on the other hand the Σ_c^{++} mass seems to follow an upward trend, possibly indicating some systematic effects. The situation is summarized in Figure 6.6.4 , where we also compare to the values for the Σ_c masses obtained by CLEO[47]. We decide to measure the Σ_c masses by using the "medium" analysis conditions of Figure 6.6.2 , for which the Σ_c^{++} mass falls in the middle of the range covered.

In order to evaluate the systematic error involved in the measurement, we used the *split sample* technique described in the Appendix. We separated both the Σ_c^0 and Σ_c^{++} samples into four statistically independent subsamples: candidates originating from different Λ_c^+ decays ($pK^-\pi^+$ or $p\overline{K}_s^0$) and data taken by our experiment during the two different run periods (1990 or 1991); then we measured the Σ_c^0 and Σ_c^{++} masses independently for each subsample (see Figure 6.6.5).

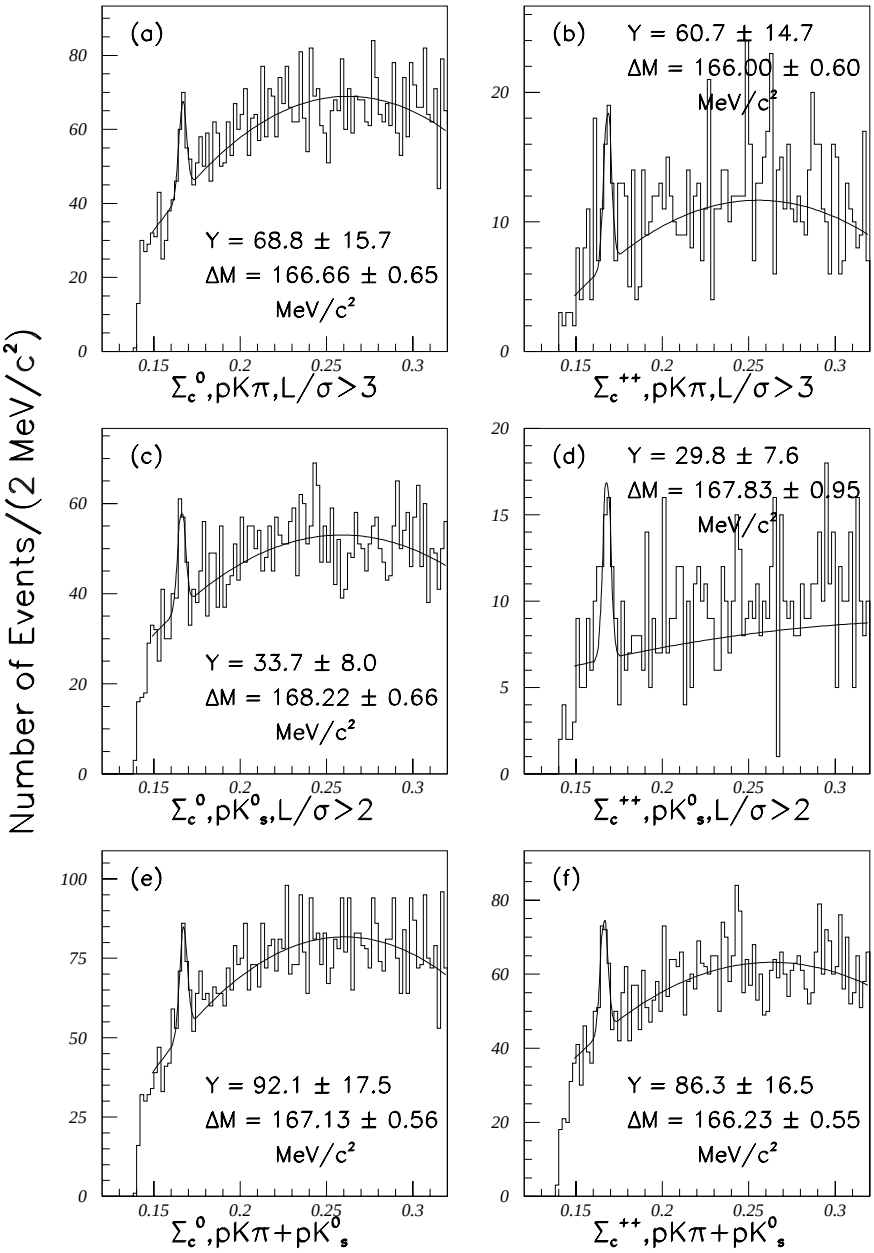

Figure 6.6.1 Σ_c^0 and Σ_c^{++} samples reconstructed through "loose" analysis cuts: same as those listed in Table 6.3.1, but with $L/\sigma_L > 3$ for $pK^-\pi^+$ and $L/\sigma_L > 2$ for $p\overline{K}_s^0$.

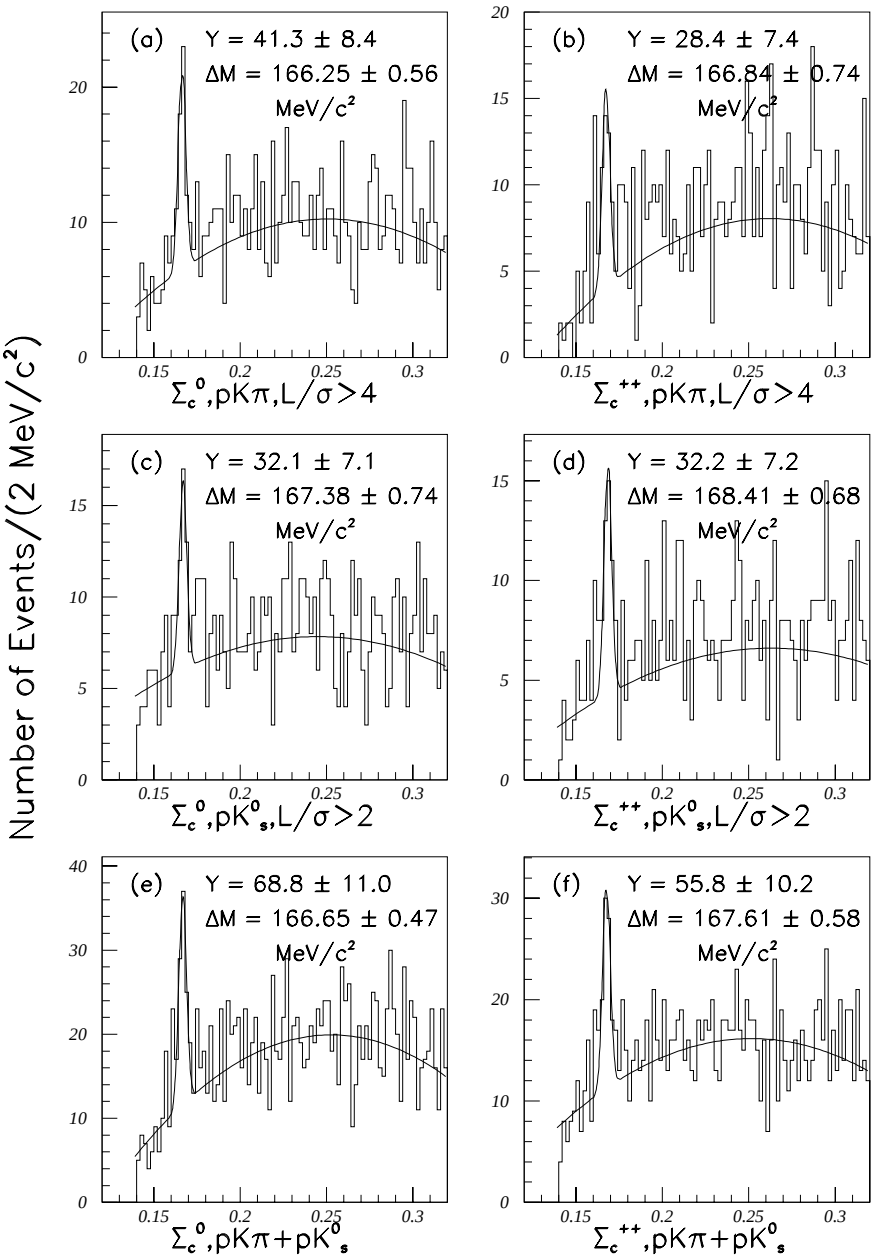

Figure 6.6.2 Σ_c^0 and Σ_c^{++} samples for "medium" analysis cuts: in addition to the cuts of Table 6.3.1, we require $\sigma < 15\ mm$ for $p\overline{K}_s^0$, while for $pK^-\pi^+$ we require $cls > 5\%$, $L/\sigma_L > 4$ and that at least one of the two heavy prongs (p or K) is positively identified by the Čerenkov counters.

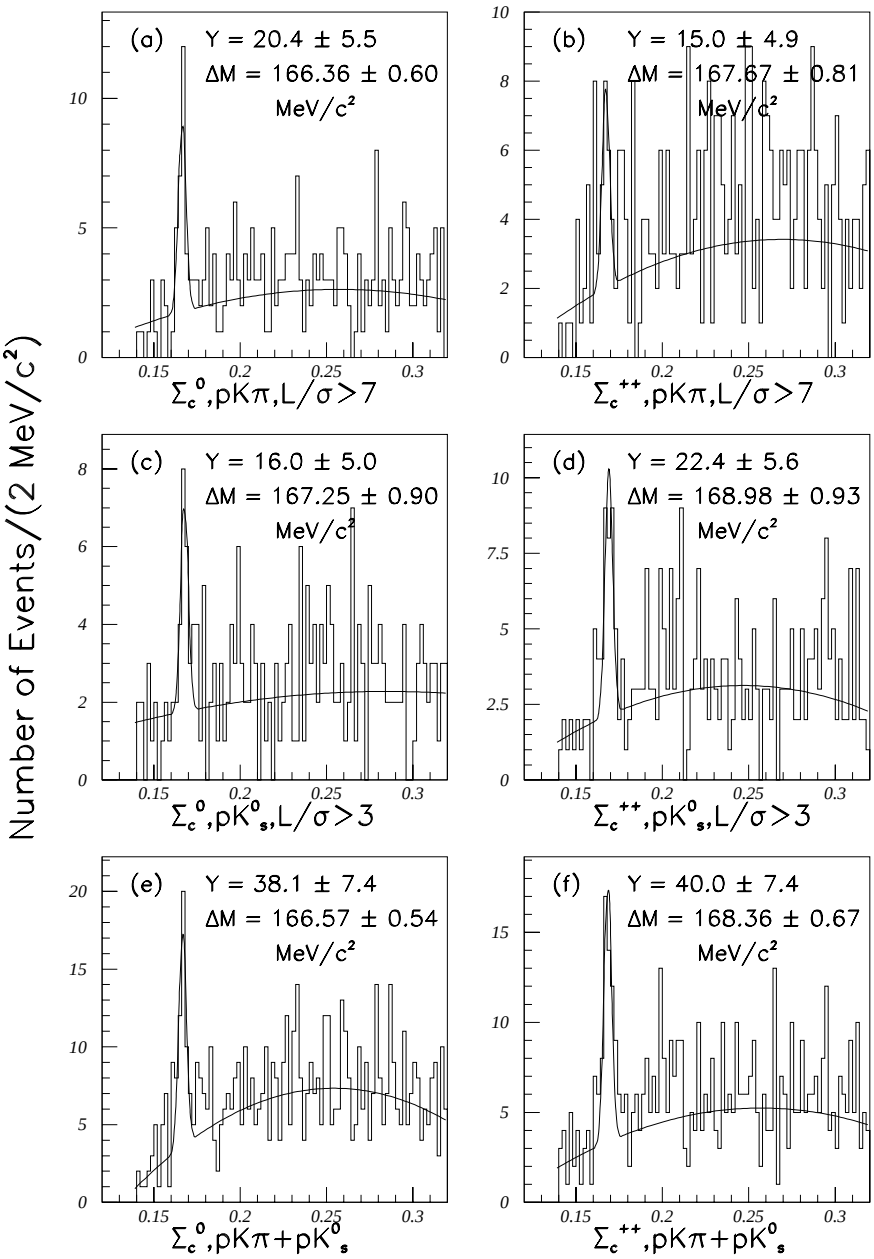

Figure 6.6.3 Σ_c^0 and Σ_c^{++} samples for "tight" analysis cuts: same as in previous figure, but harder L/σ_L conditions: $L/\sigma_L > 7$ for $pK^-\pi^+$ and $L/\sigma_L > 3$ for $p\overline{K}_s^0$.

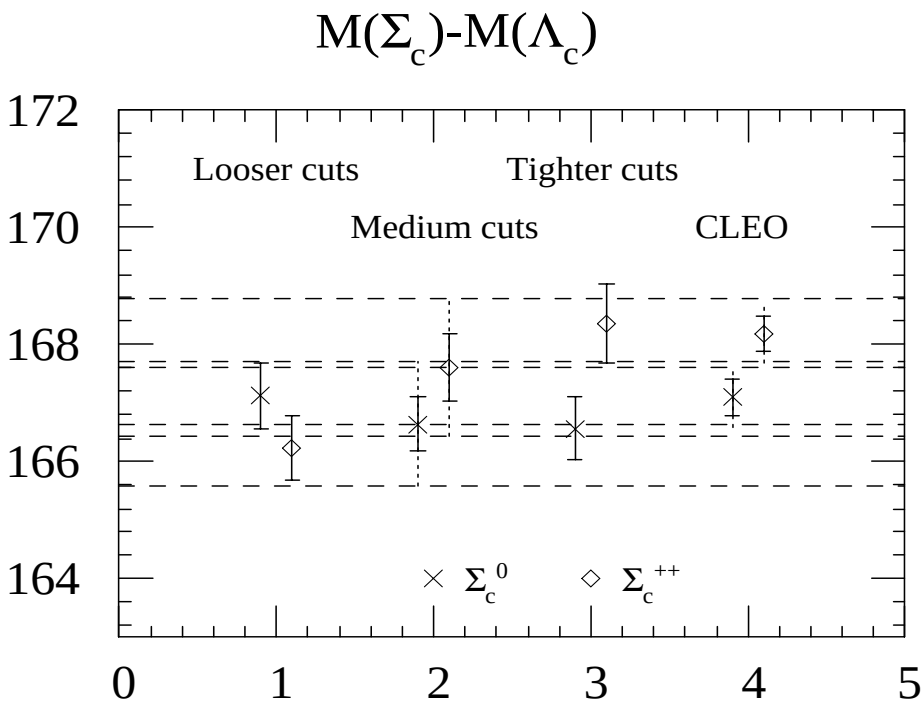

Figure 6.6.4 Σ_c^0 and Σ_c^{++} masses obtained with different analysis cuts, and comparison to CLEO results.

The final result for the M(Σ_c)-M(Λ_c^+) mass differences are:

$$M(\Sigma_c^0) - M(\Lambda_c^+) = 166.6 \pm 0.5\ (stat) \pm 0.6\ (syst)\ MeV/c^2\ ,$$

$$M(\Sigma_c^{++}) - M(\Lambda_c^+) = 167.6 \pm 0.6\ (stat) \pm 0.6\ (syst)\ MeV/c^2\ .$$

The larger systematic error in the measurement of the Σ_c masses, as compared to the measurement of the $\Lambda_c^{\star+}(2593)$ mass, reflects the higher level of background under the Σ_c^0, Σ_c^{++} signals.

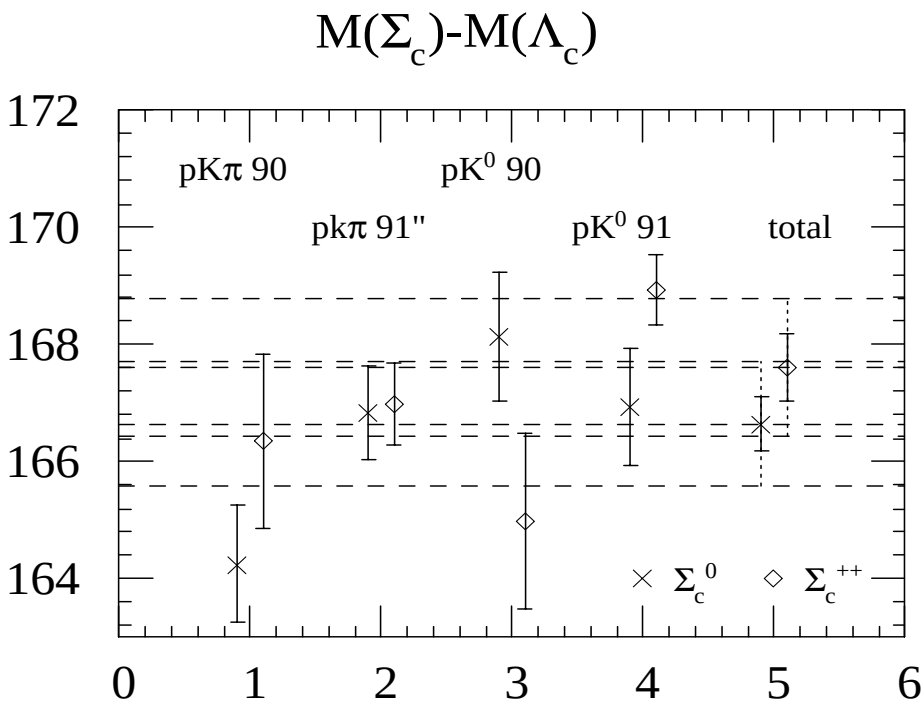

Figure 6.6.5 Different values for Σ_c^0 and Σ_c^{++}masses obtained by splitting the total samples into four independent subsamples each, and final values measured for the masses of the two states (with superimposed statistical and systematic error bars).

6.7 Summary of results

We have investigated the decay of higher mass charm baryons decaying to Λ_c^+: $\Lambda_c^{\star+}(2625) \rightarrow \Lambda_c^+\pi^+\pi^-$, $\Lambda_c^{\star+}(2593) \rightarrow \Lambda_c^+\pi^+\pi^-$, $\Sigma_c^0 \rightarrow \Lambda_c^+\pi^-$ and $\Sigma_c^{++} \rightarrow \Lambda_c^+\pi^+$. We confirm the existence of the state $\Lambda_c^{\star+}(2593)$ and measure its mass to be:

$$M(\Lambda_c^{\star+}(2593)) - M(\Lambda_c^+) = 309.2 \pm 0.7\ (stat) \pm 0.3\ (syst)\ MeV/c^2\ .$$

We estimate the resonant component of the decay $\Lambda_c^{\star+}(2593) \rightarrow \Sigma_c\pi^\pm$ to be

dominant and measure the upper limit (at 90% c.l.):

$$\frac{BR(\Lambda_c^{\star+}(2593) \to \Sigma_c \pi^{\pm})}{BR(\Lambda_c^{\star+}(2593) \to \Lambda_c^{+} \pi^{+} \pi^{-})} > 51\% \ .$$

We measure the masses of the Σ_c^0, Σ_c^{++} states to be:

$$M(\Sigma_c^0) - M(\Lambda_c^+) = 166.6 \pm 0.5 \ (stat) \pm 0.6 \ (syst) \ MeV/c^2 \ ,$$

$$M(\Sigma_c^{++}) - M(\Lambda_c^+) = 167.6 \pm 0.6 \ (stat) \pm 0.6 \ (syst) \ MeV/c^2 \ .$$

Finally, we measure the inclusive photoproduction cross section for the four states $\Lambda_c^{\star+}(2625)$, $\Lambda_c^{\star+}(2593)$, Σ_c^0, Σ_c^{++} relative to the inclusive photoproduction cross section for the Λ_c^+, and find that approximately a third of the photoproduced Λ_c^+ originate from the decay of higher mass charm baryons.

CHAPTER 7

SUMMARY AND CONCLUSIONS

In this chapter we summarize the results from this thesis and compare them to other experimental measurements and theoretical predictions.

7.1 Pseudoscalar D^0 semileptonic decays

We investigated the two pseudoscalar meson semileptonic decays $D^0 \to K^-\mu^+\nu$ (Cabibbo-favored) and $D^0 \to \pi^-\mu^+\nu$ (Cabibbo-suppressed). In order to reduce background and have cleaner signals, we used a D^{*+}-tag technique, i.e. we required the D^0 to originate from the decay $D^{*+} \to D^0\pi^+$. Combinations of $K^-\mu^+$ or $\pi^-\mu^+$ candidates originating from a common vertex were selected. Using the direction in space given by the primary and secondary vertex locations, and assuming the D^0 mass, we were able to compute the D^0 momentum. The D^0 candidate was then combined with the momentum of a soft pion from the primary vertex to construct the candidate D^{*+} invariant mass, and the $D^{*+} - D^0$ mass difference was plotted.

We observed 824.5 ± 33.0 $D^0 \to K^-\mu^+\nu$ events and 45.6 ± 11.8 $D^0 \to \pi^-\mu^+\nu$ events. This represents the world's first observation of the Cabibbo-suppressed decay $D^0 \to \pi^-l^+\nu$ with more than a 3 σ statistical significance. We measured the relative branching ratio of the two decays to be:

$$\frac{BR\ (D^0 \to \pi^-\mu^+\nu)}{BR\ (D^0 \to K^-\mu^+\nu)} = 0.099 \pm 0.026\ (stat)\ \pm 0.007\ (syst)\ .$$

In Table 7.1.1 we make a comparison with other experimental measurements and theoretical predictions. Our measurement is the most accurate to date and is compatible with previous experiments and several theoretical computations

(the only model which falls more than 2 σ out of our measurement is the ISGW theory[52], updated by Scora[53]).

Table 7.1.1 Results for D^0 pseudoscalar meson semileptonic decays

Reference	$\frac{BR\ (D^0 \to \pi^- l^+ \nu)}{BR\ (D^0 \to K^- l^+ \nu)}$	$\lvert\frac{V_{cd}}{V_{cs}}\rvert^2 \lvert\frac{f_+^\pi(0)}{f_+^K(0)}\rvert^2$	$\lvert\frac{f_+^\pi(0)}{f_+^K(0)}\rvert$
E687 (μ)	$0.099 \pm 0.026 \pm 0.007$	$0.048 \pm 0.014 \pm 0.003$	$0.97 \pm 0.14 \pm 0.03$
E687 (e)	$0.103 \pm 0.031 \pm 0.004$	$0.054 \pm 0.017 \pm 0.002$	$1.03 \pm 0.16 \pm 0.02$
E687 ($\mu + e$)	$0.101 \pm 0.020 \pm 0.003$	$0.050 \pm 0.011 \pm 0.002$	$1.00 \pm 0.10 \pm 0.02$
CLEO[49]	$0.103 \pm 0.039 \pm 0.013$	$0.052 \pm 0.020 \pm 0.007$	$1.01 \pm 0.20 \pm 0.07$
CLEO[50]	$(0.085 \pm 0.027 \pm 0.014)[*]$	$0.085 \pm 0.027 \pm 0.014$	$1.29 \pm 0.20 \pm 0.11$
MARK III[51]	$0.11^{+0.07}_{-0.04} \pm 0.02$		
Lubicz[54] (LG)	0.086 ± 0.041		0.92 ± 0.18
Bernard[61] (LG)			0.93 ± 0.10
Allton[18] (LG)	0.088 ± 0.029		1.02 ± 0.03
ISGW2[52] [53] (QM)	0.048		0.71
Narison[55] (SR)	0.083		0.91 ± 0.01
Dominguez[65] (SR)	0.102 ± 0.035		
Sadzikowski[64] (BM)	0.126		1.1
Demchuk[56]	0.073		0.87

[$*$] The value quoted in parenthesis is $\frac{BR\ (D^+ \to \pi^0 e^+ \nu)}{BR\ (D^+ \to \overline{K}^0 e^+ \nu)} = \frac{1}{2}\frac{BR\ (D^0 \to \pi^- e^+ \nu)}{BR\ (D^0 \to K^- e^+ \nu)}$, where the factor of $\frac{1}{2}$ arises from the $\frac{1}{\sqrt{2}}$ coupling of $d\overline{d}$ to the π^0.

- QM: Quark Model
- SR: QCD Sum Rules
- LG: Lattice Gauge
- BM: MIT Bag Model

Charm meson semileptonic decays are interesting because the hadronic part of the interaction can be studied. In the case of a decay into a pseudoscalar meson (like K^- or π^-), the hadronic current is expressed through two dimensionless form factors $f^h_\pm(q^2)$. Using a single pole mass parameterization $f^h_\pm(q^2) = \frac{f^h_\pm(0)}{1-q^2/\mathrm{M}^2_{pole}}$, and further assuming $\frac{f^h_+}{f^h_-} = -1$, we integrated the differential decay rates for $D^0 \to K^-\mu^+\nu$ and $D^0 \to \pi^-\mu^+\nu$ over the region of the Dalitz plot q^2 vs $m^2_{h\mu}$ for which we have acceptance, and measured the following quantity:

$$\left|\frac{V_{cd}}{V_{cs}}\right|^2 \left|\frac{f^\pi_+(0)}{f^K_+(0)}\right|^2 = 0.048 \pm 0.014\ (stat) \pm 0.003\ (syst)\ .$$

Analysis of semileptonic pseudoscalar decays does not allow us to measure independently either the ratio of the CKM matrix elements or the ratio of the form factor normalizations, but only the product of the two. Unfortunately, theoretical predictions for the ratio of form factors are still heavily model dependent, so it is not possible to use the formula above to obtain a significant estimate of the ratio $\left|\frac{V_{cd}}{V_{cs}}\right|$. Measurements of lower generation CKM matrix elements together with unitarity constraints, provide the best estimate for this quantity:

$$\left|\frac{V_{cd}}{V_{cs}}\right|^2 = 0.051 \pm 0.001\ .$$

We used this result to compute the ratio of the two form factors and found:

$$\left|\frac{f^\pi_+(0)}{f^K_+(0)}\right| = 0.97 \pm 0.14\ (stat) \pm 0.03\ (syst)\ .$$

Although this value represents the world's best estimate for $\left|\frac{f^\pi_+(0)}{f^K_+(0)}\right|$, the associated error is still too large to allow us to discriminate between different theoretical models (see Table 7.1.1).

The quoted values reflect a 10% subtraction of the $D^0 \rightarrow \pi^- \mu^+ \nu$ signal due to the estimated contamination from incompletely reconstructed $D^+ \rightarrow \varrho^0 \mu^+ \nu$ events. This estimate was based on the branching ratio $\frac{BR(D^+ \rightarrow \varrho^0 \mu^+ \nu)}{BR(D^+ \rightarrow \overline{K}^{*0} \mu^+ \nu)} = 0.044^{+0.031}_{-0.025} \pm 0.014$[32] measured by experiment E653. Other sources of background to the $D^0 \rightarrow \pi^- \mu^+ \nu$ and $D^0 \rightarrow K^- \mu^+ \nu$ signals were subtracted as well. We estimated the systematic uncertainty from the experimental sources to be small compared to the statistical errors involved. We also found that the measured quantities are affected by the form factor parameterization used in Monte Carlo generation. If a single pole mass dependence is used (as it is commonly found in literature), then the value of the pole mass becomes the critical parameter. We showed how our measurements vary within a reasonable range of the $D^0 \rightarrow \pi^- \mu^+ \nu$ and $D^0 \rightarrow K^- \mu^+ \nu$ pole masses, but we did not include this theoretical uncertainty in our quoted values.

The results of this analysis for the semi-muonic modes of the D^0 semileptonic decays were combined with the results of a similar E687 analysis for the semi-electronic modes: $D^0 \rightarrow K^- e^+ \nu$ and $D^0 \rightarrow \pi^- e^+ \nu$. Candidate electrons were reconstructed in both the Inner Electromagnetic Detector (analysis performed by Matt Nehring) and the Outer Electromagnetic Detector (analysis performed by Daniele Brambilla). The total reconstructed electron sample amounted to 681.9 ± 32.5 $D^0 \rightarrow K^- e^+ \nu$ events and 45.5 ± 13.3 $D^0 \rightarrow \pi^- e^+ \nu$ events. In Table 7.1.1, we report the results for the semi-electronic mode; the agreement with the muon results is excellent. The combined semi-muonic and semi-electronic analysis has been submitted for publication.

7.2 Vector D^+ semileptonic decays

We have investigated the vector meson semileptonic decays $D^+ \to \overline{K}^{*0}\mu^+\nu$ (Cabibbo-favored) and $D^+ \to \varrho^0\mu^+\nu$ (Cabibbo-suppressed). Decay candidates $(K^-\pi^+)\mu^+$ and $(\pi^-\pi^+)\mu^+$ were selected and required to originate from a common vertex in space. For these combinations, we plotted the two-body invariant mass $M(K^-\pi^+)$ and $M(\pi^-\pi^+)$ (respectively) and fitted for the signals of the vector meson resonances $\overline{K}^{*0}(892) \to K^-\pi^+$ and $\varrho^0(770) \to \pi^+\pi^-$. In order to reduce contamination from D_s^+ semileptonic decays, we used the longer D^+ lifetime to require the decay vertex to be outside the target region, and to have a large significance of separation from the production vertex. Residual contamination from D_s^+ decays was estimated by using the CLEO[36] branching ratios for $\frac{BR(D_s^+\to\eta e^+\nu)}{BR(D_s^+\to\phi e^+\nu)}$, $\frac{BR(D_s^+\to\eta' e^+\nu)}{BR(D_s^+\to\phi e^+\nu)}$, and by fully reconstructing the decay $D_s^+ \to \phi\mu^+\nu$ from our data. Background from other incompletely reconstructed D^+ vector meson semileptonic decays was either completely suppressed by tight invariant mass cuts ($D^+ \to \eta'\mu^+\nu$), or inserted as an additional component in the fit ($D^+ \to \eta\mu^+\nu$). Because of our low reconstruction efficiency for π^0, we were not able to impose a D^{*0}-tag requirement in this analysis.

We reconstructed 443.0 ± 22.3 $D^+ \to \overline{K}^{*0}\mu^+\nu$ events and 39.2 ± 9.0 $D^+ \to \varrho^0\mu^+\nu$ events. We measured the relative branching ratio of the two decays to be:

$$\frac{BR\ (D^+ \to \varrho^0\mu^+\nu)}{BR\ (D^+ \to \overline{K}^{*0}\mu^+\nu)} = 0.079 \pm 0.019\ (stat)\ \pm 0.013\ (syst)\ .$$

This analysis is the first statistically significant observation of the decay channel $D^+ \to \varrho^0\mu^+\nu$ (the only previous evidence was a sample of $4.0^{+2.8}_{-2.3}$ events

reported by E653[32]). We used the measured branching ratio to compute the ratio for the two decays of the only hadronic form factor which survives when the two limits $q^2 \to 0$, $m_l^2 \to 0$ are taken[22]:

$$\left| \frac{A_3^{\varrho}(0)}{A_3^{K^*}(0)} \right| = 1.29 \pm 0.15 \ (stat) \pm \ 0.11 \ (syst) \ ,$$

where the value $\left|\frac{V_{cd}}{V_{cs}}\right|^2$ from CKM unitarity was used. In Table 7.2.1 we compare the measured quantities to the other only experimental result and to several theoretical predictions. Our result for the branching ratio $\frac{BR\ (D^+ \to \varrho^0 \mu^+ \nu)}{BR\ (D^+ \to \overline{K}^{*0} \mu^+ \nu)}$ is about double what one would compute by using theoretical predictions on $\frac{BR\ (D^0 \to \varrho^- \mu^+ \nu)}{BR\ (D^0 \to \overline{K}^{*-} \mu^+ \nu)}$ and by dividing by two to take into account the $\frac{1}{\sqrt{2}}$ coupling of the $d\overline{d}$ pair to the ϱ^0. Our result for the form factors ratio, although compatible with unity, seems to favor those models which predict an $SU(3)$-flavor symmetry breaking effect in the upward direction.

We also observed a weak evidence of 6.7 ± 3.1 candidate events for the decay channel $D^+ \to \eta \mu^+ \nu$, $\eta \to \pi^+ \pi^- \pi^0$ (where the π^0 is not reconstructed). If confirmed, this would be the first observation of this D^+ semileptonic decay. The branching ratio with respect to the $D^+ \to \varrho^0 \mu^+ \nu$ decay was measured to be:

$$\frac{BR\ (D^+ \to \eta \mu^+ \nu)}{BR\ (D^+ \to \varrho^0 \mu^+ \nu)} = 2.83 \pm 1.45 \ (stat) \ \pm 0.17 \ (syst) \ .$$

Efforts are currently underway to confirm the results of this analysis using the semi-electronic decay mode $D^+ \to \varrho^0 e^+ \nu$. Combined results may be submitted for publication in the near future.

Table 7.2.1 Results for D^+ vector meson semileptonic decays †

Reference	$\frac{BR\ (D\to\varrho\mu\nu)}{BR\ (D\to K^*\mu\nu)}$	$\lvert\frac{A_3^{\varrho}(0)}{A_3^{K^*}(0)}\rvert$
E687	$0.079 \pm 0.019 \pm 0.013\ (D^+)$	$1.29 \pm 0.15 \pm 0.11$
E653[32]	$0.044^{+0.031}_{-0.025} \pm 0.014\ (D^+)$	$0.96^{+0.34}_{-0.27} \pm 0.15$††
Allton[18] (LG)	$0.087 \pm 0.037\ (D^0)$	
Abada[19] (LG)	$0.094 \pm 0.062\ \ (D^0)$	
Bowler[20] (LG)	$0.072 \pm 0.024\ (D^0)$	
Lubicz[54] (LG)	$0.080 \pm 0.023\ (D^0)$	1.06 ± 0.43
Bernard[61] (LG)		0.90 ± 0.31
Wirbel[21] (QM)	$0.070\ (D^0)$	0.92
ISGW2[53][52] (QM)	$0.05\ (D^0)$	1.06
Ball[57] (SR)		1.27 ± 1.23
Colangelo[58] (SR)		0.90 ± 0.12
Casalbuoni[59] (HQET)		1.25
Bajc[60] (HQET)		1.12 ± 0.36
Jaus[62] (LFQM)		7.67
O'Donnell[22] (LFQM)		0.88

† Experimental measurements for the branching ratio can be compared to the theoretical predictions assuming (from isospin invariance): $\frac{BR\ (D^+\to\varrho^0\mu^+\nu)}{BR\ (D^+\to K^{*0}\mu^+\nu)} = \frac{1}{2}\frac{BR\ (D^0\to\varrho^-\mu^+\nu)}{BR\ (D^0\to K^{*-}\mu^+\nu)}$.

†† Computed by using $\left|\frac{V_{cd}}{V_{cs}}\right|^2 = 0.051 \pm 0.001$.

∘ QM: Quark Model

∘ SR: QCD Sum Rules

∘ HQET: Heavy Quark Effective Theory

∘ LG: Lattice Gauge

∘ LFQM: Light-Front Quark Model

7.3 Charm baryons decaying to Λ_c^+

We analyzed the decay of higher mass charm baryons to Λ_c^+, namely: $\Lambda_c^{\star+}(2625) \to \Lambda_c^+\pi^+\pi^-$, $\Lambda_c^{\star+}(2593) \to \Lambda_c^+\pi^+\pi^-$, $\Sigma_c^0 \to \Lambda_c^+\pi^-$ and $\Sigma_c^{++} \to \Lambda_c^+\pi^+$. The total Λ_c^+ sample used for this analysis amounted to $Y_{\Lambda_c^+} = 1564 \pm 101$ events and was obtained by reconstructing Λ_c^+ candidates in five decay modes: $\Lambda_c^+ \to pK^-\pi^+$, $\Lambda_c^+ \to pK_s^0$, $\Lambda_c^+ \to pK_s^0\pi^+\pi^-$, $\Lambda_c^+ \to \Lambda^0\pi^+$, $\Lambda_c^+ \to \Lambda^0\pi^+\pi^-\pi^+$. Λ_c^+ decay candidates from each mode were then combined with one or two pions from the primary vertex to look for higher mass states, and the mass difference between the Λ_c^++pion(s) combination and the Λ_c^+ was plotted.

We reconstructed $Y_{\Lambda_c^+(2593)} = 13.9 \pm 4.5$ candidates in the decay mode $\Lambda_c^{\star+}(2593) \to \Lambda_c^+\pi^+\pi^-$, and thus we confirmed the existence of the state $\Lambda_c^{\star+}(2593)$, previously observed only by CLEO[42]. We measured its mass difference relative to the Λ_c^+ mass to be:

$$M(\Lambda_c^{\star+}(2593)) - M(\Lambda_c^+) = 309.2 \pm 0.7\ (stat) \pm 0.3\ (syst)\ MeV/c^2\ .$$

We also estimated the resonant component of the decay $\Lambda_c^{\star+}(2593) \to \Sigma_c\pi^\pm$ (where the Σ_c can either be a Σ_c^0 or a Σ_c^{++}) to be dominant and measured the upper limit (at 90% c.l.):

$$\frac{BR(\Lambda_c^{\star+}(2593) \to \Sigma_c\pi^\pm)}{BR(\Lambda_c^{\star+}(2593) \to \Lambda_c^+\pi^+\pi^-)} > 0.51\ .$$

Previous analysis from E687[41] had investigated the decay $\Lambda_c^{\star+}(2625) \to \Lambda_c^+\pi^+\pi^-$and concluded the resonant fraction to be small:

$$\frac{BR(\Lambda_c^{\star+}(2625) \to \Sigma_c\pi^\pm)}{BR(\Lambda_c^{\star+}(2625) \to \Lambda_c^+\pi^+\pi^-)} < 0.36\ ,$$

at 90% c.l. The E687 results on the resonant fraction of the decays $\Lambda_c^{\star+} \to$

$\Lambda_c^+\pi^+\pi^-$ agree with similar findings by CLEO[42][40] and support the angular momentum and parity assignment $J^P(\Lambda_c^+(2593)) = \frac{1}{2}^-$ and $J^P(\Lambda_c^+(2625)) = \frac{3}{2}^-$. The two $\Lambda_c^{\star+}$ states would then be a fine structure doublet, in which the light diquark ud carries a unit of orbital angular momentum $L = 1$ with respect to the charm quark c (L may combine with the total spin of the baryon $S = \frac{1}{2}$ to produce $J = \frac{1}{2}$ or $J = \frac{3}{2}$).

We also measured the masses of two Σ_c states to be:

$$M(\Sigma_c^0) - M(\Lambda_c^+) = 166.6 \pm 0.5\ (stat) \pm 0.6\ (syst)\ MeV/c^2\ ,$$

$$M(\Sigma_c^{++}) - M(\Lambda_c^+) = 167.6 \pm 0.6\ (stat) \pm 0.6\ (syst)\ MeV/c^2\ .$$

In Table 7.3.1 we summarize the E687 measurements of the four states $\Lambda_c^{\star+}(2625)$, $\Lambda_c^{\star+}(2593)$, Σ_c^0, Σ_c^{++} and compare them to other experimental results.

Finally, we measured the photoproduction cross section for each of the states $\Lambda_c^{\star+}(2625)$, $\Lambda_c^{\star+}(2593)$, Σ_c^0 and Σ_c^{++}relative to the inclusive photoproduction cross section for the Λ_c^+. Our data indicate that roughly a third of the photoproduced Λ_c^+'s comes from the decay of higher mass charm baryon states.

This analysis was published in Physics Letters B[66].

Table 7.3.1 Results for Mass Difference $M(\Lambda_c^*, \Sigma_c) - M(\Lambda_c)$ (MeV/c^2)

state	E687	CLEOII	Notes
$\Lambda_c^{*+}(2625)$	$340.4 \pm 0.6 \pm 0.3$[41]	$342.2 \pm 0.2 \pm 0.5$	375 [$*$]
$\Lambda_c^{*+}(2593)$	$309.2 \pm 0.7 \pm 0.3$	$307.5 \pm 0.4 \pm 1.0$	365 [$*$]
Σ_c^{++}	$167.6 \pm 0.6 \pm 0.6$	$168.2 \pm 0.3 \pm 0.2$	168.04 ± 0.27 [†]
Σ_c^0	$166.6 \pm 0.5 \pm 0.6$	$167.1 \pm 0.3 \pm 0.2$	167.3 ± 0.4 [†]

[$*$] Theoretical prediction[67].

[†] World average[33].

7.4 Final remarks

A new charm photoproduction experiment (FOCUS/E831), using an upgraded and largely modified version of the E687 spectrometer, is scheduled to start running at the Fermilab facility in July 1996. This experiment is expected to increase the reconstructed sample of charm particles by at least a factor of ten over the E687 statistics. The increase originates from using a slightly lower energy photon beam, by impacting on the radiation target both electron and positron beams, from a new reduced deadtime data-acquisition system, from using a multiply segmented production target which increases the number of charm decays in air, and from an increased efficiency of all the detectors in the spectrometer. Since the analyses presented in this thesis are limited first by statistics, it is expected that all the results will be considerably improved by the new experiment.

In particular, the analysis of charm semileptonic decays will be one of the topics to profit most from the new run. FOCUS will be able to detect

muons both in the inner and the outer region of the spectrometer, thus improving the statistics of the semi-muonic modes by another factor of two. Also, the new lead-glass inner electromagnetic calorimeter will hopefully prove to be more efficient than the E687 detector. Better efficiency in lepton identification will also cause a reduction of the hadron/lepton misidentification background, which is one of the major sources of background in the semileptonic analysis. For the analysis of Cabibbo-suppressed decays, background from K/π feedthrough should also be reduced by improvements in the particle identification software. Finally, if π^0's are reconstructed with sufficient efficiency, it will be possible to impose a D^{*+}-tag requirement on the D^+ semileptonic decays.

Larger and cleaner charm reconstructed samples will not only improve the current results, but will also allow for new measurements of interesting physical quantities: the value of the pole masses for both the $D^0 \to \pi^- l^+ \nu$ and $D^+ \to \varrho^0 l^+ \nu$ decays, the ratio of the two form factors $\xi = \frac{f_-^h(0)}{f_+^h(0)}$, and the analysis of other D^0, D^+, D_s^+ vector meson semileptonic decays. If the desired level of statistics is achieved, the challenge will be to improve our knowledge of the spectrometer in order to not be dominated by sources of systematic error. Improved theoretical estimates will be needed to confront the FOCUS results.

REFERENCES

1. The tau neutrino ν_τ is the only particle of the Standard Model which has not yet been directly observed.

2. Our distinction between "matter particles" and "force particles" is a choice of convenience: both the fundamental fermions and bosons are described by fields and exhibit at the same time properties of "matter" and "radiation".

3. Unlike the photon or the $W^\pm$ and Z^0, the gluons are supposed to carry color charge themselves, and therefore can interact within each other, besides coupling to the quarks.

4. The gravitational force is also supposed to be transmitted by a corresponding gauge boson, the *graviton*, but there are no direct or indirect experimental indications of its existence.

5. Peter H. Garbincius, *Charm Photoproduction Dynamics*, contributed talk to the *LAFEX* International School in High Energy Physics, Rio de Janeiro, Brazil, February 1995, FERMILAB-Conf-95/041.

6. In a non Standard Model, decays mediated by neutral currents might be possible: for example, $c \to uZ^0,\ Z^0 \to l^+l^-$.

7. By convention the mixing is only formulated in the (d, s, b) sector; it could as well be formulated in the (u, c, t) sector or in both by simply redefining the phases of the quark fields - no measurable physical results would change.

8. No mixing exists in the lepton sector, *provided the lepton neutrinos are massless.*

9. M. S. Witherell, *Charm Decay Physics*, UCSB-HEP-93-06.

10. Sheldon Stone, *Charmed Meson Decays*, HEPSY 1-92.

11. In a weak decay proceeding through the exchange or annihilation diagram, angular momentum conservation forces the two outcoming fermions to have the same helicity, i.e. to be both left-handed or both right-handed. Since in the Standard Model leptons are preferentially left-handed and anti-leptons are preferentially right-handed, this means that one of the to daughters is forced in the wrong helicity state, causing the decay to be suppressed. The suppression is larger for smaller mass leptons, since in the limit of zero mass the lepton is expected to be rigorously left-handed (and the anti-lepton must be right-handed). This is the reason why the decay $\pi^- \to \mu^-\overline{\nu}_\mu$ has a branching fraction which

is 10^4 times bigger than that of the decay $\pi^- \to e^-\overline{\nu}_e$, although the latter would be favored by phase space.

12. For decays into the massive τ lepton (such as $b\overline{u} \to \tau^-\nu_\tau$), helicity suppression is negligible; these decays are instead suppressed by the small hadronic decay constant.

13. L. Jauneau, *"Spectra and Polarization in K_{μ_3}"*, in *Methods in Subnuclear Physics*, Edited by M.Nikolic, Vol.III (1969), p.123-186.

14. J.D. Richman and P.R. Burchat, *Leptonic and Semileptonic Decays of Charm and Bottom Hadrons*, UCSB-HEP-95-08.

15. In a three body decay (where the masses of the daughter particles are known), the final state is completely described by the momentum vectors of the three particles. The nine components are connected by four energy-momentum conservation laws. Furthermore, the decay configuration is defined to within a rotation in space, which is described by three independent Euler angles. In conclusion, only two variables are independent.

16. Particle Data Group, L. Montanet et al., Phys. Rev. D **45** 11 (1992), pag. III.49.

17. M. Neubert, Phys. Rep. **245** (1994), 259-395.

18. C.R. Allton *et al.*, BU-HEP 94-29, CERN-TH7484/94.

19. A. Abada *et al.*, Nucl. Phys. B **416** (1994), 675.

20. K.C. Bowler *et al.*, the UKQCD collaboration, Edinburgh Preprint 94/546.

21. M. Wirbel, B. Stech, and M. Bauer, Z. Phys. C **29** (1985), 637; C **34** (1987), 103.

22. P.J. O'Donnell and Gursevil Turan, HEP-PH/9604208 (1996).

23. E687 Collab., P. L. Frabetti et al., Nucl. Instrum. Methods. A **314** (1992), 411.

24. E687 Collab., P. L. Frabetti et al., Nucl. Instrum. Methods. A **320** (1992), 519.

25. M.Giammarchi et al., *"The Monte Carlo program and the Pattern recognition for the Microvertex detector of the E687 Experiment at FNAL"*, Nucl. Instrum. Methods. A **251** (1986), 40-52.

26. Graphic display software developped by Dario Menasce

27. The signals have been obtained by running the reconstruction codes on a small subsample of the Global Vertex Skim, which is biased towards events containing SSD tracks and vertices; the relative yields of the different categories are not significant, but the mass resolution and the signal to noise of each type are.

28. E691 collab., J.C. Anjos *et all*, Phys. Rev. Lett. **62** (1989), 1587.

29. CLEO Collab., A. Bean *et al.*, Phys. Lett. B **317** (1993), 647.

30. E687 Collab., P. L. Frabetti *et al.*, Phys. Lett. B **B307** (1993), 262.

31. E691 Collab., J. C. Anjos *et al.*, Phys. Rev. Lett. **67** (1991), 1507.

32. E653 Collab., K. Kodama *et al.*, Phys. Lett. B **316** (1993), 455-462.

33. Particle Data Group, L. Montanet et al., Phys. Rev. D **50** (1994).

34. M.S. Nehring, *"Measurement of the Neutral Charmed Meson Semileptonic Decays $D^0 \to K^- e^+ \nu_e$ and $D^0 \to \pi^- e^+ \nu_e$"*, Ph.D. Thesis, University of Colorado at Boulder, 1995 (unpublished).

35. E687 Collab., P.L. Frabetti et al., Phys. Lett. B **364** (1995), 127-136.

36. CLEO collab., G.Brandenburg et al., Phys. Rev. Lett. **75** (1995), 3804.

37. The mass spectrum for a vector meson resonance decaying to two bodies $h^* \to h_1 h_2$ is parameterized in Monte Carlo with a *p-wave* Breit-Wigner[38]:

$$\frac{1}{N}\frac{dN}{dM} = \frac{\pi}{2}\,\frac{M M_0, }{(M^2 - M_0^2)^2 + M_0^2, ^2}\ ,$$

where , is the mass-dependent width given by:

$$, (M) = \left[\frac{P(M)}{P(M_0)}\right]^3 \frac{2, _0}{1 + \left[\frac{P(M)}{P(M_0)}\right]^2}\ ,$$

and $P(M)$ is the three momentum of the daughter particles in the center of mass frame, for a parent particle with mass M:

$$P(M)^2 = \left[\frac{M^2 + m_1^2 - m_2^2}{2\,M}\right]^2 - m_1^2$$
$$= \frac{M^4 + m_1^4 + m_2^4 - 2m_1^2 m_2^2 - 2m_2^2 M^2 - 2m_1^2 M^2}{4\,M^2} \;;$$

M_0 and $,_0$ are the nominal mass and full width half maximum for the resonance.

38. J.D. Jackson, Nuovo Cimento **34** (1964), 1644.

39. ARGUS collab., H. Albrecht et al., Phys. Lett. B **317** (1993), 227.

40. CLEO collab., D.Acosta et al., in *Lepton and Photon Interactions*, Proceedings of the 16th International Symposium, Ithaca, New York, 1993, edited by P.Drell and D.Rubin (AIP, New York, 1994).

41. E687 Collab., P.L. Frabetti et al., Phys. Rev. Lett. **72** (1994), 961.

42. CLEO collab., K.W.Edwards et al., Phys. Rev. Lett. **74** (1995), 3331.

43. Peter Cho, Phys. Rev. D **50** (1994), 3295.

44. S. Capstick and N. Isgur, Phys. Rev. D **34** (1986), 2809.

45. E687 Collab., P.L. Frabetti et al., Phys. Rev. Lett. **70** (1993), 1775.

46. The measured width of Monte Carlo samples is due only to our experimental resolution, since the $\Lambda_c^{\star +}$ states are generated with zero intrinsic width.

47. CLEO Collab., G. Crawford et al., Phys. Rev. Lett. **71** (1993), 3259.

48. E687 Collab., P. L. Frabetti *et al.*, *Analysis of the Cabibbo Suppressed Decay* $D^0 \to \pi^- l^+ \nu$, submitted for publication.

49. CLEO Collab., F. Butler *et al.*, Phys. Rev. D **52** (1995), 2656.

50. CLEO Collab., M.S, Alam *et al.*, Phys. Rev. Lett. **71** (1993), 1311.

51. Mark Collab., J. Adler *et al.*, Phys. Rev. Lett. **62** (1989), 1821.

52. N. Isgur, D. Scora, B. Grinstein, and M.B. Wise, Phys. Rev. D **39** (1989), 799.

53. D. Scora and N. Isgur, Phys. Rev. D **52** (1995), 2783.

54. V. Lubicz *et al.*, Phys. Lett. B **274** (1992), 415.

55. S. Narison, Phys. Lett. B **377** (1994), 163.

56. N. B. Demchuk *et al.*, INFN preprint INFN0ISS 95/18, Submitted to Sov. J. Nucl. Phys.

57. P. Ball, Phys. Rev. D **48** (1993), 3190.

58. P. Colangelo, F. De Fazio, and P. Santorelli, Phys. Lett B **327** (1994), 123.

59. R. Casalbuoni, A. Deandrea, N. Di Bartolomeo, F. Feruglio, R. Gatto, and G. Nardulli, Phys. Lett B **299** (1993), 139.

60. B. Bajc, S. Fajfer, and R.J. Oakes, IJS-TP-95/18, CMU-HEP-95-22, NUHEP-TH-95-13, November 1995.

61. C.W. Bernard, A.X. El-Khadra, and A. Soni, Phys. Rev. D **43** (1991), 2140.

62. W. Jaus, Phys. Rev. D **53** (1996), 1349.

63. J.G Korner, and G.A. Schuler, Z. Phys. C **46** (1990), 93.

64. M. Sadzikowski, Acta Physica Polonica, B **26** (1995), 835.

65. C.A. Dominguez and N. Paver, Phys. Lett. B **207** (1988), 499.

66. E687 Collab., P. L. Frabetti *et al.*, *Study of Higher Mass Charm Baryons decaying to* Λ_c^+, Phys. Lett. B **365** (1996), 461.

67. S. Capstick and N. Isgur, Phys. Rev. D **34** (1986), 2809.

APPENDIX: SYSTEMATIC ERROR TECHNIQUES

(a) Split sample technique

Let's suppose we performed the measurement of some physical quantity x over a given data sample. In order to assess possible systematic errors originating from the way the data sample was selected (for example, the analysis cuts used), we divide the total data sample into N approximately equal, statistically independent subsamples. We perform again the measurement of the physical quantity x separately for each subsample, obtaining as result $x_i \pm \sigma_i$. The weighted average of the N independent results is:

$$< x >= \frac{\sum_{i=1}^{N} x_i/\sigma_i^2}{\sum_{i=1}^{N} 1/\sigma_i^2}$$

and the corresponding error is:

$$\sigma_x = \sqrt{\frac{1}{\sum_{i=1}^{N} 1/\sigma_i^2}} \ .$$

We define the fluctuation of the N independent measurements as:

$$\sigma_{extra} = \sqrt{\frac{< x^2 > - < x >^2}{N-1}} \ .$$

For N randomly distributed measurements x_i, we would expect $\sigma_{extra} \sim \sigma_x$; if on the other hand it is found that $\sigma_{extra} > \sigma_x$, we estimate the systematic error to be:

$$\sigma_{sys} = \sqrt{\sigma_{extra}^2 - \sigma_x^2} \ .$$

(b) **Fit variant technique**

In order to investigate possible bias originating from the our fit to the experimental data, we apply the following technique. We perform N reasonable variations of the fitting process, and estimate the systematic uncertainty of the fit to be:

$$\sigma_{sys} = \sqrt{\frac{\sum_{i=1}^{N} x_i^2 - N < x >^2}{N-1}}$$

where $< x >$ is the mean value of the N measurements ($< x >= \sum_{i=1}^{N} x_i/N$).